Discovery of very high energy gamma-ray emission from 3C 279 and 3C 66A/B with the MAGIC telescope

Tesi doctoral

Manel Errando Trias

Universitat Autònoma de Barcelona
Departament de Física
08193 Bellaterra (Barcelona)
Spain
<errando@ifae.es>

July 2009

Supervised by Prof. Manel Martínez
Co-supervised by Dr. Daniel Mazin

Contents

List of Figures

List of Tables

Chapter 1

Introduction

Observational astronomy evolved over many centuries just observing astronomical objects that emit radiation in the optical frequency band. In the 20th century, radio astronomy –on the lower edge of the electromagnetic spectrum– and X-ray astronomy –on the upper edge– have shown that studying the radiation in a wider energy range can crucially revise our understanding of the universe.

Thermal processes taking place at stars, galaxies and other astrophysical bodies produce electromagnetic radiation from radio wavelengths up to X-rays. Any radiation emitted at energies higher than X-rays emerges from non-thermal processes in extremely violent astrophysical environments, such as active galactic nuclei, supernova remnants, gamma-ray bursts, pulsars or microquasars. These processes comprise acceleration, interaction, production and decay of relativistic particles, and produce highly energetic charged cosmic rays, photons and neutrinos. As charged particles are deflected by the interstellar and intergalactic magnetic fields, when they reach the Earth they do not point anymore to the location of their origin. Therefore, only gamma-rays and neutrinos trace back to their production sites.

Gamma-ray astronomy, covering the energy range between 10 MeV and 100 TeV, has progressed enormously in the last decades, from the launch of the CGRO[1] satellite to the construction of the new generation of ground-based Cherenkov Telescopes. In parallel, neutrino observatories are detecting the first hints of high energy neutrinos of astrophysical origin, although the Sun and the supernova SN 1987A are the only astrophysical sources of neutrinos detected so far. Since neutrino observatories do not have yet enough sensitivity to compensate the extremely low cross-sections with which neutrinos interact with matter, gamma-ray astronomy is nowadays the only available technique to observe the astrophysical objects that populate the non-thermal universe.

The Earth's atmosphere is opaque to gamma-rays. They interact at high altitudes producing particle showers. However, there are two ways of detecting gamma-rays of cosmic origin: studying the particle showers that gamma-rays produce in the atmosphere, or directly, by mounting a gamma-ray detector onto a satellite. Known gamma-ray sources have photon fluxes that rapidly fall with energy, typically 2 to 4 orders of magnitude per decade in energy. Satellites have a very good sensitivity at the keV to MeV energies, where the photon flux is usually high, but at GeV energies the flux is too low for them to collect enough statistics, since their effective area is limitted to approximately the size of the detector. On the other hand, MeV photons do not produce particle showers

[1] Compton Gamma Ray Observatory, in operation between 1991 and 2000

big enough to be detectable from ground. It is from few GeV on, and specially in the TeV region, where ground-based detectors have a very high performance in detecting the Cherenkov light produced by relativistic particles in the air showers, and reconstructing the shower development to estimate the origin and the energy of the primary gamma-ray.

Two complementary approaches have been experimented to reconstruct the atmospheric showers initiated by cosmic gamma-rays: the sampling of the charged particles that reach the ground, or the imaging of the Cherenkov photons emitted by this charged particles in the atmosphere. From these two techniques, the second one has proven, specially in the last fifteen years, to be the most competitive.

The first detection of a TeV gamma-ray source was the observation of the Crab Nebula by the Whipple telescope, already in 1989. In the 1990s, the HEGRA collaboration proved that imaging of an atmospheric shower with many telescopes improved the reconstruction capability. But it has been in the last decade, when a new generation of Cherenkov telescopes (CANGAROO, H.E.S.S., MAGIC, and VERITAS) has pushed down the detection energy threshold and sensitivity, increasing almost exponentially the number of detected GeV and TeV sources.

This increase in sensitivity, and in number of detected sources, allows gamma-ray astrophysicists to establish different populations of objects emitting very high energy gamma-rays. The first classification separates gamma-ray sources between the ones located inside our galaxy, and the extragalactic ones. Among the galactic objects, at least four astronomical source populations have been identified as possible gamma-ray emitters: supernova remnants, pulsars, pulsar wind nebulae and X-ray binary systems. Outside our galaxy, only active galactic nuclei have been detected to emit very high energy gamma-rays.

Active galactic nuclei are found at the center of galaxies which are thought to host a supermassive black hole. The extreme gravitational potential found in this central region forces the nearby mass to precipitate into the black hole, usually forming an accretion disk. Perpendicular to the accretion disk, two jets of ultrarelativistic particles can appear, being a natural source of very high energy photons.

Two nearby active galactic nuclei have been detected at TeV energies: M 87 and Centaurus A, both at redshift $z < 0.005$. This two sources are classified as radio galaxies, and the relativistic jet points with angles greater than 15° to the line of sight. For more distant objects, only those where the relativistic jet points within a small angle to the Earth, called blazars, have shown evidence for very high energy gamma-ray emission. So far, more than 20 objects of this class have been detected by ground-based Cherenkov telescopes, the more distant one –3C 279– being at redshift $z = 0.536$.

The search for gamma-ray emission from distant blazars faces a difficulty: the universe is not completely transparent to gamma-rays. Low energy photons in the infrared to ultraviolet range, which homogeneously fill the universe, interact with very high energy gamma-rays during their path to Earth producing an electron positron pair. This interaction is the main source of opacity to the propagation of very high energy gamma-rays, increasing with the distance of the gamma-ray source and with the energy of the gamma-rays. The absorption of very high energy gamma-rays by low energy photons fields –called generically extragalactic background light– makes the detection of distant blazars in this energy band very challenging.

The first extragalactic gamma-ray sources detected with ground-based telescopes were all nearby blazars, with $z \lesssim 0.1$. With the beginning of operation of a new generation of Cherenkov telescopes, blazars at resdhifts of $z \approx 0.2$ were detected. The energy spectrum

of the farthest detected blazars showed evidences of a photon density of the extragalactic background light lower than predicted by models and direct observations. The observational evidences of a low level of gamma-ray absorption would allow the detection of more distant sources. This is specially the case of observations with the MAGIC telescope. The fact that MAGIC has a low energy threshold of approximately 80 GeV –where absorption of gamma-rays is lower than at higher energies– together with a low density of the extragalactic background light could allow detections of bright gamma-ray emitting blazars up to $z \approx 0.5$. This possibility is tested in this thesis.

This thesis is structured as follows. An introduction on very high energy gamma-ray astrophysics together with a current status of the field is given in Chapter 2. The physics of active galactic nuclei and its interest in gamma-ray astronomy is discussed in Chapter 3. In Chapter 4, the interest of observing distant blazars with ground-based Cherenkov telescopes is motivated, and a search for the best candidates to be observed is described. The imaging atmospheric Cherenkov technique for the detection of gamma-rays is described in Chapter 5, followed by a description of the MAGIC telescope. Then, in Chapter 6 a detailed description of the analysis tools used to analyze the MAGIC telescope data is given. The upper limits derived for four of the observed distant blazars are presented in Chapter 7. Chapter 8 reports the discovery of the distant quasar 3C 279 and discusses the importance of this discovery, and Chapter 9 describes the detection of a gamma-ray source in the field of view of the blazar 3C 66A and discusses its possible associations. Finally, conclusions and a short outlook can be found in Chapter 10.

Chapter 2

Very high energy gamma-ray astronomy

This chapter includes a brief introduction on very high energy gamma-ray astrophysics, starting with short discussion on cosmic rays, and an introduction to the relevant processes of very high energy (VHE) gamma-ray production and propagation. Finally, the most relevant source populations of VHE gamma-ray emitters will be summarized, and related fundamental physics topics will be presented.

2.1 Cosmic rays

In his balloon experiments in 1912, Victor Hess observed ionizing radiation permanently impinging on the Earth's atmosphere (Hess, 1912). These particles, named 'cosmic rays', have been found to be mainly made of electrically charged particles, namely protons, alpha particles and heavier nuclei, as well as photons, and a small fraction of electrons. The overall differential cosmic ray spectrum is given in Figure 2.1. It extends over an energy range of 13 orders of magnitude with the flux dropping from about 1 particle cm^{-2} s^{-1} at energies of $10^8\,\mathrm{eV}$ to 10^{-2} particles km^{-2} year^{-1} at $10^{20}\,\mathrm{eV}$.

Below $E = 1\,\mathrm{GeV}$, the cosmic ray flux is affected by the solar wind, which modulates the magnetic field in the solar system with a period of about 11 years. At higher energies the differential spectrum can be described by a power law[1] with spectral index $\Gamma \approx 2.7$ up to $\mathrm{E} = 10^{15.5}\,\mathrm{eV}$ and $\Gamma \approx 3.0$ above that energy. The transition region is called 'knee'. The spectrum hardens again at about $E = 10^{18}\,\mathrm{eV}$ (the so-called 'ankle'). It is believed that cosmic rays below the knee are produced at galactic sites like supernova remnants, pulsars, or binary systems, while cosmic rays with higher energies are not confined to our galaxy. Due to galactic and intergalactic magnetic fields, charged cosmic rays up to $10^{19}\,\mathrm{eV}$ are isotropized. Therefore, their arrival direction at Earth does not point back to their origin. Only at even higher energies, in the regime of the ultra high energy cosmic rays, the rigidity $R = E/(Ze)$ of the particles is so high that they are not deflected by extragalactic or galactic magnetic fields ($r_{gyro} = R/B$). AGASA, a 100 km2 scintillator air shower array in Japan, found anisotropies in the arrival direction of the highest energy cosmic rays, pointing at the possibility of an astronomy of such extremely high energy particles (Takeda et al., 1999). This anisotropy ha been later confirmed by the more sensitive Pierre Auger Observatory (Abraham et al., 2007), as shown in Figure 2.2.

[1] $\mathrm{d}N/\mathrm{d}E \propto E^{-\Gamma}$

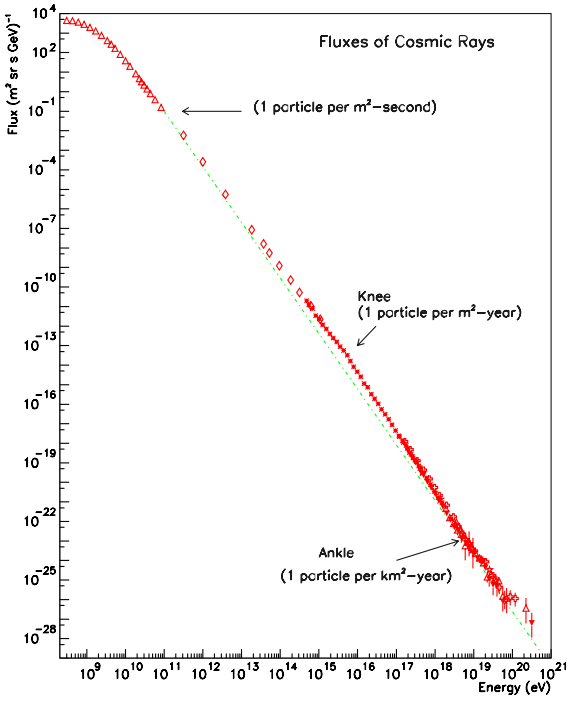

Figure 2.1: All-particle cosmic ray spectrum. From Bhattacharjee (2000).

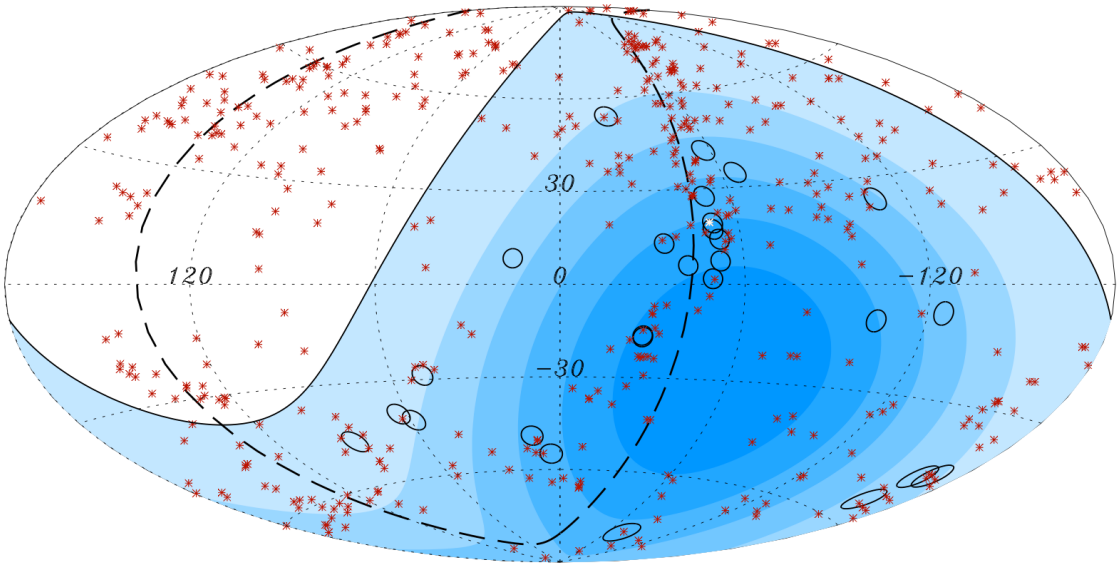

Figure 2.2: Arrival directions of the Auger highest energy events. Black circles indicate the arrival directions of the 27 highest energy events recorded by the Pierre Auger Observatory. Red asteriscs show the catalog position of nearby active galactic nuclei. Taken from Abraham et al. (2007).

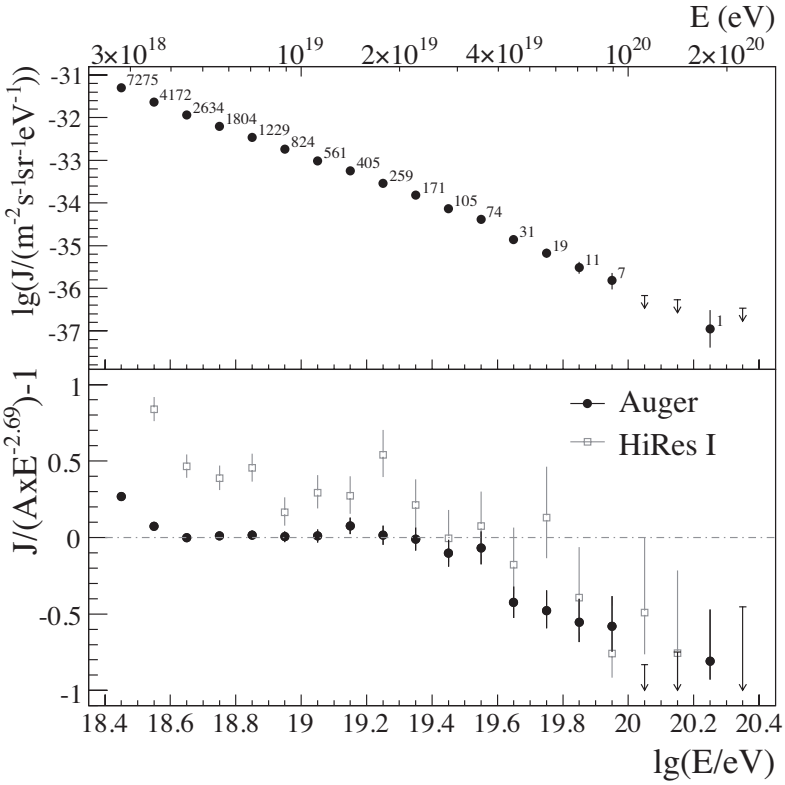

Figure 2.3: *Upper panel:* The differential flux as a function of energy, with statistical uncertainties. *Lower Panel:* The fractional differences between Auger and HiRes data compared with a spectrum with an index of 2.69. From Abraham et al. (2008).

2.1.1 The GZK cutoff

The interaction of cosmic rays with the 2.7 K microwave background radiation limits the upper edge of the cosmic ray spectrum:

$$\mathrm{p} + \gamma_{\mathrm{CMB}} \longrightarrow \Delta^{\star} \longrightarrow \mathrm{p} + \pi^{0}$$
$$\mathrm{p} + \gamma_{\mathrm{CMB}} \longrightarrow \Delta^{\star} \longrightarrow \mathrm{n} + \pi^{+}$$

The loss of energy by this process leads to the Greisen-Zatsepin-Kuzmin (GZK) cutoff in the cosmic ray (Greisen, 1966; Zatsepin and Kuzmin, 1966), which limits the maximum distance that cosmic rays of $E \sim 10^{20}$ eV can travel to ~ 50 Mpc. The existence of the GZK cutoff has been a much debated subject. While the AGASA experiment observed 11 events above the GZK cutoff energy (Takeda et al., 1998) the measurements performed by the HiRes collaboration, operating two fluorescence detectors in the U.S., showed the expected attenuation structure both in monocular and stereoscopic observations (Springer, 2005). The Pierre Auger Auger collaboration, which has already accumulated around five times larger statistics than previous experiments, confirmed the predicted attenuation by the GZK cutoff with their first published cosmic ray spectrum (Abraham et al., 2008, see Figure 2.3) with a confidence level of more than 6σ.

2.1.2 Acceleration of charged particles

In astrophysics, non-thermal processes generally lead to power law spectra of the accelerated particles (Longair, 1992). A mechanism accounting for this observation was put forward in Fermi (1949). In diffusive shock acceleration processes, particles repeatedly cross shock fronts, with an energy gain proportional to the shock velocity β at each crossing (first order Fermi acceleration). For moving plasma clouds, e.g. jets of active galactic nuclei, the energy gain is proportional to β^2 (second order Fermi acceleration). Reviews on this subject are given in Blandford and Eichler (1987) and Kirk (1994). Alternative processes discussed particularly for AGNs are associated with the magneto-rotational instability of their accretion disks via some form of magnetic reconnection (Madejski and Sikora, 2006).

2.2 Gamma-rays

Unlike the charged components of the cosmic radiation, cosmic ray photons are not deflected by magnetic fields and thus point back to their source. Therefore, the knowledge of the gamma-ray production site allows to study the physical properties of the sources and the acceleration mechanisms at work.

2.2.1 Gamma-ray production mechanisms

Thermal radiation emitted by stars is characterized by a blackbody spectrum that can be described by Planck's law of black-body radiation with temperatures spanning from 3000 K to 50000 K. This translates to photons in the range of visible to ultra-violet light. The hottest objects in the universe emit radiation up to X-rays of few keV energy. Higher energies are only reached in non-thermal processes. The most relevant elementary processes that produce gamma-rays are briefly described in the following (Longair, 1992):

π^0 decay: As the lightest hadrons with $m_\pi \approx 135\,\mathrm{MeV}$, neutral and charged pions are among the hadronic end products of nucleonic cascades. Charged ($\pi^\pm$) and neutral (π^0) pions are produced with the same probability; Neutral pions have a very short lifetime of $\sim 10^{-16}\,\mathrm{s}$ and decay into two very high energy (VHE) photons. With their considerably longer lifetime of $\sim 2.6 \times 10^{-8}\,\mathrm{s}$, high energy charged pions usually undergo further interactions before they eventually decay into electrons and neutrinos.

Inverse Compton scattering: Relativistic electrons can transfer part of their energy to low energy photons through the process called inverse Compton scattering. For $E_e \cdot E_\gamma \ll m_e^2 c^4$ the cross section for this process is the Thomson cross section:

$$\sigma_T = \tfrac{3}{8}\pi r_e^2 \tag{2.1}$$

For $E_e \cdot E_\gamma \approx m_e^2 c^4$ the exact Klein-Nishina formula has to be used (see Weinberg, 1995, pp. 362–9), whereas in the case of ultrarelativistic electrons ($E_e \cdot E_\gamma \gg m_e^2 c^4$) the approximation

$$\sigma_{KN} = \pi r_e^2 \frac{1}{\epsilon}\left(\ln(2\epsilon) + 0.5\right)\,, \epsilon = \frac{E_\gamma}{m_e c^2} \tag{2.2}$$

can be used. In this regime the electrons suffer large energy losses. It can be shown that the maximum energy gain is $E_{max} \approx 4\gamma^2 E_\gamma$ for Lorentz factors of $\gamma \approx 10^2$–10^4, which means that keV seed photons are upscattered to the GeV-TeV domain. This is the mechanism at work in synchrotron self-Compton models (see Section 3.3.1).

Synchrotron radiation: In the presence of magnetic fields, relativistic charged particles emit Synchrotron radiation. For electrons, the peak emission energy is given by $E_{peak} = 5 \times 10^{-9} B_\perp \gamma_e^2$ eV with the transverse component of the magnetic field $B_\perp$ given in units of Gauss. Synchrotron radiation of accelerated electrons is one of the most important processes in the non-thermal Universe. In the context of VHE gamma-rays, synchrotron radiation is the usual process for the generation of seed photons for the above described inverse Compton scattering. Moreover, ultra-high energy cosmic rays can emit synchrotron photons directly in the VHE domain.

Bremsstrahlung: When charged particles are deflected in electric fields they radiate bremsstrahlung. The emitted photon spectrum has a power law form with the same spectral index as the accelerated particles. Bremsstrahlung of ultra-high energy cosmic rays can reach TeV energies.

2.2.2 Absorption of VHE gamma-rays

VHE gamma-rays from extragalactic sources are absorbed by the interaction with low energy photons from the extragalactic background light (EBL). When traveling cosmological distances, the attenuation of VHE photons by γ–γ interaction producing an electron-positron pair can alter observed spectra substantially, and even constrain the maximum distance a particular detector can look back into the universe due to its energy threshold. At energies above 300 GeV, flux of gamma-rays suffers from significant absorption for sources with redshifts $z \gtrsim 0.1$. Cherenkov detectors operating with energy thresholds $\sim 300\,\mathrm{GeV}$ in fact detected only few extragalactic sources with low redshifts ($z < 0.2$), in contrast to the EGRET experiment, which detected 66 AGNs (plus 27 tentative identifications) at lower gamma-ray energies of $E > 100\,\mathrm{MeV}$ (Hartman et al., 1999), up to redshifts above $z = 1$. This discrepancy implies that most of the EGRET sources have spectra with cutoffs between 10 GeV and 300 GeV, that can either be intrinsic of the source or caused bay VHE gamma-ray attenuation by the EBL.

The extragalactic background light

The main contributions to the extragalactic background light are the (redshifted) relic emission of galaxies and star-forming systems and the light absorbed and re-emitted by dust in galaxies. The resulting spectral energy distribution comprises two distinct peaks, one in the near infrared, $\lambda \sim 1$–$2\,\mu$m, and one in the far infrared, $\lambda \sim 100$–$200\,\mu$m (see Figure 2.4). The long wavelength end of the EBL spectrum is outshined by the 2.7 K cosmic microwave background radiation. It is important to stress that the EBL undergoes evolution with redshift, as it is sensitive to the time when the different object population contributing to the EBL started to populate the universe.

Direct measurements of the present EBL spectral energy distribution (see Hauser and Dwek (2001) for a review) suffer from large uncertainties, as they are dominated by large foregrounds of galactic and zodiacal light. In turn, attempts to model the spectral energy distribution are challenged by the need for strong assumptions on cosmology, star

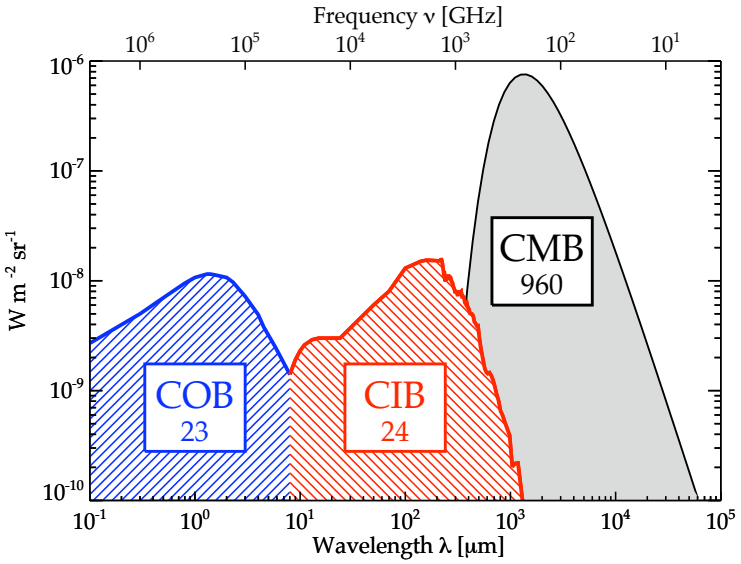

Figure 2.4: Spectral energy distribution of the most important (by intensity) backgrounds in the universe, and their approximate brightness in $\mathrm{nW\,m^{-2}sr^{-1}}$ written in the boxes. From right to left: the Cosmic Microwave Background (CMB), the Cosmic Infrared Background (CIB) and the Cosmic Optical Background (COB). The later two comprise the EBL. From Dole et al. (2006).

formation rate, and the distribution of matter in the universe. Additionally, a good understanding of the light recycling history is required. Recently, VHE gamma-ray measurements of distant AGNs were used to infer severe limits on the EBL density, making general assumptions on the AGN gamma-ray emission mechanisms (Aharonian et al., 2006*b*, 2007; Albert et al., 2008*e*).

VHE gamma-ray attenuation

To compute the attenuation of a given intrinsic VHE gamma-ray spectrum, knowledge not only of the present (i.e., currently measured, $z = 0$) EBL is required, but also of its past evolution. As this cannot be measured directly, theoretical or semi-empirical models have to be employed.

Current EBL models result in a steepening of the intrinsic spectra in the 200 GeV–2 TeV region (power law spectra are softened, but their form is retained), while for lower energies the effects are minimal. For even higher energies a cutoff is expected. Details on the modification of VHE gamma-ray spectra due to EBL can be found in Section 4.1.

2.3 Astrophysical sources of gamma-rays

The launch of the Energetic Gamma-Ray Experiment Telescope (EGRET) for gamma-rays above 20 MeV on board the Compton Gamma Ray Observatory (CGRO) in 1990 opened up the gamma-ray sky in the high energy gamma-ray domain. EGRET discovered 271 sources (Hartman et al., 1999), 101 of which could be associated with already known astronomical objects, while a large number of 170 were newly discovered and could not be identified.

The highest energy at which satellite experiments can detect a significant number of

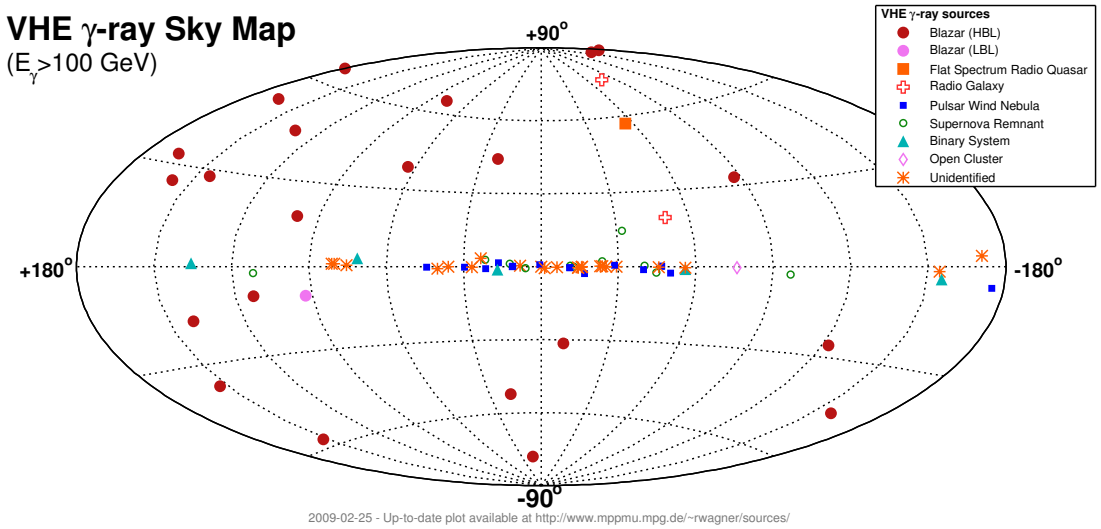

Figure 2.5: Map of all known VHE gamma-ray sources.

gamma-rays is determined by the steeply falling gamma-ray energy spectra. Thanks to their unique detection technique, ground-based Cherenkov telescopes with their huge detection areas are well suited to observe gamma-ray emitters in the very high energy (VHE) domain (see Chapter 5). Until recently, before the new generation of Cherenkov telescopes became operative, these detectors had energy thresholds of $E \approx 300\,\mathrm{GeV}$, which allowed them to detect only very few sources, the first of which was the Crab Nebula (Weekes et al., 1989). With the advent of IACT systems with substantially higher sensitivity and lower energy thresholds like CANGAROO, H.E.S.S, MAGIC, and VERITAS, the number of VHE gamma-ray sources has dramatically increased to currently about 100, with new detections nearly every month. In the following, the most prominent targets for ground-based Cherenkov telescopes will be summarized.

2.3.1 Galactic sources

At least three astronomical source populations are represented in the current VHE gamma-ray source catalog (Aharonian et al., 2008*b*): supernova remnants (SNRs), pulsars and pulsar wind nebulae (PWNe), and binary systems, In addition, observations of the central region of our Galaxy revealed a diffuse TeV gamma-ray emission component, which is apparently dominated by contributions from giant molecular clouds (Aharonian et al., 2006*c*). These massive complexes of gas and dust most likely serve as effective targets for interactions of relativistic particles from nearby active or recent accelerators. Meanwhile, many sources discovered by H.E.S.S. in the galactic plane remain unidentified (Aharonian et al., 2005*a*), and it cannot be excluded that a fraction of the still unidentified sources is related to other source classes (see Figure 2.6).

Supernova remnants

For decades it has been believed that the supernova explosions and, more specifically, the remnants of these powerful events are the principal factories of production for galactic cosmic rays. The main phenomenological argument in favor of this hypothesis is based on the kinetic energy available in supernova events and the rather large energy budget

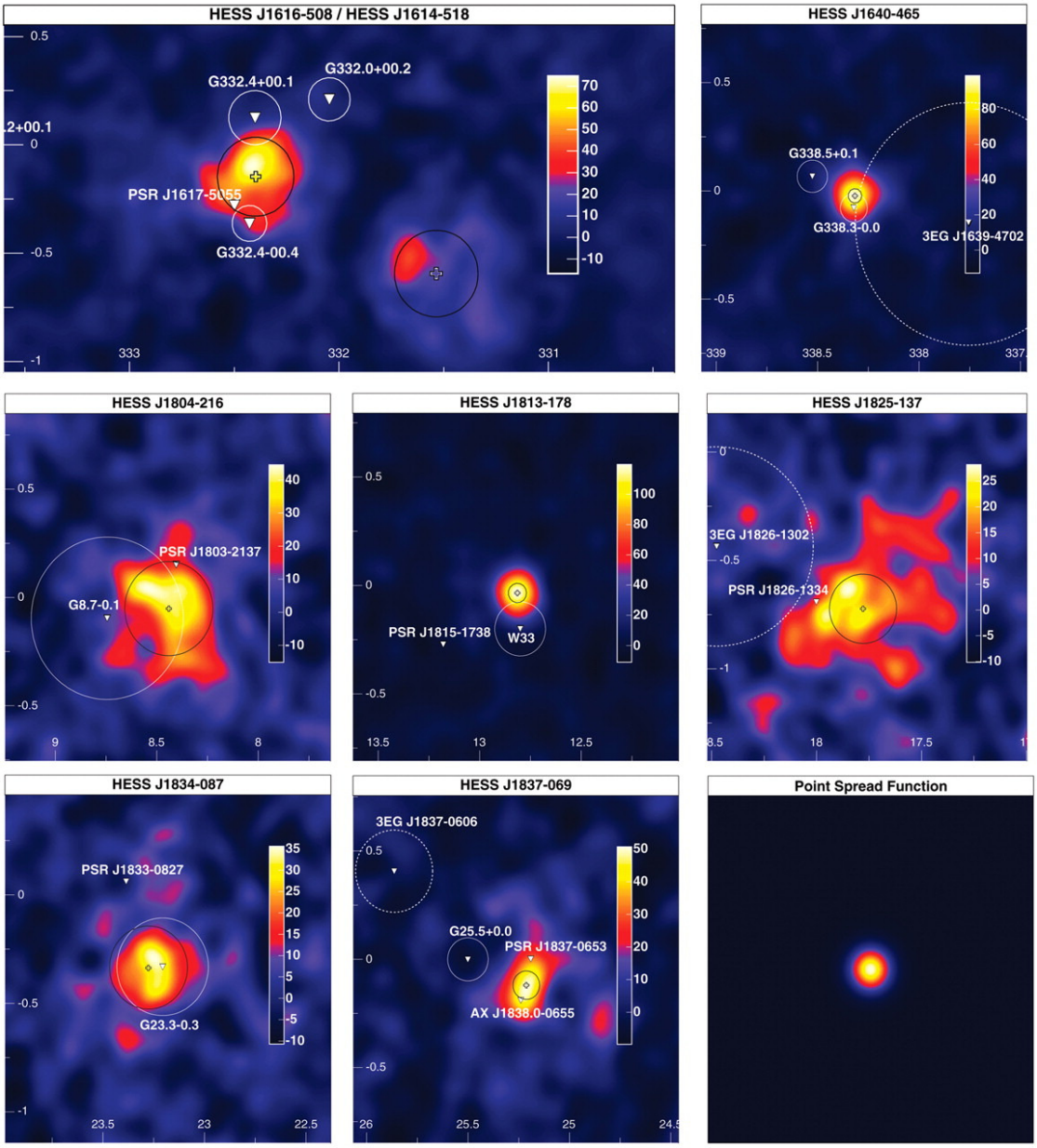

Figure 2.6: Smoothed excess maps in units of counts of the regions around each of the eight new sources in Galactic coordinates (in degrees). The best-fit centroids for the gamma-ray emission are shown as crosses, and the best-fit rms size as a black circle. Possible counterparts are marked by white triangles, with circles indicating the nominal source radius (or the position error in the case of EGRET sources). The lower right panel indicates the simulated point spread function of the instrument for these data, smoothed in the same way as the other panels. From Aharonian et al. (2005*a*).

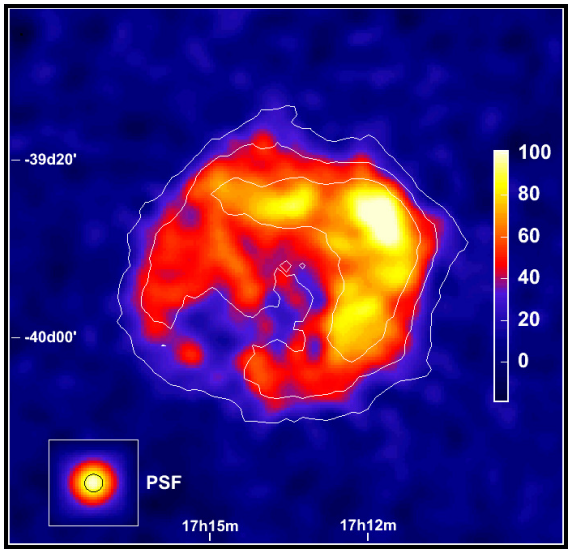

Figure 2.7: The gamma-ray image of the supernova remnant RX J1713.7-3946. From Aharonian et al. (2006*a*).

inferred for the galactic cosmic rays. Namely, the required power to maintain the cosmic ray density at the observed level is about 10% of the total mechanical energy released by supernova explosions in our Galaxy (Aharonian et al., 2008*b*).

In supernova remnants, the assumed high acceleration efficiency, coupled with hard energy spectra of protons extending to multi-TeV energies, should lead to VHE gamma-ray fluxes of hadronic origin. It should be noted, however, that almost all young SNRs are sources of non-thermal X-ray radiation, presumably of synchrotron origin radiated by electrons with energies of about 10 TeV. Since the same electrons can also upscatter the synchrotron photons to TeV gamma-rays through inverse Compton scattering, two competing emission processes can be responsible for TeV radiation. This implies that generally the gamma radiation of hadronic origin from SNRs is expected to be significantly contaminated by the IC component.

Pulsars and pulsar wind nebulae

Pulsars are rapidly rotating neutron stars formed at supernova explosions. Pulsars can emit pulsed gamma-ray emission up to energies $\sim$ 30 GeV. The energy spectra and the structure of light curves of the pulsed emission carry key information about the location of the gamma-ray production region in the pulsar magnetosphere. Only six pulsars have been firmly established by the EGRET team as high energy gamma-ray emitters. First results from the *Fermi*-LAT collaboration reported the detection of 30 gamma-ray pulsars, 15 of which were not previously known at other wavelengths (Abdo et al., 2009). Generally, due to the pairproduction in the strong magnetic field, VHE gamma-ray emission from the pulsar magnetospheres is believed to be strongly attenuated. However, the MAGIC collaboration reported a significant detection of gamma-rays from the Crab pulsar above 25 GeV (Aliu et al., 2008, see Figure 2.8(a)).

Apart from the pulsar magnetosphere, VHE gamma-rays can be effectively produced after the termination of the wind which leads to the acceleration of electrons to energies up to 100 TeV, producing continuum emission. The cosmic microwave background forms

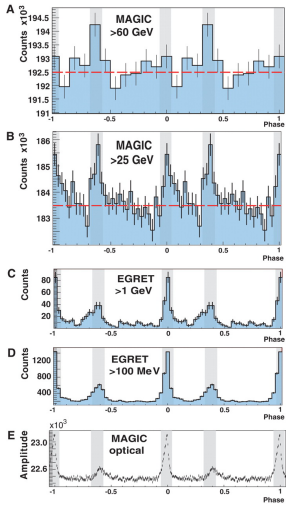

(a) Pulsed emission from the Crab Nebula pulsar in different energy bands. From Aliu et al. (2008).

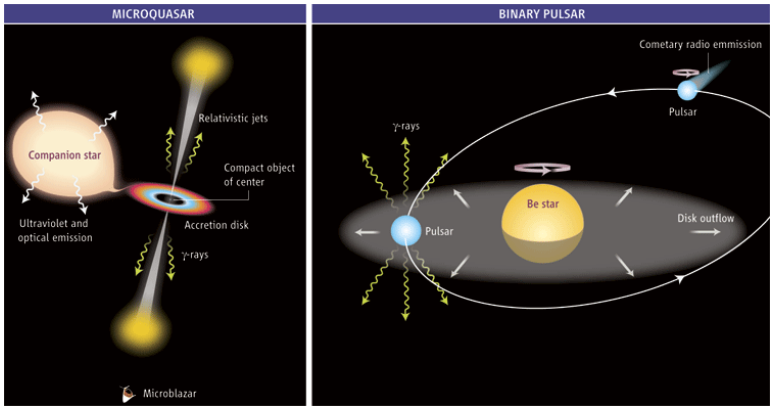

(b) Alternative models for very energetic gamma-ray binaries. Credit: P. Huey / *Science*

Figure 2.8: Pulsed emission from the Crab Nebula pulsar and scenarios for VHE emission from gamma-ray binaries.

a universal population of seed photons that guarantee VHE gamma-ray emission from any powerful accelerator of multi-TeV electrons, in general, and from PWNe, in particular. On the other hand, since the inverse Compton scattering in these objects results generally in hard energy spectra below 100 GeV, the detection of PWNe at MeV-GeV energies requires more sensitive space-borne instruments compared with EGRET. In this regard, it is quite natural that, while PWNe constitutes one of the largest TeV source populations, so far there is no strong evidence for GeV counterparts of PWNe. Since the first positive detection by the Whipple collaboration (Weekes et al., 1989), the Crab Nebula, a classical PWNe, has been independently detected by more than two dozen groups using different ground-based techniques. Presently the reported measurements from ground-based detectors cover a very broad energy range that extends from 60 GeV to 100 TeV.

Binary systems

X-ray binaries are a class of binary stars that are luminous in X-rays. The X-rays are produced by matter falling from one star to a compact object: a white dwarf, neutron star, or black hole. Generally, X-ray binaries are treated as thermal sources which effectively transform the gravitational energy of the compact object (a neutron star or a black hole) into X-ray emission radiated away by the hot accretion plasma. However, in such systems, effective particle acceleration is also possible. It can be linked to the termination of the pulsar wind or can be originated through the internal shocks in the jet formed in the vicinity of the black hole. If so, excellent conditions for high energy gamma-ray production can be created due to the dense target material in the form of optical photons or gas provided by the companion star. In the 1980s, X-ray binaries constituted the highlight source population of ground-based gamma-ray astronomy, although detections were just marginal. Recently, binary systems have gained again the interest of the VHE gamma-

ray community after the discovery of galactic sources with relativistic jets, generically named microquasars (Mirabel and Rodriguez, 1994). Another type of binary systems which are potential gamma-ray emitters are the binaries which contain young pulsars. These sources work, to a certain extent, like PWNe but located in a high radiation field environment. Three objects of this class have been firmly identified so far in the VHE domain: LS 5039 (Aharonian et al., 2005*c*), LS I+61 303 (Albert et al., 2006*c*), and PSR B1259-63 (Aharonian et al., 2005*b*). Also HESS J0632+057 is likely a gamma-ray binary (Hinton et al., 2009).

2.3.2 Extragalactic objects

Many representatives of several extragalactic source populations, in particular active galactic nuclei (AGN), radiogalaxies, starburst galaxies and clusters of galaxies, are potential VHE gamma-ray sources. First of all this concerns blazars, currently the largest class of TeV gamma ray emitters.

Blazars

AGNs are found at the center of galaxies which are thought to host a supermassive black hole. They represent a large population of objects characterized by luminous electromagnetic radiation produced in compact volumes, consisting of several classes of active galaxies with substantially different characteristics. Presently, the AGN classification schemes assume that the differences are basically due to the strongly anisotropic radiation patterns, i.e. that the pointing directions are more important than the differences in intrinsic physical properties. AGN with relativistic jets close to the line of sight are called blazars. The Doppler-boosted radiation coupled with the orientation of the jets towards the observer make these objects perfect laboratories to study the physics of relativistic outflows. First of all this concerns the BL Lac objects, a subpopulation of blazars of which more than twenty are already established as VHE gamma-ray emitters. Moreover, all but one blazars so far detected in VHE gamma-rays are BL Lac objects[2]: galaxies with extremely bright active cores which overshine the radiation from the rest of the galaxy. The rapid variability of these objects in brightness and in polarization is explained by relativistic synchrotron jets, i.e. indicates the presence of ultrarelativistic electrons. VHE gamma radiation of BL Lacs provides unique, model-independent information about the acceleration and radiation sites in these objects.

Radiogalaxies

Two nearby radiogalaxies: Centaurus A and M 87, are obvious TeV source candidates given their overall power, a significant part of which is released in nonthermal forms. M 87 is a giant radiogalaxy located in the Virgo galaxy cluster at a distance of 16 Mpc, and has been long considered as a potential gamma-ray emitter. In 2003, the HEGRA collaboration reported the discovery of a weak VHE gamma-ray signal from M 87 (Aharonian et al., 2003). This discovery has been later confirmed by H.E.S.S., MAGIC and VERITAS (Aharonian et al., 2006*d*; Albert et al., 2008*d*; Acciari et al., 2008*b*, respectively). Recently, Centaurus A has also been reported as VHE gamma-ray emitter (Aharonian et al., 2009).

[2]being 3C 279, classified as a flat spectrum radio quasar, the only exception

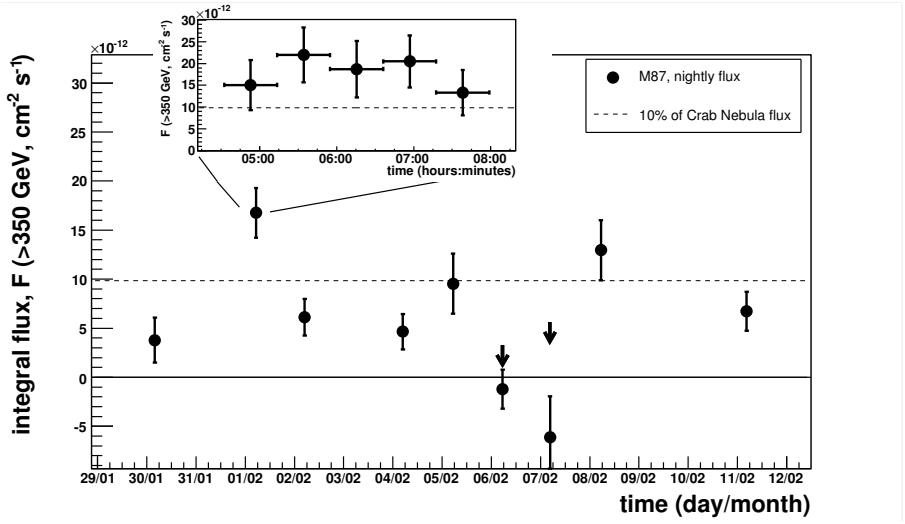

Figure 2.9: Measured gamma-ray light curve of the radiogalaxy M 87 during a strong flaring activity in February 2008. From Albert et al. (2008*d*).

Gamma-ray bursts

Although there is little doubt that gamma-ray bursts (GRBs)—short lasting solitary events of extragalactic origin detected at hard X-ray and soft gamma-ray energy bands—are produced by non-thermal particles, GRBs remain one of the most enigmatic and poorly understood phenomena in astrophysics. Many models have been suggested for explanation of the spectral and temporal properties of GRBs, both during the main events and at the afterglow stage. Some of the GRB models predict a significant energy release in VHE gamma-rays and neutrinos, although the flux predictions contain very large uncertainties.

The search for VHE episodic events benefits from large field of view (FoV)instruments such as Milagro. However, given the large redshifts of objects responsible for GRBs, the high energy threshold of Milagro (~ 5 TeV, Abdo et al., 2007) and similar installations did not allow detections of GRBs so far, although a hint of TeV emission from the gamma-ray burst GRB 970417a was reported by Milagrito, the Milagro prototype installation (Atkins et al., 2000). The small FoV of ground-based Cherenkov telescopes (typically 3–5°) limits the potential of these instruments for a search for high energy emission linked to GRBs. However, using a fast (few seconds) automatic alert system from satellites, an observation of the prompt and afterglow GRB phases is possible with ground-based Cherenkov telescopes. In this regard, the MAGIC telescope, with its relatively low energy threshold ~ 80 GeV and its fast slewing capability, is presently the best suited instrument for GRB studies in the VHE regime. The ability of the MAGIC telescope to perform rapid observations of GRBs has recently been demonstrated by observing early afterglows (within tens of seconds after the start of the main events) of nine GRBs triggered by alerts from the Swift, HETE-II and Integral satellites. So far no excess events have been detected.

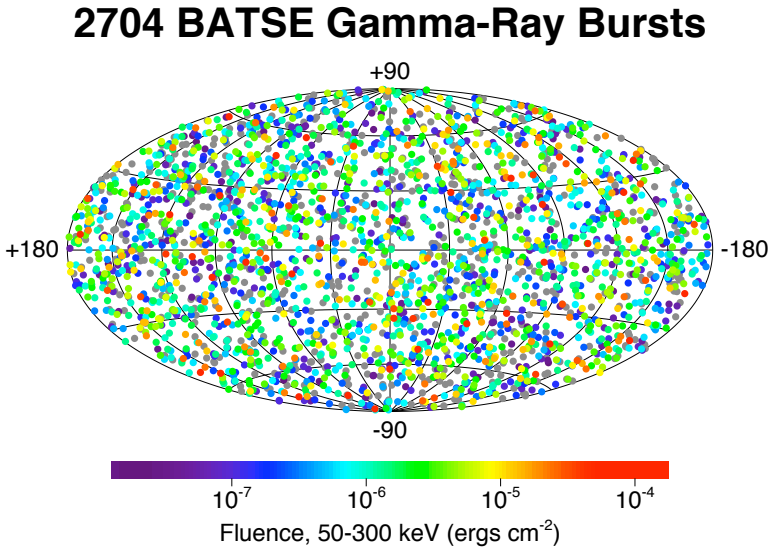

Figure 2.10: Sky map of the BATSE detected GRBs.
From `http://www.batse.msfc.nasa.gov/batse/grb/skymap`.

2.3.3 Connection to particle physics

Limits on the violation of Lorentz invariance

Observations of the electromagnetic radiation from astrophysical sources exhibiting fast flux variations –mainly AGNs, GRBs and pulsars– make possible the study of correlations between the energy and the arrival time of individual photons. Two different effects can explain the appearance of such correlations: either they are source-intrinsic or have originated during the propagation of the radiation from the source to the Earth. On the one hand, the emission mechanisms taking place at the source can cause delays between photons of different energies to appear. In the case of pulsars, a difference in the emission location for different energies can cause the shape and peak time of the pulses to change with energy. In AGNs, the delays can be caused, for instance, by the gradual acceleration of the electrons responsible for the emission. On the other hand, if the emission is assumed to be simultaneous at the source for all photons in a certain energy range, an energy-dependent propagation effect could also explain the appearance of correlations between photon energy and arrival time. Quantum gravity (QG) is the main framework where this kind of propagation effects may show up.

It is widely speculated that space-time is a dynamical medium, subject to quantum-gravitational effects that cause space-time to fluctuate on the Planck distance scales. Model realizations of QG predict that quantum fluctuations in the space-time metric make it appear 'foamy' on very short distance scales (see Rovelli, 1998; Sarkar, 2002, for reviews). The propagation of photons through this fluctuating space-time might induce an energy dependence of the speed of light, resulting in an observable difference on the propagation time for photons of different energies. The anomaly induced by QG will

always be a small perturbation of the assumed light speed c.

The possibility to observe QG efects in the propagation of photons from astrophysical sources was proposed in (Amelino-Camelia et al., 1998). If two photons of different energy are emitted simultaneously from an astrophysical object, the expected delay between their arrival times when they are detected increases with the distance to the source and with the energy of the photons. Therefore, the maximum sensitivity to energy dependent propagation effects is expected from observations of very fast flux variations coming from sources at large distances that emit photons up to very high energies.

The first candidates considered for such observations were gamma-ray bursts (Amelino-Camelia et al., 1998), but the first experimental result on possible energy-dependent speed of light came from the measurement of a flare of the active galactic nucleus Mkn 421 at TeV energies by the Whipple gamma-ray telescope (Biller et al., 1999), claiming a lower limit to the energy scale of quantum gravity of $M_{QG} > 6 \times 10^{16}\,\mathrm{GeV}$. Other bounds have been obtained by studying the emission of pulsars (Kaaret, 1999), and a combined analysis of many GRBs yielded to a robust lower limit of $M_{QG} > 0.9 \times 10^{16}\,\mathrm{GeV}$ (Ellis et al., 2006). Recent analysis by the MAGIC and H.E.S.S. collaborations using gamma-ray flares from the blazars Mrk 501 and PKS 2155-304 set respectively new constraints to the quantum gravity energy scale to $M_{QG} > 0.6 \times 10^{18}\,\mathrm{GeV}$ (Albert et al., 2008*c*; Martínez and Errando, 2009) and $M_{QG} > 0.6 \times 10^{18}\,\mathrm{GeV}$ (Aharonian et al., 2008*a*).

Search for dark matter

In the last decade, a standard cosmological picture of the Universe (the ΛCDM cosmology) has emerged, including a detailed breakdown of the main constituents of the energy density of the Universe. The Universe now appears to be spatially flat and accelerating, with ordinary baryonic matter providing only about $\sim 4\%$ of the energy budget. The balance is in the form of cold non-baryonic dark matter (CDM) accounting for about 26% of the energy density and dark energy or a cosmological constant (Λ) providing the remaining $\sim 70\%$. This new understanding has largely been driven by recent measurements of the temperature anisotropy in the cosmic microwave background radiation together with measurements of high redshift Type Ia supernovae. High energy gamma-rays from dark matter annihilation in the halo of our galaxy or other nearby galaxies may provide a means of discovering and identifying this unseen component of the Universe. Up to now, searches conducted with ground-based Cherenkov telescopes only provided upper limits.

Chapter 3

Active Galactic Nuclei

This chapter describes the physical properties of active galactic nuclei and their characteristics as source population. The possible emission models that explain the spectral properties of their emission are then discussed, with special emphasis on their output in the very high energy gamma-ray band. Finally, the observations of active galactic nuclei with ground-based Cherenkov telescopes are summarized.

In some galaxies, known as active galactic nuclei (AGNs), the nucleus of the galaxy emits more radiation than the entire rest of the galaxy. The radiation flux emitted by the core is usually highly variable. Current understanding of AGNs describes them as supermassive black holes (SMBH) which lie in the center of galaxies. The spectrum of the emission of AGNs is clearly non-thermal, and conversion of matter into energy under the strong gravitational potential of the accretion disk seems to be the engine behind the emission.

3.1 Unified model

The unification scheme of AGNs (Blandford and Konigl, 1979; Antonucci, 1993; Urry and Padovani, 1995) suggests that the different emission properties of different AGN classes (see Figure 3.1) are caused by differences in the viewing angle towards the observer, the accretion rate and the mass of the central black hole. In this unified scheme, the SMBH located in the central region accretes the surrounding material forming a disc of hot plasma (see Figure 3.2). The typical size of a galaxy is $\sim 10^4$ pc, while typical dimensions for their nuclei are 1–10 pc. The thermal radiation produced in the accretion disc ionizes the gas clouds close to the SMBH forming the broad-line region (see Figure 3.3). As the broad line emission region is close to the central black hole and, therefore, moving at high velocities, its emission lines are widened due to the Doppler effect. Further away from the SMBH, slower moving gas clouds produce the narrow-line absorption and emission spectrum of the AGN. The whole system is surrounded by a torus, which obscures the central part along the equatorial plane of the disc. If the accretion rate is high enough, a pair of collimated jets of ultra-relativistic plasma will appear in directions perpendicular to the equatorial plane.

The optical and radio observations of AGN originate its classification (see Figure 3.1). The AGNs with low optical flux are called Seyfert galaxies and Radio Galaxies, whereas

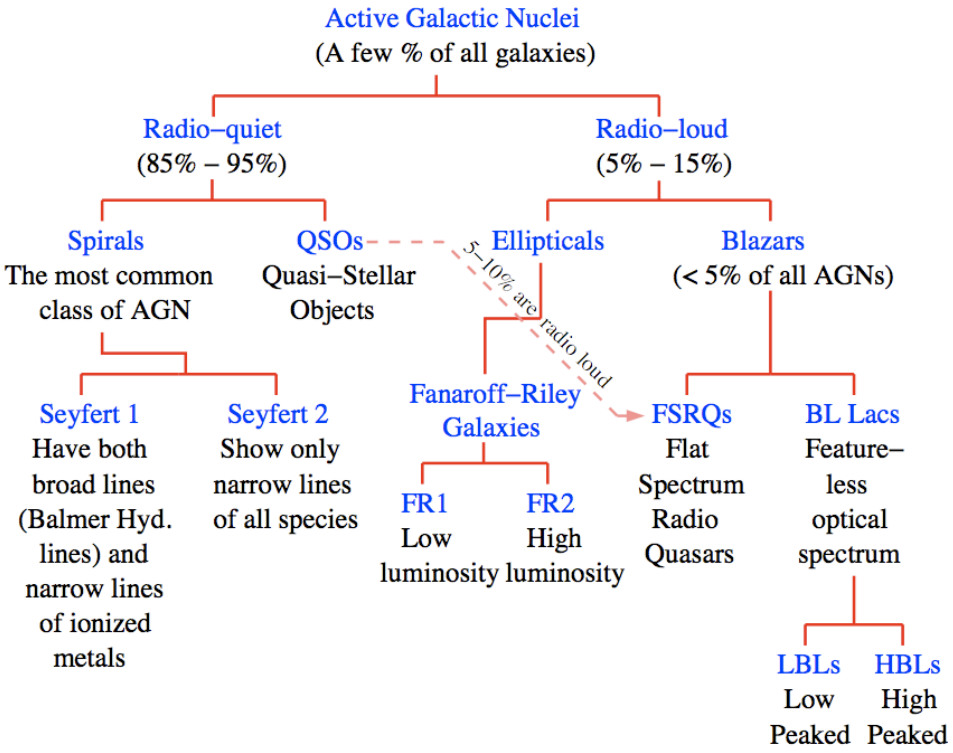

Figure 3.1: Scheme of the different AGN classes.

the powerful ones in the optical band are classified as quasars or BL Lacs. Flat spectrum radio quasars (FSRQs) and BL Lacs have their jet pointing within a small angle to the observer. These two subclasses are jointly called blazars, and all but two (the radio galaxies M 87 and Centaurus A) detected extragalactic VHE gamma-ray objects belong to this class.

3.2 Blazars

Blazars are AGNs with a jet, which is aligned close to the line of sight of the observer. Subclasses of blazars have differences in the optical emission: FSRQ have strong emission lines while BL Lacs have weak or no optical lines.

It is widely believed that the relativistic jet is the key element of the observed non-thermal blazar emission. Acceleration processes in the jet generate non-thermal emission over an energy range spanning up to twenty orders of magnitude: from radio to TeV gamma-rays. The jets are perpendicular to the accretion disc and collimated by strong magnetic fields. The jets seem to be stable up to kpc scales and often characterized by a highly polarized radiation, short variability time-scales and an apparent superluminal motion (Fugmann, 1988; Impey et al., 1991; Valtaoja et al., 1992; Wills et al., 1992).

To explain the observed broadband spectrum of blazars, most models assume that a relativistic population of electrons or protons or both is accelerated within the jet. From the observational point of view, the spectral energy distribution (SED) of blazars exhibits a two-bump structure with the first peak in the infrared up to keV energies and the second one with a maximum at MeV up to TeV energies, as seen in Figure 3.4.

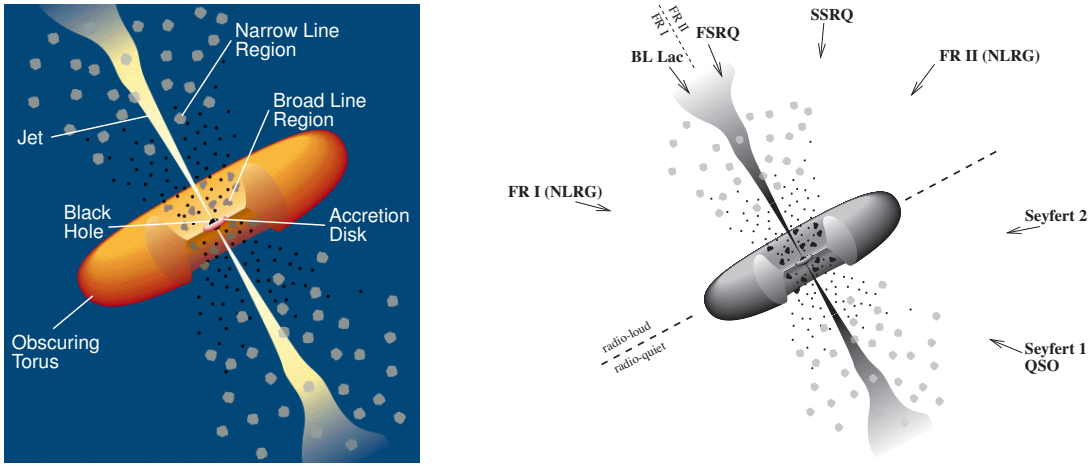

(a) (b)

Figure 3.2: Schematic view of an AGN. Adapted from Urry and Padovani (1995).

3.2.1 The blazar sequence

The variety of spectral characteristics also inside the blazar population triggered studies trying to draw general conclusions about its properties. A popular scheme to unify the blazar population is the so-called blazar sequence, proposed by Fossati et al. (1998). In this study, the authors analyze the SED of 126 blazars identifying in their sample a remarkable continuity, which they summarize in three main properties:

1. The low-energy peak of the SED occurs at different frequencies depending on the sample and luminosity class of the blazar, with most luminous sources peaking at lower frequencies.

2. The peak frequency of the high-energy bump correlates with the peak frequency of the low-energy one.

3. The luminosity ratio between the high and the low energy components increases with bolometric luminosity.

The popularity of this scheme lies in the fact that it could account for all the different types of SEDs seen in blazars varying a single parameter, related to their luminosity. The simplest form of the blazar sequence (see Figure 3.4) distinguished between low and high-frequency-peaked BL Lac objects (LBLs and HBLs). LBLs are more luminous and have their first peak in the infrared–optical band and the second one at keV–MeV energies. In LBLs the high energy component dominates over the low energy one. On the other hand, in HBLs the first peak is found at UV–X-ray frequencies and dominates over the high-energy component, which peaks at GeV–TeV energies.

It was recently shown that the luminosity to synchrotron peak frequency anti-correlation does not hold and was the result of selection effects (Padovani, 2007). FSRQs with low-energy peak frequency as high as those of LBLs have been found and HBLs are a minority among BL Lacs, which is contrary to what could be expected if the blazar sequence would hold as initially proposed. Still, this probably does not affect the correlation between low and high-energy peak frequencies, which implies that HBLs have the highest high-energy

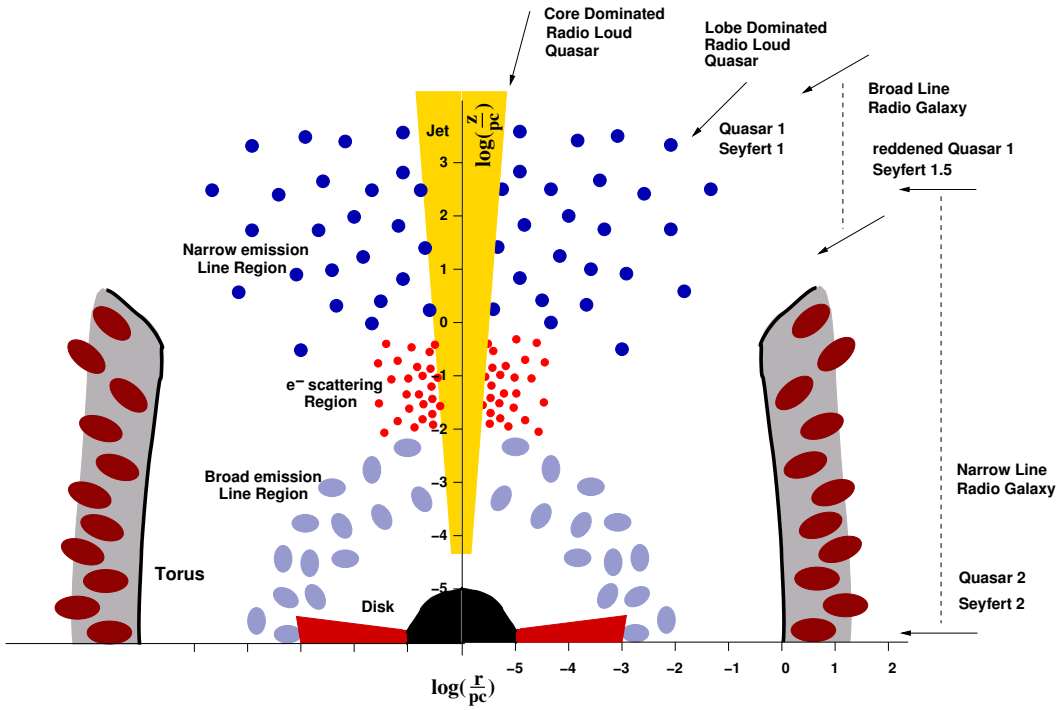

Figure 3.3: Schematic drawing of the morphology of an AGN. From Biermann et al. (2002).

bump peak frequencies and makes them more likely to be TeV emitters. This explains why only one FSRQ (3C 279) and three LBLs (BL Lacertae, W Comae and 3C 66A) have been detected at VHE gamma-rays, while all the other detected blazars are HBLs. In addition to these arguments, Nieppola et al. (2008) used the spectral energy distribution of a large blazar sample to determine their Doppler-corrected synchrotron luminosities and synchrotron peak frequencies. Using the Doppler-corrected values, the anti-correlation between luminosity and synchrotron peak frequency disappears, suggesting that the blazar sequence is an artifact of variable Doppler boosting across the peak frequency range.

3.3 Emission models

In all accepted scenarios, the SED of blazars is described by emission produced inside the blazar jets, being the relativistic beaming inside the jet a key issue to explain the short timescale variations, high luminosity and high energies (by blue shifting) of the emitted radiation. However, a complete picture of the emission mechanisms is still under debate. Since the accelerated particles responsible for the emission can be either electrons and positrons, or hadrons, the models are divided into leptonic and hadronic.

3.3.1 Leptonic models

In leptonic emission scenarios, a population of very energetic electrons in the jet is assumed to be responsible of the emission. To explain the observed radiation from blazars in the framework of leptonic emission scenarios, electrons have to be accelerated up to TeV

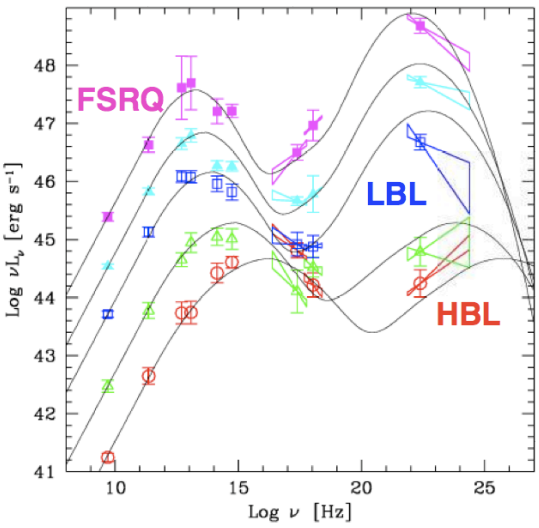

Figure 3.4: Average differential luminosity for a sample of 126 blazars, showing the transition from FSRQs to LBLs and HBLs (Fossati et al., 1998). The black solid lines show a simple leptonic model proposed by Ghisellini et al. (1998).

energies. This required non-thermal population of energetic electrons can be readily obtained through shock acceleration mechanisms (see Kirk and Duffy, 1999, and references therein), being first and second order Fermi acceleration the more often invoked processes (Longair, 1992).

In leptonic emission models, radio to X-ray emission is produced by synchrotron radiation from the population of non-thermal electrons, and VHE gamma-rays can be produced if these electrons upscatter low energy photons through inverse Compton (IC) scattering, i.e., a high energy electron collides with a photon, giving it some of its energy.

Once the production of VHE photons is working, these photons must be able to escape from the emitting region. It means that the source must be transparent to gamma-rays. Possible absorption processes that might reduce the emitted gamma-ray flux are the absorption of gamma-rays by pair production with low energy ambient photons (Bednarek, 1997), or production of an electron-positron pair by a single gamma-ray because of its interaction with the jet magnetic field (Burns and Harding, 1983).

Finally, the question of which population of low energy photons gets boosted to higher energies gives rise to different scenarios.

Synchrotron self-Compton mechanism

The simplest realization of leptonic emission mechanisms is the so-called synchrotron self-Compton (SSC) model. It assumes that relativistic electrons upscatter by IC scattering the low energy synchrotron photons emitted by the same electron population within the jet (Maraschi et al., 1992; Coppi, 1992; Bloom and Marscher, 1996).

The emission region has a characteristic size R, moving at relativistic speed $\beta = v/c$. Both relativistic electrons and photons are isotropic in the source frame. The observed radiation is strongly affected by relativistic beaming effects. The key parameter is the Doppler beaming factor $\delta = \Gamma(1 - \beta\cos\theta) - 1$, where Γ is the bulk Lorentz factor of the emission region in the jet and θ is the angle between the line of sight towards the observer

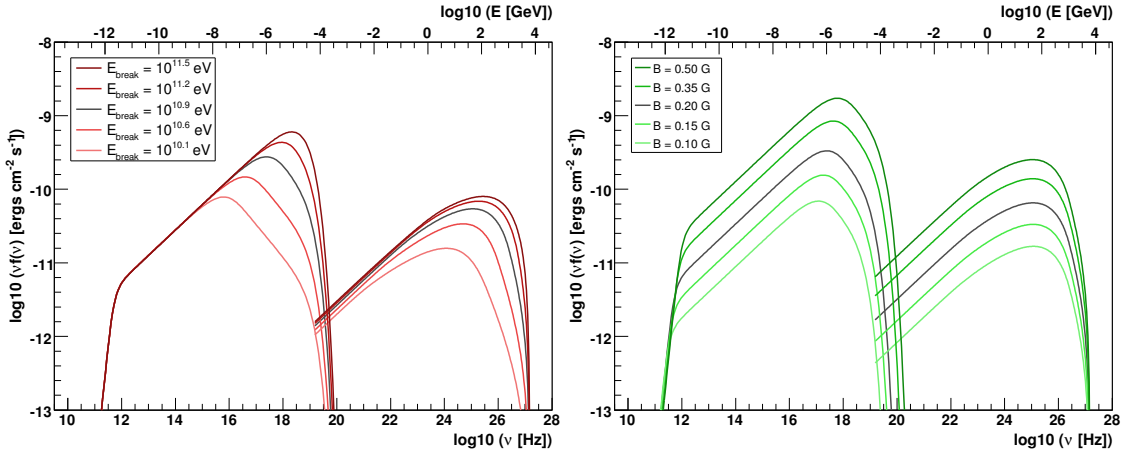

(a) Break energy of the electron spectrum

(b) Magnetic field

(c) Electron energy density

(d) Doppler factor

Figure 3.5: Scan of SED sensitivity to changes in some parameters in a one-zone synchrotron self-Compton model (Krawczynski et al., 2004). The reference spectrum (grey curves) is obtained using a set of model parameters ($R = 1.6 \times 10^{16}$ cm, $B = 0.20$ G, $\delta = 15$, $K = 0.06\,\mathrm{erg\,cm^{-1}}$, $E_{min} = 10^5$ eV, $E_{max} = 10^{11.6}$ eV, $E_{break} = 10^{10.9}$ eV, $n_1 = 2.31$, and $n_2 = 3.88$) taken from Albert et al. (2007*b*). The photon spectra are obtained for a source at a distance $z = 0.031$.

and the direction of the relativistic jet. When the observer lies with the angle of $\theta \sim 1/\Gamma$, which is assumed to be the case in blazars, then $\delta \sim \Gamma$. The observed spectral shape of the synchrotron component requires that the relativistic electron spectrum steepens at high energies. This behavior is approximated by describing the electron spectrum with a broken power-law of the form $\mathrm{d}n/\mathrm{d}E = n_0 \cdot E^{-n_i}$ with spectral indices n_1 and n_2, below and above the break energy E_b. The change in spectral index is usually of the form $n_2 \approx n_1 - 1$ (Kino et al., 2002). The softening of the electron spectrum at higher energies can be easily explained by radiative cooling, i.e. higher energy electrons escape earlier from the emitting region. This particular form for the electron spectrum is also accepted as it succeeds to describe the curved shape of the photon SED (Tavecchio et al., 1998). In this scenario, the SSC models are generally described by the following parameters: the size of the emitting region (R), the minimum and maximum frequency on the electron population (E_{min} and E_{max}), the break energy of the electrons (E_{break}), the spectral slope of the electron spectrum before and after the break (n_1 and n_2), the electron energy density (K), the magnetic field (B) and the Doppler beaming factor (δ).

In Figure 3.5 the dependency of the obtained SED with changes in some of the defining parameters of SSC models is shown. For this study, a numerical code by Krawczynski et al. (2004) is used. First, a reference set of parameters is used to produce a reference SED. For this purpose, the model parameters that describe the measured SED of Mrk 421 are used (Albert et al., 2007*b*). Then, the break energy of the electron spectrum E_{break}, the magnetic field B, the electron energy density K and the Doppler factor δ are changed separately in five steps to illustrate how each parameter contributes to the evolution of the SSC spectrum.

It is clearly seen that increasing E_{break} the peak positions of the low and high-energy components of the SED shift towards higher energies, following a dependency (Kino et al., 2002)

$$\nu_s \propto B \cdot E_{break}^2 \cdot \delta \tag{3.1}$$

in the case of the synchrotron peak frequency (ν_s), and

$$\nu_{IC} \propto E_{break} \cdot \delta \tag{3.2}$$

for the inverse Compton peak frequency (ν_{IC}). Radio to optical flux below the synchrotron peak remain unchanged. It is also shown that higher magnetic fields produce an overall increase of the SED, although the ratio between IC and synchrotron luminosity (l_{IC}/l_s) decreases, as can be seen in the following relation (Kataoka et al., 1999):

$$B^2 \propto \frac{1}{R^2} \frac{l_s^2}{l_{IC}} \tag{3.3}$$

In addition, increasing B moves the position of the synchrotron peak towards higher energies while ν_{IC} remains basically unchanged, as expected from Equations 3.1 and 3.2. An increase in the electron energy density produces the opposite effect. The overall SED increases with increasing K, but contrary to what happens with increasing B, the IC luminosity increases with respect to the synchrotron luminosity. This higher sensitivity of the IC luminosity to changes in the electron energy density is due to the fact that increasing K not only increases the number of electrons but also the number of low energy photons that can be upscattered by the electrons through IC (roughly, $l_s \propto K$ while $l_{IC} \propto K^2$). Finally, an increase in the Doppler beaming factor produces both an

increase of the overall luminosity and a shift of the synchrotron and IC peak to higher energies (see Equations 3.1 and 3.2).

The SSC model is the simplest realization of a leptonic emission model in a relativistic jet. However, models that include external populations of low energy photons that are upscattered through inverse Compton scattering have been proposed. These are called external Compton (EC) models (see Dermer and Schlickeiser, 1993; Sikora and Madejski, 2001, and references therein) . The populations of low energy photons considered in these models are photons emitted by the accretion disk, in the broad-line region, or even low energy photons escaping from the jet which are reflected by ambient dust and enter again into the jet with angles favoring their IC scattering (so-called mirror models).

EC models have been succesfully used to describe the SED of FSRQs, while in BL Lacs the absence of strong emission lines in the optical band in usually interpreted as an evidence that ambient photon fields are not important, favoring the interpretation of their emission in terms of SSC models.

3.3.2 Hadronic models

The hadronic models assume that a high energy protonic component contributes to the high-energy bump, while the low-energy bump is explained by synchrotron radiation of co-accelerated electrons. The energy of relativistic protons can be converted into high energy radiation via the following processes: direct synchrotron radiation of protons, photo-meson production ($p+\gamma \rightarrow p+k\pi$), and nuclear collisions ($p+p \rightarrow \pi+X$). The first two processes are known to be very inefficient, and they can become important in AGN jets only for proton energies larger than 10^8–10^{10} GeV. Energy losses of such energetic protons are dominated by photo-meson production, and this process was named to explain gamma-ray production in blazars by the so-called the proton-induced cascade model (Mannheim and Biermann, 1992). In that model, the target radiation for photomeson production is dominated by near/mid-infrared radiation. In blazars, such radiation can be emitted by hot dust at distances of $\sim$ 1–10 pc from the central source and/or by synchrotron radiation due to relativistic electrons in the jet.

The main outputs of the photo-meson processes are pions. Pions take about 1/3 of the proton energy and convert it to photons, neutrinos, and, through muons, to electrons and positrons. The photons injected by neutral pions immediately interact with low energy photons producing electron-positron pairs. Most of this radiation is so energetic that it produces two more generations of photons and pairs.

The final output of this synchrotron-supported pair-cascade is the high energy bump of the blazar SED, with a maximum energy that can be $\sim$ 30 GeV in FSRQs, as determined by external UV radiation, and $\sim$ TeV in BL Lac objects, as determined by infrared radiation of dust (Protheroe and Biermann, 1997).

Lower proton energies are required in models based on the assumption that the proton energy losses are dominated by collisions with the ambient gas. The final output of these collisions is the same as in the photo-meson processes, i.e., relativistic electrons/positrons, photons and neutrinos. Bednarek (1993) proposed as a target the thick accretion disk, while Dar and Laor (1997) suggested interactions of jet with cloud and/or stellar winds. The disadvantage of such models is that relativistic protons, before colliding with the nuclei, may easily suffer deflections by magnetic fields resulting in a lack of collimation of the radiation.

Finally, in case the gamma-ray radiation is of hadronic origin, one also expects to

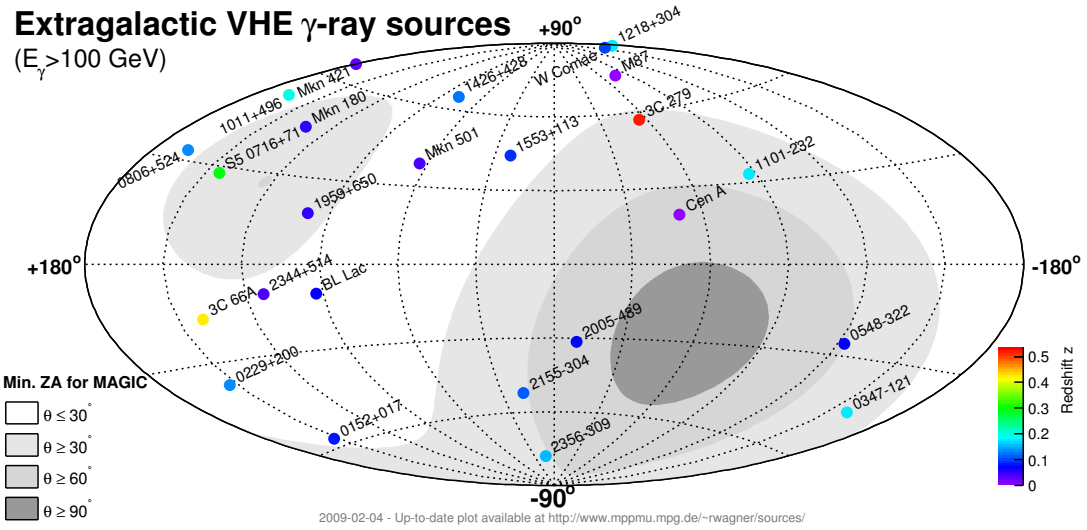

Figure 3.6: Skymap the detected TeV extragalactic sources using different ground-based telescopes. Shaded grey surfaces indicates regions where MAGIC visibility is reduced.

detect VHE neutrinos produced in the hadronic interactions, but at least km^3 sized detectors are needed. The detection of neutrinos from blazars would clearly favour hadronic models.

3.4 Detected TeV blazars

Since the discovery of TeV gamma-rays from Mkn 421 ($z = 0.031$) and Mkn 501 ($z = 0.034$), two archetypical representative of this class of galaxies, many blazars have been the focus of ground-based gamma-ray observations. Over the last 15 years, Mkn 421 and Mkn 501were the subject of intensive studies through multiwavelength observations. Both sources are variable with typical average TeV fluxes between 10% and 50% that of the Crab Nebula, but with rapid flares, as short as 0,5 hr. Actually, MAGIC detected variability of Mkn 501 on timescales of only a few minutes (Albert et al., 2007*d*). The imaging atmospheric Cherenkov telescopes are nicely suited to the search for short-lived signals from blazars in flaring states. This has been demonstrated in many observations of Mkn 421, Mkn 501, 1ES 1959+650, PKS 2155-304 and some other blazars.

So far, energy spectra with photon indices ~ 2 have been observed from Mkn 421, Mkn 501, as well as from 1ES 1959+650 during a high state in 2003. With the operation of HESS, MAGIC and VERITAS, the number of TeV detected BL Lacs has doubled in the past 3 years. Interestingly, all reported new TeV blazars have quite steep energy spectra. For relatively distant blazars, with $z > 0.1$, the energy spectra of gamma-rays are affected by the intergalactic absorption and therefore become steeper. It is, however, likely, that the observed steep VHE spectra of blazars have, at least partly, intrinsic origin. This is clear at least for some nearby AGNs such as 1ES 2344+514 ($z = 0.044$), Mkn 180 ($z = 0.045$), 1ES 1959+650 ($z = 0.047$) and PKS 2005-498 (0.071) as well as for BL Lacertae ($z = 0.069$).

However, given the spectral variability seen in other TeV blazars (mainly Mkn 421 and Mkn 501) it is quite possible that the above-mentioned BL Lacs were observed in their low state and that subsequent observations could exhibit different spectral characteristics

such as harder spectra or spectra with higher peak energies. On the other hand, because of the intergalactic absorption, one should expect steep VHE gamma-ray spectra from extragalactic objects with $z > 0.1$, even in the case of hard intrinsic spectra. Actually, the detection by HESS and MAGIC of relatively distant BL Lac objects: PKS 2155-304 ($z = 0.117$), H 2356-309 ($z = 0.165$), 1ES 1218+30.4 ($z = 0.172$), 1ES 1101-232 ($z = 0.186$), 1ES 1011+496 ($z = 0.212$) and PG 1553+113 (most likely $z > 0.25$), with gamma-ray spectra extending to relatively high energies was somehow unexpected. However, the extension of the gamma-ray transparency window to relatively high redshifts got confirmed by the detection of the FSRQ 3C 279 by MAGIC (Albert et al., 2008*e*, see also Chapter 8 of this thesis) and 3C 66A by VERITAS (Acciari et al., 2009), located respectively at redshifts of 0.536 and 0.444.

Chapter 4

Selection of distant blazars for VHE observations

This chapter introduces the interaction of VHE photons with photons from the cosmic infrared and optical background as one of the motivations for the observation of distant blazars with Cherenkov telescopes. First, the possible origin and implications of the extragalactic background light are described. Then, the status of the direct measurements of the background photon density as well as the current models describing its wavelength dependence are outlined, and the possibility of constraining this density with measurements of TeV spectra from distant objects is discussed. Finally, the best candidates of distant blazars to be observed with the MAGIC telescope are ennumerated and studied to prove the feasibility of these observations.

4.1 The extragalactic background light

Apart from the physics goals of AGN observations oulined in Chapter 3, one of the main motivations to study distant blazars in the VHE regime is that their flux gets distorted due to propagation effects. The light emitted by galaxies and stars along its formation and evolution history has accumulated in the infrared (IR) to ultraviolet (UV) wavelength bands. This radiation field is commonly referred as extragalactic background light (EBL). The EBL is the second largest isotropic radiation field, in terms of contained energy, after the 2.7 K cosmic microwave background. The interaction of VHE photons with this lower energy radiation field results in an absorption of the gamma-rays that depends on the energy of the VHE photon, the distance from the source to the observer, and the actual density and spectral distribution of the EBL.

Direct measurements of the EBL are difficult due to strong foregrounds from our solar system and galaxy. Therefore, as the measured spectra of distant VHE sources has the imprint of the absorption due to the EBL, the observation of these objects using ground-based Cherenkov telescopes provides constraints on the EBL density, which are very useful to get better knowledge of its origin and properties. The precision of the EBL constraints set by VHE gamma-ray observations of blazars improved remarkably in the last years. At the same time, there has been a rapid progress in resolving a significant fraction of this background with deep galaxy counts at IR wavelengths using satellite detectors (Spitzer and ISO).

The knowledge of the EBL photon density and its evolution with redshift is important

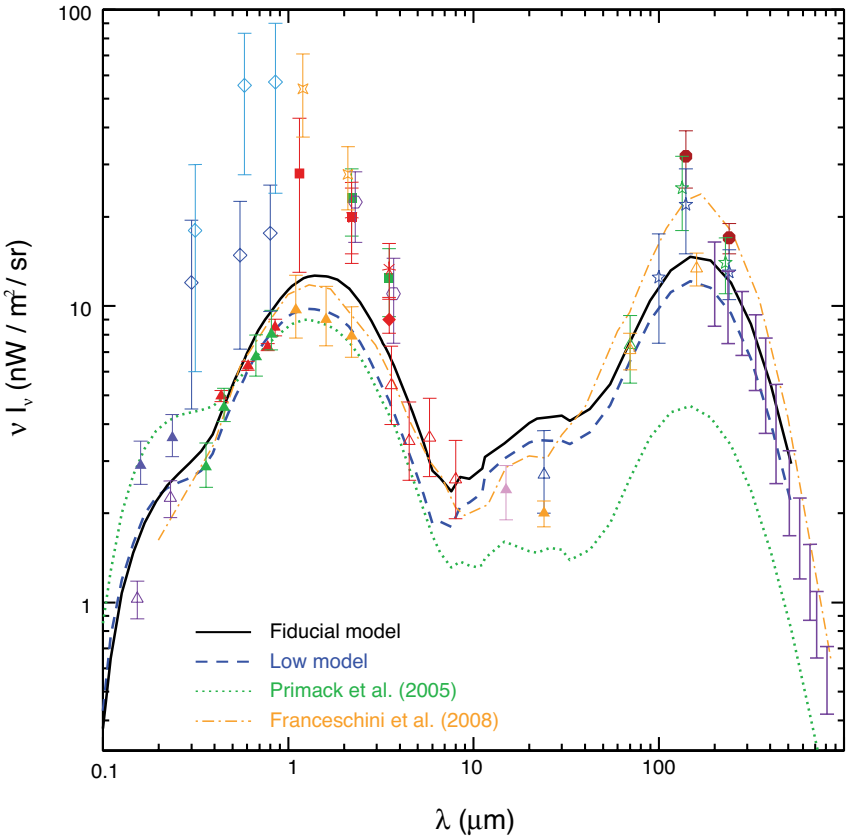

Figure 4.1: Measurements and model predictions of the spectral SED of the EBL at $z = 0$. **Lower limits:** The open blue-violet triangles are results from Hubble and STIS (Gardner et al., 2000), while the magenta triangles are from GALEX (Xu et al., 2005). The green and red triangles from Hubble Deep Field (Madau and Pozzetti, 2000) and Ultra Deep Field, combined with ground based-data. Gold triangles are also from Madau and Pozzetti (2000). Open red triangles are from IRAC on Spitzer (Fazio et al., 2004), and the pink point at 15 μm is ISOCAM (Elbaz et al., 2002) on ISO. The remaining lower limits are from MIPS at 24, 70, and 160 μm on Spitzer (Papovich et al., 2004; Chary et al., 2004; Frayer et al., 2006; Dole et al., 2006). **Direct measurements:** The higher open blue triangles are from Bernstein (2007), while the lower points are the original determinations from Bernstein et al. (2002). The high-reaching cyan points in the near-IR are from Matsumoto et al. (2005). The rest of the points in this region are based upon DIRBE data with foreground subtraction, namely Wright (2001) (dark red squares), Cambrésy et al. (2001) (orange crosses), Levenson and Wright (2008) (red diamond), Gorjian et al. (2000) (purple open hexes), Wright and Reese (2000) (green square) and Levenson et al. (2007) (red asterisks). In the far-IR, direct detection data is shown from DIRBE: Wright (2004) (blue stars) and Hauser et al. (1998) (green stars), and also purple bars showing the detection of FIRAS (Fixsen et al., 1998). **Models:** Black and dashed blue lines stand respectively for the fiducial and low models from Primack et al. (2008). A previous model Primack et al. (2005) is also shown for comparison (dotted curve). The recent model of Franceschini et al. (2008) is also shown (dash-dotted orange line). The plot is adapted from Primack et al. (2008).

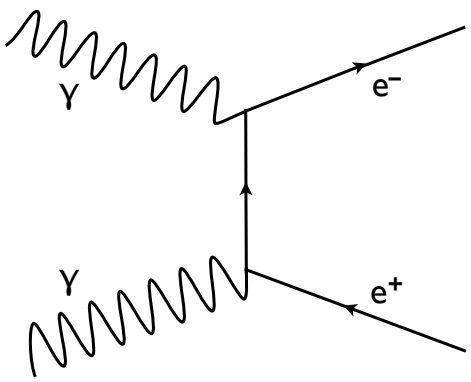

Figure 4.2: Feynman diagram of the process $\gamma_{vhe} + \gamma_{ebl} \rightarrow e^+ + e^-$.

since it carries information about the galaxy and star formation history of the universe. The formation and subsequent life cycle of stars and galaxies is accompanied by the emission of radiation. Most of this radiant energy is emitted by stars in the UV and optical wavelengths. The spectral energy distribution (SED) of the EBL can be schematically described as a two-peak distribution (see Figure 4.1). The first component, the optical background, has a peak around 1 μm and is believed to be originated directly by redshifted radiation from stars. The second component, the infrared background, peaks at $\sim 100\,\mu$m and results from starlight that has been absorbed by dust inside galaxies and reemitted at longer wavelengths. It is also important to note that the evolution of the EBL density with time (redshift) is critical to test star formation and galaxy evolution models. In addition to that, a diffuse residual excess between 1 and 4 μm was reported by the IRTS satellite (Matsumoto et al., 2005), triggering a lot of interest inside the scientific community. This excess might be interpreted as the radiation emitted by the first stars that were formed in the universe (Population III stars), being then a unique probe for the epoch when these first stars formed (Madau and Silk, 2005; Kashlinsky et al., 2005; Dwek et al., 2005; Kashlinsky, 2008; Franceschini et al., 2008). However, such a luminous Population III star generation contradicts previous predictions and indirect measurements (Dwek et al., 2005; Salvaterra and Ferrara, 2006). In addition, Dwek et al. (2005) and Matsumoto et al. (2005) pointed out that the near-IR excess could be attributed to zodiacal light, which seems nowadays the most plausible explanation for this measured excess.

4.1.1 Absorption of VHE photons by the EBL

The flux of VHE gamma-rays from distant sources is attenuated because gamma-rays interact with optical and IR photons from the EBL producing electron-positron pairs.

The pair production process between a very high energy photon and an EBL photon ($\gamma_{vhe} + \gamma_{ebl} \rightarrow e^+ + e^-$, see Figure 4.2) happens only when the energy of both photons is enough to produce an electron-positron pair:

$$E \cdot \varepsilon \cdot (1 - \cos\theta) \geqslant 2\left(m_e c^2\right)^2 \tag{4.1}$$

where E and ε indicate, respectively, the energy of the VHE and the EBL photon, and

θ is the collision angle. The cross section of this process is (Gould and Schréder, 1967; Stecker and de Jager, 1996; Vassiliev, 2000):

$$\sigma_{\gamma\gamma} = \tfrac{3}{8}\,\sigma_T\, f\,(q) \tag{4.2}$$

$$f\,(q) = q\left[\left(1+q-\frac{q^2}{2}\right)\ln\frac{1+\sqrt{1-q}}{1+\sqrt{1-q}} - (1+q)\,\sqrt{1-q}\right] \tag{4.3}$$

$$q = \frac{\left(m_e c^2\right)^2}{E\cdot\varepsilon}\,\frac{2}{1-\cos\theta} \tag{4.4}$$

where $\sigma_T = 6.67\times10^{25}\,\mathrm{cm}^{-2}$ is the Thomson scattering cross section.

To quantify the opacity –or absorption probability– to high energy photons, the optical depth ($\tau_{\gamma\gamma}$) can be defined. When the VHE-photon propagates in an isotropic low-energy photon field with spectral density $\mathrm{d}n(\varepsilon)/\mathrm{d}\varepsilon$, $\tau_{\gamma\gamma}$ per unit path length $\mathrm{d}l$ has the following form (see detailed calculations, e.g., in Gould and Schréder (1967) or Vassiliev (2000)):

$$\frac{\mathrm{d}\tau_{\gamma\gamma}}{\mathrm{d}l} = \tfrac{3}{8}\sigma_T\int_{\frac{(m_e c^2)^2}{E}}^{\infty}\frac{\mathrm{d}n(\varepsilon)}{\mathrm{d}\varepsilon}\,F\left(\frac{\left(m_e c^2\right)^2}{E\cdot\varepsilon}\right)\mathrm{d}\varepsilon \tag{4.5}$$

$$F\,(q) = 2q^2\int_q^1 f\,(x)\,x^{-3}\mathrm{d}x \tag{4.6}$$

The maximum of $F\,(q)$, which corresponds to a maximum opacity of the isotropic low-energy photon field to VHE photons, happens when $q = 0.28$ (Vassiliev, 2000). This results in the following energy –and wavelength– relation between the two photons:

$$\varepsilon = 0.93\,\mathrm{eV}\,\frac{\mathrm{TeV}}{E} \tag{4.7}$$

$$\lambda = 1.3\,\mu\mathrm{m}\,\frac{E}{\mathrm{TeV}} \tag{4.8}$$

which means that the main source of opacity for a 1 TeV photon is the interaction with photons in the near-IR band (0.7–5 μm). Above 1 TeV, gamma-rays are most attenuated by near- and mid-IR (5–35 μm) photons from the EBL. Between 300 GeV and 1 TeV, gamma-rays are sensitive to near-IR and optical light (0.38–0.75 μm). Below 300 GeV only UV photons ($\lambda < 400$ nm) will have a large enough cross section to attenuate gamma-rays. Finally, below 20 GeV, the absorption is almost negligible due to the very low density of EBL photons below 0.2 μ (see Fig. 4.1).

Generalizing Equation 4.5, one obtains the optical depth for a very high energy photon of energy E traveling from a cosmic source at redshift z:

$$\tau_{\gamma\gamma}\,(E,z) = \tfrac{3}{8}\,\sigma_T\,\frac{c}{H_0}\int_0^z\sqrt{1+z}\,\mathrm{d}z\int_{\frac{(m_e c^2)^2}{E(1+z)^2}}^{\infty}\frac{\mathrm{d}n(\varepsilon,z)}{\mathrm{d}\varepsilon}\,F\left(\frac{\left(m_e c^2\right)^2}{E\cdot\varepsilon\,(1+z)^2}\right)\mathrm{d}\varepsilon \tag{4.9}$$

where H_0 is the Hubble constant. Then, if a gamma-ray source at redshift z is emitting photons with a given intrinsic flux $F_0\,(E)$, the flux measured by the observer will be distorted by the EBL absorption in the following way:

$$F\,(E) = F_0\,(E)\cdot e^{-\tau_{\gamma\gamma}(E,z)} \tag{4.10}$$

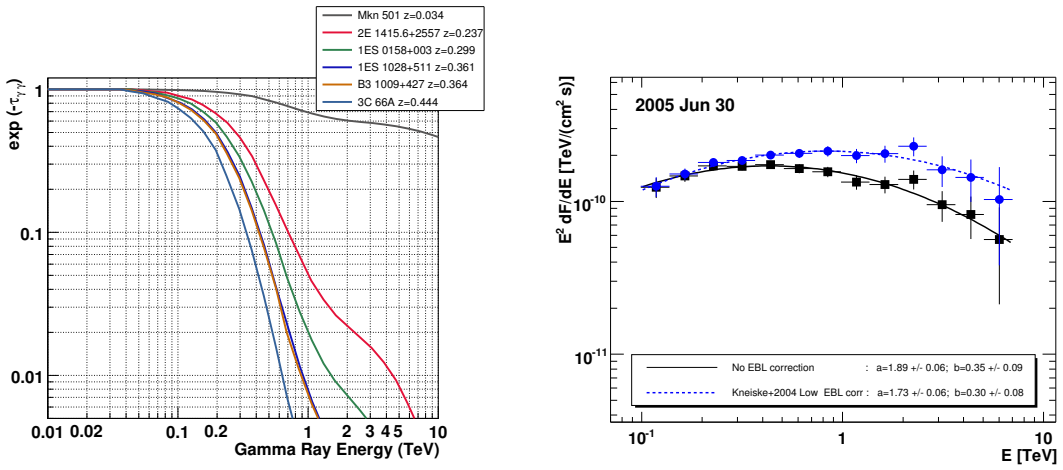

(a) (b)

Figure 4.3: (a) Transmission of the extragalactic medium to gamma-rays for the proposed sources as a function of the photon energy. For the calculation of the optical depth $\tau_{\gamma\gamma}$ the numerical templates of the Low-IR model from Kneiske et al. (2004) have been used to describe the photon density of the EBL. This model is compatible with the low level EBL proposed in Aharonian et al. (2006*b*). The attenuation for Mkn 501 is also shown for comparison. (b) Spectrum of Mkn 501 during a gamma-ray flare (Albert et al., 2007*d*). The black data points show the measured spectrum by MAGIC, and the blue points are the spectrum corrected for EBL absorption (intrinsic spectrum). Both spectra are fitted to a log parabolic function $\frac{\mathrm{d}N}{\mathrm{d}E} = N_0 \left(\frac{E}{0.3\mathrm{TeV}}\right)^{a-b\log\left(\frac{E}{0.3\mathrm{TeV}}\right)}$. The softening of the spectrum by the effect of the EBL absorption is clearly visible.

The energy dependence of $\tau_{\gamma\gamma}$ changes with the actual spectral shape of the EBL photon density ($\mathrm{d}n(\varepsilon)/\mathrm{d}\varepsilon$ in Eq. 4.9). This dependence is shown in Figure 4.3(a) for sources at different redshifts. In a zaro order approximation, $\tau_{\gamma\gamma}$ also increases linearly with the source distance. In an schematic way, the effect of EBL absorption can be described in the following manner: if a source emits photons following a power-law spectrum, the observer will measure a power-law with an exponential cutoff that will appear at a given energy, which depends on the source distance. As can be seen in Figure 4.3(a), the cutoff will move towards lower energies for more distant sources. This fact allows the detection of distant objects just at low energies ($E \sim 200\,\mathrm{GeV}$ and below), because the universe becomes more opaque for photons with higher energies.

4.1.2 Direct measurements of the EBL and EBL models

An updated compilation of measurements of the EBL photon density together with some recent models is shown in Figure 4.1.

Different methods have been followed to calculate the EBL density and its redshift evolution. A forward evolution approach relies on a parametrization of the evolving stellar populations and calculates the emission spectra of galaxies as a function of time, starting at the beginning of star formation. This semi-analitic models of galaxy formation yield luminosity functions for different galaxy types that are in reasonable agreement with the observations. This is the approach followed by Primack et al. (2005), recently updated (Primack et al., 2008) to avoid underpredicting the EBL level in the far infrared band. On the other hand, backward evolution models start with the existing galaxy population

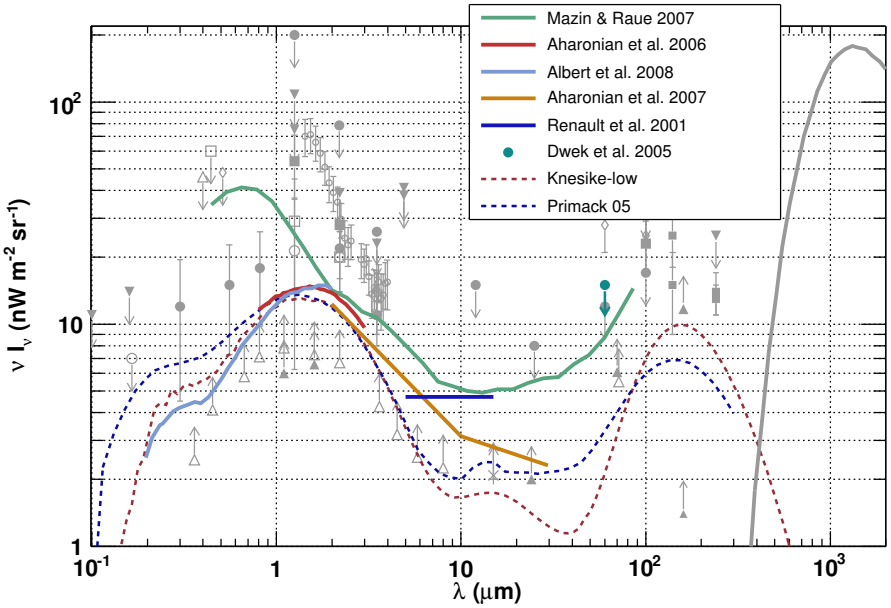

Figure 4.4: Constraints on the EBL density from VHE gamma-ray observations. The grey points indicate measurements and limits from direct observations. The limit from (Mazin and Raue, 2007) comes from a combined analysis of 13 blazars detected at VHEs. The H.E.S.S. collaboration published two constraints: from the analysis of 1ES 1101-232 and H 2356-309 (Aharonian et al., 2006*b*), and from the spectrum of 1ES 0229+200 (Aharonian et al., 2007). The detection of 3C 279 constrains the EBL density in the 0.2–2 μm range (Albert et al., 2008*e*). The mid-IR limit from Renault et al. (2001) comes from an analysis of the CAT and HEGRA spectra of Mkn 501, while the limit by Dwek et al. (2005) resulted from an analysis on Whipple and HEGRA data of the blazars Mkn 421, Mkn 501 and H 1426+428. The KneiskeLow model (Kneiske et al., 2004) and Primack05 (Primack et al., 2005) are shown for comparison.

and evolve it backward in time to obtain the EBL level and spectrum (e.g., Stecker et al., 2006). Finally, models like the ones proposed in Kneiske et al. (2002) and Franceschini et al. (2008) exploit relevant cosmological survey data –including number counts, redshift distributions, luminosity functions– fitting and interpolating it with a multiwavelength backward evolutionary model, allowing an estimate of the background photon density and its redshift evolution.

Observationally, the EBL is difficult to distinguish from the generally much brighter foregrounds contributed mainly by zodiacal light[1], stars, and the interstellar medium of the galaxy. Solid lower limits on the EBL density have been set by galaxy counts (Madau and Pozzetti, 2000; Fazio et al., 2004; Frayer et al., 2006) or extrapolated via stacking (Dole et al., 2006). Upper limits comming from direct observations (e.g., Hauser et al., 1998) and fluctuation analyses (Kashlinsky and Odenwald, 2000; Lagache and Puget, 2000; Matsuhara et al., 2000) are also available (see Figure 4.1 for more details). The measurements and limits established up to now confirm the predicted two-bump structure, although its absolute level remains still uncertain by a factor of 2 to 5.

[1]sun light reflected by dust particles in the solar system.

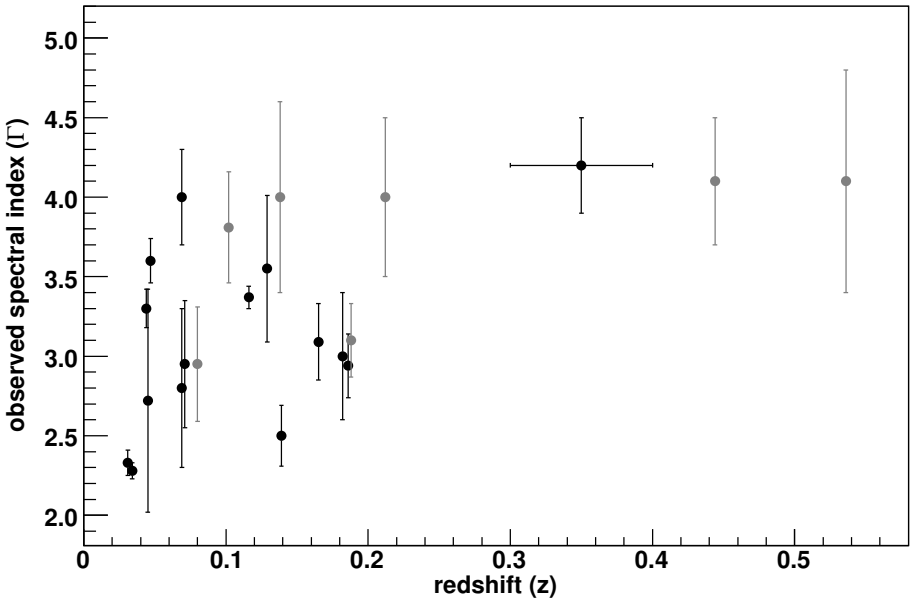

Figure 4.5: Spectral photon index of all known TeV blazars as a function of their redshift. The photon index results from fitting the observed spectrum of every source between 200 GeV and 2 TeV, with slightly modified upper bound for the very steep spectra, where data above 1 TeV is usually not available. Data extracted from De Angelis et al. (2008).

4.1.3 EBL limits from VHE gamma-ray observations

The fact that VHE gamma-rays are attenuated by interaction with EBL photons makes the observation of distant sources at these wavelengths a useful tool to extract information on the spectral distribution and density of the EBL photon field. While uncertainties on the intrinsic spectra of blazars make difficult to link the observed spectra directly to EBL attenuation, it is possible to translate limits on the spectra to EBL constraints. Following Equation 4.10, if a gamma-ray source at known redshift has a measured spectrum $F(E)$, assumptions on its intrinsic spectrum $F_0(E)$ can lead to limits on the EBL density through an estimation of $\tau_{\gamma\gamma}$. The standard assumption is that the reconstructed intrinsic spectrum should not have a spectral index harder than 1.5; i.e., $\Gamma \geqslant 1.5$ for $F_0(E) \propto E^{-\Gamma}$. This spectral index of $\Gamma = 1.5$ is the hardest that can be obtained with classical leptonic emission mechanisms (Aharonian, 2001), and such hard spectra have not been observed either in nearby less-absorbed blazars like Mkn 421 or Mkn 501 or in EGRET spectra at lower energies. This limit can be invalidated by assuming a narrow distribution of relativistic electrons, that can produce inverse Compton spectra as hard as $\Gamma \approx 0.7$ (Katarzyński et al., 2006). Also internal absorption by a dense low-energy photon field can lead to the formation of gamma-ray spectra of an almost arbitrary hardness (Bednarek, 1997; Aharonian et al., 2008*c*).

Figure 4.4 shows a current status of the constraints on the EBL photon density set by gamma-ray observations. The most recent EBL limits based on gamma-ray spectra of blazars come from observations of blazars at relatively high redshifts ($z > 0.1$). The observation by H.E.S.S. of two blazars at $z = 0.165$ and $z = 0.186$ was used to set limits on the near-IR based on the $\Gamma \geqslant 1.5$ criterion (Aharonian et al., 2006*b*), finding an allowed EBL density lower than the previously assumed by most of the models. Another paper

Object	RA	Dec	Type	Discoverer	z
Mkn 421	11 04 27.3	+38 12 32	HBL	Whipple	0.031
Mkn 501	16 53 52.2	+39 45 36	HBL	Whipple	0.034
1ES 2344+514	23 47 04.8	+51 42 18	HBL	Whipple	0.044
Markarian 180	11 36 26.4	+70 09 27	HBL	MAGIC	0.045
1ES 1959+650	19 59 59.9	+65 08 55	HBL	Telescope Array	0.048
BL Lacertae	22 02 43.3	+42 16 40	LBL	Crimea	0.069
PKS 2005-489	20 09 29.3	–48 49 19	HBL	H.E.S.S.	0.071
RGB J0152+017	01 52 33.5	+01 46 40	HBL	H.E.S.S.	0.08
W Comae	12 21 31.7	+28 13 59	LBL	VERITAS	0.102
PKS 2155-304	21 58 52.7	–30 13 18	HBL	Durham	0.116
H 1426+428	14 28 32.6	+42 40 21	HBL	Whipple	0.129
1ES 0806+524	08 09 49.2	+52 18 58	HBL	VERITAS	0.138
1ES 0229+20	02 32 48.4	+20 17 16	HBL	H.E.S.S.	0.14
H 2356-309	23 59 09.0	–30 37 22	HBL	H.E.S.S.	0.165
1ES 1218+304	12 21 21.9	+30 10 37	HBL	MAGIC	0.182
1ES 1101-232	11 03 38.0	–23 29 31	HBL	H.E.S.S.	0.186
1ES 0347-121	03 49 23.2	–11 59 27	HBL	H.E.S.S.	0.188
1ES 1011+496	10 15 04.1	+49 26 01	HBL	MAGIC	0.212
PG 1553+113	15 55 43.0	+11 11 24	HBL	H.E.S.S. & MAGIC	∼0.35
3C 66A	02 22 39.6	+43 02 08	LBL	Crimea	0.444
3C 279	12 56 11.1	–05 47 22	FSRQ	MAGIC	0.5362

Table 4.1: List of blazars detected in VHE gamma-rays, ordered by redshift. Sources shaded in grey were discovered after April 2007, when the selection of candidates described in this section was prepared. Table adapted from Horan and Wakely (2008).

by the H.E.S.S. group set constraints from the blazar 1ES 0229+200, located at redshift $z = 0.140$ (Aharonian et al., 2007). While this blazar is closer than the two featured in the 2006 publication, its measured spectrum extended up to 10 TeV and, therefore, was used to set EBL constraints in the mid-IR band. The most distant source observed at VHEs is the quasar 3C 279 ($z = 0.536$), detected by MAGIC during a flare in February 2006 (Albert et al., 2008*e*, see also Chapter 8 of this thesis). The measured spectrum was quite steep and extended from 80 to nearly 500 GeV. An analysis of the spectral modification induced by γ-γ absorption concluded that the EBL density in the optical band (0.2–2 μm) could not be much higher than the lower limits set by galaxy counts. Another possible approach is to attempt to constrain the EBL by using spectra from several sources simultaneously. Dwek et al. (2005) derived a limit at 60 μm from the spectra of Mkn 421, Mkn 501 and H 1426+428, declaring invalid those EBL realizations that led to unphysical intrinsic blazar spectra with rising TeV emissions. A combined analysis of 4 HEGRA spectra constrained the EBL in the near-IR and at 60 μm by limiting the intrinsic blazar spectra to $\Gamma \geqslant 1.0$ and 1.5 (Costamante et al., 2004). More recently, this method was used in Mazin and Raue (2007), who applied constraints from all observed TeV blazars to a large number of possible EBL functional forms providing a limit from the optical to the far-IR.

Object	RA	Dec	z	Selection
1ES 0158+003	02:01:06.18	+00:34:00.2	0.299	ASDC
3C 66A	02:22:39.61	+43:02:07.8	0.444	Costamante
1RXS J1008.1+4705	10:08:11.5	+47:05:26	0.343	Nieppola
B3 1009+427	10:12:44.4	+42:29:59	0.364	Nieppola
1ES 1028+511	10:31:18.65	+50:53:43.6	0.361	Donato
1ES 1106+244	11:09:16.3	+24:11:20	0.460	Costamante
1RXS J1353.4+5601	13:53:28.2	+56:01:02	0.404	Nieppola
2E 1415.6+2557	14:17:56.62	+25:43:25.3	0.237	ASDC
1ES 1627+402	16:29:01.31	+40:07:59.9	0.272	ASDC

Table 4.2: List of candidate blazars, ordered by right ascension.

4.2 Selection of candidates

According to Equation 4.10, if the energy spectrum of a blazar is measured and its intrinsic spectrum would be known, the EBL density could be extracted from the observed absorption pattern. As can be seen in Figure 4.3(a), this absorption becomes larger for distant sources and for the highest energies measured in the spectrum. In addition, Equation 4.8 relates the energy of the measured gamma-rays with the wavelength of the EBL photons that will mostly contribute to its absorption. To extract limits on the EBL density two kinds of objects are desired: close-by well-measured blazars ($z < 0.1$), and detections of distant blazars ($z > 0.2$).

Nearby objects like Mkn 501, Mkn 421 or 1ES 1959+650 are easily detected by Cherenkov telescopes up to energies of few TeV. Since the distance travelled by the VHE photons is relatively short, the γ-γ absorption is not large even for energies above 1 TeV (see Figure 4.3(a)). Therefore, these detections up to the highest energies probe the EBL in the near- and mid-IR band (see Equation 4.8). Moreover, continued observations of these well-known blazars, specially when accompanied by measurements at other wavelengths, help to improve the knowledge of the emission mechanisms responsible for the TeV emission, reinforcing and constraining the hypotheses on the intrinsic spectrum of blazars that must be assumed to extract EBL limits. In particular, if spectra harder than $\Gamma = 1.5$ are to be found in blazars, they will probably be observed in close-by ones, which are better monitored and do not suffer from significant absorption up to high energies.

On the other hand, for high-redshift targets, a significant absorption is expected even at energies as low as 100 GeV, providing constraints on the EBL density in the optical and near-IR in case of positive detection. In addition, the detection of distant objects extends the coverage of the Γ–z plane (see Figure 4.5), and could reveal objects whose reconstructed spectrum is still hard even with an EBL flux as low as the galaxy counts limit, providing evidence for intrinsically hard spectra. With the low EBL level suggested in Aharonian et al. (2006*b*), detections of blazars up to redshifts of $z = 0.4$–0.5 should be well within the possibilities of current Cherenkov telescopes without requiring exceptionally bright states that should only seldom occur.

In April 2007, the most distant blazars detected in the VHE band had redshifts close to 0.2 (Aharonian et al., 2006*b*; Albert et al., 2006*a*). Therefore, a search for the most suitable distant blazars that could be detected at VHE gamma-rays was carried out.

The list of proposed objects includes bright sources in the radio and X-ray bands suggested in Costamante (2007), objects with high predicted flux at GeV energies in the

Object	z	δ	B[a]	R[b]	K[c]	$E_{min} < E < E_{max}$	E_{break}[d]	n_1	n_2	ν_s[e]	P_s[f]	ν_{IC}[g]	P_{IC}[h]
Mkn 421	0.031	15	3.0	1.6	0.06	$5 < \log(E/\mathrm{eV}) < 11.6$	9.4	2.31	3.88				
1ES 0158+003	0.299	15	0.09	1.6	0.06	$5 < \log(E/\mathrm{eV}) < 11.6$	11.0	2.20	4.50	694	1.0×10^{-11}	140	1.9×10^{-11}
		15	0.20	1.6	0.015	$5 < \log(E/\mathrm{eV}) < 11.6$	10.8	2.20	4.50				
3C 66A	0.444	15	0.20	1.6	4.3	$5 < \log(E/\mathrm{eV}) < 11.6$	10.0	2.31	3.88	16	2.3×10^{-11}	3	3.0×10^{-10}
		15	3.0	1.6	0.06	$5 < \log(E/\mathrm{eV}) < 11.6$	9.4	2.31	3.88				
1RXS J1008.1+4705	0.343	15	0.20	1.6	0.07	$5 < \log(E/\mathrm{eV}) < 11.6$	11.1	2.31	3.88	2332	3.7×10^{-12}	69	7.3×10^{-13}
		15	0.23	1.6	0.06	$5 < \log(E/\mathrm{eV}) < 11.6$	11.0	2.31	3.88				
B3 1009+427	0.364	15	0.20	1.6	0.95	$5 < \log(E/\mathrm{eV}) < 11.6$	10.1	2.31	3.88	27	9.1×10^{-12}	5	2.9×10^{-11}
		15	1.0	1.6	0.06	$5 < \log(E/\mathrm{eV}) < 11.6$	9.8	2.31	3.88				
1ES 1028+511	0.361	15	0.20	1.6	1.0	$5 < \log(E/\mathrm{eV}) < 11.6$	10.7	2.31	3.88	425	2.5×10^{-11}	32	9.2×10^{-11}
		15	1.0	1.6	0.06	$5 < \log(E/\mathrm{eV}) < 11.6$	10.4	2.31	3.88				
1ES 1106+244	0.460	15	0.20	1.6	0.18	$5 < \log(E/\mathrm{eV}) < 11.6$	10.8	2.31	3.88	616	3.2×10^{-12}	40	2.0×10^{-12}
		15	0.40	1.6	0.06	$5 < \log(E/\mathrm{eV}) < 11.6$	10.7	2.31	3.88				
1RXS J1353.4+5601	0.404	15	0.20	1.6	0.07	$5 < \log(E/\mathrm{eV}) < 11.6$	10.7	2.31	3.88	435	1.4×10^{-12}	32	3.6×10^{-13}
		15	0.21	1.6	0.06	$5 < \log(E/\mathrm{eV}) < 11.6$	10.7	2.31	3.88				
2E 1415.6+2557	0.237	15	0.20	1.6	1.5	$5 < \log(E/\mathrm{eV}) < 11.6$	10.3	2.31	3.88	62	4.9×10^{-11}	11	2.8×10^{-10}
		15	1.5	1.6	0.06	$5 < \log(E/\mathrm{eV}) < 11.6$	9.9	2.31	3.88				
1ES 1627+402	0.272	15	0.20	1.6	0.08	$5 < \log(E/\mathrm{eV}) < 11.6$	10.7	2.31	3.88	425	3.7×10^{-12}	32	1.1×10^{-12}
		15	0.22	1.6	0.06	$5 < \log(E/\mathrm{eV}) < 11.6$	11.0	2.31	3.88				

Table 4.3: Synchrotron self-Compton model parameters used for the TeV flux estimation for every candidate AGN. The parameters of Mkn 421 used as a reference are also shown for completeness. The listed parameters are: source redshift (z), Doppler factor (δ), radius of the emitting region (R), electron energy density (K), minimum and maximum energy of the electrons (E_{min} and E_{max}), break energy of the electron spectrum (E_{break}), and the spectral indices of the electron spectrum before and after the break (n_1 and n_2, respectively). For each object, the set of parameters that result on a high and low TeV flux are specified in the upper and lower row, respectively. In the case of the high TeV flux model, the predicted position (ν_s, ν_{IC}) and power (P_s, P_{IC}) of the synchrotron and the inverse Compton peaks is also specified.

[a] [G]
[b] [10^{16} cm]
[c] [erg cm^{-3}]
[d] [$\log(E/\mathrm{eV})$]
[e] [eV]
[f] [erg cm^{-2}]
[g] [GeV]
[h] [erg cm^{-2}]

ASDC catalog (Giommi et al., 2002), bright sources from the Donato catalog (Donato et al., 2001) and ultra-high energy peaking BL Lacs selected from Nieppola et al. (2006). All the candidates have redshift between 0.2 and 0.5. The other important criteria taken into account to select them was that its location in the sky would allow for observations with the MAGIC telescope at zenith angles below 35°, in order to profit from the low energy threshold of the MAGIC telescope and to have a sensitivity close to the nominal one of the instrument (see the description of the MAGIC telescope in Chapter 5). This constraint limited the search to blazars located in the northern hemisphere, namely at declinations between $-5°$ and 60°. In total, nine candidate blazars were found fulfilling all the criteria (see the complete list in Table 4.2). The multiwavelength data available at NED[2] together with a simple one zone synchrotron sefl-Compton (SSC) modeling of the sources can be found in Figures 4.6 to 4.13. Objects which had been previously observed with the MAGIC telescope where excluded from the proposal unless there was some hint of signal in the existing data (as it was the case for 2E 1415.6+2557) or the data previously taken was of bad quality and could not lead to restrictive upper limits, as happened in the case of 3C 66A, which was observed by MAGIC during its commissioning phase. Other good candidates like 3C 279 or other low-frequency peaked BL Lacs and flat spectrum radio quasars where not considered either because they were already covered by a different proposal.

4.2.1 TeV flux estimation

Based on the IR, optical and X-ray data available at NED for each of the proposed sources, a simple SSC modeling of the synchrotron luminosity was done to estimate the IC component of the spectrum.

The objects were modeled using the SSC code from Krawczynski et al. (2004). In this code there are the following free parameters: the strength of the magnetic field, the radius of the emitting region, the Doppler factor as seen by the observer, the electron energy density, and the form of the electron spectrum. The electron spectrum is assumed to be a broken power law defined by the minimum and maximum electron energy, the slope of the low energy part, the break energy and the slope of the high energy part. Details on this model, and on leptonic emission models in general, are given in Section 3.3.1.

For the sake of simplicity, the model parameters of Mkn 421 (Albert et al., 2007*b*) were adopted, and just one parameter at a time was changed to fit the available multiwavelength data. This means that four parameters were varied to obtain synchrotron luminosities compatible with the data: Doppler factor, magnetic field, radius of the emitting region and electron density. In addition, the break energy of the electron spectrum was adjusted to fit the data points. In the particular case of 1ES 0158+003, an electron spectrum similar to the Mkn 421 could not simultaneously fit the soft and hard X-ray data (see Figure 4.6), and, therefore, the photon indices of the electron spectrum were also changed with respect to the reference ones (see Table 4.3).

Having four different sets of parameters that reproduce the synchrotron spectrum of each source, the ones giving the highest and the lowest luminosities in the inverse Compton (IC) region are shown in Figures 4.6 to 4.13. The sets of parameters used in the fits are also shown in Table 4.3. The highest ratio between IC and syncrotron luminosities (l_{IC}/l_s) was always achieved by increasing the electron energy density, as it

[2]NASA/IPAC Extragalactic Database. It contains, among other features, archival data of known AGNs at different wavelengths.

increases also the density of soft-photons that can be uppscattered through IC process, following roughly $l_s \propto K$, while $l_{IC} \propto K^2$. On the other hand, the lowest IC luminosities were found by increasing the magnetic field, as it makes the relativistic electrons lose more energy through synchrotron radiation, rather than through IC scattering. The IC energy density was also corrected for absorption of gamma-rays by their interaction with EBL photons using the KneiskeLow EBL photon density model (see Figure 4.4), which provides a low absorption compatible with the results from Aharonian et al. (2006*b*) and subsequent studies.

4.2.2 Priorized list of candidates

Given the predictions of the flux estimation, a priorized list of candidates was compiled. The source candidates that had a predicted flux at 100 GeV comparable to the MAGIC sensitivity at that energy (estimated according to Aliu et al. (2009*b*)) were proposed for observation, with the below given priority based on the predicted flux level and the following additional arguments:

1. **2E 1415.6+2557:** This object was given the highest priority because the predicted flux in the MAGIC energy range was the highest among the selected candidates. Additionally, a hint of signal in previous observations with MAGIC of 2E 1415.6+2557 supported this argument.
2. **3C 66A:** The previous detection claim of VHE gamma-ray emission from this blazar by the Crimean Observatory, and a predicted flux at a detectable level with MAGIC in Joshi and Böttcher (2007) also gave high priority to the observations of this source.
3. **1ES 0158+003:** This blazar is given a lower priority, because the predicted flux level is just above the MAGIC sensitivity in 30 hr.
4. **B3 1009+427:** A low priority is gives also to this source because of the low predicted VHE flux. However, it was included in the proposal as it was the most promising candidate from the Nieppola et al. (2006) catalog.
5. **1ES 1028+511:** The predicted VHE flux of this object is at detectable level with the MAGIC telescope, but the priority of its observations was lowered because previous MAGIC observations resulted in no gamma-ray excess.

The four remaining candidates were not included in the proposal as the predicted VHE gamma-ray flux was below the MAGIC sensitivity even in the most optimistic scenarios.

4.3 MAGIC observations

The five selected blazars where proposed for observation to the Time Allocation Comitee of the MAGIC Collaboration, and its observation was accepted for 30 hr per target. The main goals of the proposal were to detect new blazars at high redshift and make use of its spectra to extract new EBL limits. It aimed also to complete previous campaigns of blazar observations, where just objects at lower redshifts were selected, as the EBL absorption was expected to be higher until the result by Aharonian et al. (2006*b*) suggested the opposite. The observations took place between August 2007 and March 2008, and the results for each of these objects are described in Chapters 7 and 9 of this thesis.

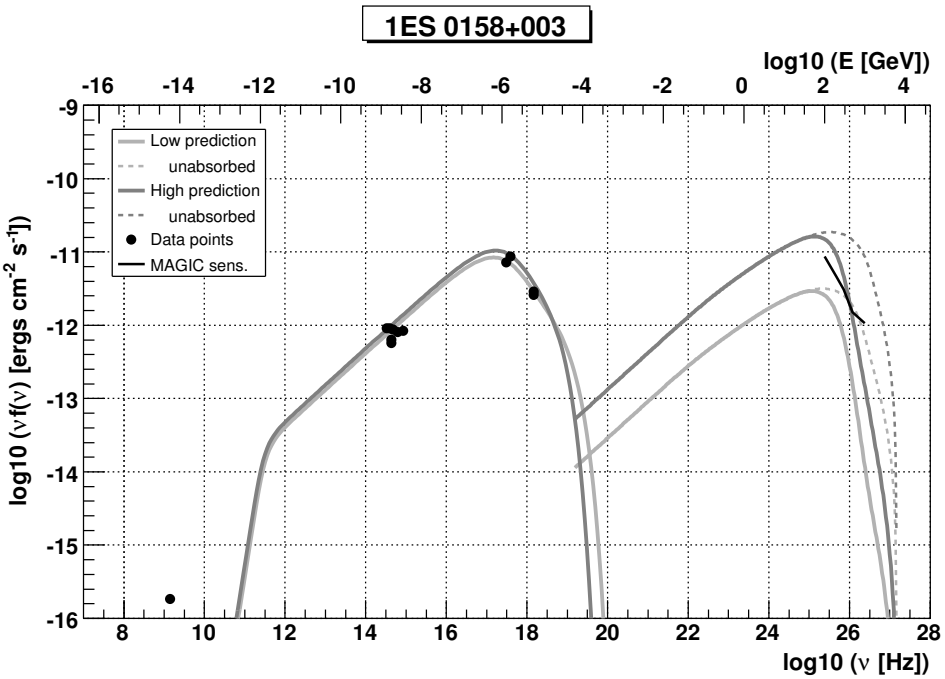

Figure 4.6: Simple SED modeling of 1ES 0158+003. MAGIC sensitivity is shown between 100 GeV and 1 TeV.

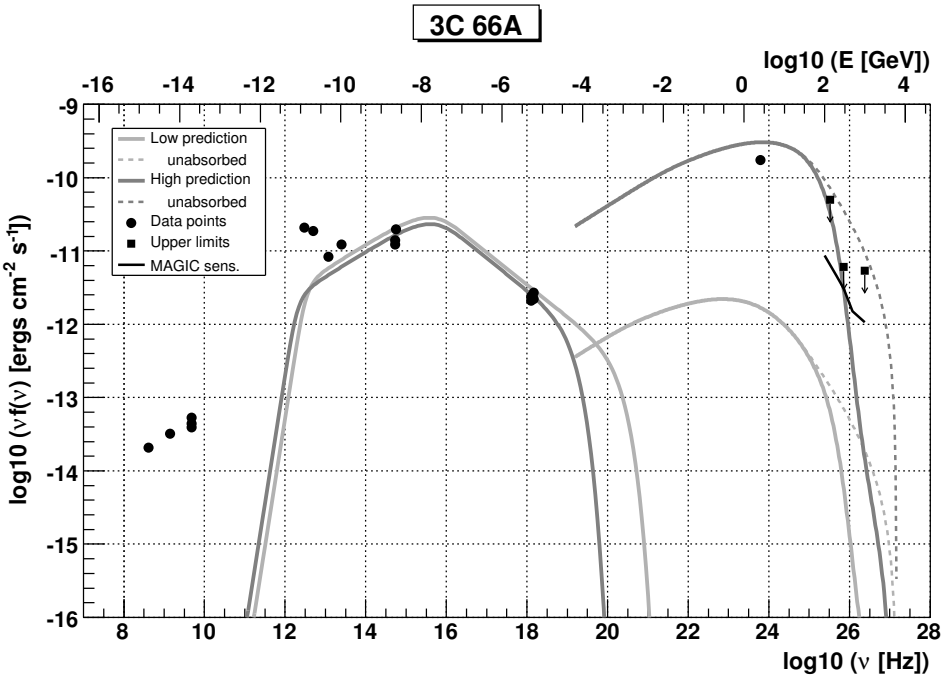

Figure 4.7: Simple SED modeling of 3C 66A. MAGIC sensitivity is shown between 100 GeV and 1 TeV. The upper limits by STACEE, Whipple and HEGRA are also shown (Bramel et al., 2005; Horan et al., 2004; Aharonian et al., 2004).

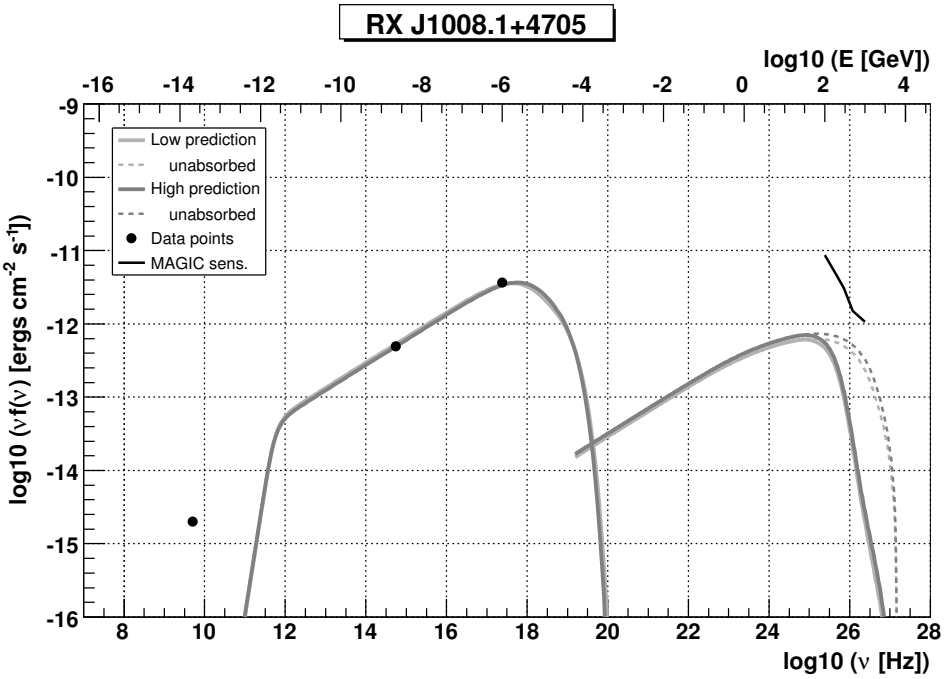

Figure 4.8: Simple SED modeling of RX J1008.1+4705. MAGIC sensitivity is shown between 100 GeV and 1 TeV.

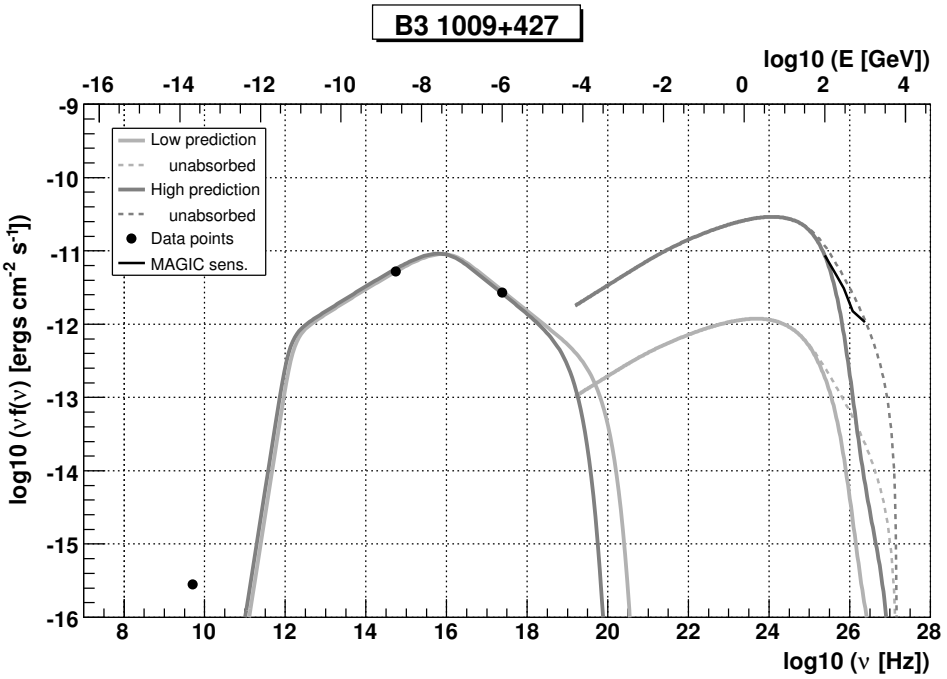

Figure 4.9: Simple SED modeling of B3 1009+427. MAGIC sensitivity is shown between 100 GeV and 1 TeV.

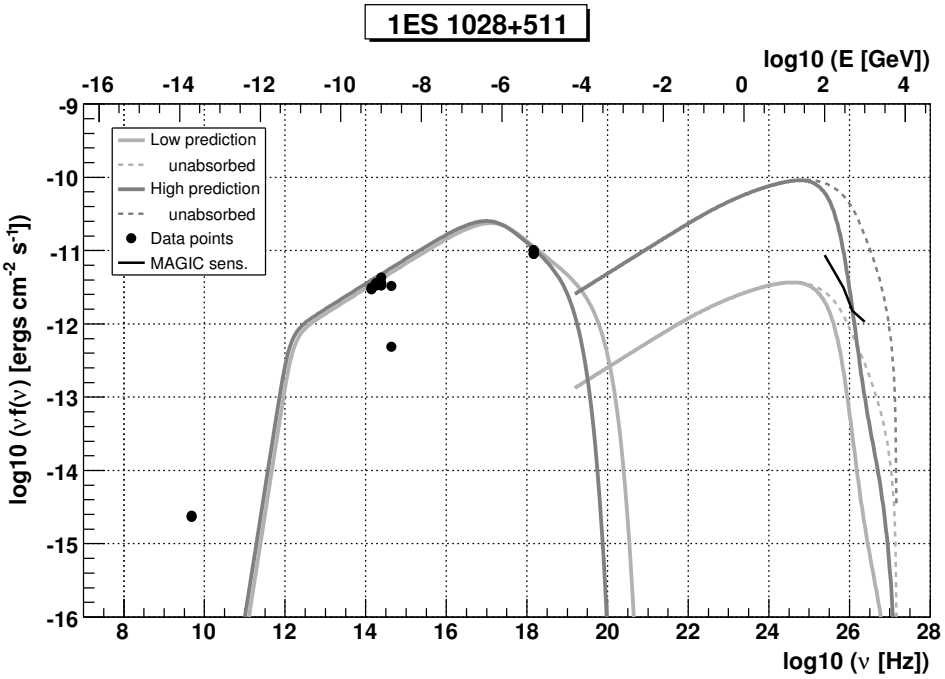

Figure 4.10: Simple SED modeling of 1ES 1028+511. MAGIC sensitivity is shown between 100 GeV and 1 TeV.

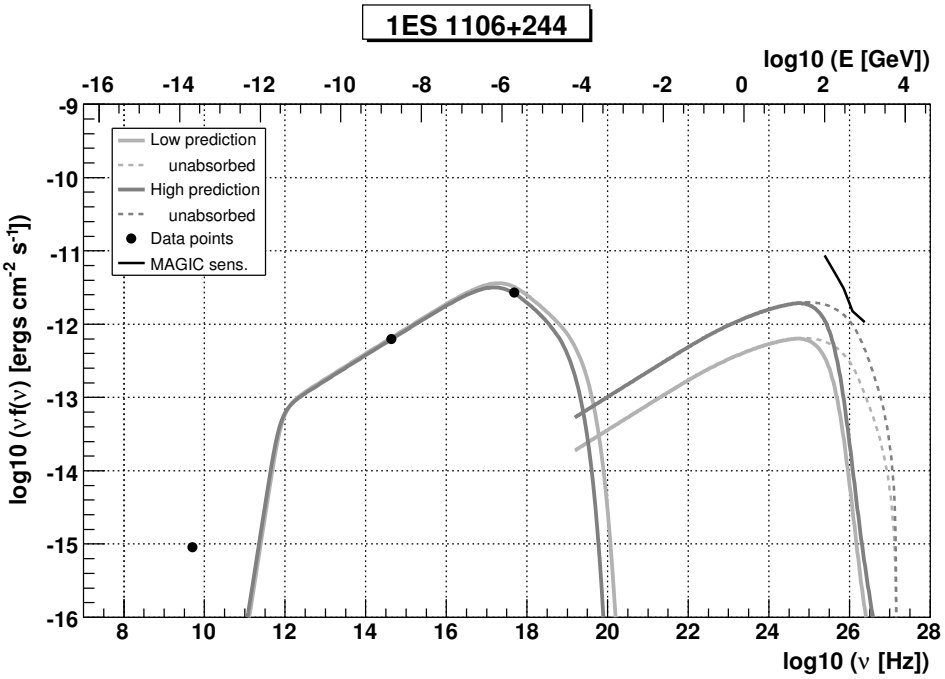

Figure 4.11: Simple SED modeling of 1ES 1106+244. MAGIC sensitivity is shown between 100 GeV and 1 TeV.

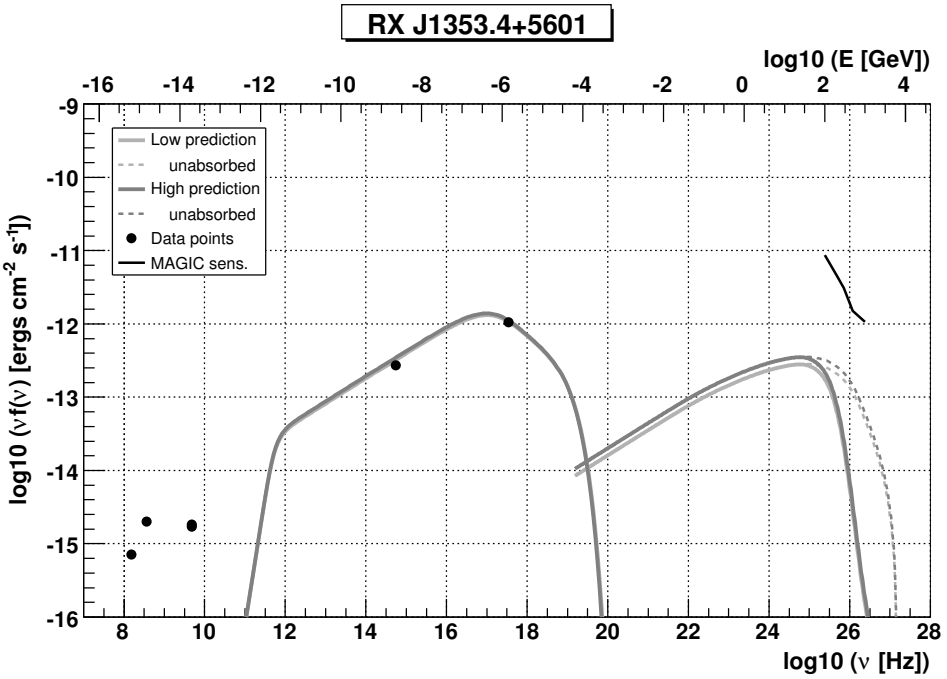

Figure 4.12: Simple SED modeling of RX J1353.4+5601. MAGIC sensitivity is shown between 100 GeV and 1 TeV.

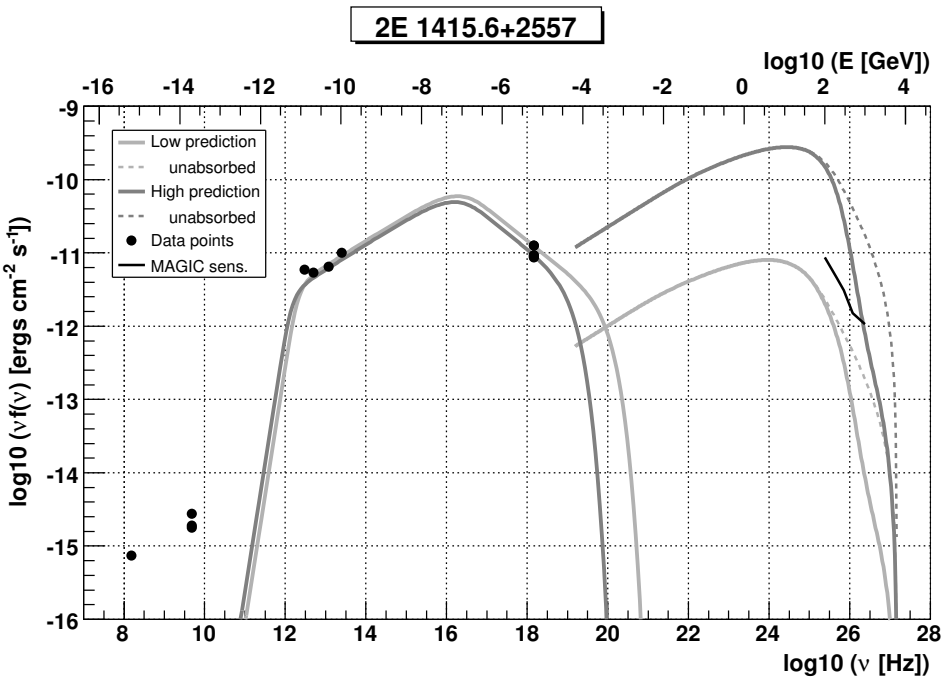

Figure 4.13: Simple SED modeling of 2E 1415.6+2557. MAGIC sensitivity is shown between 100 GeV and 1 TeV.

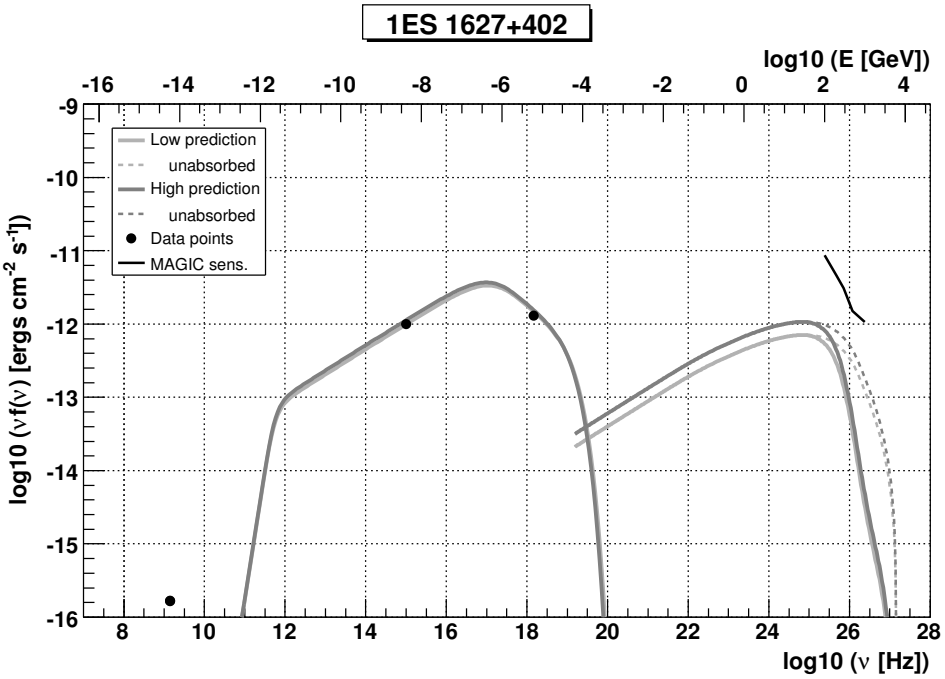

Figure 4.14: Simple SED modeling of 1ES 1627+402. MAGIC sensitivity is shown between 100 GeV and 1 TeV.

Chapter 5

The MAGIC telescope

This chapter introduces imaging air Cherenkov telescopes (IACTs) and describes the technique that allows the detection of gamma-rays using the Cherenkov light that is produced by the showers that they generate in the atmosphere. First, the development of extensive air showers (EAS) will be described with special focus on the Cherenkov light that EAS produce. Then the detection technique of the Cherenkov light of EAS using ground-based Cherenkov telescopes will be discussed. Finally, the MAGIC telescope, its components, accessible energy range, and sensitivity will be described.

5.1 Extensive air showers

Cosmic Rays (CRs) reach constantly the Earth with an approximately isotropic distribution. The main CR components are atomic nuclei (mostly protons), electrons, gamma-rays and neutrinos. Only the weakly interacting particles (neutrinos) cross the atmosphere and reach the ground. The rest of particles will interact with air molecules in the upper layers of the atmosphere (approximately at 25 km above sea level) and, if they are energetic enough ($E \gtrsim 1\,\mathrm{GeV}$), produce an extensive air shower (EAS). The physics of EAS is reviewed in detail in Longair (1992). In the following, the basic concept of the process will be sketched.

In the first interaction, the primary particle generates secondary particles that interact with air nuclei producing new generations of particles. This process repeats recursively making the number of particles in the shower grow very rapidly. Given that the energy of the primary particle is distributed over all the generated secondaries, the development of the shower reaches a point where the average energy of the particles falls below the threshold for production of new particles. At this point, called the shower maximum, the energy losses through ionization and Compton scattering start dominating above particle production processes and the shower starts dying out.

One of the biggest difficulties that imaging air Cherenkov telescopes (IACTs) have to overcome is the large amount of hadron induced cascades –which are the main source of background– compared to the showers initiated by gamma-rays. Even for strong gamma-ray sources, the signal to background ratio is 10^{-3}–10^{-4}. That is why it is very important to know the development of electromagnetic and hadronic cascades to establish their differences and reject the hadronic background from the gamma-induced signal.

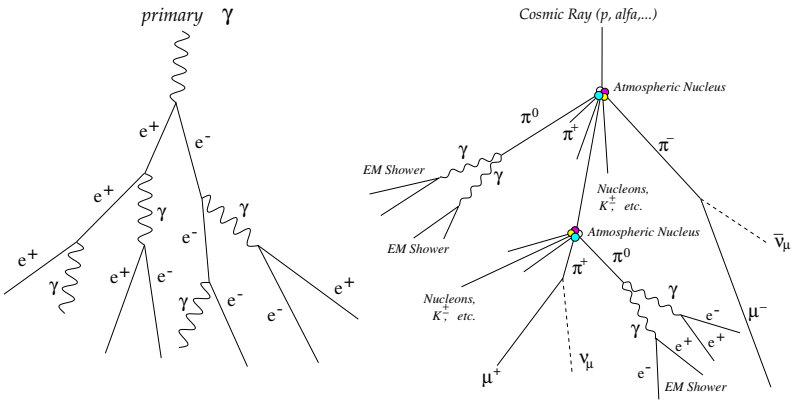

Figure 5.1: Sketch of a pure electromagnetic cascade induced by a primary gamma-ray (left) and a composite cascade initiated by a charged cosmic ray (right), with its electronic, hadronic and muonic components.

5.1.1 Electromagnetic air showers

When a cosmic gamma-ray, or a very energetic electron or positron, enters into the atmosphere, it develops an electromagnetic EAS that contains, in first order, electrons, positrons and photons. Two processes contribute mainly to the shower development: bremsstrahlung and pair production. The typical scheme is the following (see Figure 5.1 left): a primary gamma-ray produces an e^+e^- pair in presence of a nucleus of the Earth's atmosphere. The electron (and the positron) lose energy by bremsstrahlung radiating photons. If the resulting photons have an energy larger than $2\,m_e$ they can produce again e^+e^- pairs that may radiate more photons, making the number of particles in the shower increase exponentially. Both processes have very similar cross section, and the radiation length for bremsstrahlung of an electron in air is $X_0^e = 37\,\mathrm{g\,cm^{-2}}$, while the radiation length for pair production of a photon is $X_0^\gamma = 7/9 X_0^e$ (Yao et al., 2006). On the other hand, if a cosmic electron or positron is the primary particle, an electromagnetic cascade, analogousreason to the one described but starting with bremsstrahlung emission, will develop. Electron-induced showers are in fact an irreducible background for ground-based gamma-ray detectors, but their flux is much lower than that of hadronic CRs. For completeness, it should be mentioned that also muon-antimuon pair production and photo-production (γ + nucleus $\longrightarrow$ hadrons) reactions may occur in an electromagnetic cascade, leading to a muonic and hadronic component of the shower. However, these contributions can be neglected since the cross section of these processes is much smaller than that of e^+e^- production and bremsstrahlung.

All particles in the shower are strongly collimated along the incident direction of the primary gamma-ray –the shower axis– due to the relativistic energies involved. The main process that broadens the shower is multiple scattering and, at second order, the deflection of the charged particles by the Earth's magnetic field.

The development of an electromagnetic shower can be seen in Figure 5.2. As the EAS develops, the energy of the secondary particles decreases, while the number of particles increases until the shower maximum. This maximum is reached when the mean energy of the electrons and positrons in the shower falls below a critical energy E_c –which is approximately 86 MeV for an e^- in air (Berger and Seltzer, 1964)– that defines the moment when ionization becomes the dominant energy loss process instead of bremsstrahlung. At

the same time, the mean energy of the shower photons has decreased and the cross section for production of e^+e^- pairs becomes of the same order of the one for Compton scattering and photoelectric absorption (also at energies around 80 MeV). From this stage on, fewer secondaries are produced, the remaining particles rapidly lose their energy in the medium, and the shower dies out.

5.1.2 Hadron-induced air showers

As mentioned before, most of the particles hitting the top layers of the Earth's atmosphere are charged particles of hadronic origin. A charged CR interacts with an atmospheric nucleus producing pions, kaons and ions lighter that the primary nucleus. If the products of the first interaction have enough energy, they undergo successive nuclear collisions leading to an EAS.

Hadron-induced air showers have three differentiated components: hadronic, electromagnetic and muonic, as can be noticed in Fig. 5.1 right. About 90% of the secondary particles produced in the hadronic core of the shower are pions, out of which 1/3 are π^0s and 2/3 are charged pions. Neutral pions have a very short lifetime[1] and decay into two photons $\left(\pi^0 \longrightarrow \gamma + \gamma\right)$. Each of the resulting photons will initiate an electromagnetic sub-shower. It means that about 30% of the collision energy is transferred to the electromagnetic component of the shower in each hadronic interaction. This process, transfers continously energy from the hadronic to the electromagnetic component of the shower, which ends up being the dominant one at the shower tail. On the other hand, charged pions and kaons mostly decay into muons and neutrinos, feeding the mounic component of the shower. Muons only lose energy through ionization or decay into electrons and neutrinos[2] ($\mu^{\pm} \longrightarrow e^{\pm} + \nu_e + \nu_\mu$), thus an additional fraction of energy is transferred to electromagnetic sub-showers. However, muon lifetime is about two orders of magnitude longer than that of the pion and the kaon[3] and, as many muons are produced with very high energies in the upper layers of the atmosphere, their Lorentz factors are high enough so that they reach the Earth's surface in a sizeable fraction. These muons and the neutrinos produced in charged pion and muon decay prevent about 5% of the initial CR energy from being absorbed in the atmosphere (Risse, 2004).

Hence, the three components of an hadronic EAS are the electromagnetic sub-showers originated from π^0 decays, the hadronic core built up from high energy nucleons and mesons (which usually re-interact and mostly become electrons and positrons whose energy is mostly dissipated through ionization), and a fraction of nearly non-interacting muons and neutrinos.

Figure 5.2 shows the development of simulated electromagnetic and hadronic EAS. It can be noticed that hadronic showers are broader, as their lateral spread is mainly caused by the transverse momentum get by the secondary hadrons in the hadronic interactions, which is substantially larger than the scattering angle generated from multiple scattering (the dominant process in the much narrower electromagnetic showers). This broadening and clustering of hadronic cascades, together with the time profile of the Cherenkov photons produced in the showers, is one of the factors that allow IACTs to distinguish between hadronic and gamma-induced cascades.

[1] The π^0 has a decay time τ_{π^0} of only 8.4×10^{-17}s while charged pions have $\tau_{\pi^\pm} = 2.6 \times 10^{-8}$s.
[2] To make the notation simpler no difference between neutrinos and anti-neutrinos has been made.
[3] muon lifetime is $\tau_\mu = 2.2 \times 10^{-6}$s while pions and kaons have $\tau \sim 10^{-8}$s

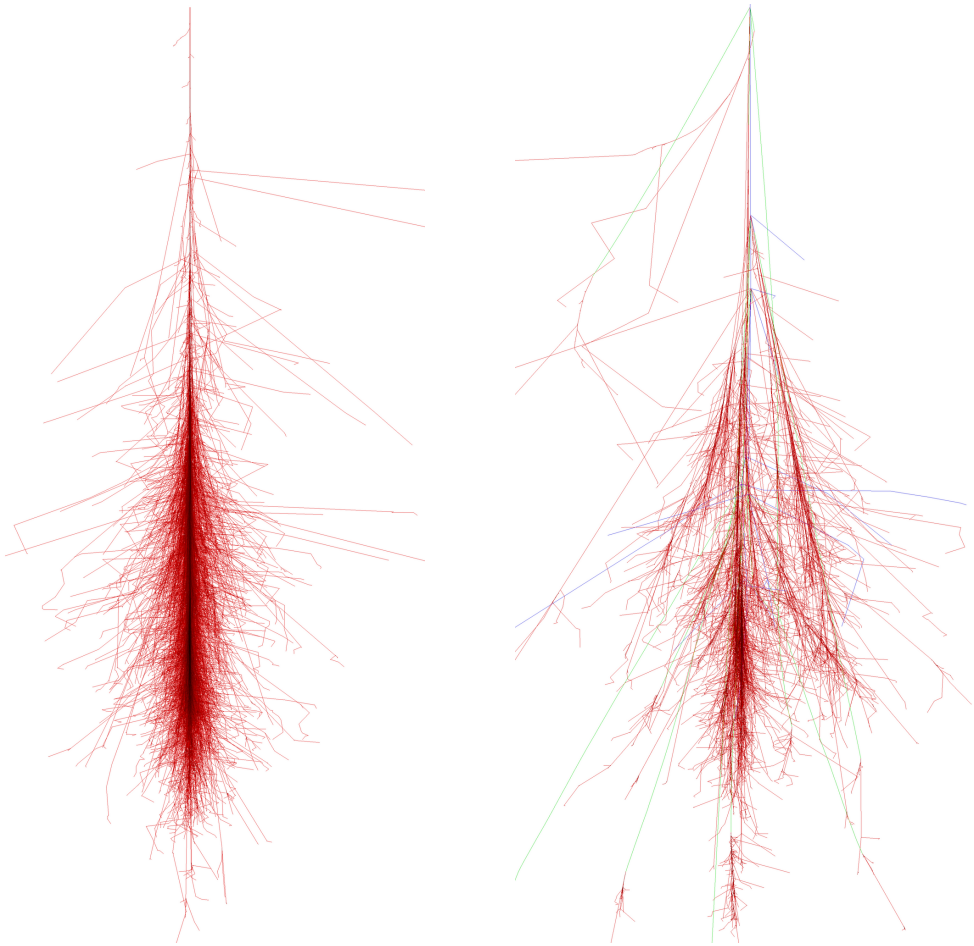

(a) photon, lateral view

(b) proton, lateral view

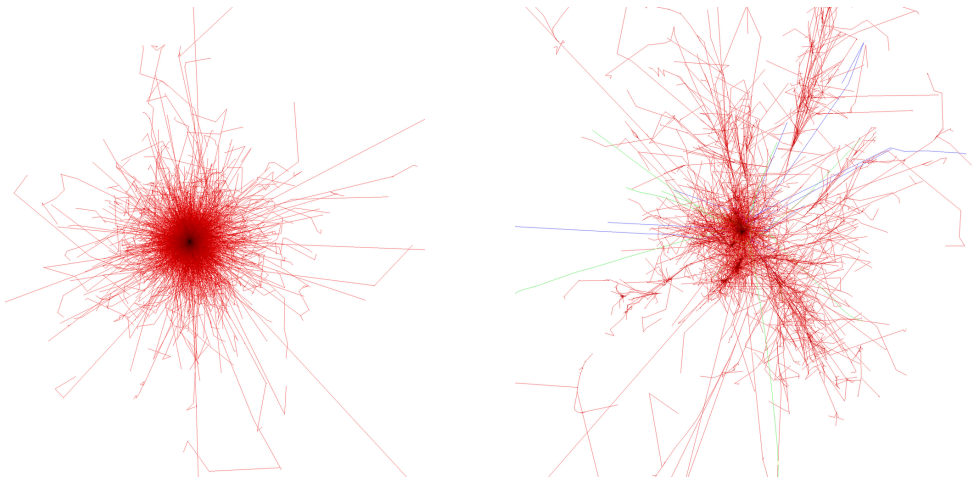

(c) photon, overhead view

(d) proton, overhead view

Figure 5.2: Monte Carlo simulated extensive air showers. The figures show the lateral and overhead view of the development of a vertical shower initiated by a 100 GeV photon (left) and by a proton of the same energy (right). Red tracks indicate the electromagnetic component of the shower: electrons, positrons and photons; blue tracks represent hadrons; and green tracks stand for muons in the shower. Plots from CORSIKA package simulations (Schmidt, 2007).

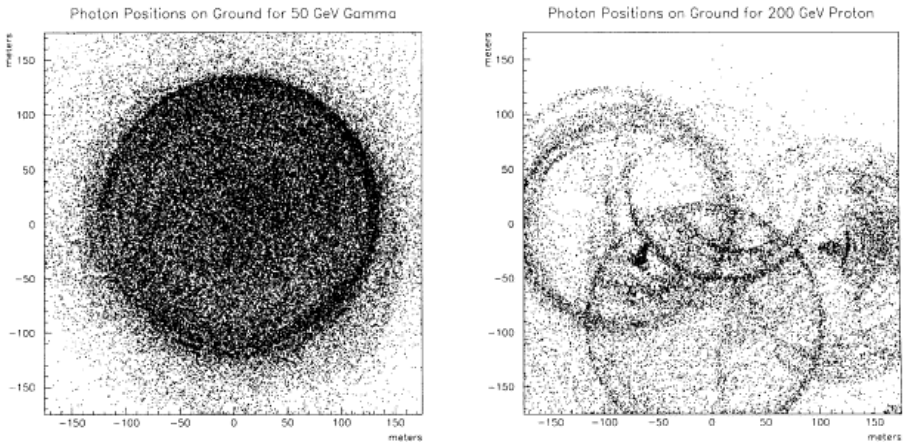

Figure 5.3: Photon distribution at ground level for showers initiated by a gamma-ray of 50 GeV (left) and a 200 GeV proton (right) as simulated using MOCCA (Hillas, 1982). It is shown that the gamma-induced shower has a more collimated development producing an homogeneous photon distribution –Cherenkov light pool– than the hadronic one.

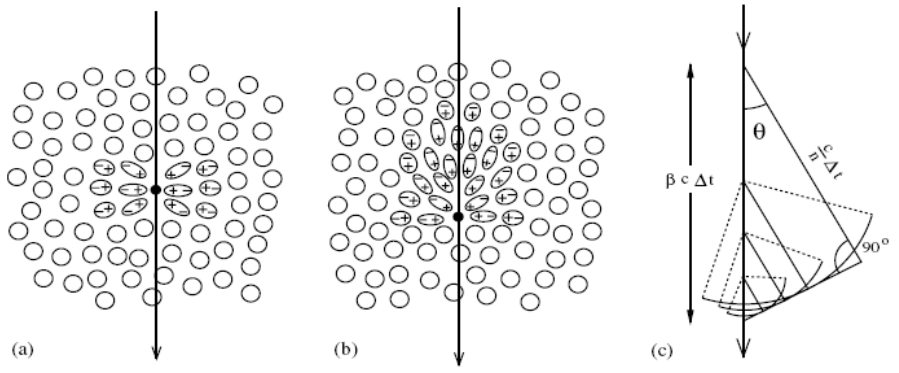

Figure 5.4: Polarization of the medium induced by a charged particle with low velocity (a) and with high velocity (b). Huygens construction of Cherenkov waves that only find coherence at the Cherenkov angle θ with respect to the charged particle trajectory (c).

5.1.3 Cherenkov radiation in EAS

When an ultrarelativistic charged particle moves inside a transparent dielectric medium at a speed $v = \beta c$ which is larger than the speed of light in this medium [4] , it emits light. The light emission results from the re-orientation of the instantaneous electric dipoles induced by the particle in the medium. This radiation was discovered by P.A. Cherenkov in 1934 (Cherenkov, 1935), whereas the theoretical explanation was later given in Tamm and Frank (1937), and it is called Cherenkov radiation.

As a charged particle travels, it disrupts the local electromagnetic field in the surrounding medium. Electrons in the atoms of the medium will be displaced and polarized by the passing electromagnetic field of a charged particle. Photons are emitted as the insulator's electrons restore themselves to equilibrium after the disruption has passed. In a conductor, the electromagnetic disruption can be restored without emitting detectable radiation. The reason is that, in normal circumstances, these photons destructively in-

[4] $c' = c/n$, where n is the refractive index of the dielectric medium.

terfere with each other and no radiation is detected (Fig. 5.4 a). However, when the disruption travels faster than the emitted photons, the photons constructively interfere in a certain direction and intensify the observed radiation (Fig. 5.4 b). The wavefront of the radiation propagates at a fixed angle θ with respect to the velocity vector of the particle, because only in this direction the wavefronts add up coherently according to Huygens construction, as shown in Fig. 5.4 c. This emission angle just depends on the velocity of the partice and the refraction index of the medium:

$$cos\,\theta = 1/\beta n \tag{5.1}$$

When the charged particles are ultrarrelativistic ($\beta \simeq 1$) the emission angle is maximum[5]. The threshold energy of charged particles to emit Cherenkov light ($\beta_{min} = 1/n$) is

$$E_{th}^{Ch} = \frac{m_0 c^2}{\sqrt{1-\beta_{min}^2}} = \frac{m_0 c^2}{\sqrt{1-(1/n)^2}} \tag{5.2}$$

where m_0 is the rest mass of the charged particle.

To calculate the production of Cherenkov photons in an EAS developed in the atmosphere a simple approximation of the refractive index of the atmospheric medium as a function of height (h) can be assumed:

$$n\,(h) = 1 + n_h = 1 + n_0\; exp\left(-\frac{h}{h_0}\right) \tag{5.3}$$

where $h_0 = 7.1$ km and $n_0 = 2.9 \times 10^{-4}$. This model describes a refractive index that decreases at higher altitudes, where the atmosphere is less dense. Smaller dependencies of the refractive index on other factors, such as air temperature or light wavelength are neglected.

Using Eq. 5.3 in Eq. 5.2 and the fact that $n_h \ll 1$, the Cherenkov energy threshold in terms of the height in the atmosphere can be expressed as:

$$E_{th}^{Ch} \simeq \frac{m_0 c^2}{\sqrt{2n_h}} \tag{5.4}$$

Since n_h decreases with height, the energy threshold for Cherenkov emission is higher in the upper layers of the atmosphere and decreases as the EAS develops on. As an example, at 10 km above sea level, $n_h = 7.1 \times 10^{-5}$ and the Cherenkov energy threshold for electrons, muons and protons is 42.9 MeV, 8.9 GeV and 78.8 GeV respectively, about two times larger than the threshold values found at sea level (h = 0 km). It is also worth noticing that nearly all Cherenkov light in an EAS is produced by the secondary electrons and positrons, as they conform the biggest fraction of the particles in the shower and they are more likely to be above the threshold of Cherenkov emission. At the shower maximum, when the average energy is equal to the critical energy threshold for production of new particles ($E_c \sim 86$ MeV), electrons are still above the threshold of Cherenkov emission. Therefore most of the electrons and positrons still emit Cherenkov radiation when the electromagnetic EAS is already dying out. Muons from hadronic EAS also emit a non-negligible fraction of Cherenkov light. Since muon trajectories are straight, because their mass in ~ 200 times the electron mass, the Cherenkov light they produce falls on cones

[5] $\theta_{max} = cos^{-1}\,(1/n)$

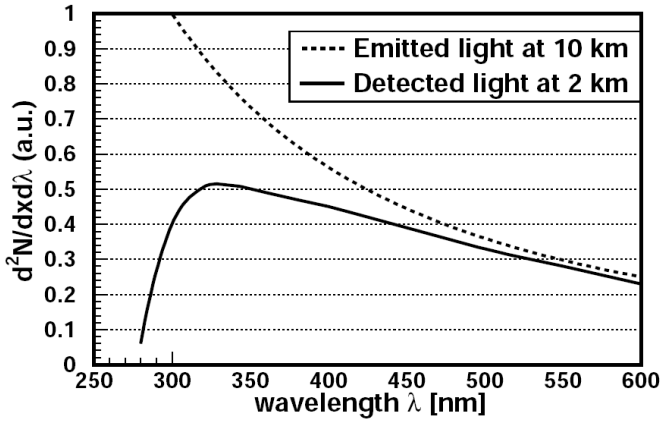

Figure 5.5: Spectrum of Cherenkov light at the shower maximum (dashed curve) and after traveling down to 2 km altitude (full curve).

of constant angle and are imaged to rings or arcs in the focal plane of an IACT. The very short arcs from muons with large impact parameters give rise to compact images that might look similar to gamma-rays. However, as muons travel through the atmosphere undeflected and with almost negligible energy losses, they constitute at the end a very powerful tool to understand and calibrate the performance of IACTs.

In general, the differences in the shower development between a hadron-induced and a gamma-induced EAS, which are reflected in the shape and the time structure of the Cherenkov light distribution at ground level (see Figure 5.3), can be used to distinguish between them with a sensitive enough ground-based instrument. Air showers develop practically at the speed of light, resulting in very short Cherenkov flashes. Typically, the front of Cherenkov photons produced in an electromagnetic EAS arrive at the ground within an interval of 2-5 ns, whereas hadronic showers have a wider time spread (10-15 ns), mainly due to the development of many electromagnetic sub-showers and the larger transverse momentum transfer of hadronic interactions.

Cherenkov radiation spectrum

For detection purposes, it is also important to know the spectrum of the Cherenkov radiation produced in an EAS. The number of Cherenkov photons emitted per unit of path length and per unit of photon wavelength (λ) by a particle with charge Ze is given by (Yao et al., 2006):

$$\frac{\mathrm{d}^2 N}{\mathrm{d}x\,\mathrm{d}\lambda} = \frac{2\pi\alpha Z^2}{\lambda^2}\left(1 - \frac{1}{\beta^2\, n^2}\right) \tag{5.5}$$

where α is the fine structure constant[6]. The $1/\lambda^2$ dependency of the spectrum indicates that most of the Cherenkov photons are emitted at short wavelengths, in the ultraviolet range, and that it decreases along the visible region. However, due to the interactions of the Cherenkov photons with the air molecules in their path through the atmosphere, the spectrum observed at ground level is quite different from the emitted one (see Fig. 5.5), and it peaks at around 330 nm. Cherenkov photons suffer the following attenuation processes in the atmosphere:

[6] $\alpha = \frac{e^2}{4\pi\epsilon_0\hbar c} = 7.297 \times 10^{-3}$

Rayleigh scattering: Photons are scattered by polarizable molecules with size smaller than its wavelength, for example, by air molecules. The Rayleigh scattering cross section is proportional to λ^4, and if the atmosphere is in optimal conditions, it is the process responsible for most of the Cherenkov light attenuation from 15 to 2 km above sea level.

Mie scattering: Cherenkov photons also suffer Mie scattering through interaction with small dust particles suspended in the air (aerosols), whose size is comparable to the wavelength of the light. This effect is specially important when the atmosphere is polluted by dust, fog, clouds, etc. The spectral dependence of the Mie cross section is proportional to λ^a with $1.0 \leq a \leq 1.5$.

Ozone absorption: The absorption in the ozone layer takes place in the upper part of the atmosphere ($h \geq 10\,km$) and affects mainly all the photons with wavelengths shorter than 290 nm, which are absorbed through the $O_3 + \gamma \longrightarrow O_2 + O$ process, which is the dominant one for absorption of ultraviolet light.

5.2 The imaging technique

Imaging air Cherenkov telescopes collect and focus the Cherenkov light produced in EAS into a camera, and are currently the most efficient ground-based experiments for the detection of cosmic gamma-rays. As any other optical or radio telescope, an IACT consists of three basic elements: a tracking mechanical system which points and tracks an astrophysical object in the sky, a collecting surface which gathers the incident radiation and focuses it, and a receiver element which converts the collected radiation into readable data. The main conceptual difference between ground-based gamma-ray telescopes and the other telescopes operating at ground level is that they do not directly detect the photon flux that they observe –very high energy gamma-rays– but the secondary photons –in the visible range– produced in the particle showers initiated by the gamma-rays in the atmosphere.

In a ground-based Cherenkov telescope, a mirror surface collects a fraction of the photons of the Cherenkov light pool. At the focal plane of the reflector, a set of light detectors converts the incident Cherenkov photons into electric signals, which together conform an image of the EAS. The very short time response of the light detectors chosen for IACTs is another important characteristic of these telescopes and is a key factor for background rejection.

The image formed in the camera is a geometrical projection of the atmospheric shower as can be schematically seen in Figure 5.6. Cherenkov photons emitted at different heights reach the mirror dish with different angles and are focused on different positions in the camera of the telescope. As a consequence, the image contains information of the longitudinal development of the EAS, i.e., the number of particles emitting Cherenkov light as a function of the height in the atmosphere. If the telescope is pointing to a gamma-ray source, the light coming from the upper part of the shower (usually called shower head), where the secondary particles are more energetic, has smaller Cherenkov angles and is mapped onto a region close to the camera center. On the other hand, the light emitted from in last stages of the shower (shower tail) has larger Cherenkov angles and is mapped further away from the camera center (see Fig. 5.6).

The imaging technique relies on the shower development information that is contained

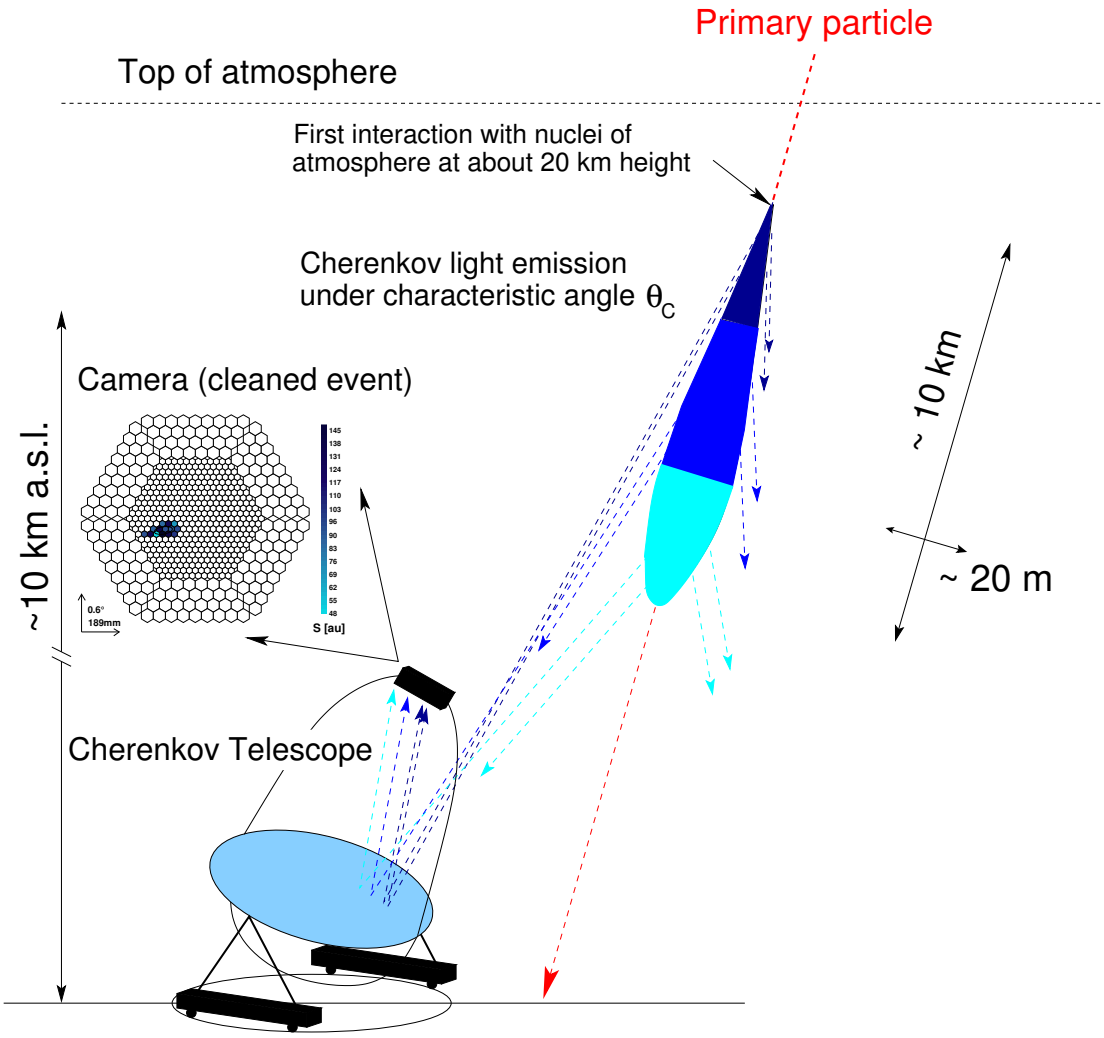

Figure 5.6: Sketch of the principle of the Cherenkov technique, through the formation of the image of an EAS in an IACT pixelized camera. The numbers in the figure correspond to a typical 1 TeV gamma-ray induced shower.

in the images formed in the telescope camera. These images are used to infer the characteristics of the particle that originated the EAS. On one hand, the total amount of light contained in the image is the main estimator of the energy of the primary particle. The primary energy is proportional to the number of secondary particles in the shower. This value can be estimated by measuring the amount of energy deposited in the atmosphere during the shower development. Particles in the shower loose energy mainly through ionization. Although the fraction of initial energy lost in form of Cherenkov radiation is about 3 or 4 orders of magnitude smaller than the energy lost through ionization, the ratio between the Cherenkov energy losses and ionization losses is constant. Therefore, the amount of Cherenkov light collected in the telescope camera is a good estimator of the energy of the primary particle. On the other hand, the shape and orientation of the image are indicators of the nature and the incoming direction of the primary particle.

5.2.1 Imaging air Cherenkov telescopes

Two main parameters characterize an IACT: its sensitivity –the minimum detectable gamma-ray flux in a given observation time– and its energy threshold, which is the minimum energy of the primary particle to which the telescope is able to disentangle the signal from the background. The dispersion of the Cherenkov light generated in an EAS at ground level crucially influences these two parameters. On one hand, the light spread allows the IACT to detect EASs over a large range of impact parameters[7]. This provides IACTs with huge collection areas (of the order of 10^5 m^2). Such collection areas turn into high sensitivities in comparison with gamma-ray detectors mounted onboard satellites, whose dimensions are clearly limited by space-launching requirements and result on small collection areas. On the other hand, the dilution of the Cherenkov radiation over the large light pool makes its detection more difficult and requires large mirrors and high sensitivity photodetectors. An efficient reconstruction of the primary particle characteristics through the image analysis requires a minimum number of detected Cherenkov photons per image (typical numbers are at least 60 photoelectrons in the camera). This implicitly means that an IACT is able to recognize gamma-ray induced showers only if the primary photon has an energy above a certain threshold (E_{th}). As the number of Cherenkov photons is proportional to the energy of the primary gamma-ray, the telescope energy threshold inversely depends on the mirror surface A and the light detection efficiency ε, which includes the mirror reflectivity and the efficiency of the light detectors in the camera. It also depends on the background flux from the night sky (ϕ), the solid angle subtended by the collection mirror (Ω) and the integration time of the signals in the camera (τ), as the larger these factors are the higher is the amount of background light collected by the telescope, which makes it more difficult to detect the signal (Longair, 1992)

$$E_{th} \sim \sqrt{\frac{\phi \Omega \tau}{\varepsilon A}} \tag{5.6}$$

These factors are taken as some of the most important input parameters for the design of a ground-based Cherenkov telescope.

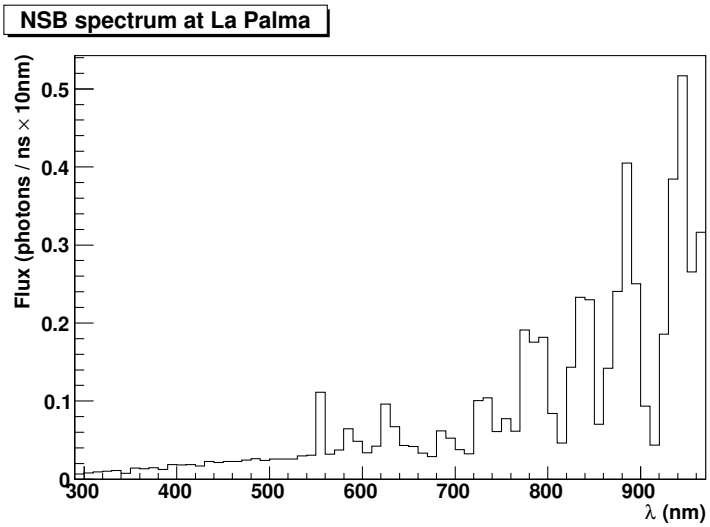

Figure 5.7: Typical spectrum of the sky in La Palma on a moonless night as measured by Benn and Ellison (1998). Most of the distinctive features of the NSB spectrum are due to airglow.

5.2.2 The Night Sky Background

Night sky background (NSB) is the main background source for atmospheric Cherenkov detectors. Its components are light coming from planets, stars, airglow, and zodiacal light (Roach and Gordon, 1973). Depending on the observation site and zenith angle, also the man-made artificial light may contribute to NSB. The measured spectrum of the NSB at the canary island of La Palma is shown in Fig. 5.7. IACTs observe during dark nights, when zodiacal light is very weak or negligible. Therefore the main components of NSB influencing Cherenkov telescopes are the integrated starlight and airglow. In case of IACTs that can perform measurements during moderate moonlight nights, the moonlight should also be taken into account as a background component.

Although the intensity of the NSB is much lower than that of the Cherenkov light produced in an EAS, typical NSB photoelectron rates are in the order of 0.2 phe/ns/pixel in normal observation conditions (Armada, 2005). This signal level is high enough to produce accidental triggers that may mimic low energy gamma-ray induced cascades or sub-showers created in hadronic cascades.

5.3 The MAGIC telescope

There are currently four major IACT systems operating worldwide. CANGAROO III is an Australian-Japanese collaboration that operates an array of four 10 m telescopes in Australia. The european collaboration H.E.S.S. has built four 12 m telescopes in Namibia, and the Irish-British-USA collaboration VERITAS operates four 12 m telescopes in Arizona (USA). The location of these three installations, together with MAGIC, can be found in Figure 5.9. The MAGIC telescope (Major Atmospheric Gamma Imaging Cherenkov telescope) is currently the largest stand-alone telescope of its kind operating in the world.

[7]The impact parameter of the primary particle that produces an EAS is defined as the distance between the telescope location and the point where the shower axis intersects the plane perpendicular to the telescope axis. An IACT can detect showers with impact parameters approximately from 0 to 150 m.

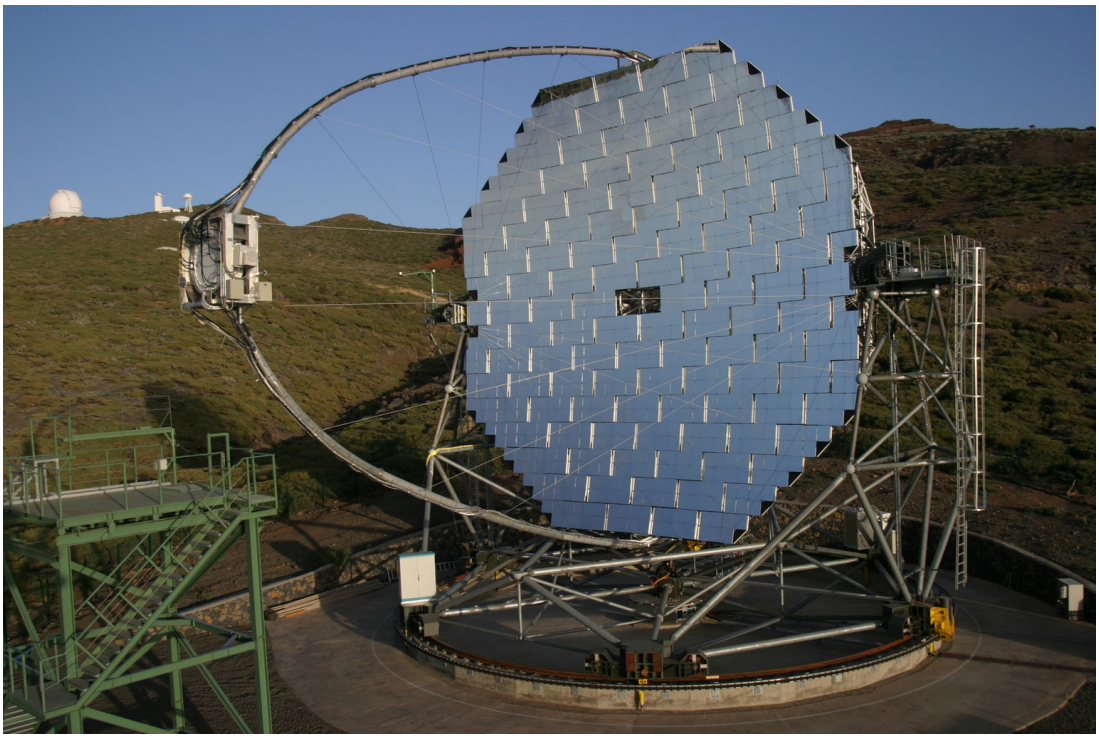

Figure 5.8: The MAGIC telescope standing at the Roque de los Muchachos observatory, in La Palma.

Figure 5.9: Locations of the 4 major IACT experiments.

The site was chosen to be on the area of Observatorio del Roque de los Muchachos, on the Canary Islando of La Palma (2200 m a.s.l., 28°45′N, 17°54′W). The site is well known for its very good atmospheric conditions for most of the year and its low luminic contamination. It was previously used for the HEGRA experiment, and it also hosts several optical telescopes and solar observatories, including the 10.4 m diameter Gran Telescopio CANARIAS.

MAGIC is a collaboration of more than 150 scientists from 20 institutions based in Europe and the United States. It was designed to achieve an energy threshold as low as possible allowing to detect gamma-rays in an unexplored energy range: the gap between 10 and 200 GeV, where the particle flux was too low to allow significant detections with the EGRET satellite[8] and the Cherenkov light produced in EAS is insufficient for a clear detection by the previous generation of ground-based Cherenkov telescopes. To achieve this ambitious goal, MAGIC has the biggest optical reflector in the world so far, extending its sensitivity below 100 GeV. MAGIC has just one telescope in its first phase, which is equipped with technological innovations never used before in the field of IACTs to lower the energy threshold as much a possible.

5.3.1 Reflector and telescope structure

One of the design goals of the MAGIC Telescope was to reposition to any direction in the sky in less than one minute, in order to make follow up observations of the prompt emission of Gamma-Ray Bursts (GRB) after an alert from an X-ray or gamma-ray satellite. To achieve this goal, the weight of the moving parts of the telescope was required to be as low as possible, especially for the mirror frame. The choice was to support the mirror dish with a three layer structure made of low-weight carbon fiber-epoxy tubes joined by aluminum knots.

The frame design is inspired on a pre-existing 17 m diameter solar collector with alt-azimuth mount. For image analysis purposes, it is important to keep the distribution of the arrival times of Cherenkov photons narrow to minimize the effect of the NSB and to use the timing information to distinguish between gamma-induced cascades and hadronic background. In order to minimize the spread in the arrival times at the camera plane, the overall curvature of the reflector is parabolic. The focal length to diameter ratio (f/D) is about 1. This ratio ensures that the effect of the optical aberrations in the shower images is smaller than the size of one pixel, and also that the torque produced by the camera is not to large for the relatively lightweight telescope frame. The telescope reflector is composed of 964 mirror elements of 49.5×49.5 cm each, making a total reflector area of 239 m^2. The mean reflectivity of the mirrors in the range of interest (300-650 nm) is about 85%.

The drive system of the MAGIC Telescope has been another challenging issue due to the high pointing accuracy required, the large dimensions of the telescope and the fast repositioning goal. The azimuth axis of the telescope is equipped with two 11 kW motors, while the elevation axis has a single motor of the same power. The current maximum repositioning time is about 120 seconds[9], while the average is around 40 seconds.

[8] Fermi-LAT has an effective area of ∼8000 cm^2 compared EGRET's 1500 cm^2, and has an energy range that also covers this gap.

[9] This is the time spent to move the telescope 360° in azimuth. Generally the sky position where the telescope is pointing to and the position where it has to be pointed because of a prompt alert are not that separated.

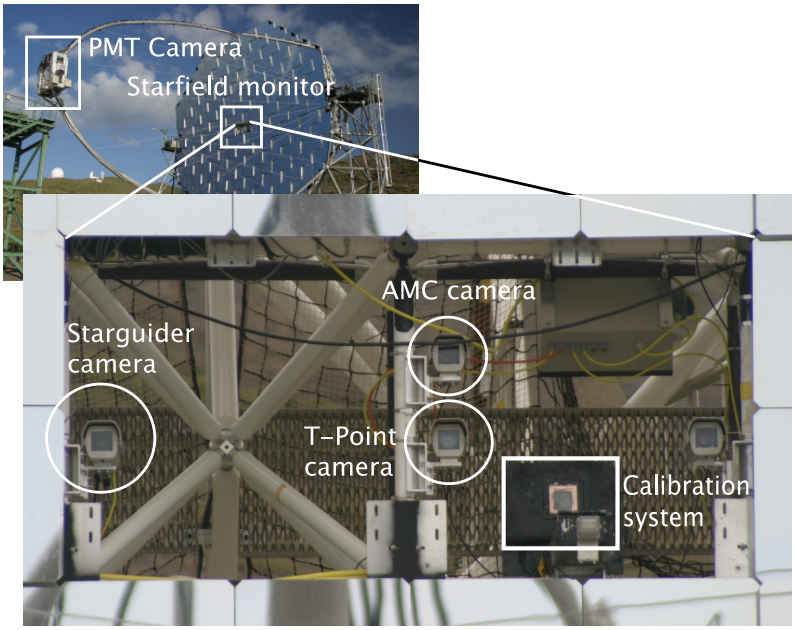

Figure 5.10: The CCD cameras in the middle of the reflector of the MAGIC telescope. The starguider CCD camera and the calibration system are indicated. Picture from Mazin (2007).

The active mirror control

The lightweight telescope structure of MAGIC suffers deformations due to its own weight when the telescope is pointing to different sky directions, causing the mirror surface to slightly deform. In order to correct for this distortions when tracking a source, an active mirror control (AMC) system is implemented. In the center of each mirror panel there is a red laser pointer installed, and two mechanical actuators on the back of the panel allow to change the orientation of the mirrors. On demand by a control software, the laser is switched on and projects a red spot on the cover of the camera, which is viewed by a CCD camera located at the center of the mirror dish (AMC camera, see Figure 5.10). The AMC camera determines the position of the laser spot with respect to some reference positions and, according to the measured deviation, steers the mirror panels by controlling the actuators. The reference positions for each mirror are defined with respect to LEDs mounted on the camera cover, that allow to reference the optical axis of the telescope in the camera.

The adjustment can also be done using stars. A control software uses the image of a star in the camera cover to adjust the panels such that the spot is focused on the camera center. The corresponding positions of the actuators are then stored in a look-up-table. Having aligned all the mirrors at different zenith angle positions of the telescope, these look-up-tables can be used during operation to align the mirrors without the need of switching on the lasers and closing the camera, avoiding a loss of observation time.

Starguider

In order to monitor the tracking system and correct for a possible mispointing, there is a starguider camera installed at the center of the mirror dish. It is a sensitive CCD camera with a field of view of 4.6°. The starguider camera points to the camera of MAGIC,

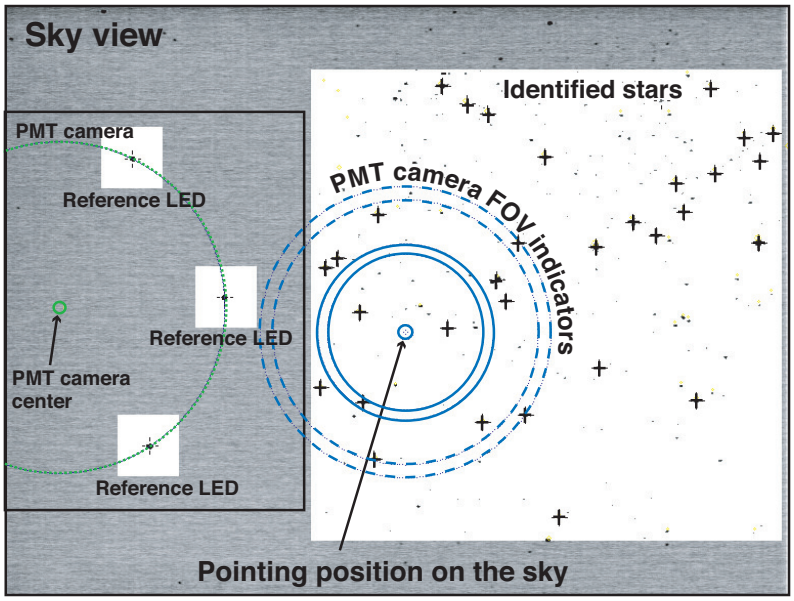

Figure 5.11: Field of view of the starguider camera. On the left part, three reference LEDs are visible, which are used to interpolate the position of the camera center. The white field of view shows a patch of the sky, which is used to identify stars and determine the pointing of the telescope. the identified stars are marked by crosses. The MAGIC field of view is marked by blue circles: inner camera (solid circles) and outer camera (dashed blue circles). Picture from Mazin (2007).

but its field of view is large enough to see field stars (see Figure 5.11). The position of the MAGIC camera is recognized by the starguider software using 6 LEDs mounted on the border of the MAGIC camera. The starguider identifies the pointing direction of the telescope by comparing star positions in the field of view with a starfield catalog. It ensures that the actual pointing position of the telescope is well defined. The starguider information is used offline in the data analysis to correct for possible mispointings that might happen during the tracking. As a side benefit of the system, the number of stars identified by the starguider software can be compared from expected values coming from catalogs to judge about weather conditions and atmospheric transmission of particular observations.

5.3.2 Camera

The camera is a decisive element in the general performance of an IACT. First of all, it is the device where Cherenkov photons are collected and converted to photoelectrons, so its efficiency strongly determines the sensitivity and the energy threshold of the telescope. Secondly, the gamma/background separation power is highly dependent on the quality of the shower images, so it also directly influences the sensitivity of the telescope. Therefore, a fine-pixelized, fast-response camera allows the subtle differences between hadron and gamma showers to be better revealed. Due to the high cost of each photosensor, the layout of the camera is always a compromise between a large field of view (FOV) and a fine pixelization. Anyway, it makes no sense to go below a certain pixel size limit because there the images are dominated by the optical imperfections produced by the reflector and the statistical fluctuations on the shower development, which do not add any information

Figure 5.12: Picture of the camera of the MAGIC telescope. The two different regions –smaller pixels in the inner region and larger ones in the outer rings– can be clearly distinguished.

to the captured shower images.

Camera layout

The camera was designed to meet the minimum weight requirements for fast repositioning. Most of the trigger and readout electronics are not part of the camera but are installed in the central data acquisition building located 150 m away from the telescope site. This choice minimizes the weight and the complexity of the camera, but increases the amount of data that has to be transmitted from the camera to the main building.

As can be seen in Fig. 5.12, the hexagonal detecting area is divided into two regions: an inner part with 396 hexagonal fine pixels of 0.1° angular diameter –30 mm ϕ at the camera plane– and an outer part with 180 hexagonal bigger pixels of 0.2° angular diameter –60 mm ϕ at the camera plane. The total FOV covered by the camera is 3.5°. This configuration allows a good sampling of the small images that are produced by low energy gamma-rays with the finer inner pixels, and a mapping of the shower tails of the larger images with the outer pixels.

To improve the light collection efficiency a plate of light guides (Winston cones) has been placed in front of the photodetector pixel matrix. The Winston cones provide two important benefits: a nearly 100% active area camera by minimizing the dead space between photosensors, and the rejection of a large fraction of the background light coming from outside the incident angle defined by the edge of the reflector dish.

Photosensors

The photosensors used for the construction of the camera of the MAGIC telescope had to match some basic requirements: adequate pixel size, good photon collection inside the light guides, low gain, good time resolution, wide dynamic range, high quantum efficiency, low afterpulse rate and good single photoelectron resolution.

Two models of photomultiplier tubes were developed and constructed by Electron Tubes: ET9116A (25 mm ϕ) for the inner pixels and ET9117A (38 mm ϕ) for the outer

pixels. The main characteristics of these photomultipliers are an hemispherical photocathode and an only 6-stage dynode system in circular-focused configuration. A deep performance study of these photomultipliers can be found in Ostankov et al. (2000). The hemispherical shape of the photocathode has an additional advantage: for large incident angles, photons cross the photocathode twice. In these cases, if the photon is not absorbed in the first crossing it still has a second chance of being absorbed at the other side of the hemispherical sensitive area. Therefore, double-crossing photons have a higher probability to create a photoelectron and hence be converted into signal. A further enhancement of the effective quantum efficiency of the PMTs was achieved with the application of a light scattering lacquer mixed with a wavelength shifter (Paneque et al., 2003).

Ideally, photosensors should allow single phe detection, which makes the calibration of the camera much simpler, but also should have low afterpulsing probability to avoid spurious triggers. These are, however, contradictory requirements: a high amplification in the first dynode provides a good single phe response, but goes against a low afterpulse rate. The approach chosen was to use a base with an overall high voltage of $\sim 1.1\,\mathrm{kV}$ (i.e., $\sim$120 V between dynodes and $\sim$360 V between the photocathode and the first dynode). It was also found that increasing by about 50 V the voltage applied to the 5th and 6th dynodes a linear behavior over the whole desired dynamic range is achieved. This is implemented by using an active load system which fixes the last two dynodes to -350 V and -175 V with respect to the anode, and a zener diode which sets the photocathode to 1st dynode voltage to 350 V. With this configuration the overall gain is within the required values, and the afterpulsing rate is below an acceptable level.

Signal transmission

The decision of housing the main readout electronics outside the camera implied that the transmission should not distort the photomultiplier signal along a 150 m transmission cable. The chosen option was to use optical fibers, for which the degradation of analog signals is much lower than in coaxial cables. The use of optical fibers for the signal transmission has additional advantages: there is no crosstalk between different channels (which are typically packed very close to each other in their way to the data acquisition building), signals can not be affected by external electromagnetic interferences, optical fibers are much lighter, and individual channels can be packed more compactly.

To optically transfer the data, the electrical photomultiplier pulses are converted into light pulses. Right after the photomultiplier base, the signal is amplified by a fast low noise transimpedance amplifier. After the amplification, the pulse enters a transmitter board where it is transformed to a light pulse by means of a Vertical Cavity Surface Emitting Laser (VCSEL). The output of the VCSEL is coupled to an optical fiber, which transmits the signal from the camera to the control house. Once in the control house, the optical signals are converted back to electrical signals in the receiver boards.

5.3.3 Trigger and data acquisition

The trigger system of the MAGIC telescope consists of 3 levels. Only the signals of the innermost 325 pixels of the camera are considered for the trigger. The level 0 trigger is located still within the receiver boards and acts on each individual PMT signal. Each analog pulse passes through a discriminator and, if its amplitude is larger than a tunable threshold, a new digital signal is produced and sent to the next trigger level. The level 1 searches for coincidences of neighbor pixels. After a logical comparison of the digital

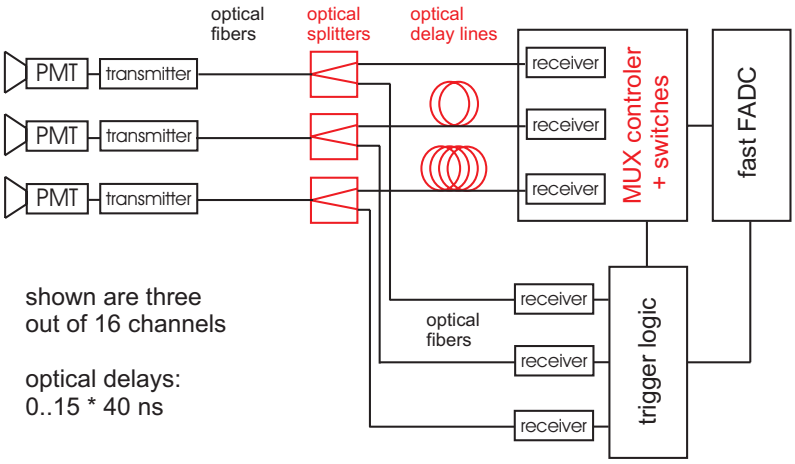

Figure 5.13: Scheme of the signal flow and the data readout in the MAGIC Telescope. From Goebel et al. (2008).

outputs coming from the receiver boards, coincidence on the arrival times of the signals from groups of 2, 3, 4 or 5 next-neighbor pixels within a short time window is required. The level 1 configuration, which is used for normal data taking, is four closed-packed pixels, although the lowest energy showers can be partly rejected by this trigger level configuration selection. The level 2 trigger can perform a digital analysis of the shower image which considers the topology of the event. Up to now, level 2 trigger is not used in regular observations.

Whenever an event passes all the trigger levels, it is recorded by the data acquisition system. In April 2006 a new multiplexed FADC readout working at 2 GSamples/s was installed (Bartko et al., 2005; Goebel et al., 2008). It uses a novel fiber-optic multiplexing technique, which can be used as the signal duration (few ns) and the trigger frequency (lower than 1 kHz) result in a very low duty cycle for the digitalizer system. A scheme of the signal transmission from the camera to the FADC system is shown in Figure 5.13.

The fiber-optic multiplexing system (MUX) uses a 2 GSamples/s FADC to digitalize 16 read-out channels consecutively, i.e. 1 FADC digitalizes 16 channels. The analog signals are delayed using optical fibers, and each channel is delayed by 40 ns with respect to the previous one. The signals are then electrically multiplexed and finally sent to the FADC system. A trigger signal is generated using a fraction of the light signal, which is branched off by fiber-optic light splitters before the delay fibers.

5.3.4 Calibration

The calibration of the signals from each channel is done to translate the information recorded by the FADCs into incident light flux in the camera. This is accomplished by calculating a conversion factor between number of recorded FADC counts and number of incident photons for each individual pixel.

The MAGIC calibration system[10] provides fast light pulses at different wavelengths and variable intensity in order to calibrate the whole dynamic range of the camera photosensors and their readout chain. The system consists of a box located at the center of the telescope mirror dish which houses 64 LEDs emitting at three different wavelengths:

[10]See Gaug (2006) for a detailed description of the MAGIC calibration system.

370 nm (UV LEDs), 460 nm (blue LEDs) and 520 nm (green LEDs). The light pulses have about 3-4 ns FWHM duration, and are nearly as short as the Cherenkov light flashes reaching the individual pixels from the air showers.

The calibration of the signals recorded by each pixel of the camera is done basically in two steps: first a relative calibration and then an absolute calibration. The relative calibration equalizes the response of different channels when subjected to the same input signal.

An absolute calibration is needed in order to convert the signal recorded by a pixel in FADC counts into physical quantities more related to the flux of photons arriving at the camera. The calibration system of the MAGIC telescope provides three independent methods to perform the absolute calibration:

Blind Pixel: The Blind Pixel is an attenuated pixel that is able to resolve single photoelectrons. By analyzing the single photoelectron spectrum recorded by the blind pixel, the mean number of photoelectrons produced in the photocathode can be estimated and, together with the well-known quantum efficiency and the pixel geometry, the mean number of photons arriving from the calibration pulses per unit area can be computed.

Pin Diode: The PIN diode –Positive-Intrinsic-Negative diode– is used to monitor the light pulses emitted by the calibration box. The mean number of photons that arrive per unit area onto the camera plane can be estimated from the signal collected in the PIN-diode, its quantum efficiency, the light spectrum of the LED and the geometry of the system. The PIN diode itself is calibrated with a ^{241}Am source, and is located 110 cm from the calibration box.

F-Factor: A complementary method to calibrate the signal is the Excess Noise Factor or F-Factor method. It is based on the fact that a photomultiplier adds only a small excess noise to the intrinsic fluctuations of the photoelectron flux, excess noise which is linearly related to the initial number of photoelectrons that produce its output signal. The F-Factor of any electronic device is simply defined as:

$$F = \frac{(Signal/Noise)_{input}}{(Signal/Noise)_{output}} \tag{5.7}$$

being therefore a numerical value which account for the additional noise introduced by the readout and amplification chain, assuming it is independent on the signal intensity. From the knowledge of the F-Factor of the photomultipliers and the analysis of the output signal of each pixel, one can extract the average number of photoelectrons impinging on the first dynode of each photomultiplier. More details on the implementation of the F-Factor are given in Section 6.5.

5.4 MAGIC II

A second 17 m diameter telescope has been built by the MAGIC collaboration at the same site as the first telescope, on the Roque de los Muchachos observatory in La Palma, and is being commissioned during Spring and Summer 2009. MAGIC II is located at a distance of 80 m from the first telescope . The two telescopes can be operated independently or in stereoscopic mode. The stereoscopic mode leads to a better reconstruction of the

Figure 5.14: Picture of the two MAGIC telescopes at the Roque de los Muchachos observatory in La Palma. MAGIC I is on the left, and MAGIC II, now in commissioning phase, is on the right of the picture.

image parameters and a stronger background suppression. When an image of the shower is obtained with two telescopes, image parameters are individually obtained from the signal of each of the telescopes and then combined to calculate stereo parameters. The source position is obtained from the intersection of the major axes of the two images of the shower. In addition, the height of the shower maximum can also be estimated. The stereo analysis promise to result in an improvement of approximately 20% in angular resolution, an improvement of the energy resolution from 25% to 15%, and a better background rejection due to the coincidence trigger. According to the latest Monte Carlo simulations, the overall improvement in sensitivity of the system is in the order of a factor of 2-3 compared to that of a single telescope, depending on the energy (Figure 5.15).

The frame of the second telescope is almost identical to that of the MAGIC-I telescope. The lightweight reinforced carbon fiber reflector frame, the drive system and the active mirror control (AMC) are only marginally improved with respect to the first telescope. The reflector uses larger mirror elements ($1\,m^2$) with reflectivity between 80 and 85%.

The main improvements with respect to the first telescope are in the camera and the readout system. MAGIC II has an improved camera with 1039 pixels of 25.4 mm diameter each, covering a field of view of 3.5°, the same as MAGIC I. The number of pixels is larger because no larger pixels on the outer rings of the camera are used anymore. The trigger configuration also changed with respect to the original of MAGIC, covering now a larger trigger radius of 1.25°. Every seven pixels are grouped in a hexagonal configuration to form one cluster (Figure 5.17(b)). This modular design allows easier control and maintenance of the camera. The pixels are based on the use of superbialkali photomultipliers (Hamamatsu R10408) with a quantum efficiency of approximately 32%

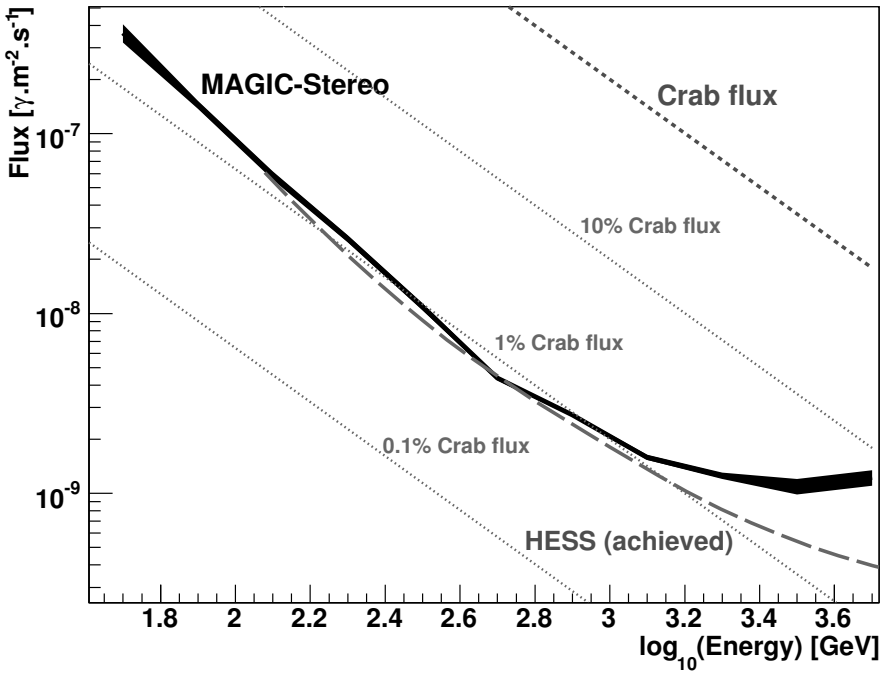

Figure 5.15: Integral sensitivity of the MAGIC II system compared to other experiments. The sensitivity is defined as integral flux of gamma ray events, exceeding a background fluctuation by a factor 5 in 50 hours of observation.

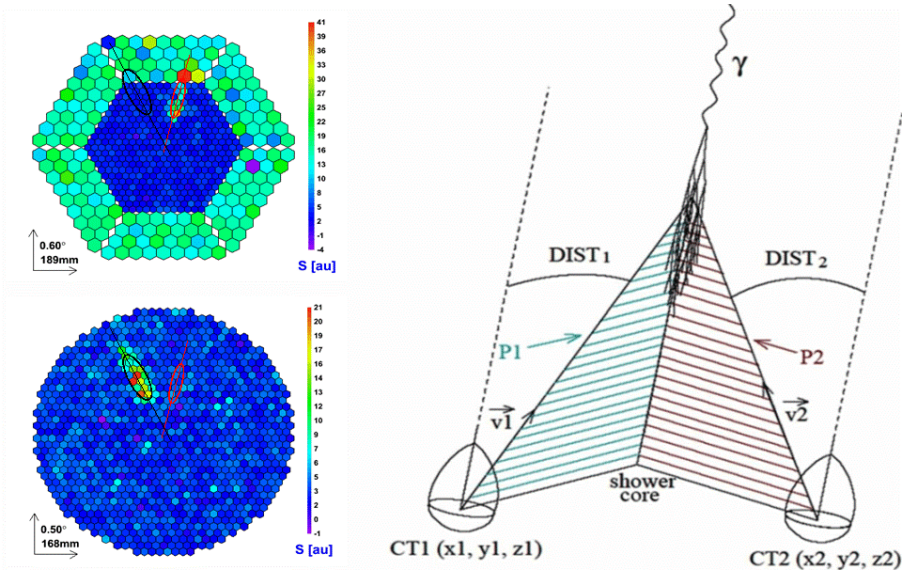

Figure 5.16: Stereoscopic principle. The incoming direction of the shower and core distance are obtained by combining the information of the images in MAGIC I (top-left) and MAGIC II (bottom-left). From Carmona et al. (2008).

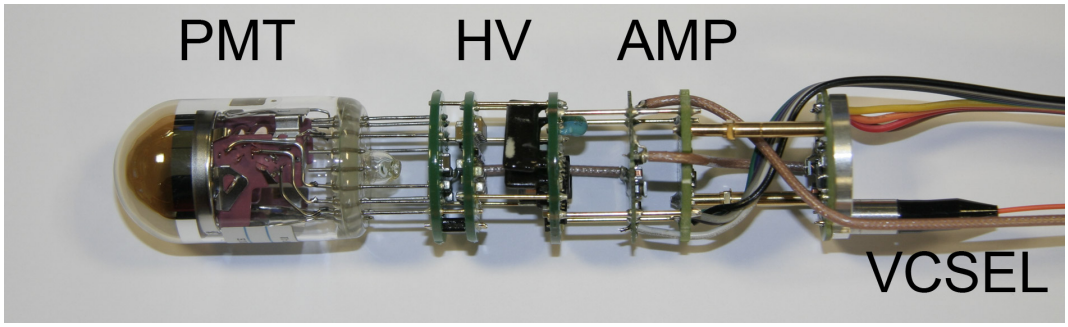

(a) Assembled pixel module formed by a photomultiplier tube, a high voltage source, an amplifier and a VCSEL to convert electric signals into optical signals.

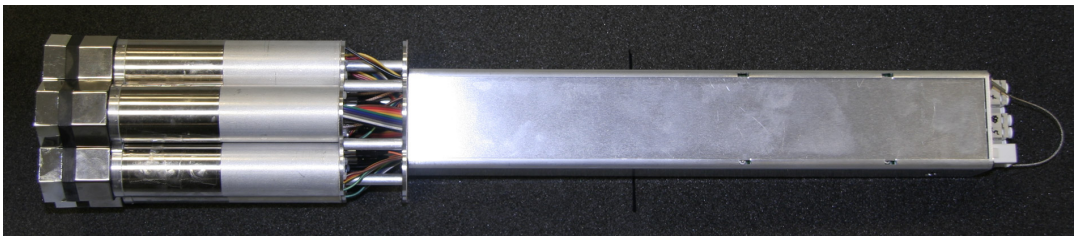

(b) Full cluster with 7 pixels.

Figure 5.17: Pictures of the elements that conform the MAGIC II camera.

at the peak (around 330 nm).

The other significant upgrade is on the readout system. The optical signal from the camera are transmitted via optical fibers to a digitalization system based on a low power analog sampler called Domino Ring Sampler. The analog signals are stored in a multi capacitor bank that is organized as a ring buffer. The capacitors sample the signal at 26 samples/s. Once a trigger is received, the sampling is stopped and a region of interest in the ring buffer (currently 70 capacitors, corresponding to 35 ns) is read out at a lower frequency of 40 MHz and sent to a computer, where the data are organized in events and stored to a disk.

Chapter 6

The MAGIC data analysis chain

This Chapter describes the standard analysis chain used to analyze data taken with the MAGIC telescope, from the checks to ensure the quality of the data to the data reduction chain: the signal extraction, calibration, image cleaning and parameterization, gamma/hadron separation and final evaluation of the signal, including the calculation of energy spectra, light curves and sky maps.

The final goals of the data analysis software of a ground-based Cherenkov telescope are three: distinguish between gamma-like and background-like events, determine the energy of the primary gamma-ray in gamma-like images to derive the energy spectrum of the detected emission, calculate the incoming direction of the gamma-ray showers to estimate the position of the possible gamma-ray emitter, and determine the arrival time of each gamma-ray candidate to produce light curves.

6.1 Monte Carlo generated gamma-rays

The MAGIC analysis chain relies on Monte Carlo (MC) simulated gamma-ray showers to know the detector response to gamma-rays. MC simulations are unavoidably needed because there is no natural or artificial calibrator of VHE gamma-rays in the sky that can be used to learn about the response of the atmosphere and the telescope to gamma-ray-induced air showers. Several studies have been made to compare MC with real data, and the agreement has been proven to be good (Albert et al., 2008*f*).

In the MAGIC analysis, MC gamma showers are also used to optimize the cuts for background rejection and to estimate the effective collection area after all cuts, which allows converting excess events into a physical flux of gamma-rays.

The Monte Carlo simulation software used in MAGIC generates gamma-ray showers following three steps. First, the development of the gamma-ray initiated air showers is simulated with the CORSIKA 6.019 package (Heck et al., 1998) using the US standard atmosphere. The Cherenkov photons produced in the simulated shower that arrive at ground in the vicinity of the telescope location are stored. In a second step, a program called `reflector` simulates the absorption of Cherenkov light in the atmosphere and the light scattering, using again the US standard atmosphere to take into account the Rayleigh scattering due to the molecular atmosphere. The effect of Mie scattering losses is also calculated at this stage using the Elterman model (Elterman, 1964) for the distribution

of ozone and aerosols in the atmosphere. The `reflector` program calculates then the reflection of the surviving photons on the telescope mirror dish (through ray-tracing) to obtain their distribution, incoming direction and arrival time on the camera plane. In this step the mirror reflectivity and possible mirror misalignments are taken into account. Finally, the `camera` program simulates the response of the MAGIC photomultiplier camera, trigger and data acquisition system. At this stage, the arrival directions are smeared out according to the measured spread of the projection of a star into the camera plane after being reflected on the mirror (optical point spread function). After this final step, the resulting files can be plugged into the standard MAGIC analysis chain. More details on the `reflector` and `camera` programs can be found in Majumdar et al. (2005).

6.2 Crab test data sample

The Crab Nebula is the remnant of a supernova explosion occurred in year 1054 at an approximate distance of 2 kpc.[1] It is one of the best-studied non-thermal emitting celestial objects in almost all bands of electromagnetic radiation. It is clearly detected from the radio band ($\sim 10^{-5}$ eV) to gamma-rays ($\sim 10^{14}$ eV).

The Crab Nebula was the first detected source in the VHE gamma-ray domain (Weekes et al., 1989). The nebula turned out to be the strongest steady source of VHE gamma-rays in the sky. Therefore, it is used by ground-based gamma-ray experiments as a standard calibration source to test their performance.

In this chapter, the performance of the MAGIC analysis chain is tested at their different steps using a test sample of data taken on the Crab Nebula. This test sample refers to observations made on five consecutive nights between January 1 and January 5 2008. The data were taken in *wobble* mode (see Section 6.3) with excellent weather conditions. Each observation lasted approximately 1 hr, for a total observation time of 5.14 hr.

6.3 Observation modes

MAGIC observation data are taken basically in either of two different observation modes: *tracking* mode or *wobble* mode, being the main difference between these two methods the way to estimate the background (see Section 6.9).

The *tracking* mode is the most natural way to observe a point-like gamma-ray candidate. In this observation routine, the telescope points directly to the sky position of the observed source and tracks it, so that the source position is always located at the center of the telescope camera. These observations are called *on* pointings. When this approach is used, additional data are needed to reliably estimate the background. For that purpouse, supplementary *off* pointings are done, selecting a sky position with similar conditions (number and magnitude of stars, NSB brightness, etc) as in the *on* region, but with no known or potential gamma-ray source in the field of view.

An alternative observation strategy is the *false-source tracking* mode (Fomin et al., 1994), also called *wobble* mode. In this method, the telescope tracks alternately two sky directions, each at 0.4° from the source position (see Figure 6.1). Pointings to each *wobble* position last typically 20 minutes. When using the *wobble* observation mode, there is no need for additional *off* data to be taken. As the source position is located 0.4° off the camera center, several regions in the camera can be defined with the same offset and at

[1] 1 pc (parsec) = 3.262 light-years = 3.086×10^{18} cm

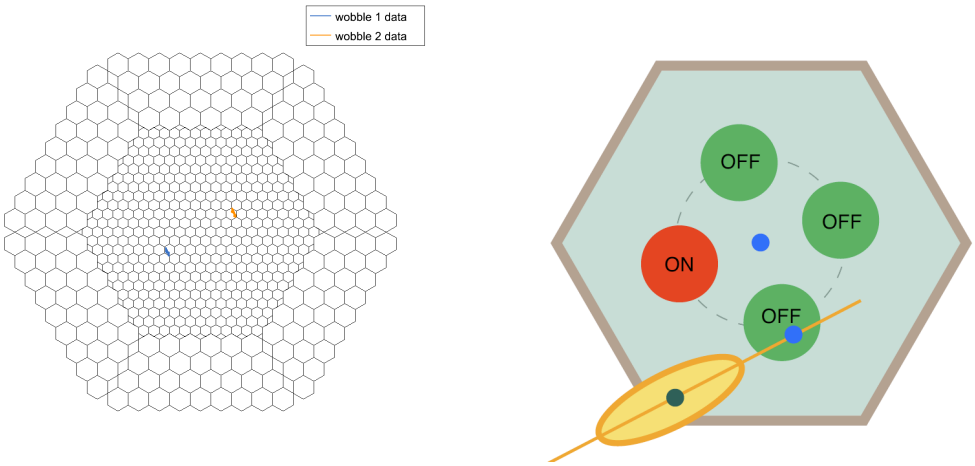

(a) (b)

Figure 6.1: (a) Distribution of the source position in the camera for the two observed *wobble* positions in the Crab Nebula test sample. (b) Sketch of the definition of the signal (*on*) and background (*off*) regions in *wobble* observations. From Mazin (2007).

symmetrical locations with respect to the center of the camera (see Figure 6.1). Usually, three off regions are used in MAGIC standard analysis.

Currently, most MAGIC data are taken in *wobble* mode, which provides some significant advantages. The most evident advantage is that there is no extra time needed for *off* observations, increasing the telescope duty cycle and also the time coverage of the source activity, which is critical for observations of variable sources. The other main advantage of *wobble* observations is that the background estimation is done simultaneously with the *on* data taking. This fact reduces the systematic effects induced by divergences between non-simultaneous *on* and *off* pointings, which can be due to different weather conditions, NSB levels, mismatching zenith and azimuth angle distributions, or changes in the telescope performance. On the other hand, it has to be considered that having the gamma-ray source off the camera center reduces the gamma-ray acceptance of the camera by 15–20%. depending on the gamma-ray energy (see Figure 6.2).

6.4 The MAGIC Analysis and Reconstruction Software

The MARS software package (MAGIC Analysis and Reconstruction Software) has been developed to cover all data reduction and analysis steps: from the reading of the raw FADC data to the calculation of energy spectra, lightcurve and sky map of the detected gamma-ray signal. The MARS software is written in C++ language and is based on the ROOT[2] framework. The MARS package includes different programs which execute the different steps of the analysis process. The main analysis steps are:

- Conversion of the FADC information for each pixel into number of photoelectrons (phe) using the calibration information. Also the timing information of the signal is saved at this stage. The program that does the signal calibration is called `callisto`.
- Cleaning of the recorded images, by rejecting all pixels containing only noise. After

[2]object oriented data analysis framework, `http://root.cern.ch`

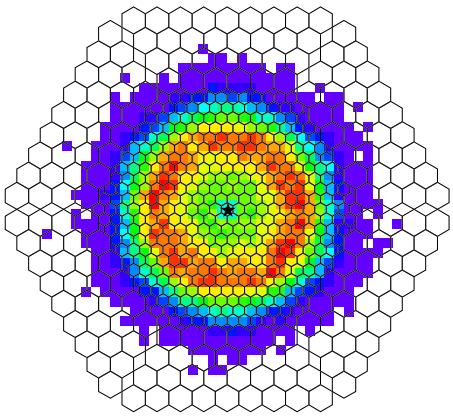

(a) *Source tracking* mode. $80\,\mathrm{GeV} < E < 200\,\mathrm{GeV}$

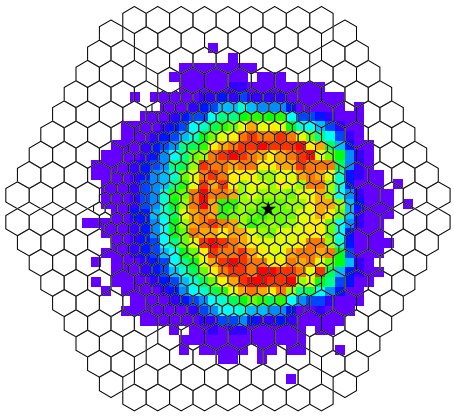

(b) *Wobble* mode. $80\,\mathrm{GeV} < E < 200\,\mathrm{GeV}$

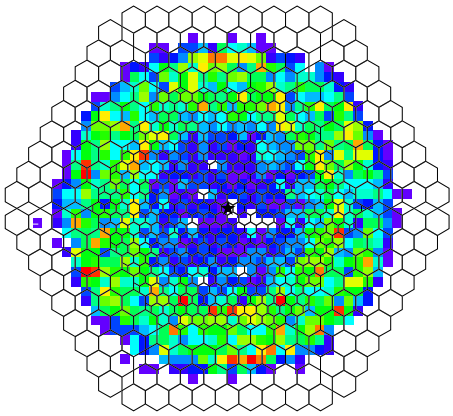

(c) *Source tracking* mode. $E > 1\,\mathrm{TeV}$

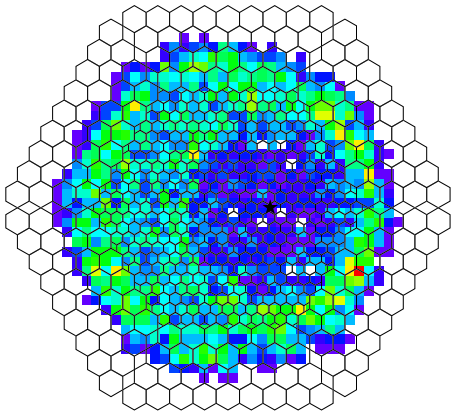

(d) *Wobble* mode. $E > 1\,\mathrm{TeV}$

Figure 6.2: Center of gravity distribution of MC simulated gamma-ray showers superimposed on the MAGIC camera layout. Distributions are shown for simulated source position in the center of the camera and 0.4° off-axis, and also for low and high energy events. The simulated source position is indicated with a black star.

the cleaning, the image of the recorded shower is parametrized by a set of variables called *image parameters*. The image cleaning and calculation of image parameters is done with a program called `star`.

- Training of the matrices that will be used for gamma/hadron separation. For this training, two subsamples of MC generated gamma-rays and real background events are used. For the energy estimation, a subsample of MC gamma-ray events is used. The training program is called `osteria`.

- Application of the matrices trained in `osteria` to the Monte Carlo gamma-ray sample, the signal, and the background data, to calculate the *Hadronness* parameter of each event, which estimates the probability of an event to be hadron or gamma-like. The estimated energy of each shower image is also calculated at this stage. This program is called `melibea`.

- Application of the background reduction cuts, calculation of the effective time of the observations, determination of the number of excess events and determination of the effective area using the corresponding Monte Carlo generated gamma-ray sample. After these steps, the energy spectrum and the light curve of the observed source are derived. This is accomplished by a program called `fluxlc`.

- Projection of the arrival directions of the selected gamma-ray candidates into celestial coordinates to produce a sky map of the observed region. The program is called `celestina`.

6.5 Calibration

In the following, the basic concepts of the calibration of MAGIC data are sketched. The MAGIC telescope uses 2 GSamples/s flash analogic to digital converters (FADCs) to sample air shower signals. The signal extraction method interpolates the FADC contents using a cubic spline algorithm (see Albert et al. (2008*a*) for details). In a second step, it searches for the position of the maximum of the interpolation function. The charge of the signal is then obtained by integrating the interpolation function in a window of fixed size, with integration limits fixed with respect to the position of the spline maximum. The arrival time is defined as the position of the rising edge of the pulse at 50% of the peak value.

Once the signal level and arrival time for each pixel have been extracted, the charge, given in FADC units, has to be converted into an equivalent number of photoelectrons arriving to the first dynode of the PMTs. This is done using a proportional relation between both quantities, which is extracted from dedicated calibration runs using the F-Factor method (Mirzoyan, 1997). This method assumes a uniform photoelectron efficiency, a constant excess noise introduced by gain fluctuations, and the number of phe generated per calibration event in every pixel is Poisson distributed, with a mean of N phe and a root mean square (RMS) of $\sqrt{N}$. Now, the measured charge in FADC counts after pedestal subtraction Q has a mean of $\langle Q \rangle$ and a RMS σ. The RMS σ is, however, wider than the pure Poissonian expectation. It means that the relative widths of the two distributions can be written as:

$$F \frac{1}{\sqrt{N}} = \frac{\sigma}{\langle Q \rangle} \tag{6.1}$$

The F-factor is introduced in Equation 6.1 to account for the additional broadening of the measured distribution, which is due to the multiplication process of electrons in the PMT dynodes. In principle, the transmission and amplification chain of the PMT signal can also contribute to the broadening of the measured distribution, although this contribution is negligibly small compared to the intrinsic F-factor of the PMT. The F-factor is individually measured in the laboratory for each PMT. In the case of MAGIC, the distribution of F-factor among the PMTs installed in the camera is narrow, and an average value of 1.15 is used for all PMTs in the calibration.

Since $\langle Q \rangle$ and σ are quantities extracted from calibration events, and the F-factor is known, Equation 6.1 can be used to calculate the average number of phe of a calibration event and then the conversion factor C:

$$C = \frac{N}{\langle Q \rangle} = F^2 \frac{\langle Q \rangle}{\sigma^2} \tag{6.2}$$

Special calibration runs with 4096 events each are taken before the observation of every new source to calculate the conversion factors. Apart from this calculation, interlaced calibration light flashes are fired with a rate of 50 Hz during the data taking of cosmic events. This additional calibration events are used to update the conversion factors during the telescope operation, which change mainly due to variations in the output of the VCSELS used for the signal transmission from the camera to the control house. The derived, and constantly updated, conversion factors are applied to obtain the number of phe per event and per pixel N from the measured number of FADC counts Q:

$$N = C \cdot Q \tag{6.3}$$

During typical MAGIC observations, 3–5% of the camera pixels cannot be correctly calibrated because of hardware problems or strong starlight contamination. Instead of excluding those problematic pixels from the analysis, their signals are interpolated, averaging the value of the signal in their neighboring pixels.

A complete description of the MAGIC calibration can be found in Gaug (2006).

6.6 Image cleaning

Once the charge and arrival time of the signals in every pixel is calculated, the camera images are cleaned. The aim of image cleaning is to select only the pixels whose signals are due to shower light and remove the rest, as many pixels will only contain fluctuations of the night sky background. Those pixels are rejected before parametrizing the air shower image. In Figure 6.3 an example of an event before and after different cleaning configurations is shown.

The standard cleaning method used in MAGIC data analysis is the *standard-absolute* method. This procedure uses a threshold signal value q_{core} (a fixed value given in number of phe per pixel) to select the *core* pixels of the image. A pixel is selected as *core* pixel if its charge is above q_{core} and has at least one neighboring pixel also above this charge threshold. This additional requirement avoids the selection of pixels unrelated to the image whose large charge results from an afterpulse in the PMT. In a second stage, all pixels having at least one *core* neighbor, and whose charge is above $q_{boundary}$ (with $q_{core} > q_{boundary}$) are also included in the image (these are called *boundary* pixels).

Relaxing the cleaning levels q_{core} and $q_{boundary}$ results in a larger number of pixels per image (see Figure 6.3). In principle, having more pixels which belong to the shower

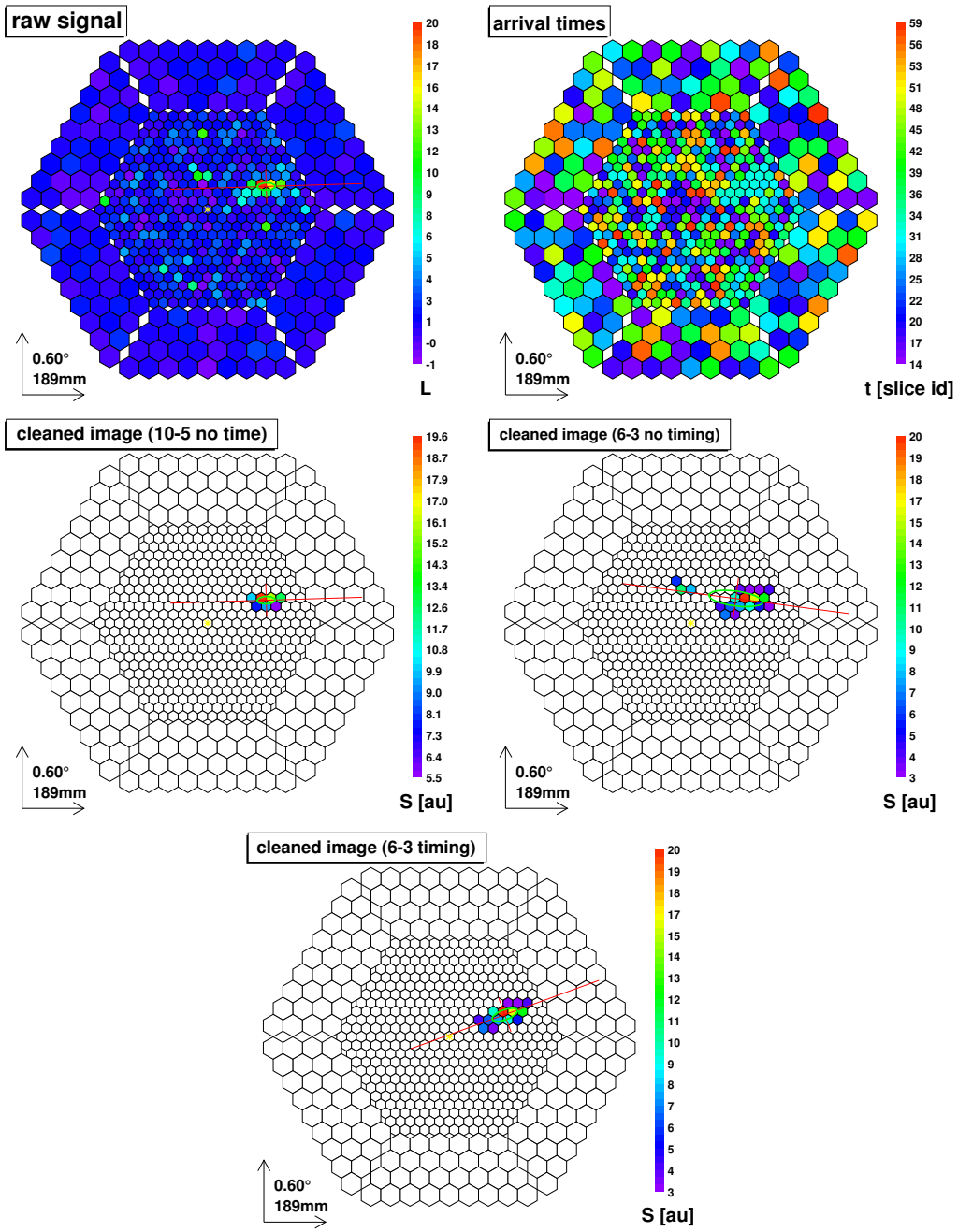

Figure 6.3: Illustrative γ-event images (Monte Carlo data, Energy = 71 GeV, Impact Parameter = 110 m). First row: display of raw recorded data (left) and arrival times information (right). Second row: comparison of standard cleaning with 10-5 phe minimum charge levels (left) and 6-3 minimum charge levels (right). Bottom: image obtained with the time image cleaning (6-3 phe minimum charge levels and 4.5 ns and 1.5 ns as time constrains). The simulated gamma-ray source is located in the center of the camera (yellow star). From Aliu et al. (2009*b*).

image maximizes the amount of information that is used in the image parametrization, improving the calculation of the image parameters. This is specially convenient for the analysis of low-energy events, since a minimum number of pixels is needed to proceed with the analysis. On the other hand, a low cleaning level increases the probability to include noise pixels in the cleaned image, which would degrade the image parameters and worsen the performance of the later analysis.

The arrival time of the signals for each pixel can also be used to improve the performance of the cleaning procedure. Since Cherenkov flashes are very brief (of the order of few ns), and NSB fluctuations produce pulses asynchronous with respect to the shower image, timing information can help to further reject pixels unrelated to the shower image. This timing constraint is implemented as a time coincidence window between the mean arrival time and the individual pixel arrival time. This further constraint allows also to relax the cleaning levels q_{core} and $q_{boundary}$, maximizing the amount of shower information that is used in the image parametrization without significantly increasing the accepted amount of noise.

The standard time cleaning used in the analysis of MAGIC data works in the following way. After selecting the *core* pixels as described above, the mean arrival time of all *core* pixels is calculated. Then, those *core* pixels whose arrival time is not within an interval Δt_{core} with respect to the mean arrival time are rejected. In the selection of *boundary* pixels, it is required that the difference between the arrival time of the *boundary* pixel candidate and its neighbor *core* pixels is smaller than a second fixed time $\Delta t_{boundary}$.

For standard analysis of MAGIC data the charge threshold levels are set to $q_{core} = 6\,\text{phe}$ and $q_{boundary} = 3\,\text{phe}$. Concerning the time constraints, values of $\Delta t_{core} = 4.5\,\text{ns}$ and $\Delta t_{boundary} = 1.5\,\text{ns}$ are selected. This choice of threshold values is motivated by a study based on Monte Carlo data (Tescaro et al., 2007), and was used in the analysis presented in this thesis.

6.7 Calculation of image parameters

The pixels remaining after the image cleaning represent the light distribution of the air shower on the camera plane. The gamma-ray induced images have an elliptical form, with the major axis being related to the longitudinal development of the shower and the minor axis to the lateral development. For further analysis of the images it is useful to characterize them by a set of parameters, which were first proposed in Hillas (1985). In addition, other quantities are suggested by differences between gamma-ray- and hadron-induced shower images. In general, image parameters can be grouped into two categories: *source dependent*, which are the ones where the position of the expected gamma ray-source in the camera is used, and *source independent*, were this information is not needed. Some of the main image parameters are illustrated in Figure 6.4.

Source independent parameters: These parameters describe the shape of the shower image in the camera, and can all be calculated without any prior assumption on the position of the gamma-ray source. Most of the source independent parameters are defined following Hillas (1985).

Size: Total charge contained in the cleaned image. This parameter is the best indicator to estimate the energy of the primary gamma-ray that initiates the air shower, as can be seen in Figure 6.5.

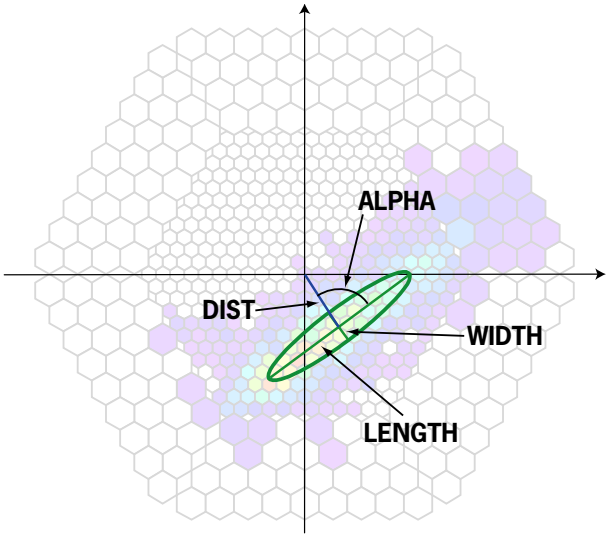

Figure 6.4: Sketch showing the definition of the main image parameters. From Albert et al. (2008*f*).

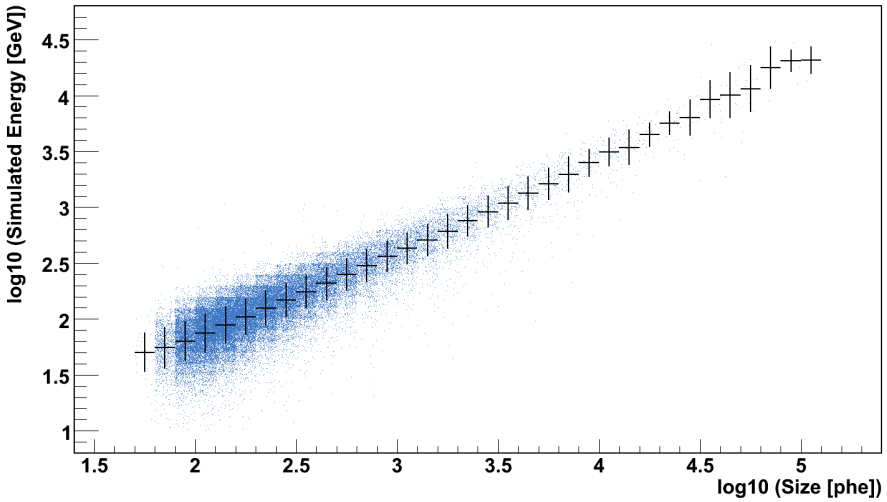

Figure 6.5: Correlation between the simulated energy of the primary gamma-rays and the *Size* parameter of the resulting shower images, for MC simulated gamma-rays with Impact Parameter $<$ 120 m.

Length: The RMS spread of the light along the major axis of the shower ellipse, which is a measure of the longitudinal development of the shower.

Width: The RMS spread of the light along the minor axis of the shower ellipse, which is a measure of the lateral spread of the shower.

M3long: Third moment of the light distribution in the image along its major axis, which indicates the shower direction. This parameter is used to determine which side of the image is closer to the direction of the incident particle, and it is very useful for background rejection. However, for low *Size* images, *M3long* is not well defined and its background rejection power reduces dramatically.

Conc(N): Fraction of the image charge contained in the N brightest pixels in respect to the total charge of the image. Represents the compactness of the shower image, which tends to be larger in gamma-induced showers than in background events. In the standard analysis chain, *Conc (2)* is generally used, and designated simply as *Conc*.

Leakage: It is defined as the fraction of light contained in the outermost ring of pixels in the camera. Images with large *Leakage* values are likely to be truncated, and this fact has to be taken into account when estimating the energy of the primary gamma-ray. This is specially the case for gamma-ray energies above $\sim 2\,\mathrm{TeV}$.

Time RMS: It is the root mean square of the arrival times of all pixels that survived the image cleaning, and measures the time spread of the arrival times irrespective of the pixel position in the camera.

Source dependent parameters: These parameters are defined with respect to a reference point of the camera, which is usually the projection of the source position in the sky.

Dist: Angular distance between the center of gravity of the shower image and the expected source position in the camera. It is the best estimator of the impact parameter of the air shower, and its use improves the accuracy of the energy estimation.

Alpha: Is the angle between the major axis of the image and the line connecting the center of gravity of the image and the center of the camera. In the case of gamma-ray showers, its resulting images point to the source position in the camera, having the images a small *Alpha* value. On the other hand, hadronic showers are isotropically distributed and its alpha distribution tends to be flat. Because of this significant difference on the *Alpha* distributions of gamma-like and hadron-like events, it is the most powerful discrimination parameter.

Time Gradient: This parameter measures how fast the arrival time changes along the image major axis. The arrival time versus the space coordinate along the major axis is fitted to a linear function $t = q + m \cdot x$. The slope m is called the *Time Gradient* of the image. The sign of this parameter is defined as positive if the arrival time increases when moving away from the location of the source in the camera, and negative otherwise. Therefore, the position of the source must be assumed to calculate this parameter.

Time gradient and *Time RMS* parameters use the timing information of the shower image, and are introduced to exploit the timing characteristics of the showers in the

analysis stage. The use of these parameters is the gamma/hadron separation has been proven to reduce the background level by a factor of two, enhancing the flux sensitivity to point-like sources by a factor 1.4 (Aliu et al., 2009*b*).

The distributions of some of the above parameters for unselected events (hadronic) and Monte Carlo simulated gamma-ray showers are shown in Figure 6.6. While for images with large *Size* values, the differences between parameter distributions of gamma-rays and hadrons are evident, these differences fade for images with $Size \lesssim 200\,\mathrm{phe}$.[3] *Alpha* is also shown as the most discriminating parameter, and it is the only one that still has some rejection power for images with $Size < 150\,\mathrm{phe}$.

6.8 Background rejection

In ground-based gamma-ray experiments, the ratio of recorded gamma to hadron-induced showers is of the order of 10^{-3}–10^{-4} even for the strongest gamma-ray sources. To reject most of the hadronic background events without filtering gamma-candidates, a multi-tree classification method called *Random Forest* (RF) method (Albert et al., 2008*b*) is used.

The *Random Forest* method is based on a collection of decision trees, built up with some elements of random choices. The method is constructed on the basis of training samples suitable for the application. The used training samples are Monte Carlo simulated gamma events (gamma sample) and unfiltered data events (hadron sample). In the ideal case, *off* data containing no gamma-showers would be used as hadron sample. But in most analysis, a subsample of the *on* data is usually taken. As said before, even for sources as bright as the Crab Nebula the number of gamma-ray showers in the data is less than 1%, and this contamination does not affect the results.

Each event is characterized by a vector which has the image parameters described in Section 6.7 as components. Those parameters which have proven discrimination power between gamma and hadron-induced images are used as input parameters for the RF method. From the training samples, a binary decision tree can be constructed, subdividing the parameter space first in two parts depending on one of the parameters, and subsequently repeating the process again and again for each part.

The RF classification process can be briefly described taking a completely grown tree as starting point (see Figure 6.7). The task is to classify an event characterized by a vector v in the image parameter space. v is fed into the decision tree. At the first (highest level) node there is a split in a certain image parameter (e.g. 'length'). Depending on the component (image parameter) 'length' in v, the event v proceeds to the left node ($v_{length} <$ lengthcut) or to the right node ($v_{length} \geq$ lengthcut) at the next lower level. This node again splits in some other (or by chance the same) component, and the process continues. The result is that v follows a track through the treecut determined by the numerical values of its components, and the tree nodes' cut values, until it will end up in a terminal node. This terminal node assigns a class label l to v, which can now be denoted as $l_i(v)$, where i is the tree number.

The vector v will be classified by all trees. Due to the randomization involved, different trees will often give different results. As a final result, a mean classification is calculated:

$$h(v) = \frac{\sum_{i=1}^{n_{trees}} l_i(v)}{n_{trees}} \tag{6.4}$$

[3] $\log_{10}(Size\,[\mathrm{phe}]) \lesssim 2.3$

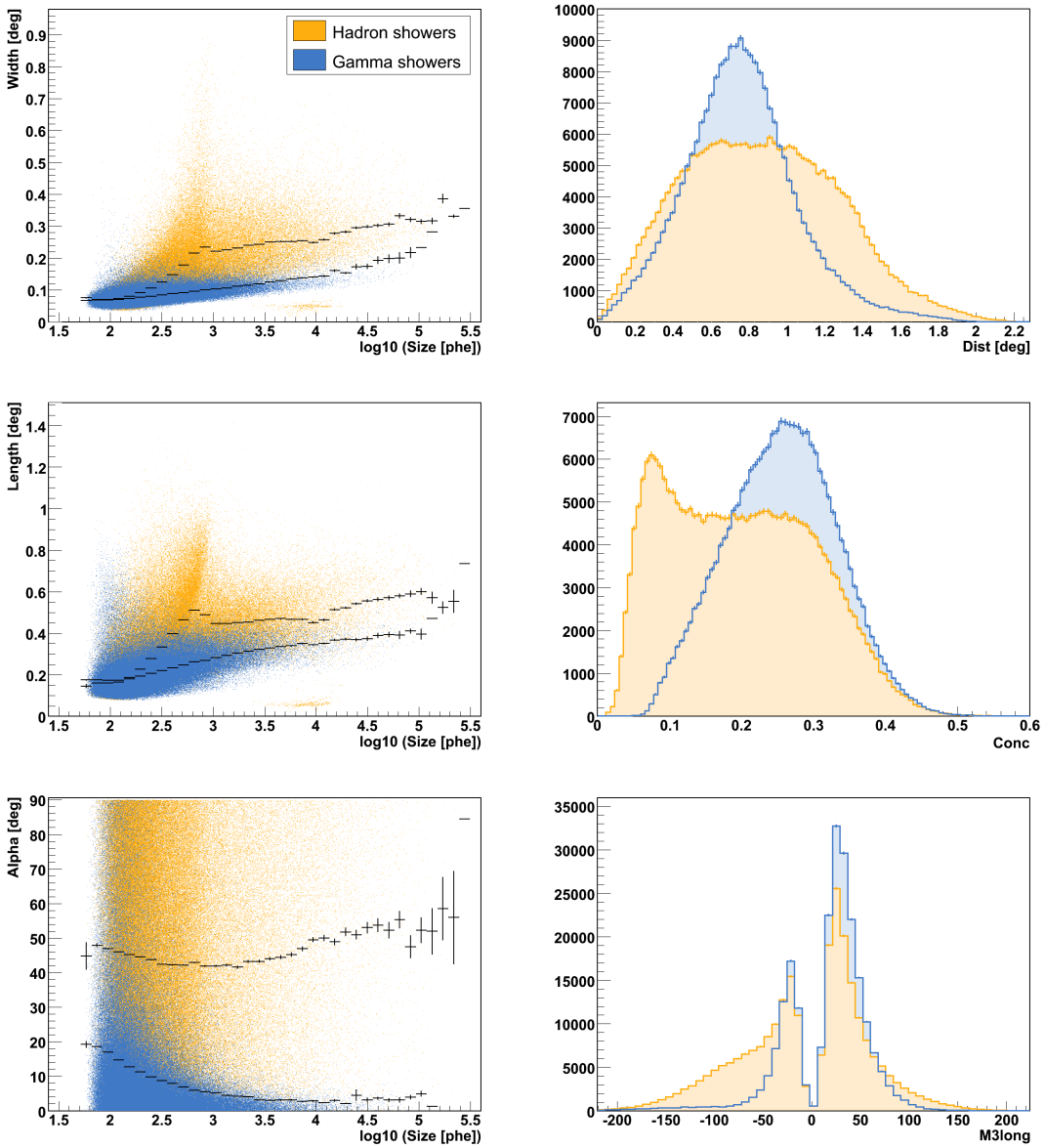

Figure 6.6: Distributions of different image parameters for MC simulated gammas and unselected data events (mostly hadronic showers). *Width*, *Length* and *Alpha* are shown as a function of the image *Size*. Black crosses show the position of the mean value of the parameter in each *Size* bin.

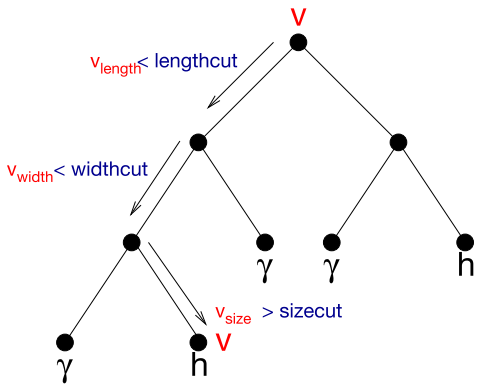

Figure 6.7: Sketch of a tree structure for the classification of an event v with components v_{length}, v_{width}, and v_{size}. The decision path through the tree, leading to classification of the event as hadron can be followed.

This mean classification is called *Hadronness*, and is the main rejection parameter used for the gamma/hadron separation in the analysis.

There are two kinds of parameters that are used to train the *Hadronness* parameter in standard MAGIC data analysis. First, parameters which have power to discriminate between hadrons and gammas are input into the RF. The standard parameters of this kind are *Width*, *Length*, *Conc*, *Dist*, *M3Long*, *Time RMS* and *Time Gradient*. The discriminating power of each of the used RF input parameters is shown in Figure 6.8.

In addition, two more parameters are generally used as input for the RF: *Size* and *Zenith Distance*[4] (ZD). In Figure 6.6 it is shown that the separation power of some parameters strongly depends on the *Size* on the shower images. If *Size* is included as a parameter in the *Hadronness* calculation, the resulting background rejection cuts will scale dynamically with the *Size* of the image. The same happens with the *Zenith Distance*, because due to geometrical and atmospheric absorption effects, similar showers will leave different images on the telescope camera if the pointing angle is different. To use these parameters just for scaling, and not make them directly contribute to the gamma/hadron separation, the *Size* and *Zenith Distance* distributions of the gamma and hadron samples must be adjusted to be equal.

Figure 6.9 shows the distributions of *Hadronness* versus *Size* for a gamma and hadron test samples. *Hadronness* assigns to each event a number betweeen 0 and 1, which identifies the event as being more gamma-like (close to 0) or hadron-like (close to 1). It is shown that gammas and hadrons are well distinguishable with respect to the *Hadronness* parameter for images with $Size \gtrsim 300\,\text{phe}$.[5] Below that limit, the separation of the *Hadronness* distributions is less clear. This is because the differences between gammas and hadrons in image parameter distributions vanish for low *Size* events (see Figure 6.6).

6.9 Signal search

After applying a cut in the *Hadronness* parameter, or any other cut in a parameter or combination of parameters to select gamma-like images, a search for a possible gamma-ray

[4] Angle with respect the celestial zenith at which the telescope is pointing at any given moment
[5] $\log_{10}(Size\,[\text{phe}]) \lesssim 2.5$

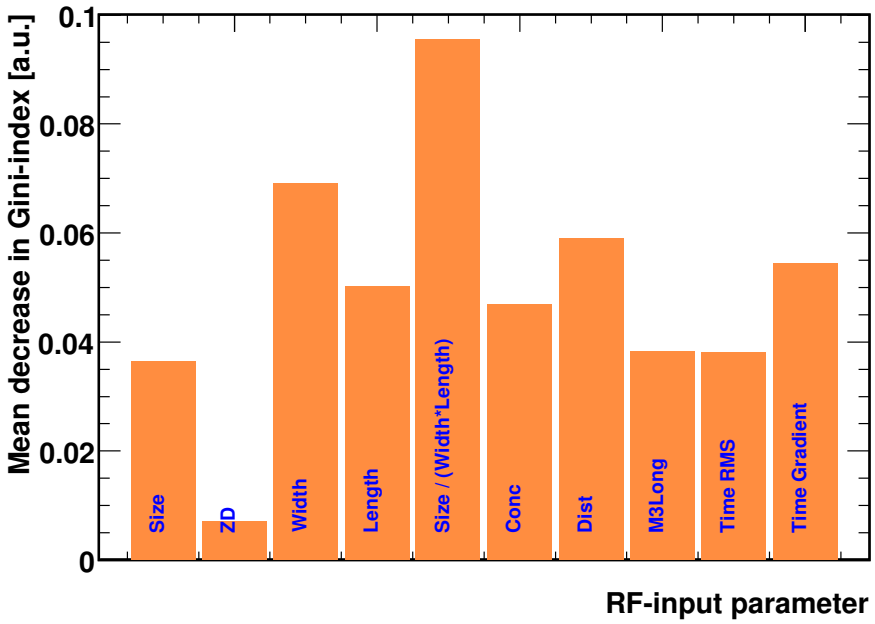

Figure 6.8: Relative importance of the RF input parameters characterized by the mean decrease in Gini index (Albert et al., 2008*b*).

signal is carried out in a certain parameter space called signal region, where gamma-ray events are expected to cluster.[6] The number of events in the signal region is called N_{on}. Many of the gamma-ray candidates that survived the background rejection cuts, however, are still hadronic events. In order to estimate their amount, independent *off* samples are used. Applying the same gamma/hadron separation cuts as in the *on* data, the number of background events in the signal region for the *off* data sample is called N_{off}. The number of gamma-ray showers N_{ex} is given by the the excess of *on* events over the scaled background:

$$N_{ex} = N_{on} - \alpha \cdot N_{off} \tag{6.5}$$

where α is the normalization factor between the *on* and the *off* samples. To test the statistical significance of the gamma-ray excess, the hypothesis that all the observed excess events are compatible with background fluctuations ($N_{ex} = 0$) is tested using equation (17) in Li and Ma (1983):

$$S = \sqrt{2}\left(N_{on} \cdot \ln\left[\frac{1+\alpha}{\alpha}\left(\frac{N_{on}}{N_{on}-N_{off}}\right)\right] + N_{off} \cdot \ln\left[(1+\alpha)\left(\frac{N_{off}}{N_{on}-N_{off}}\right)\right]\right)^{1/2} \tag{6.6}$$

6.9.1 *Alpha* analysis

The standard way of searching for a gamma-ray signal in MAGIC data analysis is the *Alpha* analysis, which is used all through this thesis. The method consists on making

[6] The signal region is usually defined by a cut in the *Alpha* parameter, as explained in the next subsection

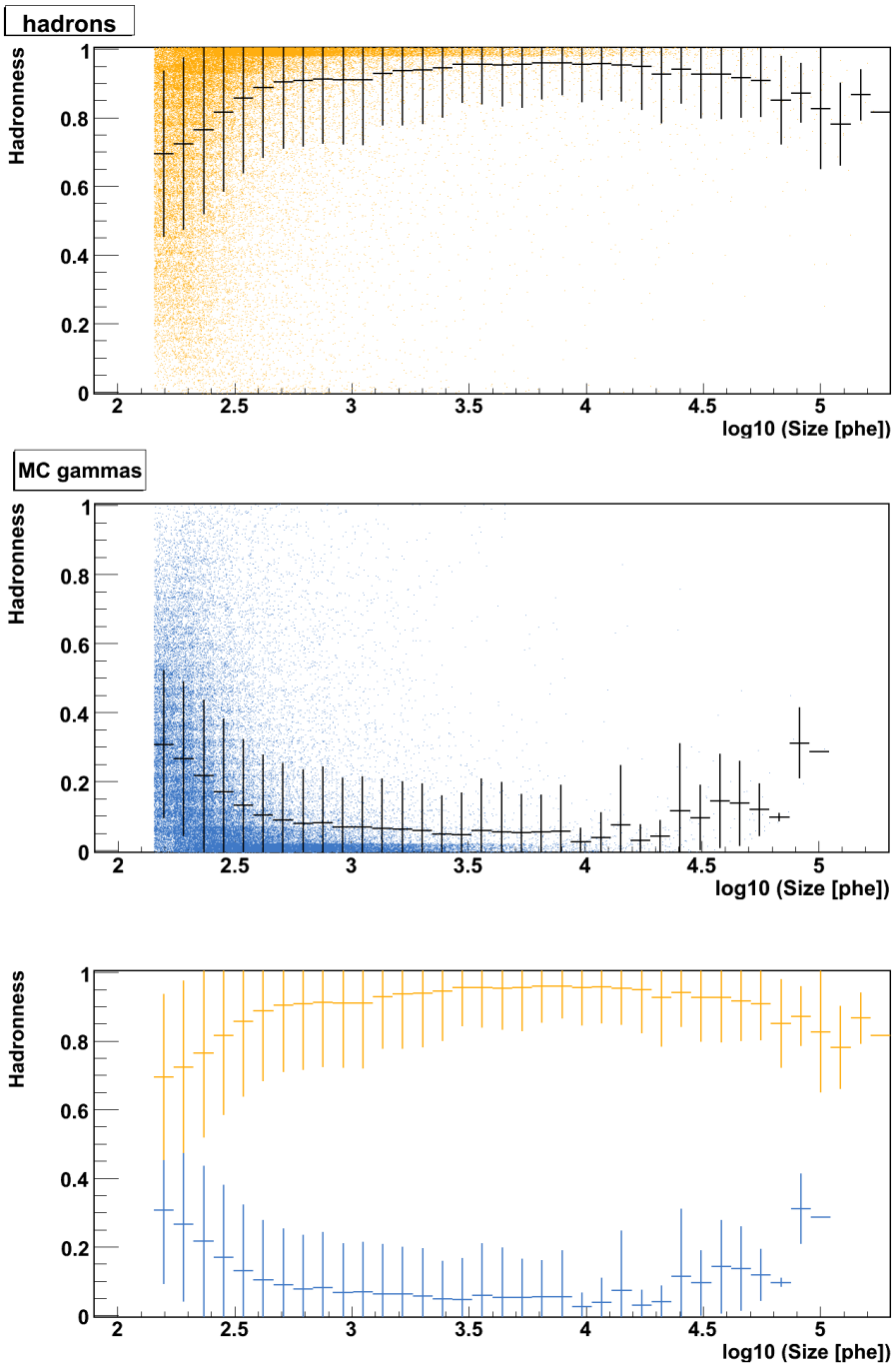

Figure 6.9: *Hadronness* distributions of hadron (upper panel) and gamma-like images (middle panel)as a function of *Size*. The black lines show the average *Hadronness* value for each *Size* bin and the error represents its RMS. These average profiles are compared in the lower panel.

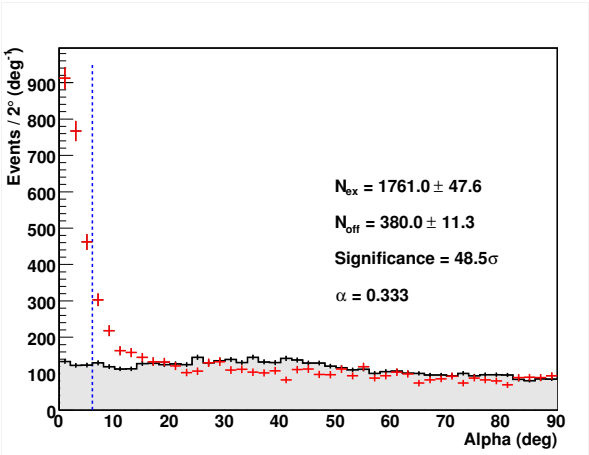

Figure 6.10: *Alpha* distributions for the *on* events (red crosses) and *off* events (grey filled histogram), for the Crab Nebula test data sample.

distributions of the *Alpha* parameter for the *on* and *off* events that survive the gamma/hadron separation cuts. It relies on the fact that remaining gamma images will have an *Alpha* distribution peaking at 0°, while background events will show an approximately flat distribution. This is shown in Figure 6.10.

For *wobble* mode observations, the *on* region is defined around the source position in the camera, while the *off* region is centered at a position opposite to the source with respect to the camera center. The standard MAGIC analysis uses also two additional *off* regions corresponding to the source position rotated by ±90° with respect to the camera center. This geometrical distribution of the *on* and *off* regions in the camera is shown in Figure 6.1(b).

To calculate the significance of the signal, the signal region is defined by a cut in the *Alpha* parameter. Then, N_{on} and N_{off} are defined as the number of events in the signal region for the *on* and *off* distributions. The normalization between the *on* and *off* distributions (α) is defined by the number of *off* regions defined in the camera, being in most of the cases $\alpha = 1/3$. Then, the significance of the signal is calculated using Equation 6.6.

6.9.2 Selection and optimization of the cuts

In order to maximize the significance of the signal excess, optimal values of cuts in *Alpha* and *Hadronness* are found using an independent data sample of a known gamma-ray source with similar characteristics to the one that is being studied. In most of the cases, the reference data sample is taken from Crab Nebula observations.

Usually, a scan in the *Alpha* and *Hadronness* cuts is performed on the reference data sample, and the pair of values yielding the highest significance are then applied to extract the signal level on the main sample. To get optimal values for these cuts, it is important that the reference and the main data samples are taken from the same epoch, to ensure that the telescope performance was the same. In addition, the *Zenith Distance* range of the observations must also be similar. Finally, the expected spectrum of the analyzed source has to be comparable to the reference source, as different flux level and spectral indices have a non-negligible effect in the choice of the optimal *Alpha* and *Hadronness*

cuts. In particular, if the source is expected to have a much lower flux level than the reference source, the search for the optimal cuts is done by scaling down the number of excess events to values close to the expected flux level.

In addition to the *Alpha* and *Hadronness* cuts, a minimum cut in the *Size* parameter is applied all through the analysis chain. As discussed in Section 6.8, the gamma/hadron separation performs well for events with $Size \gtrsim 300\,\text{phe}$. The use of the *Time Gradient* parameter in the *Random Forest* makes background rejection work reasonably well down to $Size \approx 150\,\text{phe}$. As gamma/hadron separation degrades significantly below these values, a lower *Size* cut of 150 phe is applied to the data.

This *Size* cut removes small images from the analysis, and not only improves the significance of the signal but also reduces the effect of camera inhomogenities. The inhomogeneities appear because of malfunctioning pixels and trigger inefficiencies in the telescope camera, which make the camera response to be non-uniform. The inhomogeneities affect specially low *Size* events, as small images are more sensitive to small camera defects, as for instance a single pixel with no signal. For images with $Size > 150\,\text{phe}$, the effect of inhomogenities in the camera response is much smaller, as shown in Figure 6.11.

6.9.3 Sensitivity

The *Alpha* plot obtained for the Crab test sample after background rejection is shown in Figure 6.10. The significance obtained using Equation 6.6 is 48.5σ. In the plot it can be seen a small mismatch between the *on* and *off* event distributions in the range of $20^\circ \lesssim Alpha \lesssim 50^\circ$. This mismatch is caused by the fact that, specially for strong gamma-ray sources, a significant number of signal events can contaminate the *off* distribution, showing up as an small and very broad excess, peaking at angles of $\sim$ 30–40°. The contamination is reduced if just 1 *wobble* position is used to estimate the background.

Apart from the significance of the signal computed in Equation 6.6, the analysis can also be quantified in terms of its sensitivity. The sensitivity of ground-based gamma-ray telescopes is usually quoted as the gamma-ray flux that will be detected with a significance of 5σ after 50 hr of observation. It is, however, not common to use Equation 6.6 to compute the sensitivity but instead a Gaussian approximation of it. The resulting number os standard deviations for a given observation time t is then:

$$S(t) = \frac{N_{ex}}{\sqrt{N_{off}}} \cdot \sqrt{\frac{t}{T}} \tag{6.7}$$

where T is the time in which N_{ex} and N_{off} were measured. In the particular case of the analysis presented here, the observation time is $T = 5.14\,\text{hr}$, resulting in a significance $S(t) = \frac{1761}{\sqrt{380}} \cdot \sqrt{t[\text{h}]/5.14} = 39.8\,\sigma\sqrt{t[\text{h}]}$. In 50 hr of observation, an excess with a significance $S(t) = 39.8\,\sigma\sqrt{50} = 281.8\sigma$ would be measured for a source like the Crab Nebula. Equivalently, in 50 hr of observation a source with a flux level of $5\sigma/281.8\sigma = 1.8\%$ of the Crab Nebula flux would be detected at a 5σ level, in agreement with the sensitivity quoted in Aliu et al. (2009*b*) for a similar analysis in the optimal energy range.

6.10 Gamma-ray sky map

Sky maps are calculated by reconstructing the arrival directions of the gamma-like showers in camera coordinates and projecting them into celestial coordinates. As in the calculation

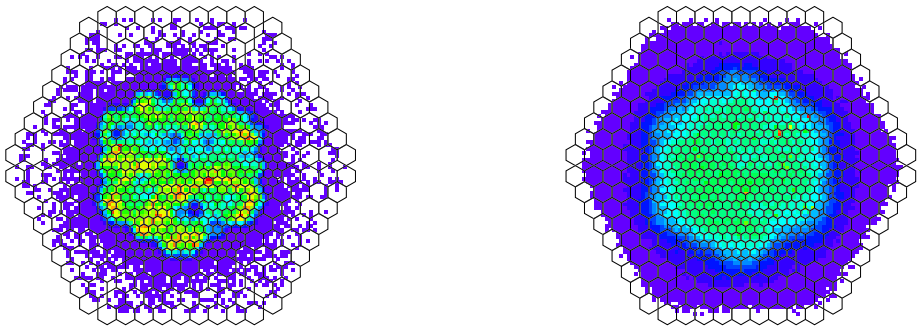

(a) *Size* < 150 phe (b) *Size* > 150 phe

Figure 6.11: Center of gravity distribution of MC simulated gamma-ray showers superimposed on the MAGIC camera layout. It is shown that showers with small *Size* are more sensitive to camera inhomogeneities, mainly caused by malfunctioning pixels and trigger inefficiencies while larger *Size* images show a uniform distribution along the trigger region.

of the significance of the signal, its presence is calculated by subtracting two histograms –one for the *on* and one for the *off* data. In this case, the histograms will be two-dimensional, as they represent the distribution of events in sky coordinates.

The arrival direction of the gamma-ray images is estimated using the *Disp* method (Lessard et al., 2001; Domingo-Santamaria et al., 2005). The method assumes that the arrival direction of the primary particle lies on the major axis of the shower. This approximation is plausible because the major axis is a projection of the shower axis into the camera plane, and, therefore, the major axis coincides in a good approximation with the trajectory of the incident primary particle.

The *Disp* parameter is defined as the angular distance between the reconstructed source position in the camera –assumed to be along the shower axis– and the center of gravity of the shower image. The larger *Disp* is, the more elongated is the projected image of the shower in the camera. The parameterization used to calculate *Disp* is optimized using a MC gamma-ray sample, and is a function of the image parameters (see Section 6.7) except *Conc* and *Dist*.

There is an important degeneracy in the *Disp* method. There are two solutions for a source location once *Disp* is calculated: one in the *head* of the image and another in the *tail*. The *M3long* parameter is used to judge which of these solutions is the correct one, placing the source position always closer to the *head* of the image.

A correct estimation of the background is the major difficulty when trying to produce a sky map of a certain region. The reason for that is that the camera acceptance for gamma-rays is not homogeneous, and there are changes due to different star fields, zenith angles, bad pixels in the camera, trigger inefficiencies, etc. This problem is simplified in *wobble* observations, where the background estimation can be done from the same data set.

The background estimation is done as follows. First, the camera is divided into two halves. The dividing line is chosen so that the source lies in one of the camera halves in the first *wobble* position, and in the other half in the second *wobble* pointing. Then, the

arrival direction in camera coordinates of each event is reconstructed. The events whose arrival direction is reconstructed in the half of the camera that does not contain the source position will be used to estimate the background. After this step, two histograms containing the distribution of arrival directions in each camera half are constructed. These two histograms are later merged into one, taking into account the proper normalization factor between them. These normalization is usually very close to 1, since there is usually the same amount of time spent in each *wobble* position during observations.

To produce the background acceptance in sky coordinates, a second histogram is produced based on the previous one. For every gamma-ray candidate, 30 random background events are projected into sky coordinates. This process is done by projecting the arrival direction of the gamma-ray candidate using the arrival time of a randomly selected event from the camera acceptance histogram. The resulting histogram, in sky coordinates, represents the projection of the camera acceptance into the sky, also taking into account the asymmetry introduced by the fact that the observations are done in *wobble* mode.

Finally, the distribution of background events is subtracted to that of the gamma-ray candidates, obtaining a map of excess events. This excess map is then smoothed using a gaussian point spread function (PSF) with $\sigma = 0.1^\circ$, corresponding to the gamma-ray PSF of the telescope. The smoothing polishes the sky map, averaging over the fluctuations and leaving over (or even highlighting) regions which are above the fluctuation level of the map. This might be specially important for weak gamma-ray sources. The resulting sky map is shown in Figure 6.12.

6.10.1 Pointing correction

Possible mispointings of the telescope are taken care by a pointing correction using information from the starguider camera (see Section 5.3.1). The starguider camera provides information of the location of bright stars near the MAGIC field of view. This stars are identified using predefined catalogs. As the starguider camera also sees part of the MAGIC camera (see Figure 5.11), it can interpolate the position of the MAGIC camera center and project it into the sky. This projection is done using a model that describes the bending of the telescope structure as a function of the pointing position, and it is calibrated by pointing to bright stars when the telescope is not taking data.

The deviation between the projected position of the camera center estimated using the starguider and the nominal pointing position of the telescope is corrected offline in the data. As can be seen in Figure 6.12, the starguider correction reduces the difference between the reconstructed source position from the gamma-ray sky map and the catalog position for a known point-like gamma-ray source as the Crab Nebula.

6.11 Differential energy spectrum

The calculation of the differential energy spectrum involves three main steps: the estimation of the energy of the incident gamma-ray for each event, the calculation of the effective collection areas and effective observation times that allow a conversion from number of excess events into flux units, and the correction of the energy estimation biases by unfolding the obtained spectrum.

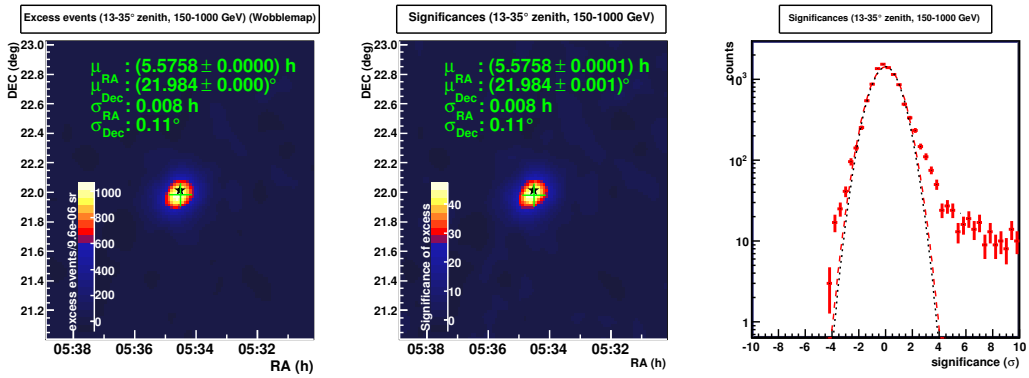

(a) Sky map before applying starguider pointing correction

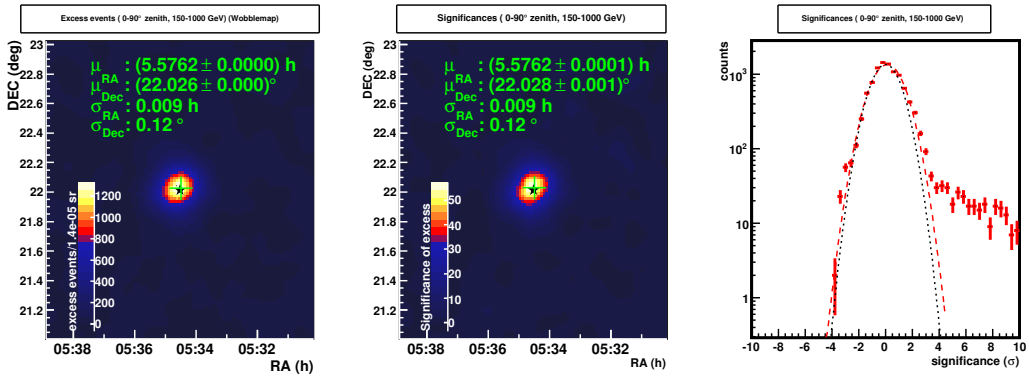

(b) Sky map after starguider pointing correction

Figure 6.12: Maps of excess events and significance, together with the significance distribution, for the Crab Nebula test data sample. The mean and sigma of a 2-dimensional gaussian fitted to the excess and the significance map are also displayed. A black star indicates the catalog position of the Crab Nebula, while the light green cross shows the mean value of the fitted excess position.

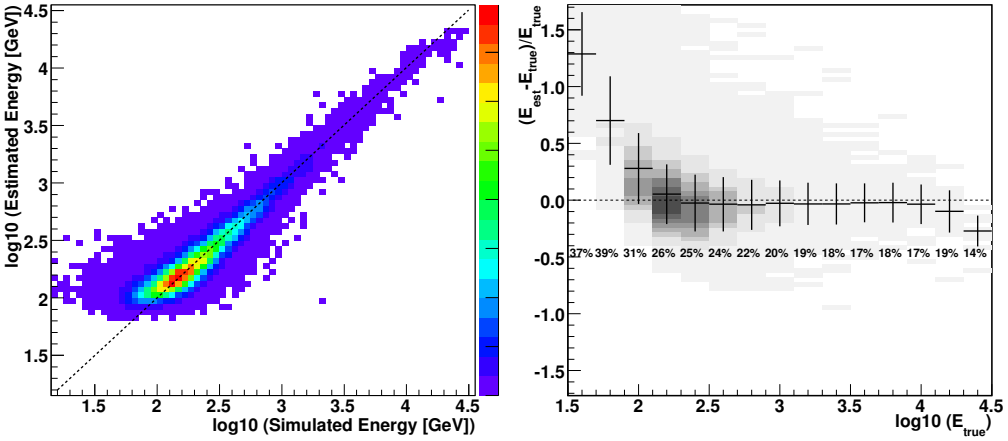

Figure 6.13: Migration matrix between estimated and simulated energy (left panel). A perfect correlation is shown by a dashed line. (Right panel) Resolution of the energy reconstruction. Numbers indicate the energy resolution for each bin of simulated energy.

6.11.1 Energy reconstruction

The energy of the gamma-ray events is also reconstructed by means of the *Random Forest* method, with training MC gamma-ray samples, as it can also be used to construct an algorithm for estimating a continuous quantity. A MC simulated gamma-ray set with known simulated energy of primary gamma-ray is filled in fine bins of a logarithmic energy. For each of those bins, respectively, a classifier is trained to discern events that belong into that particular energy bin. The actual migration matrix from the MC simulated energy to the estimated energy is shown in Figure 6.13.

The energy resolution is approximately 25% between 100 GeV and 1 TeV, being close to 20% for higher energies and increasing above 30% below 100 GeV. The energy estimation tends to overestimate the energy of the primary gamma-ray at low energies (below 100 GeV) and underestimate it at high energies (above 10 TeV). In the rest of the energy range the correlation between true and estimated energy is approximately linear. The biases introduced by the energy estimation are later corrected by the spectrum unfolding.

6.11.2 Spectrum calculation

The differential gamma-ray energy spectrum is defined as:

$$\frac{\mathrm{d}F(E)}{\mathrm{d}E} = \frac{N_\gamma}{\mathrm{d}E\,\mathrm{d}A_{\mathrm{eff}}\,\mathrm{d}t_{\mathrm{eff}}} \tag{6.8}$$

The effective collection area A_{eff} is the area in which air showers can be observed by the gamma-ray telescope, folded by the detection efficiency after all cuts. The detection efficiency is the ratio between the number of gamma-ray showers surviving all the filter cuts and the total number of simulated showers.

To derive the energy spectrum, the gamma/hadron separation cuts applied to the data are looser than for the signal extraction (see Table 6.1). In this case, the used cuts are dynamic, which means that the actual cuts on the *Hadronness* and *Alpha* parameters are calculated for each bin in energy of the spectrum, so that their efficiency of the cuts

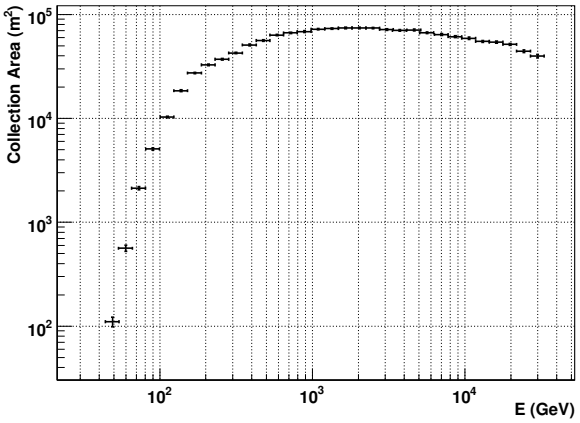

Figure 6.14: Collection area after all cuts as a function of the gamma-ray energy.

is constant. The reason to apply loose cuts is to keep a larger number of excess events and also have a larger collection area.

The calculation is done in the following way: the number of excess events per estimated energy bin is calculated, and divided by the collection area and the effective time calculated for that bin. The collection area as a function of the estimated energy is shown in Figure 6.14. The errors on the spectrum include the error on the number of excess events and collection area.

6.11.3 Unfolding of the spectrum

The unfolding methods used in MAGIC data analysis are described in Albert et al. (2007*c*). This procedure tries to correct the energy spectrum for the biases introduced by the energy estimation. This biases are due to the fact that the true energy of the incoming gamma-rays is not measured but indirectly estimated. The distortion due to biases and finite resolution can be written in the following form:

$$Y(y) = \int M(x, y)\, S(x)\, \mathrm{d}x \tag{6.9}$$

Cuts	**Bkg. suppr. (γ-acceptance)**	**Signal region (γ-acceptance)**	**Combined acceptance**	**Energy threshold**
loose	dynamic (60%)	dynamic (70%)	42%	140 GeV
tight	$h < 0.04$ (36%)	$\alpha < 6°$ (89%)	32%	160 GeV

Table 6.1: Sets of cuts used to estimate the significance of the gamma-ray signal. *Tight* cuts are used to calculate the significance of the gamma-ray signal, while *loose* cuts are used in the calculation of the differential energy spectrum and the lightcurve. Indicated in the table are the cut in the *Hadronness* (h) parameter used to reject background events and the *Alpha* (α) cut that defines the signal region. The gamma-ray acceptance is estimated using MC generated gamma-ray events, and indicate the fraction of gamma-ray showers that survive the background rejection cut, the fraction surviving the *Alpha* cut after the background rejection has been applied, and the total efficiency after both cuts (Comb. eff.). The energy threshold is also shown.

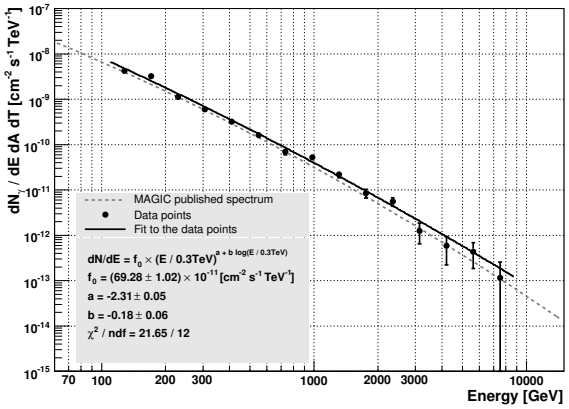

Figure 6.15: Energy spectrum of the Crab Nebula. The MAGIC spectrum published in Albert et al. (2008*f*) is shown as a reference.

where y is the estimated energy, x is the true energy, M describes the response of the detector, Y is the measured distribution and S the true distribution. The aim of the procedure is to determine S knowing Y and M. In the case of the MAGIC analysis, M is the energy migration matrix shown in Figure 6.13, and Y is the spectrum obtained as described above.

Conceptually, the simplest solution is to invert the migration matrix, although it is not convenient due to the large correlations between adjacent bins. In addition, this apparently straightforward solution can not be easily implemented as the migration matrix M is usually not invertible. The next solution in simplicity is to assume a certain parametrization for the true distribution S. This method is called *forward* unfolding. In the case of a gamma-ray spectrum, a power law can be assumed as a parametrization of the true spectrum. The output of this unfolding methods the best fit to the true energy distribution of events with their errors, but does not provide the actual values of the individual data points. More complex methods, which give as output the actual spectral points with their errors, are described in Albert et al. (2007*c*). The usual procedure is to apply the different unfolding methods available to a particular data sample and compare their results, which are usually compatible.

In Figure 6.15, the spectrum of the Crab Nebula test sample unfolded using the *Tikhonov* (Tikhonov and Arsenin, 1977) method is shown. The resulting spectrum is fitted to a curved power law, and gives a differential flux (TeV^{-1} cm^{-2} s^{-1}) of:

$$\frac{\mathrm{d}N}{\mathrm{d}E\,\mathrm{d}A\,\mathrm{d}t} = (6.93 \pm 0.10) \times 10^{-10} (E/300\,\mathrm{GeV})^{[(-2.31\pm0.05)+(-0.18\pm0.06)\log(E/300\,\mathrm{GeV})]} \tag{6.10}$$

The fit parameters in Equation 6.10 are compatible within errors with those published by the MAGIC collaboration in Albert et al. (2008*f*).

6.12 The gamma-ray light curve

A light curve shows the integral flux of gamma-rays above a certain energy in bins of time. To get a large number of excess events and increase the collection areas, minimizing the

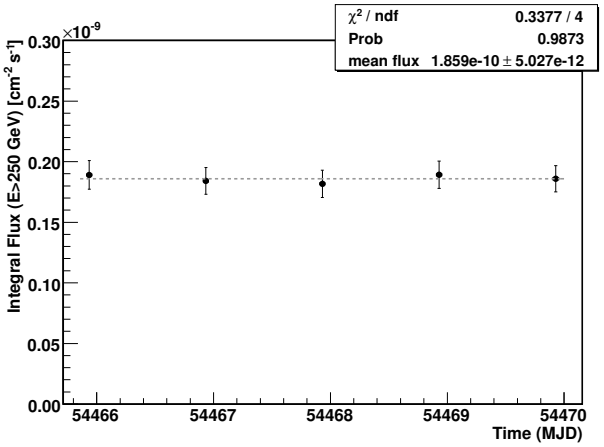

Figure 6.16: Night-by-night light curve of the Crab Nebula. The dashed line indicates the average flux measured during the 5 selected nights.

effect of systematic errors, the same loose cuts used in the energy spectrum calculation are used to calculate the gamma-ray lightcurve (see Table 6.1).

The Crab Nebula light curve is shown in Figure 6.16. A fit by a constant yields an average integral flux above 250 GeV of:

$$F(E > 250\,\mathrm{GeV}) = (1.86 \pm 0.50) \times 10^{-10}\,\mathrm{cm}^{-2}\,\mathrm{s}^{-1} \tag{6.11}$$

which is compatible with previous gamma-ray measurements of the Crab Nebula in the VHE band.

6.13 Study of systematic uncertainties

In addition to statistical errors, the reconstructed gamma-ray flux is also affected by systematic uncertainties. The systematic effects influence both the energy reconstruction and flux calculation. In this section, the main sources of systematic effects are described. Discussion of the systematic errors of the MAGIC telescope is also found in (Albert et al., 2008*f*). The main sources for errors in the energy reconstruction are:

Atmospheric conditions: The MC simulation does not take into account the climate conditions. The production rate of Cherenkov light in the atmosphere can vary because of density fluctuations on seasonal basis. In addition, the atmospheric transmittance (e.g., Mie scattering) also changes depending on the weather conditions (e.g., dust, moisture and clouds) in timescales as short as some minutes. Data affected by bad atmospheric transmission is usually rejected from the analysis. Even after bad quality data rejection, the effect of atmospheric transmission can affect the reconstructed gamma-ray energy by about 15% (Bernlöhr, 2000).

Light losses in the telescope optical system: The telescope optical system consists of mirrors, the camera entrance window and the Winston cone light guide. Degradation of their reflectivities may cause additional losses of the Cherenkov light. The overall light loss in the optical system is adjusted in the MC simulations to the

results of dedicated measurements. However, there might be errors in the simulated light distribution on the camera (e.g. the size of the PSF and halos of the focused spot on the camera) and errors in improper simulations of the light guides. The systematic errors on the energy reconstruction may be 10%.

PMT performance: This contribution to the systematic errors comes from calibration uncertainties in the quantum efficiency measurements of the PMTs, degradation of the coating enhancing the UV sensitivity, uncertainties in the photoelectron collection efficiency of the PMTs, and the error of the F-factors used to calibrate the recorded signal. In total, the systematic errors of PMT performances is approximately 10–12%.

The overall systematic uncertainty in the energy scale is estimated to be 16%. The energy is likely underestimated as most of the effects result in a loss of Cherenkov photons.

The second type of systematic errors are uncertainties of flux calculation caused by the determination of effective collection area.

Camera acceptance: In the MC simulations a camera with homogeneous acceptance is simulated. Malfunctioning PMTs and trigger inefficiencies may introduce a systematic error of 5% of the flux level, which might be even larger at low energies due to the larger effect of camera inhomogeneities.

Estimation of efficiencies for gamma-ray events: The trigger efficiency and the cut efficiency in the analysis chain for gamma-ray events are estimated using MC simulated gamma-ray samples. Differences between the real and simulated images of gamma-ray showers may introduce systematic errors. Overall uncertainty can be estimated by applying different cut values in e.g., *Size* and *Hadronness* during the analysis. The overall efficiency is estimated to be uncertain by about 10%. In addition, different analysis parameters may introduce systematic errors.

Those effects introduce a systematic uncertainty in the flux scale by 11%. This uncertainty may increase up to 30% for the lower energies ($E < 150\,\mathrm{GeV}$). Finally, there are also effects which result in a distortion of the energy scale. They are caused by non-linearities in the PMT gain, the amplifiers, the optical transmission (transmitter/receiver) and the FADCs. The estimate of the systematic error on the spectral slope is rather difficult. In case of a power law spectrum the systematic error has been estimated to be ± 0.2 in the spectral slope (Albert et al., 2008*f*).

Chapter 7

Upper limits on the VHE emission of selected distant blazars

This chapter describes the results of the observations of the five selected distant blazars that were presented in Chapter 4. No positive detection was found in four of the observed blazars, and the resulted upper limits are presented in this chapter. The detection of a VHE gamma-ray source in the field of view of the blazar 3C 66A is reported in Chapter 9.

7.1 Motivation of the observations

The selection criteria used to select distant blazars to be observed with the MAGIC telescope are described in Section 4.2. The main motivation of these observations was to look for moderately distant blazars with high synchrotron luminosity, and with the syncrhotron peak located at high frequencies. In synchrotron self-Compton models of blazar emission, which successfully describe the spectral energy distribution of most of the TeV detected blazars, the synchrotron and the inverse Compton components of the emission are naturally connected.[1] A bright synchrotron component peaking at high frequencies (UV or soft X-rays) would result in a bright inverse Compton component, also peaking at high frequencies (gamma-ray band). These two facts would maximize the chances of a detection in the MAGIC energy range.

The five selected candidates are shown in Table 7.1, and were selected from one or more of the following catalogs, based on observations in the radio, optical or X-ray band:

- Costamante (2007) studies the correlation between hard blazar spectra in the VHE band and a low density of the EBL, suggesting bright distant blazars that could be observed to further test EBL absorption.

- Giommi et al. (2002) present the SED of 84 blazars observed with the X-ray satellite BeppoSAX during its first five years of operation. From this catalog, the objects with high predicted GeV flux were selected.

- Donato et al. (2001) consider 268 blazars observed in the X-ray band for which the slope of the X-ray spectrum is available. The bright blazars at high X-ray frequencies from this catalog were considered.

[1] see Section 3.3.1 for details

- Nieppola et al. (2006) studied the SED of more than 300 BL Lacs and fitted the synchrotron component with a parabolic function to determine the synchrotron peak frequency. 22 of the studied blazars were classified as ultra-high energy peaking BL Lacs, as their synchrotron peak frequency was estimated to be at $\nu_s > 10^{19}$ Hz, and were considered as candidate VHE emitters.

The selected objects from the described catalogs had also to fulfill the following criteria:

- The source has a redshift of $0.2 < z < 0.5$.
- The expected VHE gamma-ray flux of the source is above MAGIC sensitivity for 30 hr of observation, being the VHE gamma-ray flux estimated by using a simple one-zone synchrotron self-Compton model (Krawczynski et al., 2004) and available archival data at radio, infrared, optical, ultraviolet and X-ray frequencies, as it is detailed in Section 4.2.1.
- The source has a declination between $-5°$ and $60°$, to guarantee that the objects can be observed at zenith distances below $35°$, where the MAGIC telescope has a low energy threshold and the best possible sensitivity.

This search for distant candidates for VHE gamma-ray emission was motivated by previous findings of blazars at redshift $z \sim 0.2$ with relatively hard measured spectra (Aharonian et al., 2006*b*; Albert et al., 2006*a*; Aharonian et al., 2007). The interpretation that followed these detections was that the density level of the extragalactic background light is lower than expected. Therefore, gamma-rays could propagate from sources at $z = 0.2$–0.5 with moderate absorption, making detections at 100–500 GeV of such distant objects possible.

After the selection of candidate objects, five blazars were picked up for observations with the MAGIC telescope. The list of observed candidates is detailed in Table 7.1. Previous observations in the VHE gamma-ray band were only reported in the case of 3c 66A and 1ES 1028+511. For 1ES 1028+511, Whipple observations resulted in an upper limit of 28.7% of the Crab Nebula flux at energies $E > 300$ GeV (Horan et al., 2004). The results of previous gamma-ray observations of 3C 66A are detailed Chapter 9. For the other three objects, nu upper limits in the VHE gamma-ray band could be found in the literature.

7.2 Observations and data analysis

An observation time of 30 hr with the MAGIC telescope was granted between Summer 2007 and Spring 2008 for each of the selected candidates. The actual observation time for each object, and the effective exposure time after discarding the runs taken under bad atmospheric conditions are detailed in Table 7.1. Bad runs were rejected based on the event rate after image cleaning. An additional cut removed the events with total charge (*Size*) less than 150 photoelectrons. This quality cut ensures a better background rejection, since including smaller images in the analysis worsens the performance of background suppression methods.

The sources were observed in *wobble* mode, pointing alternately to two different sky directions, each at 24' distance from the catalog position of the target sources. Fixed target observations were programmed for these objects, i.e., the observation time was

Object	Obs. epoch	Total obs. time	Eff. exposure	ZD
1ES 0158+003	Oct–Nov 2007	30.0 hr	24.6 hr	28°–35°
3C 66A	Aug–Dec 2007	54.2 hr	45.3 hr	14°–35°
B3 1009+427	Jan–Mar 2008	27.9 hr	23.3 hr	13°–35°
1ES 1028+511	Dec 2007–Feb 2008	30.0 hr	22.64 hr	21°–35°
2E 1415.6+2557	Mar–Apr 2008	23.4 hr	13.8 hr	6°–29°

Table 7.1: Observations of the selected blazars, ordered by right ascension. Indicated are the epoch when the source was observed, the real and effective observation times and the *Zenith Distance* (ZD) range of the observations.

scheduled just considering the best epoch to observe each source, and not relying on external triggers from monitoring at other wavelengths.

7.3 Search for a VHE gamma-ray signal

A VHE gamma-ray signal was found in the analysis of 3C 66A. The results of this analysis are described and discussed in Chapter 9. The results of the analysis of the other four sources are detailed here.

The data sets were analyzed using the MAGIC standard tools and methods described in Chapter 6. Figure 7.1 shows the *Alpha* distribution of *on* and *off* events for each of the observed sources. No significant gamma-ray excess was found. To search for a VHE gamma-ray signal, background rejection was achieved by a cut in the *Hadronness* parameter, which was optimized using Crab Nebula data taken in similar conditions. The cut in the *Alpha* parameter that defines the signal region was optimized following the same procedure. Both cuts were separately optimized for each source to take the different *Zenith Distance* distributions of the data sets into account. The difference in cut values are small though. The used cuts, together with the gamma-ray efficiency and the resulting energy threshold, calculated on MC gamma-rays assuming a Crab-like spectrum ($\mathrm{d}N/\mathrm{d}E \sim E^{-2.6}$), are summarized in Table 7.2.

To further investigate the possible presence of a positive VHE gamma-ray signal, an sky map of the arrival directions of gamma-like showers was produced for each of the

Object	ZD	Bg. suppr. (γ-acceptance)	Signal region (γ-acceptance)	Comb. eff.	Energy threshold
1ES 0158+003	28°–35°	$h < 0.03$ (33%)	$\alpha < 6°$ (88%)	29%	220 GeV
B3 1009+427	13°–35°	$h < 0.04$ (36%)	$\alpha < 6°$ (89%)	32%	170 GeV
1ES 1028+511	21°–35°	$h < 0.03$ (33%)	$\alpha < 6°$ (88%)	29%	190 GeV
2E 1415.6+2557	6°–29°	$h < 0.04$ (34%)	$\alpha < 6°$ (88%)	30%	160 GeV

Table 7.2: Description of the cuts used in the analysis for each object. Indicated are the *Zenith Distance* (ZD) range of the observations for each object, the cut in the *Hadronness* (h) parameter used to reject background events, the *alpha* (α) cut that defines the signal region, and the individual and combined gamma-ray acceptances of every set of cuts. The gamma-ray acceptance is estimated using MC generated gamma-ray events. The energy threshold of the analysis for each object is also shown.

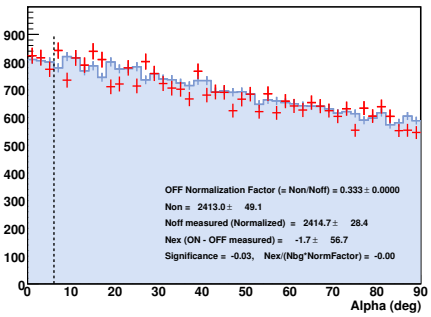

(a) 1ES 0158+003

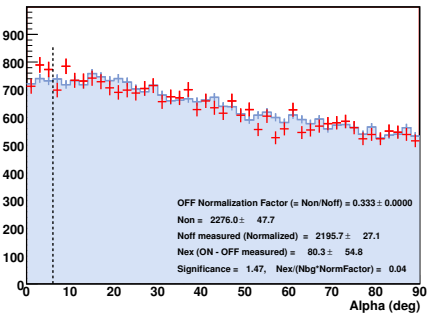

(b) B3 1009+427

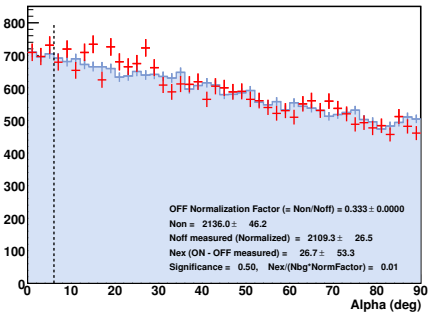

(c) 1ES 1028+511

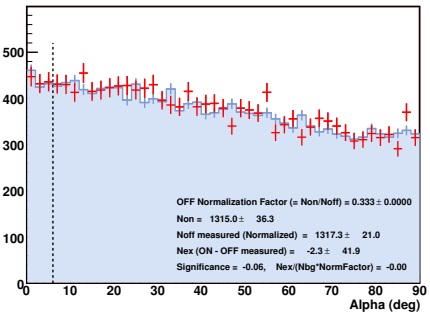

(d) 2E 1415.6+2557

Figure 7.1: *Alpha* plots to estimate the significance of the gamma-ray signal in the observations of the four selected blazars. Shown are *on* (red crosses) and *off* events (blue filled area). The black dashed line indicates the signal region.

Object	N_{ex}	A_{eff} $[\times 10^8 cm^2]$	t_{eff} [hr]	S	u.l. $[cm^{-2}s^{-1}$ (c.u.)]
1ES 0158+003	-58.3 ± 53.4	2.60 ± 0.03	24.57	-1.1σ	8.57×10^{-12} (0.027)
B3 1009+427	85.3 ± 47.6	2.80 ± 0.02	23.31	1.8σ	4.13×10^{-11} (0.128)
1ES 1028+511	18.3 ± 47.9	2.61 ± 0.03	22.64	0.4σ	2.07×10^{-11} (0.064)
2E 1415.6+2557	-28.7 ± 35.4	2.70 ± 0.02	13.77	-0.81σ	1.13×10^{-11} (0.035)

Table 7.3: Summary of the upper limits derived from the observations of the selected blazars with confidence level of 3σ and assuming an spectral index of $\Gamma = 2.6$, and for energies $E > 150$ GeV. Shown are the observed number of excess events (N_{ex}), the effective area (A_{eff}), the effective observation time (t_{eff}), and the obtained significance (S). The upper limits (u.l) are shown in flux units and in crab units (c.u.), i.e., compared to the flux of the Crab Nebula.

observed sources.

7.4 Derivation of upper limits

As no significant VHE gamma-ray excess was found when searching for a positive signal, flux upper limits were derived. To calculate the integral flux upper limits derived from the observations, a lower energy cut has to be specified. For these reason, the *Alpha* plots were calculated again, with an additional cut that removed the events for which the estimated energy was below 150 GeV,. The value of 150 GeV was chosen to ensure that events significantly below the energy threshold of the analysis were not included. The derived *Alpha* plots for $E > 150$ GeV are shown in Figure 7.3.

The obtained significances for each candidate blazar were calculated, and are summarized in Table 7.3. From the number of *on* and *off* events in the signal region, and their associated errors, upper limits on the number of excess events ($N_{ex}^{u.l.}$) were derived with a confidence level of 99.9%, using the method described in Rolke et al. (2005). The flux upper limits ($F^{u.l.}$) were then obtained:

$$F^{u.l.} = \frac{N_{ex}^{u.l.}}{A_{eff} \cdot t_{eff}} \tag{7.1}$$

where A_{eff} is the telescope effective area after all cuts (calculated using MonteCarlo simulated gamma-ray showers), and t_{eff} is the effective observation time. The derived integral upper limits assume a source spectral index of $\Gamma = 2.6$, which is used to generate the MonteCarlo simulated showers used to calculate the effective areas. The resulting upper limits for each of the observed objects are reported in Table 7.3.

All observed objects have reported to be variable at different wavelengths (radio, infrared, optical, ultraviolet and/or X-ray). Because of the observed variability at other wavelengths, and the fact that many of the detected blazars in the VHE gamma-ray band have reported to be variable, a search for possible short periods of detectable gamma-ray activity was carried out.

The search for short flares of VHE gamma-ray emission was done on a nightly time basis, taking into account that, depending on the source schedule of the MAGIC telescope and the observation conditions, typical observation times are between 30 min and 2 hr per night. For each source, a light curve with the integral gamma-ray flux for energies $E > 150$ GeV was obtained (see Figure 7.4), where each point represents one observation

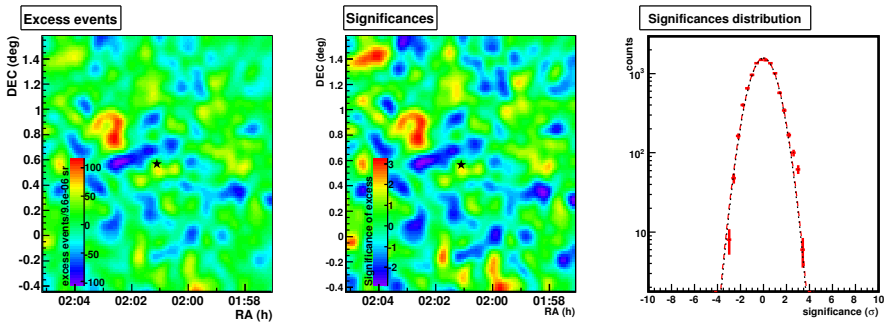

(a) 1ES 0158+003

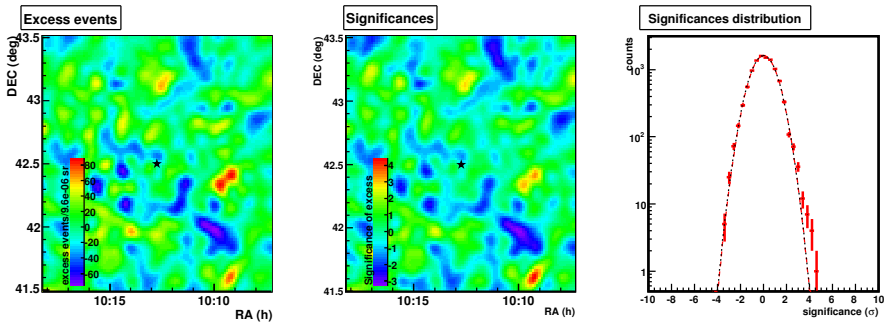

(b) B3 1009+427

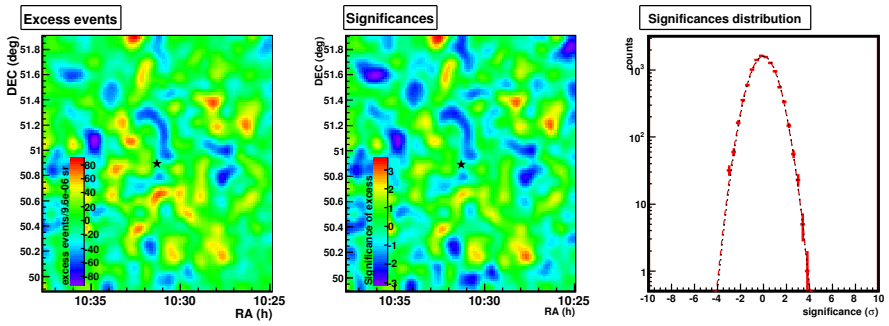

(c) 1ES 1028+511

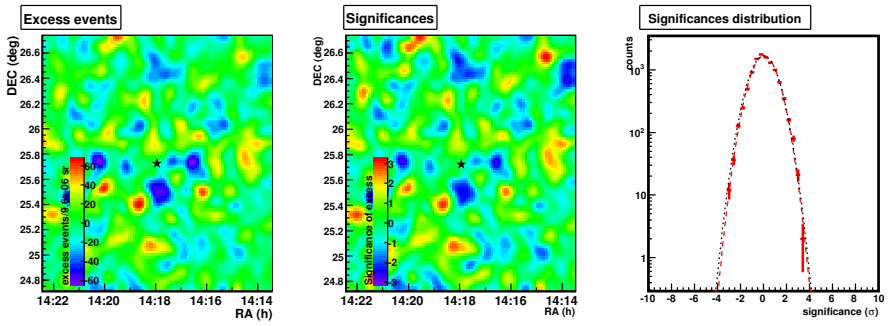

(d) 2E 1415.6+2557

Figure 7.2: Sky maps of the excess events (left), significance (center), and distribution of significances (right) for the four observed sources. The central star indicated the catalog position of each blazar.

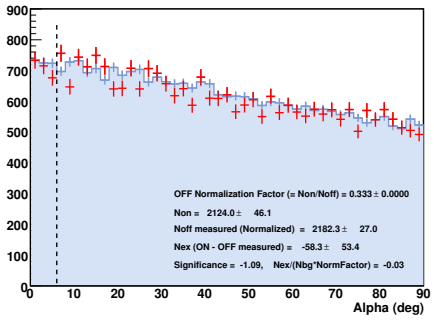

(a) 1ES 0158+003

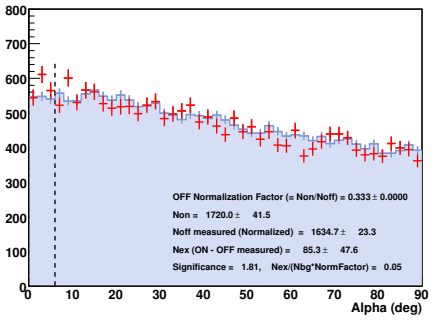

(b) B3 1009+427

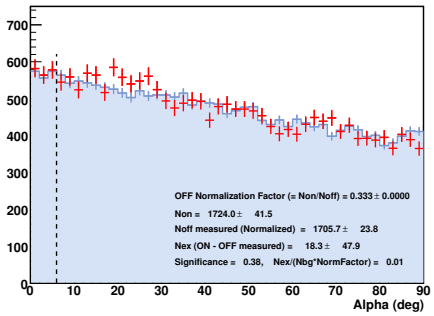

(c) 1ES 1028+511

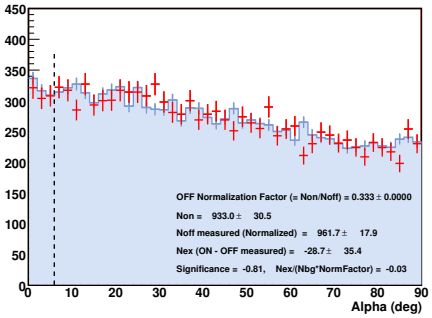

(d) 2E 1415.6+2557

Figure 7.3: *Alpha* plots at $E > 150\,\mathrm{GeV}$ to derive the flux upper limits of the observed sources. Shown are *on* (red crosses) and *off* events (blue filled area). The black dashed line indicates the signal region.

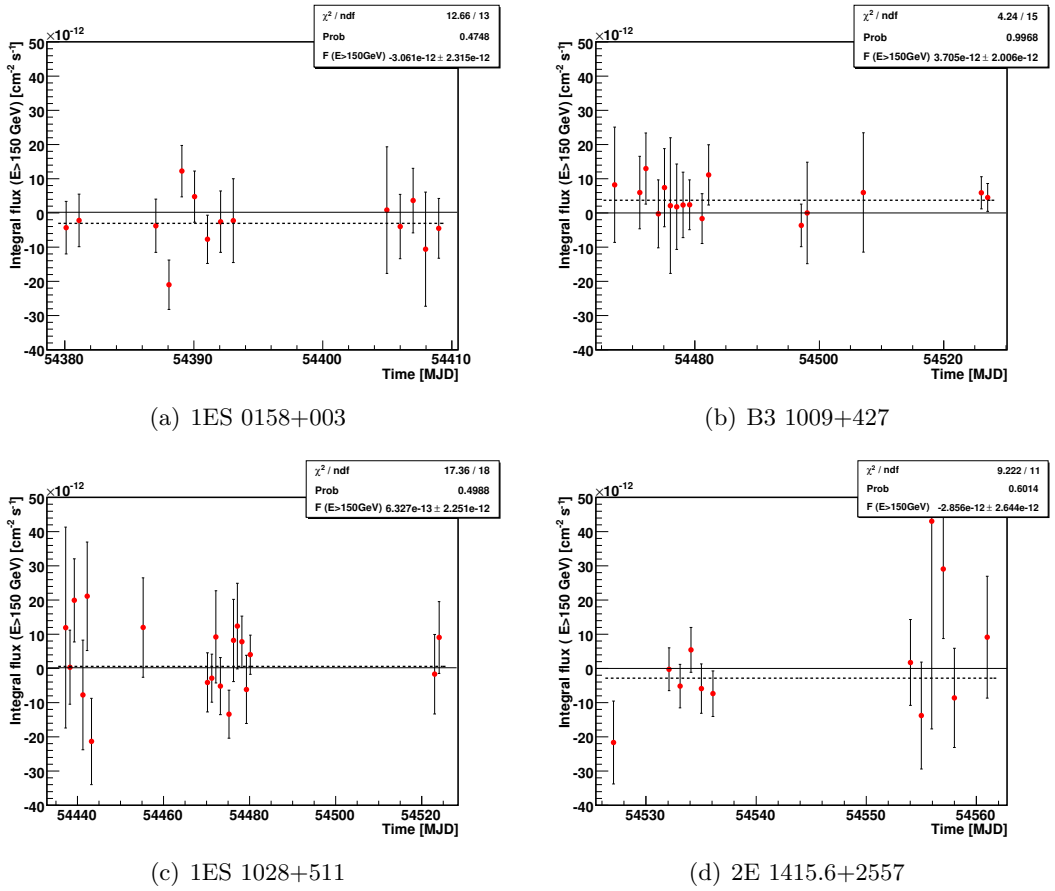

(a) 1ES 0158+003

(b) B3 1009+427

(c) 1ES 1028+511

(d) 2E 1415.6+2557

Figure 7.4: Gamma-ray light curves of the four observed blazars. Each point corresponds to one observation night. A dashed line indicates a fit to a constant flux.

night. The four derived light curves are compatible within statistical fluctuations with a zero flux, and no significant excess in any individual night was found in any of the observed sources.

7.5 Interpretation of the results

The observations of four of the selected distant blazars with the MAGIC telescope resulted in flux upper limits at levels between 2.6% and 12.8% of the Crab Nebula flux at energies $E > 150\,\mathrm{GeV}$. All derived limits are the most constraining obtained so far for these sources at VHE gamma-rays.

According to the study presented in Chapter 4, these four objects were among the best candidates to exhibit VHE gamma-ray emission within the known blazars with redshift $z = 0.2$–0.5. The fact that observations were fixed without relying in monitoring information at other wavelengths avoids the possible bias to observe sources in active flaring states. One (3C 66A/B, Aliu et al., 2009*a*) out of five observations produced a positive detection. Based on these long exposure observations, and on other observations of closer-by blazars performed with the MAGIC telescope, it can be concluded that most of the known blazars that were considered to be good candidates for VHE gamma-ray emission have already been observed. On the other hand, very long exposures (e.g. 3C 66A/B,

Aliu et al., 2009*a*, see also Chapter 9) and observations of blazars during flaring states (e.g. W Comae, Acciari et al. (2008*a*), or S5 0716+714, Teshima (2008)) of some blazars have recently yielded positive detections.

Therefore, it can be concluded that fixed target observations of blazars, specially the distant ones, with the MAGIC telescope will benefit very much from an observation strategy that relies on triggers from other wavelengths to observe sources in high states, maximizing the chances of VHE detections.

Chapter 8

Discovery of VHE gamma-ray emission from the quasar 3C 279

This chapter describes the results from the observations of the quasar 3C 279 done in January–April 2006 with the MAGIC telescope, that led to the discovery of VHE gamma-ray emission from this object. The properties of this object are described and the results obtained are presented and discussed. The impact of this result in the field is analyzed: specially concerning its influence on the current knowledge on the density of the EBL, and the emission mechanism responsible for the VHE emission. The detection of 3C 279 with the MAGIC telescope was published in Teshima et al. (2008), Albert et al. (2008e), and Errando et al. (2008).

8.1 Motivation of the observations

The quasar 3C 279 is one of the best observed flat spectrum radio quasars (FSRQs), and it is located at a redshift of $z = 0.538$ (Burbidge and Rosenberg, 1965). It was extensively studied in the gamma-ray energy band by the EGRET detector, specially after the prominent flare that exhibited shortly after the launch of the satellite in 1991 (Kniffen et al., 1993). 3C 279 was persistently detected by EGRET each time it was observed, even in low states, and it was reported to vary in gamma-ray flux by roughly two orders of magnitude (Maraschi et al., 1994; Wehrle et al., 1998). It has been monitored in radio, optical and X-ray frequencies, and has been subject of extensive multiwavelength campaigns (Maraschi et al., 1994; Hartman et al., 1996; Wehrle et al., 1998; Böttcher et al., 2007).

Also at optical wavelengths, 3C 279 has exhibited substantial variability over up to 2 orders of magnitude, observed on a variety of different time scales, ranging from years down to intraday flux variations. Observatitions in the ultraviolet band revealed the existence of a thermal emission component, possibly related to an accretion disk, that is just visible when the source is in a very low activity state (Pian et al., 1999). The quasar 3C 279 was also the first object in which superluminal motion was discovered (Whitney et al., 1971; Cotton et al., 1979; Unwin et al., 1989).

The broadband SED of 3C 279 in different emission states has been successfully described in Hartman et al. (2001) by radiation from a leptonic jet, with combined synchrotron self-Compton plus external Compton gamma-ray production, following a model from Böttcher et al. (1997) and Böttcher and Bloom (2000). In this model, blobs of ultra-

relativistic pair plasma are moving outward from the central accretion disk along the jet. The blobs emit through synchrotron radiation, synchrotron self-Compton radiation, and inverse Compton scattering of external photons from the accretion disk, either entering the jet directly or after being rescattered by the surrounding material from the broad-line region. The central accretion disk is assumed to radiate a standard disk spectrum (Shakura and Sunyaev, 1973) around a black hole of $\sim 1.5 \times 10^8\,\mathrm{M}_\odot$, and the blazar jet is misaligned by an angle $\theta \sim 2^\circ$ to the observers line of sight.

3C 279 has been suggested as a promising candidate for detection at VHE gamma-rays with ground-based detectors (e.g. Stecker, 1999). Assuming that the intrinsic spectrum of 3C 279 is a simple continuation of the best-fit power law to the EGRET spectrum, the flux at $E \sim 100\,\mathrm{GeV}$ should be detectable by the MAGIC telescope during bright gamma-ray flares. However, models predict that the intrinsic spectrum at multi-GeV energies of 3C 279 would be rather steep, with photon indices $\gtrsim 3.5$ (Hartman et al., 2001). The steep predicted spectrum, and the gamma-ray absorption caused by the EBL, would diminish the detection chances in the VHE band. The only previous observations of 3C 279 in the VHE band are reported in Kerrick et al. (1993) from observations with the Whipple Observatory, providing an integral flux upper limit of 20% of the Crab Nebula flux above 600 GeV.

8.2 Observations and data analysis

The observations of 3C 279 were carried out during ten nights between late January and April 2006, for a total exposure of 9.7 hr. During the MAGIC observations, simultaneous optical R-band observations with the 1.03-m telescope at the Tuorla Observatory (Finland) and the 35-cm KVA telescope on La Palma. The optical observations revealed that during MAGIC observations, 3C 279 was in a high optical state, a factor of 2 above its long-term baseline flux (see Figure 8.2).

MAGIC observations were done in *tracking* mode, with the telescope pointing directly at the source. Additional *off* pointings for background estimation were made off-axis at a field of view near the source with no gamma-ray candidate, accumulating 4.9 hr. of *off* data. All relevant image parameters were checked for consistency between *on* and *off* data (see Figure 8.1).

8.3 The VHE gamma-ray signal

The data was analyzed using the MAGIC standard tools and methods described in Chapter 6, with the only feature of the data being taken in *tracking* mode, with different *on* and *off* pointings, instead of the more commonly used *wobble* mode. Additionally, since the data was taken with the 300 MHz FADCs (the new 2 GHz system was still under commissioning) no time image parameters were used in the gamma/hadron discrimination (see Sections 6.7 and 6.8 for more details).

The analysis presented in this section was performed with the main goal of checking the presence of a VHE gamma-ray signal and verifying the energy spectrum of the source, with special emphasis in understanding the significance of the signal at the high energy end of the spectrum. The results of this analysis are presented and then compared with two other independent analyses performed within the MAGIC collaboration.

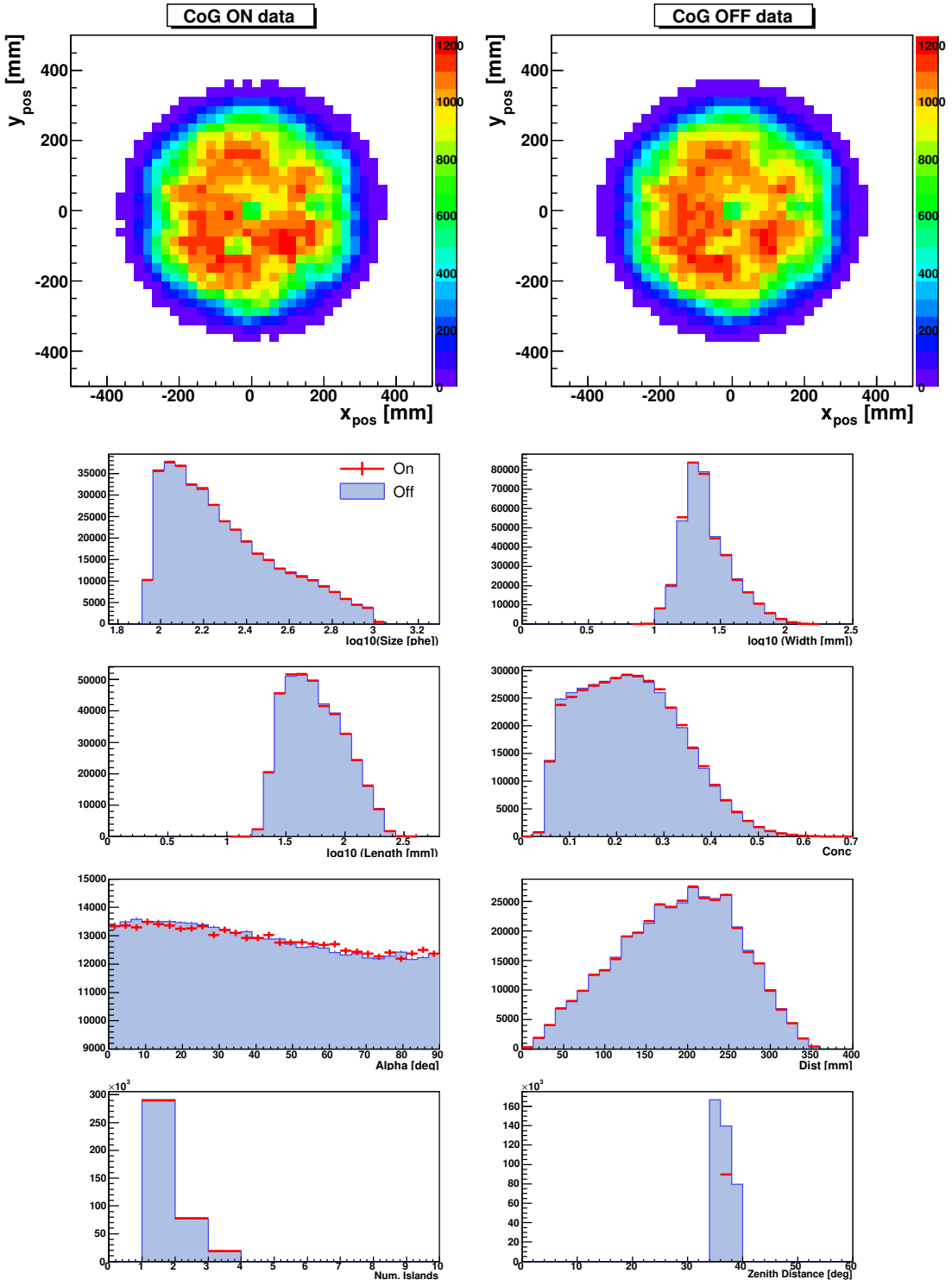

Figure 8.1: Distributions of image parameters for *on* and *off* events, before background rejection cuts. Shown are the distributions of the center of gravity (*CoG*), *Size*, *Width*, *Length*, *Conc*, *Alpha*, *Dist*, number of islands in the cleaned image (*Num. Islands*) and *Zenith Distance*, for *on* and *off* events.

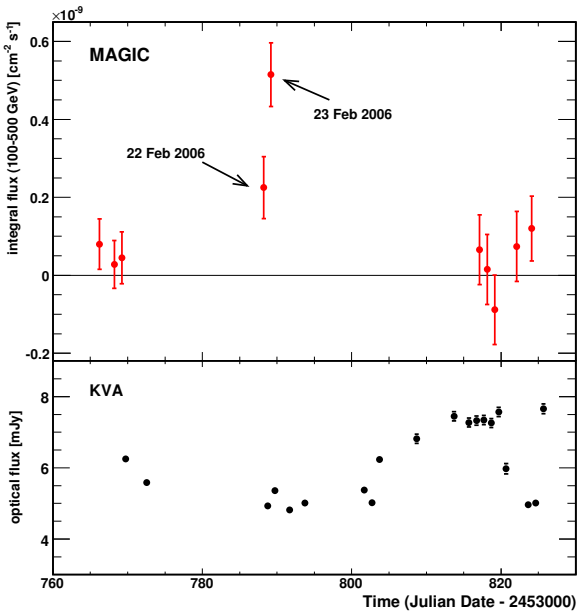

Figure 8.2: MAGIC (top) and optical R-band (bottom) light curves obtained for the quasar 3C 279 from February to March 2006. The long term baseline for the optical flux is 3 mJy (host galaxy subtracted). The VHE gamma-ray detection on the night of 23 February 2006 is clearly visible, together with a signal hint from the night before. As determined by the χ^2 test, the probability that the gamma-ray flux was 0 during the observed period is 2.3×10^{-7}, corresponding to 5.0σ in a gaussian distribution.

8.3.1 Significance of the detection

A significant VHE gamma-ray signal was observed in the night of 23 February. The *Alpha* distribution *on* events after a background rejection cut (see Table 8.1) is plotted together with the normalized distribution of *off* events in Figure 8.3(a). The *on* effective exposure time is 82 minutes. The background rejection cut, and the definition of the signal region by means of a cut in the *Alpha* parameter, are optimized using contemporaneous Crab Nebula data taken in similar observation conditions, specially concerning the *Zenith Distance* distribution of the data.

Figure 8.3(a) shows a clear gamma-ray excess, with 119 excess events and a significance of 5.6σ. Since the observations of 3C 279 lasted for ten nights, and only the data of the night of 23 February is used to claim the detection, a trial factor of 10 has to be applied

Background suppr. (γ-acceptance)	**Signal region (γ-acceptance)**	**Combined acceptance**	**Energy threshold**
$h < 0.05$ (23%)	$\alpha < 10°$ (96%)	22%	240 GeV

Table 8.1: Set of cuts used to estimate the significance of the gamma-ray signal. Indicated are the cut in the *Hadronness* (h) parameter used to reject background events, the *Alpha* (α) cut that defines the signal region, and the individual and combined gamma-ray acceptances of every set of cuts. The gamma-ray acceptance is estimated using MC generated gamma-ray events. The energy threshold is also shown.

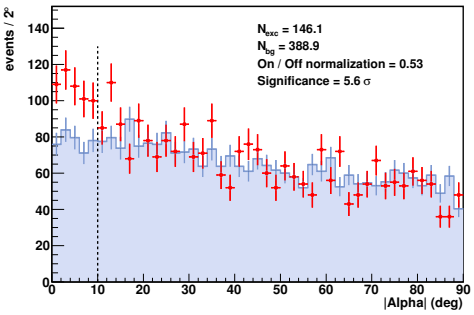

(a) *Alpha* distributions for the *on* (red crosses) and *off* (filled histogram) events, resulting from the analysis presented in this chapter.

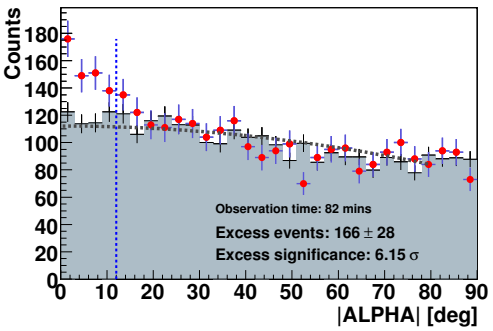

(b) Published detection plot. The dotted line is a parabolic fit without linear term to the *off* events between 0° and 80°, used to smoothen the background distribution for a better extrapolation towards *Alpha* = 0°. The number of excess events is obtained with respect to this line. Taken from Albert et al. (2008*e*).

Figure 8.3: *Alpha* plots to estimate the significance of the 3C 279 detection by MAGIC. Shown are *on* events from the night of 23 February 2006 (dots) and suitable *off* data (crosses and filled area).

to correct the significance. After this trial factor correction[1], the overall significance of the detection is 5.2σ.

8.3.2 Energy spectrum

For the energy spectrum of 3C 279, loose cuts are applied to keep the gamma-ray acceptance high. The cuts were set independently for each energy bin in the spectrum, requiring that the acceptance of MC simulated gamma-rays was 70% for the *Hadronness* cut and 80% for the *Alpha* in each bin. The obtained differential energy spectrum was unfolded using the Tikhonov unfolding technique and is shown in Figure 8.4(a). The spectrum can be well fitted by a power law, which gives a differential flux (TeV^{-1} cm^{-2} s^{-1}) of:

$$\frac{\mathrm{d}N}{\mathrm{d}E\,\mathrm{d}A\,\mathrm{d}t} = (6.1 \pm 2.7) \times 10^{-10} (E/200\,\mathrm{GeV})^{-4.20\pm0.99} \tag{8.1}$$

The quoted errors are statistical only. The systematic uncertainty is estimated to be 30% in the flux level and 0.2 in the power law photon index.

8.3.3 Comparison with MAGIC published results

The results obtained with the analysis presented in this chapter are compared to the MAGIC published results in Figures 8.3 and 8.4.

The detection plot published in Albert et al. (2008*e*) (Figure 8.3(b)) is obtained with slightly looser cuts as the indicated in Table 8.1, having a combined efficiency of 40%. The obtained result is a detection with significance of 6.2σ, which translates into 5.8σ when

[1]Given a probability P, the corrected probability $P_{corrected}$ after a trial factor n is given by $P_{corrected} = P^n$

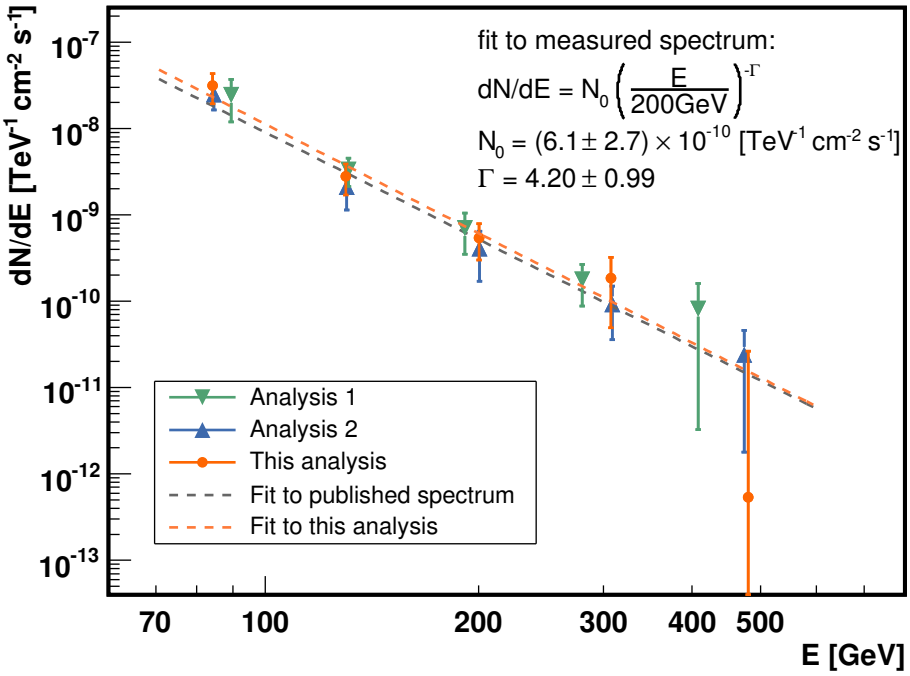

(a) Differential energy spectrum obtained for 3C 279. The result obtained with the presented analysis is compared with two independent analyses performed within the MAGIC collaboration: Analysis 1 by Pratik Majumdar, and Analysis 2 by Elisa Prandini.

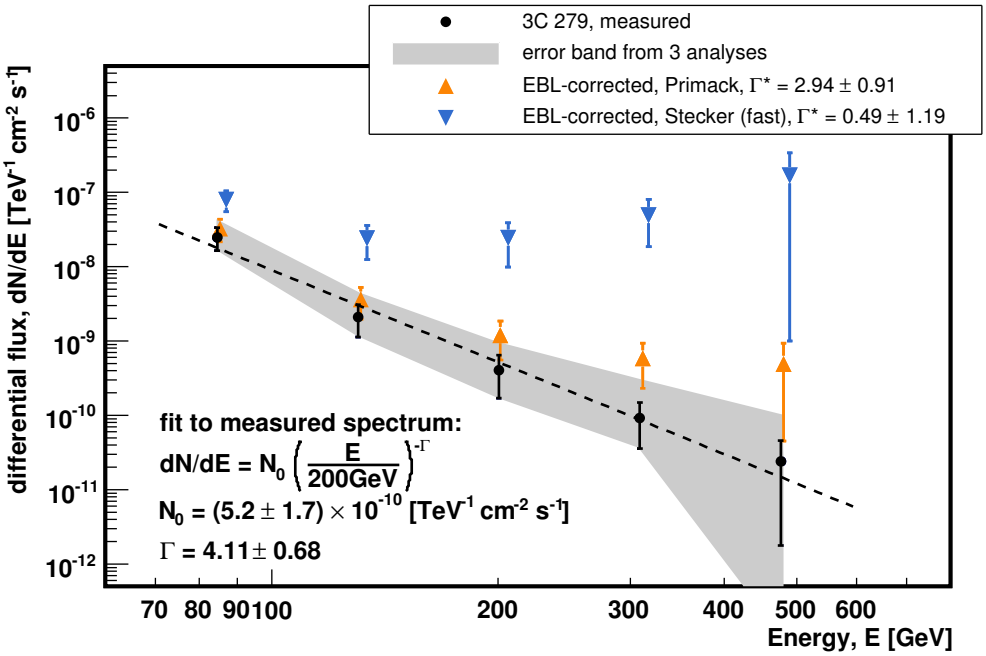

(b) Published differential energy spectrum of 3C 279 as measured by MAGIC. The grey area includes the combined statistical and systematic errors, underlining the marginal significance of the detections at high energy. In triagles are shown the measured points corrected on the basis of two extreme models in the density prediction of EBL. Adapted from Albert et al. (2008*e*).

Figure 8.4: Differential energy spectrum of the quasar 3C 279.

corrected with a trial factor corresponding to 10 nights of observation. As determined by the χ^2 test, the probalility that the gamma-ray flux on all 10 nights was zero is 2.3×10^{-7}, corresponding to 5.0σ in a Gaussian distribution. The light curve also shows a hint of signal the night before the gamma-ray flare was measured.

The energy spectra obtained by the three independent analyses are compared in Figure 8.4(a). All three analyses agree very well within statistical errors. The published differential VHE spectrum (Figure 8.4(b)) can be described by a power law with spectral index of $\Gamma = 4.1 \pm 0.7_{\mathrm{stat}} \pm 0.2_{\mathrm{syst}}$. The measured integrated flux above 100 GeV on 23 February is $(5.15 \pm 0.82_{\mathrm{stat}} \pm 1.50_{\mathrm{syst}}) \times 10^{-10}\,\mathrm{cm}^{-2}\,\mathrm{s}^{-1}$. The fit to the spectrum obtained with this analysis also agrees within statistical errors with the published one. The differences between the three independent analyses are reflected in the published result as a grey band combining statistical and systematic errors, and underlines the marginal significance of the detection at energies above 300 GeV.

8.4 Interpretation of the results

The EBL influences the propagation of gamma-ray emitted from distant sources resulting in an exponential decrease with energy and a cutoff in the measured gamma-ray spectrum. Several models have been proposed for the EBL (see Section 4.1). All have limited predictive power for the EBL density, particularly as a function of the redshift, as many details about star and galaxy evolution remain uncertain. To illustrate this uncertainty two extreme models were used to calculate the source intrinsic spectrum: a model by Primack et al. (2005) close to the lower limits set by galaxy counts (Madau and Pozzetti, 2000; Fazio et al., 2004) and the 'fast-evolution' model by Stecker et al. (2006) corresponding to the highest possible attenuation. These models will be referred as *low* and *high*, respectively, and are shown in Figure 8.5. In fact, the model from Primack et al. (2005) predicts the EBL level at wavelengths above 5 μm slightly below the galaxy counts obtained from the Spitzer data (Fazio et al., 2004; Papovich et al., 2004; Dole et al., 2006) and the ISOCAM results (Metcalfe et al., 2003; Elbaz et al., 2002). This model also lies below the FIRAS measurements in the far-infrared, an undershoot attributed to the abundance of ultra-luminous infrared galaxies, only recently discovered and not taken into account in the model. However, the EBL domain above 3 μm does not influence the spectrum of 3C 279, given that the highest energy measured by MAGIC is below 500 GeV. At those energies, EBL photons with $\lambda > 2.5$ μm do not reach the energy necessary for pair production. Therefore, the model by Primack et al. (2005) was chosen as the *low* limit for the EBL level in the frequency range relevant for the MAGIC 3C 279 measurement.

Using the published spectrum of 3C 279, a power-law fit to the EBL-corrected spectral points results in an intrinsic photon index $\Gamma^\star = 2.9 \pm 0.9_{\mathrm{stat}} \pm 0.5_{\mathrm{syst}}$ (*low* absorption) and $\Gamma^\star = 0.5 \pm 1.2_{\mathrm{stat}} \pm 0.5_{\mathrm{syst}}$ (*high* absorption). The *high* model leads to an intrinsic VHE spectrum difficult to reconcile with an extrapolation of the EGRET data, and with general constraints on the spectral energy distribution. On the other hand, the *low* model apparently gives an acceptable result. The distance at which the flux of photons of a given energy is attenuated by a factor e (the path corresponding to an optical depth $\tau = 1$) is called the gamma-ray horizon (Fazio and Stecker, 1970) and is usually expressed as a function of the redshift. This energy-redshift relation is shown in Figure 8.6.

Assuming a hardest intrinsic photon index $\Gamma^\star = 1.5$ and no significant pile-up of the spectrum at high energies (Mazin and Raue, 2007), a model based on Kneiske et al. (2002) and Kneiske et al. (2004) can be tuned to give an upper limit to the EBL density in the

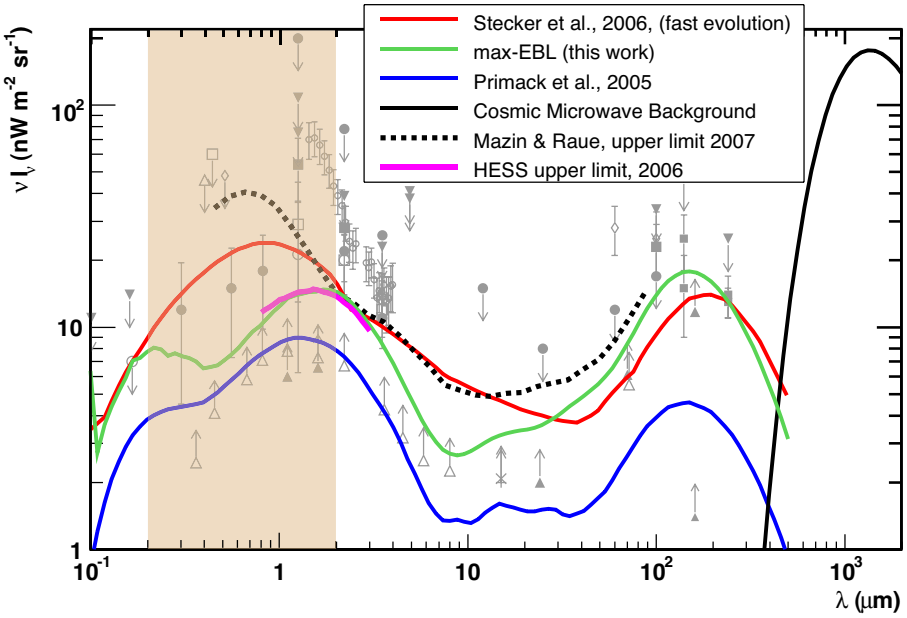

Figure 8.5: EBL models at $z = 0$ and direct measurements of the EBL photon density at various wavelengths. The upper limit derived from the detection of 3C 279 (black line) is based on Kneiske et al. (2002) with parameters adapted to the results from the latest galaxy counts (see Supporting Material in Albert et al. (2008*e*) for details). The dotted line is an upper limit from Mazin and Raue (2007). The shaded region corresponds to the range of frequencies where the MAGIC measured spectrum is sensitive. Taken from from Supplementary Material in Albert et al. (2008*e*).

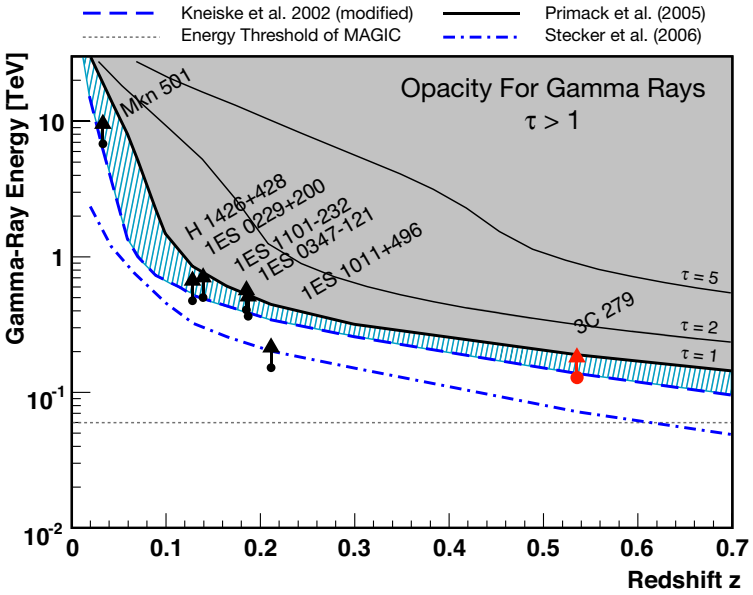

Figure 8.6: The gamma-ray horizon. The prediction range of EBL models is illustrated by Primack et al. (2005) (thick solid line) and Stecker et al. (2006) (dashed-dotted line). The EBL limit based on Kneiske et al. (2002) (dashed line) derived using the VHE spectrum of 3C 279 is also shown (arrow corresponding to 3C 279). Limits obtained for other sources are shown by black arrows. The narrow blue filled band is the region allowed between this model and a minimum EBL level, given by Primack et al. (2005). The gray area indicates an optical depth $\tau > 1$, where the flux of gamma rays is strongly suppressed. Taken from Albert et al. (2008*e*).

0.2–2 μm range as shown in Figure 8.5. This result supports the conclusion drawn from VHE measurements at lower redshifts (Aharonian et al., 2006*b*; Mazin and Raue, 2007) that the EBL density is close to the lower limits set by galaxy counts. It is important to point out that this limit is only valid under the assumption that the intrinsic photon index cannot be harder than 1.5, which is the hardest value given for EGRET sources and is also the hardest that can be obtained with classical leptonic emission mechanisms. Alternative scenarios can produce intrinsic spectra with $\Gamma^\star < 1.5$. SSC models with a narrow electron distribution can produce spectra with $\Gamma^\star \approx 0.7$ (Katarzyński et al., 2006), and internal absorption by soft photons can also harden the spectrum (Bednarek, 1997; Aharonian et al., 2008*c*; Liu et al., 2008; Sitarek and Bednarek, 2008). However, an accurate modeling of the internal absorption in 3C 279 finds no important hardening of the intrinsic spectrum in the energy band measured by MAGIC (Tavecchio and Mazin, 2009).

The emission mechanism responsible for the observed VHE radiation remains uncertain. Leptonic emission models (assuming relativistic electrons in the jet as source of the gamma rays), generally successful in describing blazar data (e.g., Maraschi et al., 1992) can, with some assumptions, also accommodate the MAGIC spectrum. Hadronic models (involving relativistic protons, e.g. Mannheim and Biermann, 1992) provide a possible alternative.

The simplest leptonic model ("one-zone") assumes that the bulk of the emission is produced within a single region. In order to properly model the emission, good coverage of the entire SED is required, since only with known position and luminosity of both peaks is it possible to fully constrain the physical parameters (e.g., Tavecchio et al., 1998). In the case of the 3C 279 flare, only a simultaneous measurement in the optical R–band with the VHE spectrum derived by MAGIC is available. With this input, the observed SED could be reconstructed assuming a simple one-zone model leptonic model with external comptonization (for a full description, see Maraschi and Tavecchio, 2003).

The MAGIC observations contribute data to the important energy range above 10^{25}Hz, poorly studied so far because lying above the range of satellite-borne instruments and below that of most ground-based Cherenkov telescopes. The SED in Figure 8.7 shows the MAGIC points corrected according to the two extreme EBL models previously discussed, together with measurements at lower frequencies from different epochs. In the same figure, the generic one-zone model that reproduces the data is shown. It is clearly seen from Figure 8.7 that leptonic models can reproduced the intrinsic source spectrum if a *low* model for the EBL density is assumed.

8.5 Impact of the VHE detection of 3C 279

After the publication of the measured VHE spectrum of 3C 279 in the *Science* magazine(Albert et al., 2008*e*), several authors have discussed this result and its impact, both in implication of this detection in the current understanding of the EBL density and its absorption, and possible models responsible for the emission.

The main important aspects of the detection at VHE of 3C 279 are:

- It is the farthest detected source at VHE, with a redshift of $z = 0.536$, being more than two times more distant than the farthest detected blazar at the time of the publication, which was 1ES 1011+113 (Albert et al., 2007*a*, $z = 0.212$).

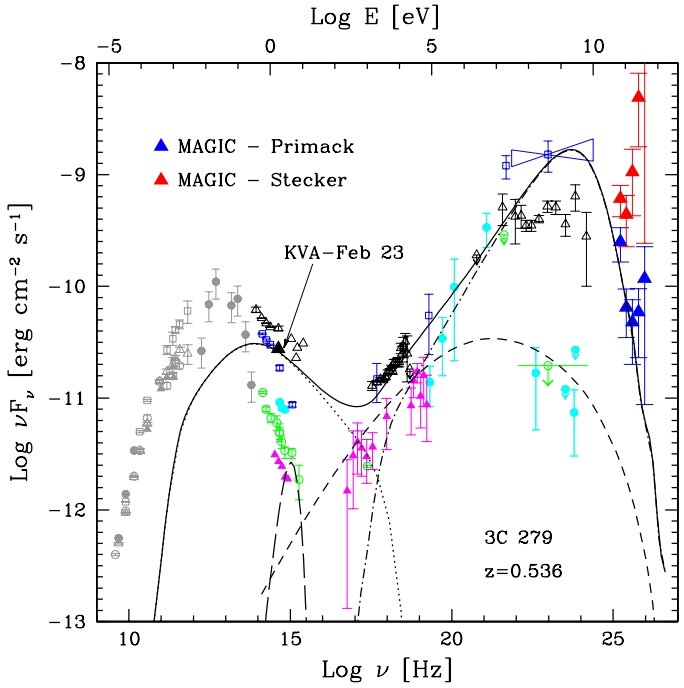

Figure 8.7: Spectral energy distribution for 3C 279 at different source intensities, over the years from 1991 to 2003, taken from Ballo et al. (2002) and Collmar et al. (2004), with MAGIC spectral points (2006) at the high-energy end. The MAGIC points are corrected according to the two extreme EBL models discussed on the text. The spectrum corrected with the *low* EBL model gives clearly a more plausible result. An emission model and its individual components are also shown: the solid line represents the total model emission, fitted only to the MAGIC points unfolded with a *low* EBL density and the simultaneous optical point from the KVA telescope. The individual components of the emission model are synchrotron radiation (dotted line), disk emission (long-dashed), synchrotron-self-Compton (short-dashed) and external Compton (dot-dashed). Taken from from Supplementary Material in Albert et al. (2008*e*).

- It is the first quasar detected in the VHE range, since all blazars detected so far were of the BL Lac subclass. The main differences of 3C 279 with respect to BL Lacs are:
  - Significant emission from the broad line region (BLR), implying an source of low energy photons near the region where VHE gamma-rays are produced.
  - Peak of the SED located at lower frequencies than in BL Lacs, implying few high-energy electrons available to sustain a strong VHE emission

Concerning the high redshift of the source, the detection of 3C 279 at VHE is not a surprise. Previous detections of closer blazars already indicated that the density of EBL photons is probably lower than expected (Aharonian et al., 2006*b*, 2007), allowing the detection of bright VHE sources with $z \sim 0.5$–0.6 in the range of 100–300 GeV, which is accessible for MAGIC, and other ground-based Cherenkov telescopes currently in operation.

On the other hand, some authors criticized that the VHE spectrum of 3C 279 is used to derive upper limits on the EBL density, arguing that the possible presence of low-energy photons from the broad-line region can cause intrinsic absorption effects in the source. Costamante et al. (2008) argued that the presence of a photon field in the source coming from the BRL can strongly affect the spectrum of the source, and could eventually produce a hardening in the intrinsic spectrum (Bednarek, 1997; Reimer, 2007; Aharonian et al., 2008*c*; Liu et al., 2008; Sitarek and Bednarek, 2008). This hardening of the source intrinsic spectrum could invalidate the assumption of $\Gamma^\star > 1.5$ used to derive the EBL upper limits. However, Tavecchio and Mazin (2009) have shown that, using specific calculations to predict the radiation field expected from the BLR in 3C 279, the internal absorption of VHE gamma-ray photons does not produce a significant hardening of the energy spectrum in the range of energies measured by MAGIC and, thus, the derived EBL limit can be considered as robust.

Finally, the possible emission mechanism responsible for the VHE gamma-ray signal observed by MAGIC has been discussed in the recent literature. Using simultaneous optical and X-ray data, Böttcher (2008) suggested that a one-zone SSC model can be ruled out. Also a SSC model with external comptonization of the radiation from the BLR is excluded, as it fails to reproduce the observed X-ray flux. The compiled SED can be reproduced by an SSC model with a second component where the emission region is far outside the BLR. Alternatively, a hadronic models is also able to reasonably reproduce the observed SED of 3C 279. However, according to Böttcher (2008), the extreme jet power required by the hadronic model still favors the leptonic origin of the observed emission.

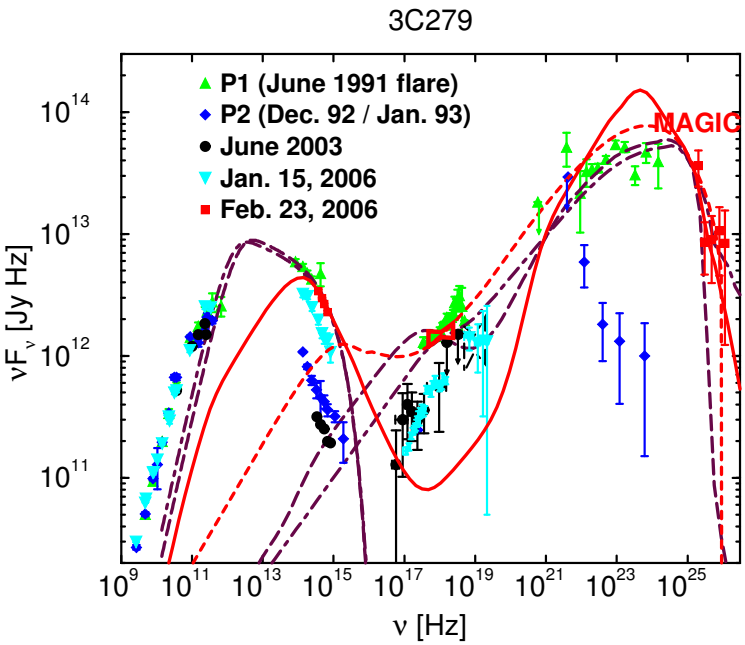

Figure 8.8: Spectral fits to the SED of 3C 279 in February 23, 2006: (solid red line) using a leptonic external Compton model; (short-dashed red line) leptonic SSC model fits only to the X-ray–gamma-ray spectrum; (dot-dashed maroon line) fit with the hadronic synchrotron-proton blazar model with internal (synchyrotron) photons only as targets for pγ pion production, and (long-dashed maroon line) with synchrotron + external (BLR) photons as targets for pγ pion production. Taken from Böttcher (2008).

Chapter 9

Detection of VHE gamma-rays from the 3C 66A/B region

This chapter describes the detection of a gamma-ray source in the field of view of 3C 66A/B with the MAGIC telescope, in observations carried out between August and December 2007. The properties of the two candidate counerparts for this detection, the blazar 3C 66A and the radio galaxy 3C 66B, are described. The obtained results are presented and discussed, with special emphasis on the position of the gamma-ray excess and the origin of the lower energy gamma-ray events. This result was published in Aliu et al. (2009a).

9.1 Motivation of the observations

The Third Cambridge (3C) radio survey at 159 MHz (Edge et al., 1959) resulted in a catalog of 471 sources in the Northern hemisphere. It was later found that the source numbered 66 was composed of two unrelated objects, a BL Lac object now identified as 3C 66A and a radio galaxy, 3C 66B (see Figure 9.1). Both radio sources are coincident with the EGRET source 3EG 0222+4253 (Hartman et al., 1999), although there are other objects in the EGRET error box, including the pulsar PSR J0218+4232, which is at 1 degree distance from 3C 66A and B. It has been suggested in Kuiper et al. (2000) that the pulsar contributes to the observed gamma-ray flux at energies less than 500 MeV while the BL Lac object dominates at higher energies (see Figure 9.2).

9.1.1 3C 66A

3C 66A is classified as a low-frequency-peaked BL Lac object, and it has historically exhibited rapid variability at optical and near-IR wavelengths (Folsom et al., 1976; de Diego et al., 1997; Lainela et al., 1999). It was first identified as a quasi-stellar object in Wills and Wills (1974) using optical observations (see Figure 9.1(b)), and later classified as a BL Lac (Maccagni et al., 1987).

3C 66A has been observed several times with satellite-borne and ground-based gamma-ray detectors. In the TeV regime, the Crimean Astrophysical Observatory's GT-48 imaging atmospheric Cerenkov telescope has claimed repeated detections of this source above 900 GeV (Neshpor et al., 1998; Stepanyan et al., 2002) with an integral flux as high as $(3 \pm 1) \times 10^{-11}\,\mathrm{cm}^{-2}\,\mathrm{s}^{-1}$. Since the Crimean detection, 3C 66A has been a primary target for TeV telescopes, although its large quoted redshift ($z = 0.444$) dimin-

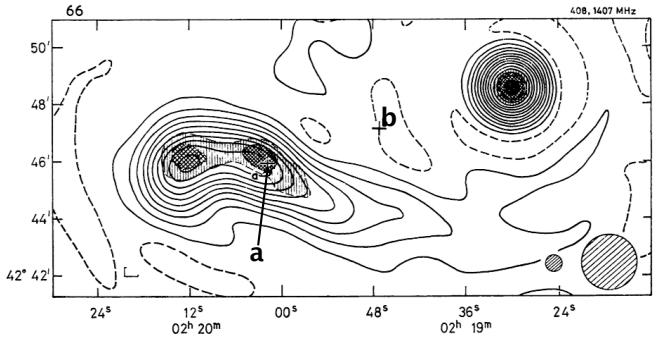

(a) Contours of the radio source 3C 66 at 408 MHz, with the superposed shaded areas indicating the structure at 1407 MHz. The $'a'$ in the map shows the catalog position of 3C 66B, while $'b'$ indicates another galaxy of the Abell cluster. The radio source on the upper right part of the image corresponds to 3C 66A. Taken from MacDonald et al. (1968).

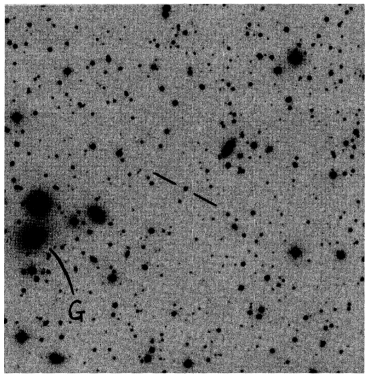

(b) Image of the 3C 66 field of view at optical wavelengths. The quasi-stellar object identified with 3C 66A is shown between bars, while $'G'$ shows the position of 3C 66B. Taken from Wills and Wills (1974).

Figure 9.1: Radio and optical maps where 3C 66A and 3C 66B are resolved.

ished the probability of detection because of the EBL absorption. HEGRA and Whipple reported upper limits, $F(>630\,\mathrm{GeV}) < 1.42 \times 10^{-11}\,\mathrm{cm}^{-2}\,\mathrm{s}^{-1}$ (Aharonian et al., 2004, 99% C.L.) and $F(>350\,\mathrm{GeV}) < 0.59 \times 10^{-11}\,\mathrm{cm}^{-2}\,\mathrm{s}^{-1}$ (Horan et al., 2004, 99.9% C.L.) respectively, from observations that were non-simultaneous with the detection by the Crimean Observatory. The STACEE solar array also provided an upper limit of $F(>184\,\mathrm{GeV}) < 1.2 \times 10^{-10}\,\mathrm{cm}^{-2}\,\mathrm{s}^{-1}$ (Bramel et al., 2005). In 2008 September, the VERITAS collaboration reported a clear detection of 3C 66A (Swordy, 2008; Acciari et al., 2009) above 200 GeV with an integral flux on the level of 6% of the Crab Nebula flux. Shortly after, a high state of 3C 66A was also reported by the *Fermi* Gamma-ray Space Telescope at energies above 20 MeV (Tosti, 2008). The VERITAS and *Fermi*-LAT detections occurred 1 year after the MAGIC data presented in this chapter was taken.

Modeling of the 3C 66A gamma-ray flux by Costamante and Ghisellini (2002) predicts a moderate flux of $7.0 - 9.6 \times 10^{-11}$ cm^{-2} s^{-1} above 40 GeV, but negligible flux ($< 0.14 \times 10^{-11}$ cm^{-2} s^{-1}) above 300 GeV. Without EBL absorption, 3C 66A has the potential to be an easily detected TeV source and for this reason detections and upper limits of the source are very useful for EBL studies.

In addition, an extensive multiwavelength campaign on 3C 66A was coordinated in 2003-2004 covering frequencies from radio to VHE gamma-rays (Böttcher et al., 2005). Joshi and Böttcher (2007) reproduced the data collected during this campaign with a time-dependent leptonic model predicting a detectable signal in the MAGIC energy range during high state episodes of the source (see Figure 9.3).

The redshift of 3C 66A

Blazars have typically few, if any, detectable emission lines, which makes determining their redshift difficult. As pointed out in Bramel et al. (2005), the often referred redshift of 0.444 (Miller et al., 1978) for 3C 66A is based on one emission line only, interpreted as Mg II, and the authors quoted it as uncertain. In addition to this, Kinney et al. (1991) identified a weak Ly-α line corroborating these results. Since both measurements rely on

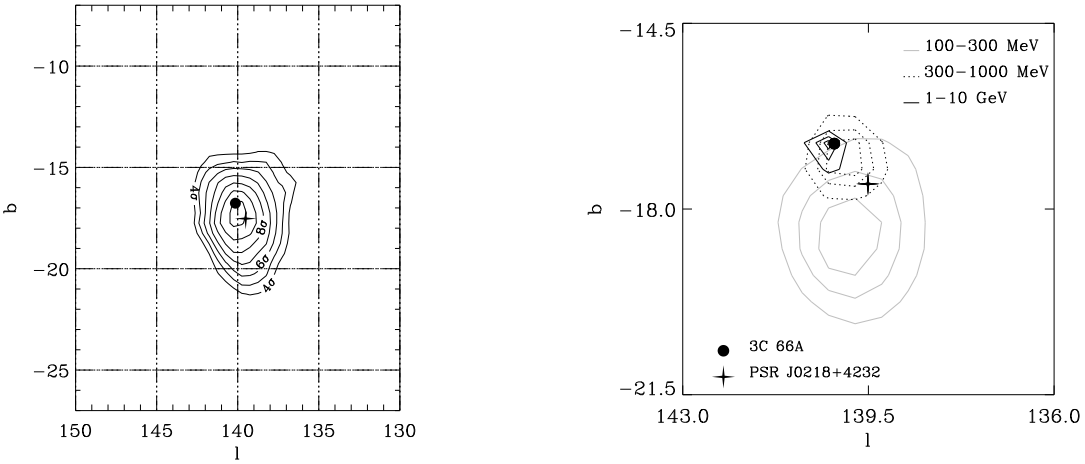

(a) Sky map for energies > 100 MeV of the region centered on the EGRET source 3EG J0222+4253. The position of PSR J0218+42 is indicated by a star and 3C 66A by a dot.

(b) Sky map showing 1, 2 and 3 σ location confidence contours of 3EG J0222+4253 for 3 different energy bands. The shift of the excess towards the blazar 3C 66A for increasing energies is evident.

Figure 9.2: EGRET maps of the 3C 66A region. From Kuiper et al. (2000).

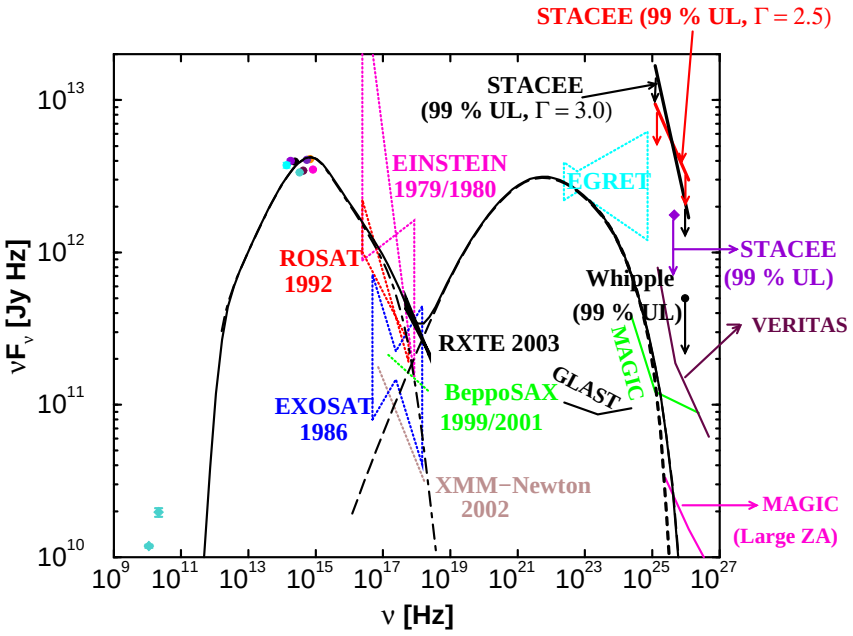

Figure 9.3: Time-averaged SED modelling of 3C 66A during a high state taken from (Joshi and Böttcher, 2007), predicting a VHE flux detectable by MAGIC at low energies.

a single line, the redshift of this BL Lac is considered uncertain. In later observations (e.g., Finke et al., 2008), no lines have been seen in the spectra of 3C 66A. Based on the marginally resolved host galaxy (Wurtz et al., 1996) the photometric redshift was determined to be 0.321, the determination having large error bars (Finke et al., 2008).

9.1.2 3C 66B

3C 66B is a large Fanaroff-Riley-I-type (FRI) radio galaxy located at $z = 0.021$ (Stull et al., 1975), which lies in the same field of view as the blazar 3C 66A, at $6'$ distance (approximately the size of one pixel in the MAGIC camera). It has similar characteristics as M 87, which was detected at VHE gamma-rays (Aharonian et al., 2003). However, 3C 66B is approximately three times more distant to Earth than M 87 (Luminosity distance 22.5 Mpc (M 87) compared to 85.5Mpc (3C 66B)). VLBI observations of the radio core of this galaxy revealed orbital motion, showing evidence for a supermassive black hole binary with period of 1.05 ± 0.03 years (Sudou et al., 2003) being at the center of 3C 66B. Although less obvious than the blazar 3C 66A, the radio galaxy 3C 66B can also be considered as a candidate TeV emitter, since already two other radio galaxies have been detected at those energies: the already mentioned M 87, and the newly discovered Centaurus A (Aharonian et al., 2009).

9.2 Observations and data analysis

An observation time of 30 hr with the MAGIC telescope on the blazar 3C 66A was granted for the Summer–Autumn campaign in 2007, within the framework of a proposal for observation of distant blazars described in Chapter 4. Observations started in August 2007, and were intensified and extended because 3C 66A underwent an optical outburst in the same epoch, activating a target of opportunity program, which had resulted in discoveries of new VHE gamma-ray sources in the past (Albert et al., 2006*b*, 2007*a*; Teshima, 2008).

In total 54.2 hr of observations were made in August, September, and December 2007, out of which 45.3 hr passed the quality cuts. Bad runs were rejected based on the event rate after image cleaning, removing data taken under bad atmospheric conditions. An additional cut removed the events with total charge (*Size*) less than 150 photoelectrons. This quality cut assures a better background rejection, since including smaller images in the analysis worsens the performance of the background suppression methods.

A summary of the observations can be found in Table 9.1. The observations were made in *wobble* mode, pointing alternately to two different sky directions, each at $24'$ distance form the 3C 66A catalog position (see Section 6.3 for details). The zenith distance distribution of the data extends from 14° to 35°.

Just before the start of the observation campaign $\sim 5\%$ of the mirrors on the telescope were replaced, worsening the optical point-spread function (PSF). As a consequence, a new calibration of the mirror alignment system became necessary, which took place within the observation campaign and improved the PSF again. The sigma of the Gaussian PSF (40% light containment) was measured to be $3.'0$ (14.8 mm) in 12–14 August, $2.'6$ (13.0 mm) in 15–26 August and $2.'1$ (10.6 mm) in September and December. Estimations of the nightly optical PSF are shown in Table 9.1. To take this changes into account, data were analyzed separately for each period and the results were combined at the end of the analysis chain. However, the realignment resulted in a mispointing, which was taken care of by a new pointing model (Bretz et al., 2009) applied offline using starguider information (Riegel

Date	**Observation time**	**Zenith distance range**	**optical-PSF**
yyyy.mm.dd	[hr]	[°]	[mm]
2007.08.12	0.83	17.1–24.3	14.7 ± 1.0
2007.08.13	0.82	16.4–23.3	15.6 ± 1.0
2007.08.14	0.93	16.3–24.3	14.8 ± 1.0
2007.08.15	0.99	15.7–23.2	13.1 ± 1.1
2007.08.16	1.06	15.0–24.1	12.6 ± 1.1
2007.08.17	1.66	14.9–34.5	13.2 ± 1.1
2007.08.18	2.26	14.6–35.4	13.6 ± 1.1
2007.08.19	2.40	14.5–35.2	12.7 ± 1.1
2007.08.20	2.43	14.3–35.7	13.3 ± 1.1
2007.08.21	2.43	14.4–35.2	13.0 ± 1.1
2007.08.22	2.05	14.3–35.2	12.6 ± 1.0
2007.08.23	2.41	14.3–34.0	11.8 ± 1.0
2007.08.24	3.00	14.3–39.4	13.0 ± 1.0
2007.08.25	1.19	14.3–22.8	13.6 ± 1.1
2007.08.26	0.93	14.3–17.4	12.4 ± 1.1
2007.09.12	1.04	14.4–21.3	10.6 ± 1.0
2007.09.13	0.91	14.6–20.2	10.9 ± 1.0
2007.09.14	1.05	14.3–20.2	10.6 ± 1.0
2007.09.15	0.95	14.3–18.3	10.6 ± 1.0
2007.09.16	0.85	14.3–18.6	10.6 ± 1.0
2007.09.17	1.00	14.3–18.0	10.7 ± 1.0
2007.09.18	1.09	14.3–17.6	10.6 ± 1.0
2007.09.19	1.01	14.3–17.1	10.1 ± 1.0
2007.09.20	1.13	14.3–16.8	10.1 ± 1.0
2007.09.21	1.09	14.3–16.1	9.9 ± 0.9
2007.09.22	3.58	14.3–30.5	10.5 ± 1.0
2007.09.23	2.59	14.3–31.8	N.A.
2007.09.24	1.51	18.9–34.3	10.9 ± 1.0
2007.09.25	0.50	29.0–34.9	9.4 ± 1.0
2007.12.03	1.73	14.3–24.4	11.2 ± 1.0
2007.12.04	0.45	22.7–26.4	10.8 ± 1.0
2007.12.05	0.19	17.2–20.1	11.2 ± 1.0
2007.12.06	1.98	14.3–26.9	11.3 ± 1.0
2007.12.08	1.76	14.3–23.6	11.5 ± 1.0
2007.12.09	1.98	14.3–25.2	11.0 ± 1.0
2007.12.11	1.21	14.3–18.3	11.1 ± 1.0
2007.12.12	1.20	14.3–18.7	11.6 ± 1.0

Table 9.1: Night by night summary of the 3C 66A observations. The date corresponds to that of the morning next to the observations. The optical-PSF corresponds to the radius that contains 40% of the light from a point-like source. On 2007.09.23 the bad data quality didn't allow the calculation of the optical-PSF. The data corresponding to that particular day was rejected for the analysis.

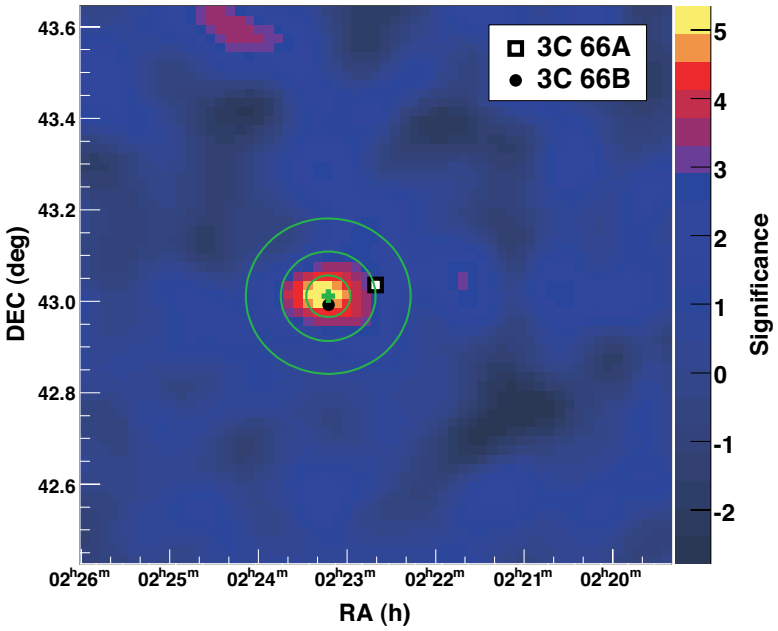

Figure 9.4: Significance map for gamma-like events above 150 GeV in the observed sky region. The green cross corresponds to the fitted maximum excess position of MAGIC J0223+403. The probability of the true source to be inside the green circles is 68.2%, 95.4%, and 99.7% for the inner, middle, and outer contour, respectively. The catalog positions of 3C 66A and 3C 66B are indicated by a white square and a black dot, respectively.

et al., 2005, see also Chapter 6). Considering the additional uncertainty caused by the offline corrections, the systematic uncertainty of the pointing accuracy is estimated to be $2'$ on average. Note that in the case of an optimal pointing model the systematic uncertainty is below $2'$, being $1'$ on average (Bretz et al., 2009; Albert et al., 2008*f*).

9.3 The VHE gamma-ray signal

The data was analyzed using the MAGIC standard tools and methods described in Chapter 6.

Cuts	**Bkgnd. suppr. (γ-acceptance)**	**Signal region (γ-acceptance)**	**Combined acceptance**	**Energy threshold**
loose	$h < 0.10$ (51%)	$\alpha < 10°$ (78%)	43%	140 GeV
tight	$h < 0.04$ (32%)	$\alpha < 8°$ (81%)	26%	190 GeV

Table 9.2: Description of the tight and loose sets of cuts used in the analysis. Indicated are the cut in the *Hadronness* (h) parameter used to reject background events, the *alpha* (α) cut that defines the signal region, and the individual and combined gamma-ray acceptances of every set of cuts. The gamma-ray acceptance is estimated using MC generated gamma-ray events. The energy threshold for the two sets of cuts is also shown.

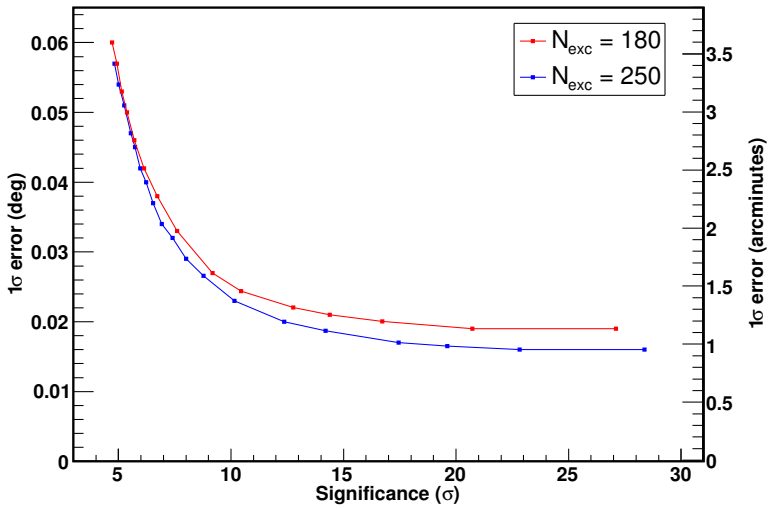

Figure 9.5: Uncertainty of the source location as a function of the signal strength. In this case, the number of excess events in the simulated sky maps is kept fixed, and different significances of the signal are produced by changing the amount of background events. It is clearly visible that for high significant signals the uncertainty in the reconstruction of the source location is dominated by the number of excess excess events that build the signal. On the other hand, if the significance of the signal is low, the fluctuations of the *on* and *off* maps increase the uncertainty of the source location.

9.3.1 Gamma-ray sky map

Figure 9.4 shows a significance map produced from the signal and background maps, both smoothed with a Gaussian of $\sigma = 6'$ (corresponding to the gamma-PSF), for photon energies between 150 GeV and 1 TeV. For the background rejection, a loose cut in the *Hadronness* parameter is applied to keep a large number of gamma-like events. The actual values and efficiencies of the cuts are shown in Table 9.2.

The sky map shows a significant gamma-ray excess, at a level of 5.4σ, displaced from the catalog position of the blazar 3C 66A, which was the target of the observations. The actual center of gravity of the γ-ray emission is derived from Figure 9.4 by fitting a bell-shaped function of the form

$$F(x,y) = A \cdot \exp\left[-\frac{(x-\bar{x})^2 + (y-\bar{y})^2}{2\sigma^2}\right] \tag{9.1}$$

for which the distribution of the excess events is assumed to be rotationally symmetric, i.e., $\sigma_x = \sigma_y = \sigma$. In addition, the width of the function for a point source seen by the MAGIC telescope was estimated using a contemporaneous Crab Nebula data sample to be $\sigma = 5.'1$, and this variable (σ) was fixed in the fit. The fit yields reconstructed coordinates of the excess center of R.A. $= 2^{\mathrm{h}}23^{\mathrm{m}}12^{\mathrm{s}}$ and decl.$= 43°0.'7$. The detected excess, which is named MAGIC J0223+430, is $6.'1$ away from the catalog position of 3C 66A, while the distance to 3C 66B is $1.'1$.

Statistic uncertainty of the excess position

This statistic uncertainty is dominated by the fact that the sky map is obtained by subtracting an *off* map from an *on* map. If the signal level is large compared to the fluctuations on both maps (signal with high significance), the uncertainty is dominated by the number of excess events that build the signal (see Figure 9.5). If the signal level is lower (as it is the case in the MAGIC J0223+430 detection), the intrinsic fluctuations in the *on* and *off* maps cause a higher uncertainty of the fitted source position. This effect is investigated using a toy-MC simulation.

In order to estimate the statistical uncertainty of the reconstructed position, 10^4 sky maps were simulated with the same number of background and excess events as in the data. The excess position in the sky maps was fitted using Equation 9.1 and the distance to the simulated source position was calculated. From the histogram of the deviations (see Figure 9.7), the probabilities to obtain a reconstructed source position with a larger or equal offset from the true source than a given deviation can be computed. The probabilities shown in Figure 9.4 by the green contours correspond to 68.2%, 95.4%, and 99.7% for the inner, middle, and outer contour, respectively.

The measured excess coincides with the catalog position of 3C 66B. The origin of the emission from 3C 66A can be statistically excluded with a probability of 95.6% (2.0σ). Adding linearly the systematic uncertainty of the pointing of the data set ($2'$, see above), i.e., shifting the excess position by $2'$ toward the catalog position of 3C 66A, the exclusion probability is 85.4% (1.5σ).

9.3.2 Significance of the detection

To calculate the significance of the detection, an *Alpha* distribution was produced. For the calculation of the source-dependent image parameters used in the analysis, the fitted position of the excess was considered. Background rejection was achieved by a tight *Hadronness*, which was optimized using Crab Nebula data taken in similar conditions and diluted to 5% of its real flux. The cut in *Alpha* that defines the signal region was also optimized in the same way. This set of tight cuts is described in Table 9.2. A signal of $6.0\,\sigma$ significance (pre-trial) was found (see Figure 9.8). The number of trials of the signal search was estimated by projecting the gamma-ray acceptance of the MAGIC camera into the field of view of the observations, and defining the search region where the gamma-ray acceptance after cuts is larger than 50% (see Figure 9.9). In this way, an area of $2.18\,\mathrm{deg}^2$ was obtained as search region. Given that the 68% containment radius for γ-rays from a point-like source is $0.^\circ152$, the number of independent trials was calculated to be 30:

$$N_{trials} = \frac{A_{search}}{A_{68\%}} = \frac{A_{search}}{\pi r_{68\%}^2} = \frac{2.18\,\mathrm{deg}^2}{\pi\,(0.152\,\mathrm{deg})^2} \approx 30 \tag{9.2}$$

After correcting for the estimated trial factor, the significance of the MAGIC J0223+430 detection is 5.4σ.

9.3.3 Gamma-ray light curve

Figure 9.10 shows the gamma-ray light curve of MAGIC J0223+430 together with the flux of 3C 66A in optical wavelengths. The integral flux above 150 GeV corresponds to $(7.3 \pm 1.5) \times 10^{-12}\,\mathrm{cm}^{-2}\,\mathrm{s}^{-1}$ (2.2% of the Crab Nebula flux) and is the lowest flux detected with the MAGIC telescope so far. The gamma-ray light curve is consistent with a constant

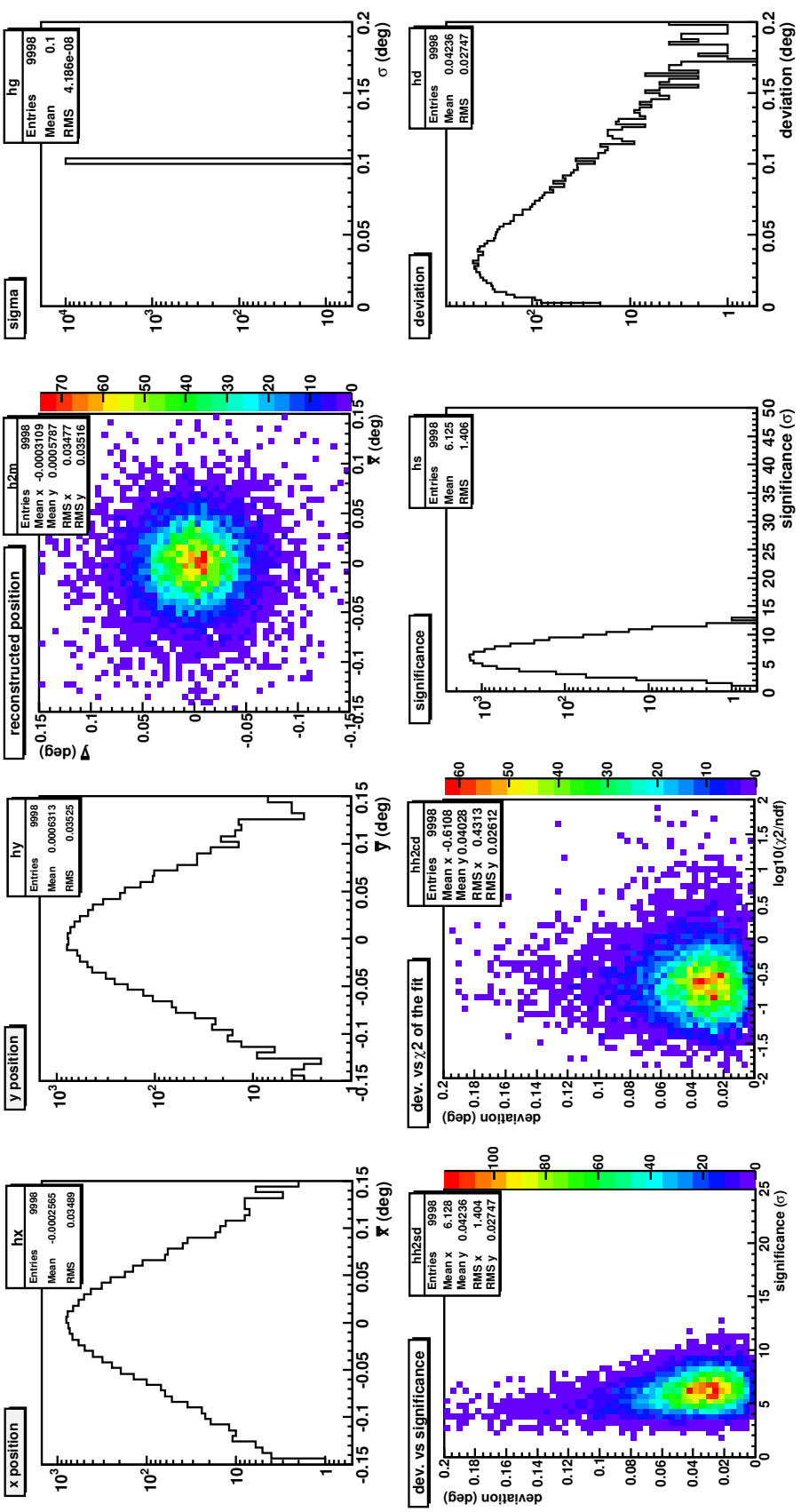

Figure 9.6: Distributions of the different parameters from Equation 9.1 fitted to the 10^4 MC generated skymaps. The deviation is defined as the distance between the reconstructed source position obtained from the fit and the simulated source position (0,0). The σ parameter in Equation 9.1 is fixed in the fit. The number of background and excess events was fixed to be the same as in the MAGIC J0223+430 sky map (Figure 9.4).

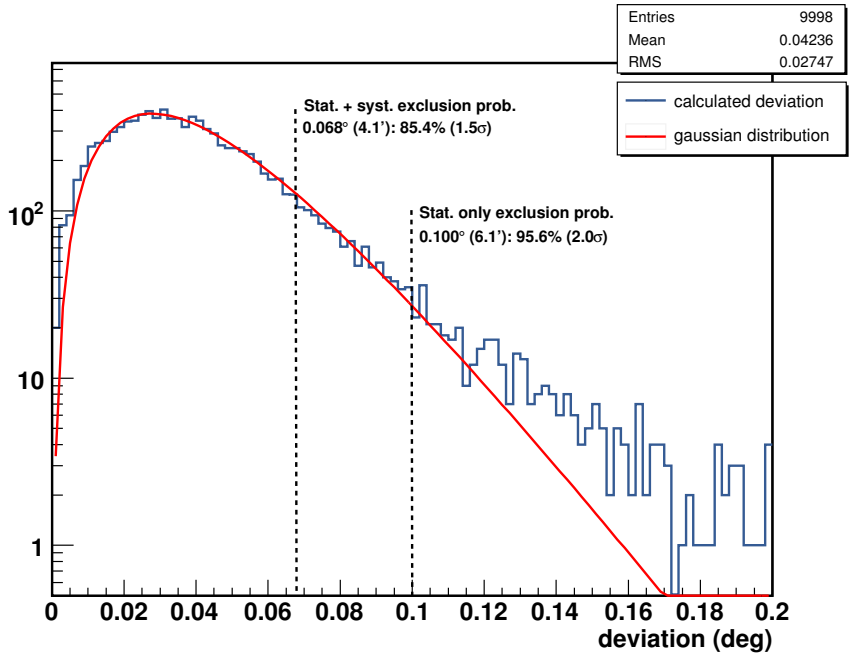

Figure 9.7: Deviation of the reconstructed source position with respect to the simulated source location in the MC generated sky maps.

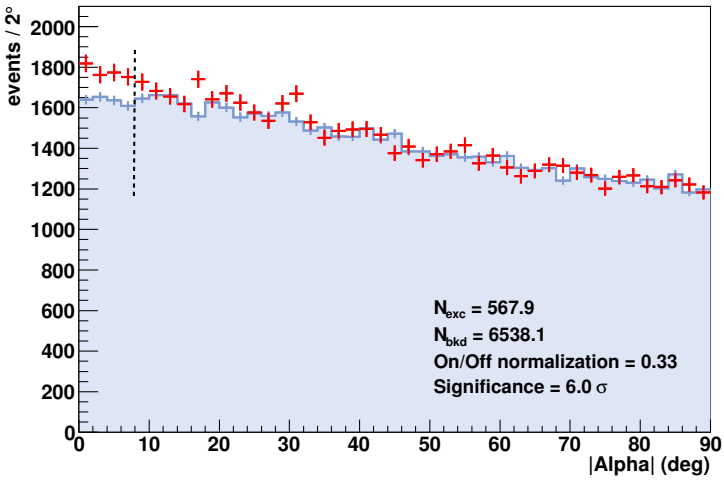

Figure 9.8: *Alpha* distribution after all cuts evaluated with respect to the position of MAGIC J0223+430. A gamma-ray excess with a significance of $6.0\,\sigma$ is found, which corresponds to a post-trial significance of $5.4\,\sigma$.

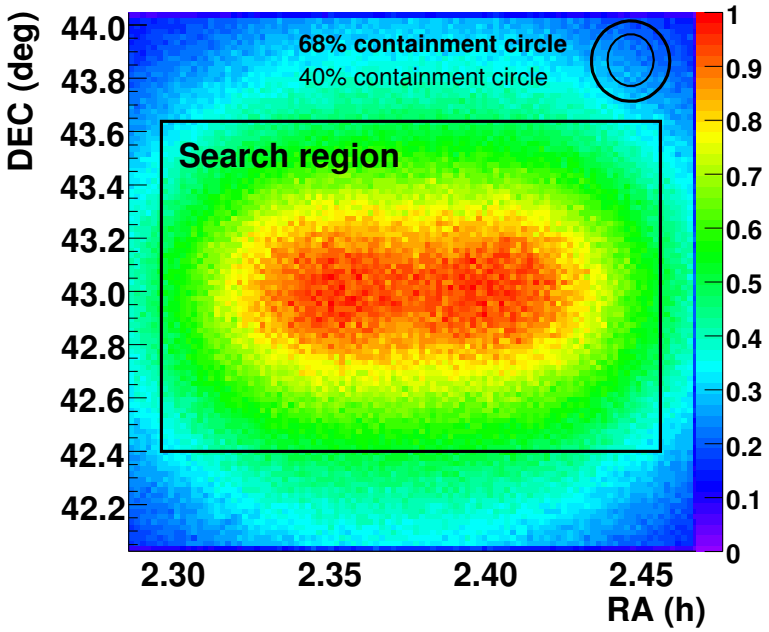

Figure 9.9: Acceptance of the MAGIC camera projected into the MAGIC J0223+430 field of view.

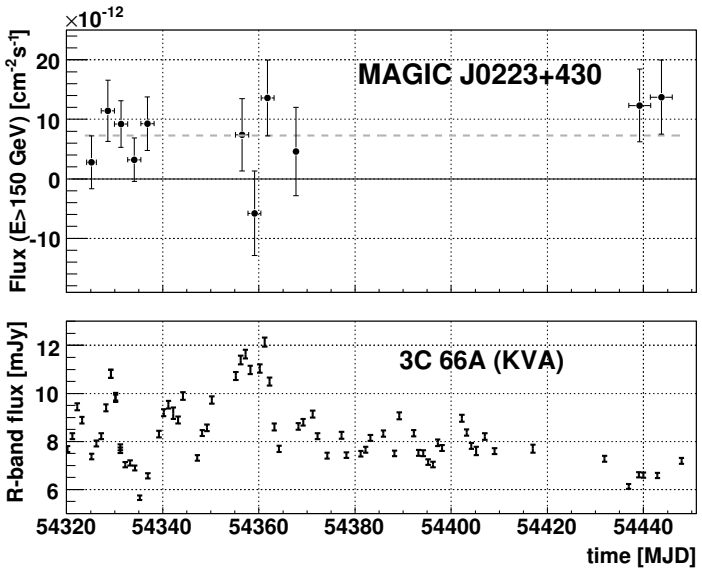

Figure 9.10: Light curve of MAGIC J0223+430. Upper panel: MAGIC integral flux above 150 GeV in bins of 3 days (except for periods where the sampling was coarser). The gray dashed line indicates the average gamma-ray flux. Lower panel: optical light curve of 3C 66A as measured by the KVA telescope.

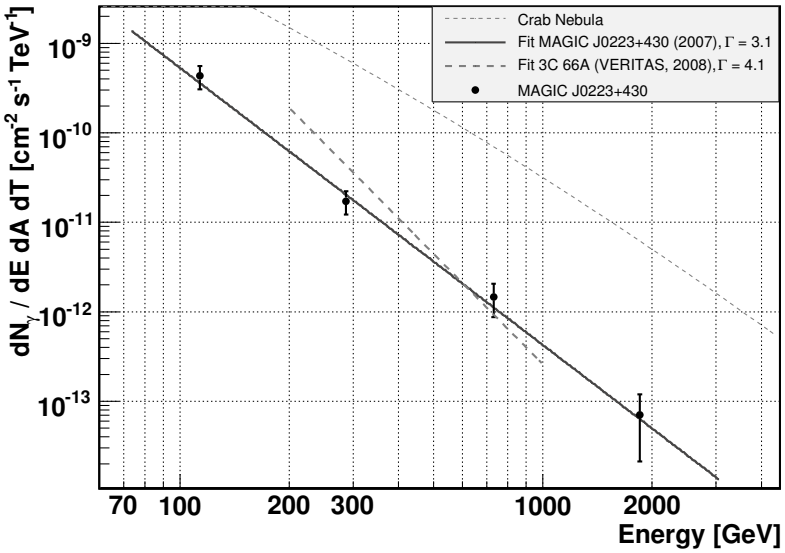

Figure 9.11: Differential energy spectrum of MAGIC J0223+430. The fit to the data is shown by the solid gray line and the fit parameters are listed in the inset. No correction for the $\gamma - \gamma$ attenuation due to the EBL has been made. The Crab Nebula spectrum (Albert et al., 2008*f*) is also shown as a reference (dashed gray line).

flux within statistical errors. These errors, however, are large, and some variability of the signal below MAGIC sensitivity cannot be excluded. During the MAGIC observations 3C 66A was very bright at optical wavelengths varying from 6 mJy to 12 mJy in the *R*-band (the baseline flux in the historical data being $\sim$ 6 mJy). In the same period the optical flux of 3C 66B remained constant, which is a typical behavior for large radio galaxies.

9.3.4 Energy spectrum

For the energy spectrum of MAGIC J0223+430, loose cuts are made to keep the gamma-ray acceptance high (see Table 9.2). The differential energy spectrum was unfolded using the Tikhonov unfolding technique and is shown in Figure 9.11. The spectrum can be well fitted by a power law, which gives a differential flux (TeV^{-1} cm^{-2} s^{-1}) of:

$$\frac{\mathrm{d}N}{\mathrm{d}E\,\mathrm{d}A\,\mathrm{d}t} = (1.7 \pm 0.3) \times 10^{-11} (E/300\,\mathrm{GeV})^{-3.1\pm0.3} \tag{9.3}$$

The quoted errors are statistical only. The systematic uncertainty is estimated to be 35% in the flux level and 0.2 in the power law photon index.

9.3.5 Origin of the low energy events

The possibility of a contribution of VHE gamma-rays from 3C 66A at low energies to the detected signal was investigated in the MAGIC data sample. An sky map of gamma-like events with energy 75 GeV $< E <$ 150 GeV was produced, showing no statistically significant emission. It must be noted that the production of sky maps at such low energies faces two main problems. First, the sensitivity of the analysis worsens appreciably

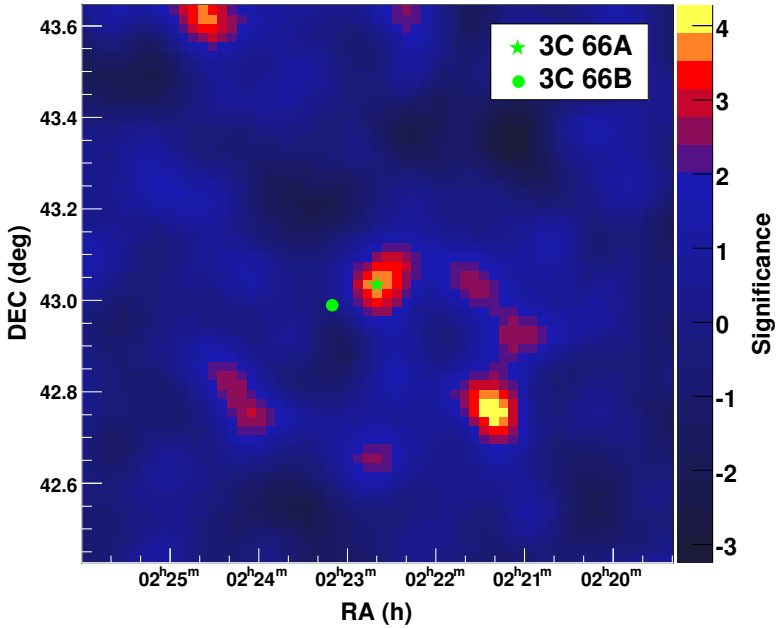

Figure 9.12: Significance map for gamma-like events with energy 75 GeV $< E <$ 150 GeV in the observed sky region, for the days 15–18 August 2007 (MJD 54327–30) and 18–20 September 2007 (MJD 54361–3). The catalog positions of 3C 66A and 3C 66B are indicated by a green star and a green dot, respectively.

at energies below $\sim$ 200 GeV, mainly because the background rejection power of the *Hadronness* parameter decreases significantly for low energy images. In addition, the capability of the analysis to determine the arrival direction of the shower also decreases with the gamma-ray energy, worsening the gamma-PSF.

The blazar 3C 66A has been reported to be a variable VHE gamma-ray emitter by the VERITAS collaboration (Acciari et al., 2009), and the detection coincided with an optical high state of the source (Larionov et al., 2008). Given this possible connection between optical and VHE gamma-ray high states, already proposed for blazars in general in Lindfors et al. (2009), a search for gamma-ray emission from 3C 66A in connection with the periods when the source was brighter in the optical band was conducted.

The days close to the highest recorded optical fluxes where chosen. The selection included the days around the bright optical flare in August 2007 (15–18 Aug, i.e. MJD 54327–30) and also close to the historical maximum flux in September (18–20 Sept, i.e. MJD 54361–3). The light curve of 3C 66A in the optical R-band is shown in Figure 9.10. The resulting sky map of gamma-like events with estimated energy of 75 GeV $< E <$ 150 GeV, for data selected around the optical high states, is shown in Figure 9.12. The sky map shows a small gamma-ray excess spatially coinciding with the catalog position of 3C 66A. However, the excess is just above the level of noise fluctuations, as can be seen by the fact that there are other hotspots in the sky map with comparable, or even larger significance. Therefore, no strong conclusion can be extracted about possible gamma-ray flares of 3C 66A during the MAGIC observation campaign.

9.4 Discussion of the results

A VHE gamma-ray source MAGIC J0223+430 was detected in August–December 2007. Given the position of the excess measured by MAGIC above 150 GeV. The VHE gamma-ray flux was found to be on the level of 2.2% Crab Nebula flux, and no hint of variability was found within statistical errors. The differential spectrum of MAGIC J0223+430 has a photon spectral index of $\Gamma = 3.10 \pm 0.31$ and extends up to ~ 2 TeV.

The VERITAS collaboration recently detected VHE gamma-ray emission from 3C 66A (Acciari et al., 2009), with most of the signal coming from a gamma-ray flare 2008 September–October. The measured integral flux above 200 GeV is 6% of the Crab Nebula flux, and the energy spectrum is characterized by a soft power law with photon index $\Gamma = 4.1$ (see Figure 9.11). In view of this detection, it is noted that if 3C 66A was emitting gamma-rays in August–December 2007 (i.e., during the MAGIC observations), then its flux was at a significantly lower level than in 2008.

A possible interpretation of the detection of MAGIC J0223+430 would be that this signal originates from the blazar 3C 66A. Based only on the location of the gamma-ray source, this possibility can just be excluded at a 1.5σ level. However, the misplacement of the gamma-ray excess is not the only argument against this interpretation. Due to the energy-dependent absorption of VHE gamma-rays with low-energy photons of the EBL (see Figure 4.3(a)), the gamma-ray flux of a source at a distance comparable with that of 3C 66A would be strongly suppressed at high energies. This absorption is estimated to be of more than 99% already at energies around 600 GeV. In this scenario, it is difficult to accommodate the measured energy spectrum of MAGIC J0223+430 as being originated by a distant blazar at redshift $z = 0.444$.

Following the prescription of Mazin and Raue (2007), and assuming a low EBL density (lower limit derived in Albert et al., 2008*e*) it is possible to derive an upper limit for MAGIC J0223+430 of $z < 0.17$ ($z < 0.24$) under the assumption that the intrinsic energy spectrum cannot be harder than $\Gamma = 1.5$ ($\Gamma = 0.666$). This assumption of $\Gamma > 1.5$ is based on particle acceleration arguments (Aharonian et al., 2006*b*), and the fact that none of the sources in the EGRET energy band (not affected by the EBL) have shown a harder spectrum, a trend confirmed by *Fermi*-LAT in their first three months of observations. The latter assumption of $\Gamma > 0.666$ can be considered as an extreme case of the spectrum hardness, suggesting a monochromatic spectrum of electrons when interacting with a soft photon target field (Katarzyński et al., 2006). If $z > 0.24$ for MAGIC J0223+430, an alternative explanation for a hard intrinsic spectrum at energies above 100 GeV can be given if gamma-rays are passing through a narrow band of optical-infrared photons in the vicinity of the blazar. Such narrow radiation fields can produce arbitrarily hard intrinsic spectra by absorbing specific energies of gamma-rays (Aharonian et al., 2008*c*). In this case, the intrinsic VHE luminosity of 3C 66A should exceed $10^{47}\,\mathrm{erg\,s^{-1}}$, which is an unusually large value for a BL Lac object.

Being the association of MAGIC J0223+430 improbable because of the position of the gamma-ray excess and its energy spectrum, the interpretation that the signal could be originated in the radio-galaxy 3C 66B seems plausible. The location of MAGIC J0223+430 spatially coincides with the catalog position of 3C 66B, which can be considered as a natural candidate for TeV emission since it has similar characteristics to another radio-galaxy: M 87, which has been detected at VHE gamma-rays. Since the distance of 3C 66B is 85.5 Mpc, its intrinsic VHE luminosity would be two to eight times higher than the one of M 87 (22.5 Mpc) given the reported variability of M 87 (Aharonian et al., 2006*d*; Albert

et al., 2008*d*).

As in the case of M 87, there would be several possibilities for the region responsible of the TeV radiation in 3C 66B: the vicinity of the supermassive black hole (Neronov and Aharonian, 2007), the unresolved base of the jet (in analogy with blazar emission models, Tavecchio and Ghisellini, 2008) and the resolved jet. Unlike for M 87, significant variability in the VHE gamma-ray flux is not observed, and therefore no constraints on the size of the emission region can be derived. However, as the angle to line of sight is even larger than in M 87 (M 87: 19°, Perlman et al. (2003); 3C 66B: 45°, Giovannini et al. (2001)) the resolved jet seems an unlikely site of the emission. On the other hand, the unresolved base of the jet seems a likely candidate for the emission site as it could point with a smaller angle to the line of sight. If the viewing angle was small, blazar-like emission mechanisms cannot be excluded. The orbital motion of 3C 66B shows evidence for a supermassive black hole binary with a period of 1.05 ± 0.03 years (Sudou et al., 2003). If the central black hole would indeed be a binary system, it would likely cause the jet to be helical, and the pointing direction of the unresolved jet could differ significantly from the direction of the resolved jet.

It has also been proposed that the spectrum obtained by MAGIC could be interpreted as combined emission from 3C 66B, dominating above ~ 200 GeV, and 3C 66A (Tavecchio and Ghisellini, 2009, see Figure 9.13). The high-energy emission from the blazar would be strongly attenuated by the interaction with the EBL, and could only contribute to the measured excess at low energies. The emission from 3C 66B could be explained as radiation coming from the layer of the jet, in the framework of the structured jet model Ghisellini et al. (2005) already used to interpret the TeV emission of M 87 (Tavecchio and Ghisellini, 2008).

Given the likely association of MAGIC J0223+430 with 3C 66B, this detection would establish radio galaxies as a new class of VHE gamma-ray emitting sources. According to Ghisellini et al. (2005), there are eight FR I radio galaxies in the 3CR catalog that should have a higher gamma-ray flux at 100 MeV than 3C 66B, but possibly many of these sources are rather weak in the VHE gamma-ray band. Further observations of radio galaxies with the Fermi Gamma-ray Space Telescope as well as by ground-based telescopes are needed to further study the gamma-ray emission properties of radio galaxies.

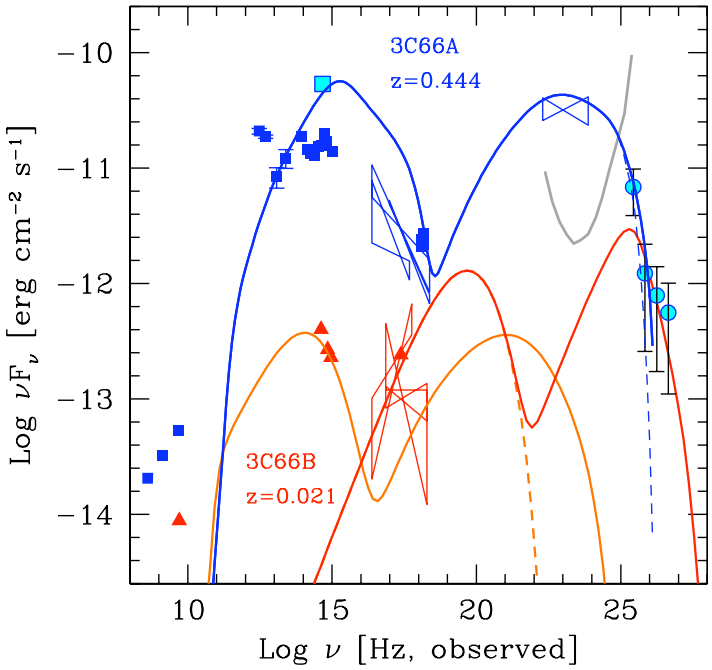

Figure 9.13: SED of 3C 66B and of 3C 66A. Data for 3C 66A (blue squares and bow-ties) The square in cyan reports the average optical (R–band) flux during the observations of MAGIC. The SED of 3C 66A has been reproduced with the model for the blazar emission described in Celotti and Ghisellini (2008). The solid line is the spectrum emitted at the source, while the dashed line reports the γ–ray emission reaching the Earth after being absorbed by the interaction with the extragalactic background light (assuming the LowSFR model of Kneiske et al. (2004) and a redshift of $z = 0.444$). The measured VHE spectrum of MAGIC (cyan circles) is reproduced as the sum of the emission from both sources, 3C66A being dominant below 200 GeV, and 3C66B accounting for the emission above 200 GeV. The grey line reports the *Fermi* sensitivity (for 1 year and 5σ significance). Figure taken from Tavecchio and Ghisellini (2009).

Chapter 10

Discussion and conclusions

Before the work of this thesis started, there were 14 blazars detected by ground-based Cherenkov telescopes in the energy range between 80 GeV and 20 TeV. The farthest known object at VHE was the H.E.S.S. detected blazar 1ES 1101-232, located at redshift $z = 0.186$. Additionally, all those blazars belonged to the BL Lac subclass, while the EGRET satellite detector had detected mostly quasars in the energy range from 0.1 GeV to 30 GeV. The observed spectral properties of the farthest detected blazars showed evidences of a lower level of gamma-ray absorption due to the interaction with EBL lower than expected by most of the models describing the EBL density. If true, this lower level of EBL would show up as a lower attenuation level for gamma-rays, making the detection of VHE gamma-ray sources at larger distances possible.

This possibility motivated a search for distant BL Lacs that could be candidates to emit VHE gamma-rays, resulting in the identification of five candidates that were proposed and accepted for observation with the MAGIC telescope. The selection was based on a search of candidates in optical and X-ray catalogues, finding for the sources with high synchrotron luminosity, and also with the synchrotron peak located at the highest frequencies, maximizing the chances of detection. Because of these criteria, all the selected candidates were high-frequency-peaked BL Lacs.

The observation of this sources resulted in four gamma-ray flux upper limits, and a detection of a gamma-ray source in the field of view of the blazar 3C 66A. The derived upper limits for the blazars 1ES 0158+003, B3 1009+427, 1ES 1028+511 and 2E 1415.6+3557 are the most restrictive set up to now at energies $E > 150$ GeV, constraining their flux level to be $\lesssim$ 2–13% of the Crab Nebula flux with a 99.9% confidence level. These results discourage continuous observations of these sources, only motivating observations when their flux at other frequencies (optical, X-ray, or low-energy gamma-rays) indicates the possibility of a gamma-ray flare, triggering a target of opportunity observation.

In parallel to this search for distant BL Lacs emitting VHE gamma-rays, a similar program focused on low-frequency-peaked BL Lacs and quasars was set up. It resulted in the detection of VHE gamma-rays from the quasar 3C 279 ($z = 0.536$) during a gamma-ray flare on 23 February 2006. This is the first detection of a quasar in the VHE range, and also represents the most distant object detected at these energies so far. The discovery confirmed the interpretation of a low-level of EBL photons, probing it up to redshifts of $z \simeq 0.5$ and extending the previously set density upper limits in the optical and UV range.

Additional interest on this detection was triggered because the measured spectrum of 3C 279 is difficult to reconcile with standard leptonic emission models, that where

previously used to describe the multiwavelength spectral energy distribution of this quasar up to energies of few GeV. In view of the MAGIC detection, several authors have discussed the need of a second emission component, or suggested hadronic models, to explain the observed spectrum.

The observations of the blazar 3C 66A ($z = 0.444$, uncertain), performed in August–December 2007, yielded a positive detection of a VHE gamma-ray source. A detailed analysis of the gamma-ray signal concluded that the position of the detected gamma-ray source was offset the catalog position of 3C 66A by 6.'1, and spatially coinciding with the radio-galaxy 3C 66B. Considering the statistical and systematic uncertainty of the reconstructed source position by MAGIC, the blazar 3C 66A could be spatially excluded as the origin of the VHE gamma-ray emission with a confidence level of 1.5σ. Additionally, the spectrum of the detected source –named MAGIC J0223+430– was extending up to energies $E > 1\,\mathrm{TeV}$, where the absorption of gamma-rays by the EBL is expected to be larger than 99% for a source at redshift $z = 0.444$. These two facts: misplaced source position, and spectrum detected up to energies larger than 1 TeV, leave three possible scenarios for the association of MAGIC J0223+430:

- The origin of the detected emission is not the blazar 3C 66A but the radio-galaxy 3C 66B. This association is supported by the fact that the location of the emission detected by MAGIC coincides with the catalog position of 3C 66B, and because this radio-galaxy is much closer than 3C 66A, having a redshift of $z = 0.021$. The closeness of 3C 66B makes the absorption of gamma-rays by the EBL almost irrelevant, being compatible with the detection of gamma-rays at energies $E > 1\,\mathrm{TeV}$. On the other hand, the radio-galaxy 3C 66B has similar characteristics to M 87, another nearby radio-galaxy, which was already detected at TeV energies.

- The entire flux of gamma-rays detected by MAGIC is indeed originated by the blazar 3C 66A. If that is the case, the misplacement of the gamma-ray excess could be caused by the signal level being close to the background fluctuations, given the low significance of the signal (5.4σ after trial factor). Additionally, the detection of gamma-rays with energy $E > 1\,\mathrm{TeV}$ has to be explained by either of these arguments:

  - The redshift of 3C 66A, usually quoted as $z = 0.444$ but still uncertain, is in fact lower. Actually, a redshift upper limit can be derived from the MAGIC J0223+430 spectrum, assuming a low model for the EBL density and its gamma-ray emission to be of blazar-like origin (meaning that its intrinsic photon index can not be harder than $\Gamma^\star = 0.66$). Under these assumptions, a redshift upper limit of $z < 0.24$ can be derived.
  - The redshift of 3C 66A is larger than $z = 0.24$ but the mechanism responsible for the gamma-ray emission is not within the standard accepted emission models for blazars. Exotic scenarios that could produce very hard intrinsic spectra include a very narrow distribution of the energy of the high energy electrons responsible for the emission, or a dense photon field near the source that could cause an additional absorption at mid-energies, causing the intrinsic spectrum to harden.

- The two objects: the blazar 3C 66A and the radio-galaxy 3C 66B contribute to the MAGIC detected emission. If that is the case, emission from 3C 66B would

be dominant at energies $E \gtrsim 200\,\mathrm{GeV}$, and 3C 66A would only contribute at low energies as its flux would be attenuated by EBL absorption.

In addition to these arguments, the VERITAS collaboration published the detection of VHE gamma-rays from the blazar 3C 66A one year after the observations by MAGIC, with most of the signal coming from a gamma-ray flare in October–November 2008. This detection confirms the blazar 3C 66A to be a variable emitter of VHE gamma-rays, and suggests that its flux during MAGIC observations was at a much lower state than the one detected by VERITAS.

Future observations of this region both with ground-based Cherenkov telescopes and satellite detectors like *Fermi*-LAT will help to clarify the origin of the emission detected by MAGIC. The observed spectrum of MAGIC J0223+430 does not predict a detectable flux by *Fermi*-LAT at few GeV, being the blazar 3C 66A likely dominant at those low energies. Therefore, ground-based telescopes are, because of their sensitivity at energies $E > 100\,\mathrm{GeV}$ and their better angular resolution, the best suited instruments to explore this sky region, being the simultaneous detection of the blazar 3C 66A and the radio-galaxy 3C 66B possible if both are confirmed as VHE gamma-ray sources and are simultaneously observed in an active state.

Acknowledgements

First I would like to thank Enrique Fernandez and Matteo Cavalli-Sforza for providing me the opportunity to make my PhD thesis at IFAE.

I am very thankful to my supervisor Manel Martínez for opening the doors of MAGIC to me, and for all his support during my whole stay at IFAE. Apart from giving me good advice, he always trusted me and gave me the freedom to make my own decisions and learn through my own mistakes. His deep knowledge on hardware, statistics and fundamental physics, together with his enthusiasm, made every discussion with him very fruitful. Daniel Mazin also played a fundamental role in the elaboration of this thesis. He supervised all I did in data analysis in the last two years. The huge amount of scientific and practical stuff I learned with him is priceless. Besides, due to his easygoing nature, working with him does not feel like working. In addition, both Manel and Daniel were very busy in the last months, but always found some time to discuss the final details of this thesis and to revise my drafts, and I am extremely grateful for that.

There are other people that crucially contributed to the results presented in this thesis. It has been a real pleasure to work with Pratik Majumdar and Elisa Prandini in the analysis 3C 279. Part of this work was done in Munich, and I seize the opportunity to thank the people from the MAGIC group at the MPI for treating me so well every time I stayed there, and turning my visits into enjoyable experiences of intense work and restoring leisure. I am very grateful again to Elisa for her very fast and efficient crosscheck of the 3C 66A/B analysis, and to Elina Lindfors for the one-year-lasting discussions about this result, which were always liven up by her arctic sense of humor. I would also like to spread my gratitude to the whole MAGIC collaboration for the very friendly atmosphere that we have worked in. I keep good memories of every workshop, meeting and shift I took part in, where I always found encouraging comments, pleasant chats, and the proper company to meet the Sun after an endless night of work.

The people from the MAGIC group at IFAE always had the doors wide open in every occasion, from desperate troubles to ridiculous matters. I am very thankful to all of them for their full time predisposition when I needed a helping hand. All this specially applies to Diego, who is the best possible office mate in the Northern Hemisphere. I also thank the younger PhD students, and the UAB ones as well, for sharing lunchtime and some beers and night life after work. This has been an electrifying energy input from which I hope never to be unplugged. For sure I will miss their contagious good mood: prevailing some days, a bit more elusive in others. Separate mention deserve the colleagues that already left IFAE for a better life. They showed me all the friendly spaces along the corridor when I joined the group. At this point, special thanks to Ester. She asked about the status of my thesis every single time we spoke in the last two years, and helped me a lot with my U.S. trip. I am also very thankful to Manuel Delfino for easing my teaching duties, and to the other colleagues who worked with me at class.

Through all these years, I always profited from sharing experiences with my friends from the Physics Faculty, specially with Antonio and Noelia, who are the ones that will testify for me in the Judgement Day, speaking in my name. Great acknowledgements go also to our alpine hiking team. It is good to have you guys on the other end of the rope.

An finally, I would like to acknowledge the help of my parents for their continuous encouragement, my brother and cousin for invading my flat every Friday night, and the attention and support I always got from the rest of my family and friends.

Bibliography

Abdo A.A., Allen B., Berley D. et al. (2007). *TeV Gamma-Ray Sources from a Survey of the Galactic Plane with Milagro.* ApJ **664** L91–L94. 0705.0707.

Abdo A.A. et al. (2009). *Fermi Large Area Telescope Bright Gamma-ray Source List.* ArXiv e-prints 0902.1340.

Abraham J., Abreu P., Aglietta M. et al. (2007). *Correlation of the Highest-Energy Cosmic Rays with Nearby Extragalactic Objects.* Science **318** 938–. 0711.2256.

Abraham J., Abreu P., Aglietta M. et al. (2008). *Observation of the Suppression of the Flux of Cosmic Rays above* $4{\times}10^{19}$ *eV.* Physical Review Letters **101** 061101–+. 0806.4302.

Acciari V.A., Aliu E., Arlen T. et al. (2009). *Veritas Observations of a Very High Energy* γ*-Ray Flare From the Blazar 3C 66A.* ApJ **693** L104–L108. 0901.4527.

Acciari V.A., Aliu E., Beilicke M. et al. (2008*a*). *VERITAS Discovery of* $>$ 200 *GeV Gamma-Ray Emission from the Intermediate-Frequency-Peaked BL Lacertae Object W Comae.* ApJ **684** L73–L77. 0808.0889.

Acciari V.A., Beilicke M., Blaylock G. et al. (2008*b*). *Observation of Gamma-Ray Emission from the Galaxy M87 above 250 GeV with VERITAS.* ApJ **679** 397–403. 0802.1951.

Aharonian F., Akhperjanian A., Beilicke M. et al. (2003). *Is the giant radio galaxy M 87 a TeV gamma-ray emitter?* A&A **403** L1–L5. arXiv:astro-ph/0302155.

Aharonian F., Akhperjanian A., Beilicke M. et al. (2004). *Observations of 54 Active Galactic Nuclei with the HEGRA system of Cherenkov telescopes.* A&A **421** 529–537.

Aharonian F., Akhperjanian A.G., Anton G. et al. (2009). *Discovery of Very High Energy* γ*-Ray Emission from Centaurus A with H.E.S.S.* ApJ **695** L40–L44. 0903.1582.

Aharonian F., Akhperjanian A.G., Aye K.M. et al. (2005*a*). *A New Population of Very High Energy Gamma-Ray Sources in the Milky Way.* Science **307** 1938–1942. arXiv:astro-ph/0504380.

Aharonian F., Akhperjanian A.G., Aye K.M. et al. (2005*b*). *Discovery of the binary pulsar PSR B1259-63 in very-high-energy gamma rays around periastron with HESS.* A&A **442** 1–10. arXiv:astro-ph/0506280.

Aharonian F., Akhperjanian A.G., Aye K.M. et al. (2005*c*). *Discovery of Very High Energy Gamma Rays Associated with an X-ray Binary.* Science **309** 746–749. arXiv:astro-ph/0508298.

Aharonian F., Akhperjanian A.G., Barres de Almeida U. et al. (2007). *New constraints on the mid-IR EBL from the HESS discovery of VHE γ-rays from 1ES 0229+200.* A&A **475** L9–L13. 0709.4584.

Aharonian F., Akhperjanian A.G., Barres de Almeida U. et al. (2008*a*). *Limits on an Energy Dependence of the Speed of Light from a Flare of the Active Galaxy PKS 2155-304.* Physical Review Letters **101** 170402–+. 0810.3475.

Aharonian F., Akhperjanian A.G., Bazer-Bachi A.R. et al. (2006*a*). *A detailed spectral and morphological study of the gamma-ray supernova remnant RX J1713.7-3946 with HESS.* A&A **449** 223–242. arXiv:astro-ph/0511678.

Aharonian F., Akhperjanian A.G., Bazer-Bachi A.R. et al. (2006*b*). *A low level of extragalactic background light as revealed by γ-rays from blazars.* Nature **440** 1018–1021. arXiv:astro-ph/0508073.

Aharonian F., Akhperjanian A.G., Bazer-Bachi A.R. et al. (2006*c*). *Discovery of very-high-energy γ-rays from the Galactic Centre ridge.* Nature **439** 695–698. arXiv:astro-ph/0603021.

Aharonian F., Akhperjanian A.G., Bazer-Bachi A.R. et al. (2006*d*). *Fast variability of tera-electron volt rays from the radio galaxy M87.* Science **314** 1424–1427. arXiv:astro-ph/0612016.

Aharonian F., Buckley J., Kifune T. et al. (2008*b*). *High energy astrophysics with ground-based gamma ray detectors.* Reports on Progress in Physics **71** 096901–+.

Aharonian F.A. (2001). *TeV blazars and cosmic infrared background radiation.* In O.G. Gladysheva, G.E. Kocharov, G.A. Kovaltsov and I.G. Usoskin, editors, *International Cosmic Ray Conference*, vol. 27 of *International Cosmic Ray Conference*, I250+.

Aharonian F.A., Khangulyan D. and Costamante L. (2008*c*). *Formation of hard very high energy gamma-ray spectra of blazars due to internal photon-photon absorption.* MNRAS **387** 1206–1214. 0801.3198.

Albert J., Aliu E., Anderhub H. et al. (2006*a*). *Discovery of Very High Energy Gamma Rays from 1ES 1218+30.4.* ApJ **642** L119–L122. arXiv:astro-ph/0603529.

Albert J., Aliu E., Anderhub H. et al. (2006*b*). *Discovery of Very High Energy γ-Rays from Markarian 180 Triggered by an Optical Outburst.* ApJ **648** L105–L108. arXiv:astro-ph/0606630.

Albert J., Aliu E., Anderhub H. et al. (2006*c*). *Variable Very-High-Energy Gamma-Ray Emission from the Microquasar LS I +61 303.* Science **312** 1771–1773. arXiv:astro-ph/0605549.

Albert J., Aliu E., Anderhub H. et al. (2007*a*). *Discovery of Very High Energy γ-Rays from 1ES 1011+496 at z = 0.212.* ApJ **667** L21–L24. 0706.4435.

Albert J., Aliu E., Anderhub H. et al. (2007*b*). *Observations of Markarian 421 with the MAGIC Telescope.* ApJ **663** 125–138. arXiv:astro-ph/0603478.

Albert J., Aliu E., Anderhub H. et al. (2007*c*). *Unfolding of differential energy spectra in the MAGIC experiment.* Nuclear Instruments and Methods in Physics Research A **583** 494–506. 0707.2453.

Albert J., Aliu E., Anderhub H. et al. (2007*d*). *Variable Very High Energy γ-Ray Emission from Markarian 501.* ApJ **669** 862–883. arXiv:astro-ph/0702008.

Albert J., Aliu E., Anderhub H. et al. (2008*a*). *FADC signal reconstruction for the MAGIC telescope.* Nuclear Instruments and Methods in Physics Research A **594** 407–419. arXiv:astro-ph/0612385.

Albert J., Aliu E., Anderhub H. et al. (2008*b*). *Implementation of the Random Forest method for the Imaging Atmospheric Cherenkov Telescope MAGIC.* Nuclear Instruments and Methods in Physics Research A **588** 424–432. 0709.3719.

Albert J., Aliu E., Anderhub H. et al. (2008*c*). *Probing quantum gravity using photons from a flare of the active galactic nucleus Markarian 501 observed by the MAGIC telescope.* Physics Letters B **668** 253–257. 0708.2889.

Albert J., Aliu E., Anderhub H. et al. (2008*d*). *Very High Energy Gamma-Ray Observations of Strong Flaring Activity in M87 in 2008 February.* ApJ **685** L23–L26. 0806.0988.

Albert J., Aliu E., Anderhub H. et al. (2008*e*). *Very-High-Energy gamma rays from a Distant Quasar: How Transparent Is the Universe?* Science **320** 1752–. 0807.2822.

Albert J., Aliu E., Anderhub H. et al. (2008*f*). *VHE γ-Ray Observation of the Crab Nebula and its Pulsar with the MAGIC Telescope.* ApJ **674** 1037–1055. 0705.3244.

Aliu E., Anderhub H., Antonelli L.A. et al. (2008). *Observation of Pulsed γ-Rays Above 25 GeV from the Crab Pulsar with MAGIC.* Science **322** 1221–. 0809.2998.

Aliu E., Anderhub H., Antonelli L.A. et al. (2009*a*). *Discovery of a Very High Energy Gamma-Ray Signal from the 3C 66A/B Region.* ApJ **692** L29–L33. 0810.4712.

Aliu E., Anderhub H., Antonelli L.A. et al. (2009*b*). *Improving the performance of the single-dish Cherenkov telescope MAGIC through the use of signal timing.* Astroparticle Physics **30** 293–305. 0810.3568.

Amelino-Camelia G., Ellis J., Mavromatos N.E. et al. (1998). *Tests of quantum gravity from observations of γ-ray bursts.* Nature **393** 763–765. arXiv:astro-ph/9712103.

Antonucci R. (1993). *Unified models for active galactic nuclei and quasars.* ARA&A **31** 473–521.

Armada A. (2005). *Characterization and some applications of the anode current monitoring system of the magic telescope.* Master's thesis, Univ. Autònoma de Barcelona.

Atkins R., Benbow W., Berley D. et al. (2000). *Evidence for TEV Emission from GRB 970417A.* ApJ **533** L119–L122.

Ballo L., Maraschi L., Tavecchio F. et al. (2002). *Spectral Energy Distributions of 3C 279 Revisited: BeppoSAX Observations and Variability Models.* ApJ **567** 50–57. arXiv:astro-ph/0111499.

Bartko H., Goebel F., Mirzoyan R. et al. (2005). *Tests of a prototype multiplexed fiber-optic ultra-fast FADC data acquisition system for the MAGIC telescope.* Nuclear Instruments and Methods in Physics Research A **548** 464–486. arXiv:astro-ph/0505204.

Bednarek W. (1993). *On the gamma-ray emission from 3C 279.* ApJ **402** L29–L32.

Bednarek W. (1997). *Gamma-rays from synchrotron pair cascades in blazars?* MNRAS **285** 69–81.

Benn C.R. and Ellison S.L. (1998). *Brightness of the night sky over La Palma.* New Astronomy Review **42** 503–507. arXiv:astro-ph/9909153.

Berger M.J. and Seltzer S.M. (1964). *Tables of Energy Losses and Ranges of Electrons and Positrons. NASA SP-3012.* NASA Special Publication **3012**.

Bernlöhr K. (2000). *Impact of atmospheric parameters on the atmospheric Cherenkov technique.* Astroparticle Physics **12** 255–268. arXiv:astro-ph/9908093.

Bernstein R.A. (2007). *The Optical Extragalactic Background Light: Revisions and Further Comments.* ApJ **666** 663–673.

Bernstein R.A., Freedman W.L. and Madore B.F. (2002). *The First Detections of the Extragalactic Background Light at 3000, 5500, and 8000 Å. I. Results.* ApJ **571** 56–84. arXiv:astro-ph/0112153.

Bhattacharjee P. (2000). *Origin and propagation of extremely high energy cosmic rays.* Phys. Rep. **327** 109–247. arXiv:astro-ph/9811011.

Biermann P.L., Chirvasa M., Falcke H. et al. (2002). *Single and binary Black Holes and their active environment.* ArXiv Astrophysics e-prints arXiv:astro-ph/0211503.

Biller S.D., Breslin A.C., Buckley J. et al. (1999). *Limits to Quantum Gravity Effects on Energy Dependence of the Speed of Light from Observations of TeV Flares in Active Galaxies.* Physical Review Letters **83** 2108–2111. arXiv:gr-qc/9810044.

Blandford R. and Eichler D. (1987). *Particle Acceleration at Astrophysical Shocks - a Theory of Cosmic-Ray Origin.* Phys. Rep. **154** 1–+.

Blandford R.D. and Konigl A. (1979). *Relativistic jets as compact radio sources.* ApJ **232** 34–48.

Bloom S.D. and Marscher A.P. (1996). *An Analysis of the Synchrotron Self-Compton Model for the Multi–Wave Band Spectra of Blazars.* ApJ **461** 657–+.

Böttcher M. (2008). *Implications of the VHE γ-Ray Detection of 3C279.* In F.A. Aharonian, W. Hofmann and F. Rieger, editors, *American Institute of Physics Conference Series*, vol. 1085 of *American Institute of Physics Conference Series*, 427–430.

Böttcher M., Basu S., Joshi M. et al. (2007). *The WEBT Campaign on the Blazar 3C 279 in 2006.* ApJ **670** 968–977. 0708.2291.

Böttcher M. and Bloom S.D. (2000). *Analyzing the Multiwavelength Spectrum of BL Lacertae during the 1997 July Outburst.* AJ **119** 469–477.

Böttcher M., Harvey J., Joshi M. et al. (2005). *Coordinated Multiwavelength Observation of 3C 66A during the WEBT Campaign of 2003-2004.* ApJ **631** 169–186. arXiv:astro-ph/0506209.

Böttcher M., Mause H. and Schlickeiser R. (1997). *γ-ray emission and spectral evolution of pair plasmas in AGN jets. I. General theory and a prediction for the GeV - TeV emission from ultrarelativistic jets.* A&A **324** 395–409.

Bramel D.A., Carson J., Covault C.E. et al. (2005). *Observations of the BL Lacertae Object 3C 66A with STACEE.* ApJ **629** 108–114. arXiv:astro-ph/0504515.

Bretz T., Dorner D., Wagner R.M. et al. (2009). *The drive system of the major atmospheric gamma-ray imaging Cherenkov telescope.* Astroparticle Physics **31** 92–101. 0810.4593.

Burbidge E.M. and Rosenberg F.D. (1965). *The Redshift of the Quasi-Stellar Radio Source 3c 279.* ApJ **142** 1673–+.

Burns M.L. and Harding A.K. (1983). *Comparison of photon-photon and photon-magnetic field pair production rates.* In M.L. Burns, A.K. Harding and R. Ramaty, editors, *Positron-Electron Pairs in Astrophysics*, vol. 101 of *American Institute of Physics Conference Series*, 416–420.

Cambrésy L., Reach W.T., Beichman C.A. et al. (2001). *The Cosmic Infrared Background at 1.25 and 2.2 Microns Using DIRBE and 2MASS: A Contribution Not Due to Galaxies?* ApJ **555** 563–571. arXiv:astro-ph/0103078.

Carmona E., Majumdar P., Moralejo A. et al. (2008). *Monte Carlo Simulation for the MAGIC-II System.* In *International Cosmic Ray Conference*, vol. 3 of *International Cosmic Ray Conference*, 1373–1376.

Celotti A. and Ghisellini G. (2008). *The power of blazar jets.* MNRAS **385** 283–300. 0711.4112.

Chary R., Casertano S., Dickinson M.E. et al. (2004). *The Nature of Faint 24 Micron Sources Seen in Spitzer Space Telescope Observations of ELAIS-N1.* ApJS **154** 80–86. arXiv:astro-ph/0406386.

Cherenkov P.A. (1935). *Visible emission of clean liquids by action of gamma radiation.* Dokl. Akad. Nauk. USSR **2** 451.

Collmar W., Böttcher M., Burwitz V. et al. (2004). *Multifrequency Observations of the Gamma-Ray Blazar 3C 279 in Low-State During INTEGRAL AO-1.* In V. Schoenfelder, G. Lichti and C. Winkler, editors, *5th INTEGRAL Workshop on the INTEGRAL Universe*, vol. 552 of *ESA Special Publication*, 555–+.

Coppi P.S. (1992). *Time-dependent models of magnetized pair plasmas.* MNRAS **258** 657–683.

Costamante L. (2007). *A low density of the extragalactic background light revealed by the H.E.S.S. spectra of the BL Lac objects 1ES 1101-232 and H 2356-309.* Ap&SS **309** 487–495. arXiv:astro-ph/0612709.

Costamante L., Aharonian F., Bühler R. et al. (2008). *The new surprising behaviour of the two "prototype" blazars PKS 2155-304 and 3C 279.* In F.A. Aharonian, W. Hofmann and F. Rieger, editors, *American Institute of Physics Conference Series*, vol. 1085 of *American Institute of Physics Conference Series*, 644–647.

Costamante L., Aharonian F., Horns D. et al. (2004). *Constraining the cosmic background light with four BL Lac TeV spectra.* New Astronomy Review **48** 469–472. arXiv:astro-ph/0308025.

Costamante L. and Ghisellini G. (2002). *TeV candidate BL Lac objects.* A&A **384** 56–71. arXiv:astro-ph/0112201.

Cotton W.D., Counselman III C.C., Geller R.B. et al. (1979). *3C 279 - The case for 'superluminal' expansion.* ApJ **229** L115–L117.

Dar A. and Laor A. (1997). *Hadronic Production of TeV Gamma-Ray Flares from Blazars.* ApJ **478** L5+. arXiv:astro-ph/9610252.

De Angelis A., Mansutti O., Persic M. et al. (2008). *Photon propagation and the VHE gamma-ray spectra of blazars: how transparent is really the Universe?* ArXiv e-prints 0807.4246.

de Diego J.A., Kidger M.R., Gonzales-Perez J.N. et al. (1997). *Rapid infrared spectral variability of 3C 66A in outburst.* A&A **318** 331–336.

Dermer C.D. and Schlickeiser R. (1993). *Model for the High-Energy Emission from Blazars.* ApJ **416** 458–+.

Dole H., Lagache G., Puget J.L. et al. (2006). *The cosmic infrared background resolved by Spitzer. Contributions of mid-infrared galaxies to the far-infrared background.* A&A **451** 417–429. arXiv:astro-ph/0603208.

Domingo-Santamaria E. et al. (2005). *The DISP analysis method for point-like or extended gamma source searches/studies with the MAGIC Telescope.* In *International Cosmic Ray Conference*, vol. 5 of *International Cosmic Ray Conference*, 363–+.

Donato D., Ghisellini G., Tagliaferri G. et al. (2001). *Hard X-ray properties of blazars.* A&A **375** 739–751. arXiv:astro-ph/0105203.

Dwek E., Arendt R.G. and Krennrich F. (2005). *The Near-Infrared Background: Interplanetary Dust or Primordial Stars?* ApJ **635** 784–794. arXiv:astro-ph/0508262.

Edge D.O., Shakeshaft J.R., McAdam W.B. et al. (1959). *A survey of radio sources at a frequency of 159 Mc/s.* MmRAS **68** 37–60.

Elbaz D., Cesarsky C.J., Chanial P. et al. (2002). *The bulk of the cosmic infrared background resolved by ISOCAM.* A&A **384** 848–865. arXiv:astro-ph/0201328.

Ellis J., Mavromatos N.E., Nanopoulos D.V. et al. (2006). *Robust limits on Lorentz violation from gamma-ray bursts.* Astroparticle Physics **25** 402–411. arXiv:astro-ph/0510172.

Elterman L. (1964). *Parameters for attenuation in the atmospheric windows for fifteen wavelengths.* Appl. Opt. **3** 745–+.

Errando M., Bock R., Kranich D. et al. (2008). *Discovery of very high energy gamma-rays from the flat spectrum radio quasar 3C 279 with the MAGIC telescope.* In F.A. Aharonian, W. Hofmann and F. Rieger, editors, *American Institute of Physics Conference Series*, vol. 1085 of *American Institute of Physics Conference Series*, 423–426.

Fazio G.G., Ashby M.L.N., Barmby P. et al. (2004). *Number Counts at 3 $\mu m < \lambda < 10$ μm from the Spitzer Space Telescope.* ApJS **154** 39–43. arXiv:astro-ph/0405595.

Fazio G.G. and Stecker F.W. (1970). *Predicted High Energy Break in the Isotropic Gamma Ray Spectrum: a Test of Cosmological Origin.* Nature **226** 135–+.

Fermi E. (1949). *On the Origin of the Cosmic Radiation.* Physical Review **75** 1169–1174.

Finke J.D., Shields J.C., Böttcher M. et al. (2008). *Redshift limits of BL Lacertae objects from optical spectroscopy.* A&A **477** 513–516. 0711.2089.

Fixsen D.J., Dwek E., Mather J.C. et al. (1998). *The Spectrum of the Extragalactic Far-Infrared Background from the COBE FIRAS Observations.* ApJ **508** 123–128. arXiv:astro-ph/9803021.

Folsom G.H., Miller H.R., Wingert D.W. et al. (1976). *Investigation of optical variability in 3C 66A.* AJ **81** 145–+.

Fomin V.P., Stepanian A.A., Lamb R.C. et al. (1994). *New methods of atmospheric Cherenkov imaging for gamma-ray astronomy. I. The false source method.* Astroparticle Physics **2** 137–150.

Fossati G., Maraschi L., Celotti A. et al. (1998). *A unifying view of the spectral energy distributions of blazars.* MNRAS **299** 433–448. arXiv:astro-ph/9804103.

Franceschini A., Rodighiero G. and Vaccari M. (2008). *Extragalactic optical-infrared background radiation, its time evolution and the cosmic photon-photon opacity.* A&A **487** 837–852. 0805.1841.

Frayer D.T., Huynh M.T., Chary R. et al. (2006). *Spitzer 70 Micron Source Counts in GOODS-North.* ApJ **647** L9–L12. arXiv:astro-ph/0606676.

Fugmann W. (1988). *Are all flat-spectrum radio sources blazars?* A&A **205** 86–92.

Gardner J.P., Brown T.M. and Ferguson H.C. (2000). *Ultraviolet Galaxy Counts from Space Telescope Imaging Spectrograph Observations of the Hubble Deep Fields.* ApJ **542** L79–L82.

Gaug M. (2006). *Calibration of the MAGIC telescope and Observation of Gamma Ray Bursts.* Ph.D. thesis, Univ. Autònoma de Barcelona.

Ghisellini G., Celotti A., Fossati G. et al. (1998). *A theoretical unifying scheme for gamma-ray bright blazars.* MNRAS **301** 451–468. arXiv:astro-ph/9807317.

Ghisellini G., Tavecchio F. and Chiaberge M. (2005). *Structured jets in TeV BL Lac objects and radiogalaxies. Implications for the observed properties.* A&A **432** 401–410. arXiv:astro-ph/0406093.

Giommi P., Capalbi M., Fiocchi M. et al. (2002). *A Catalog of 157 X-ray Spectra and 84 Spectral Energy Distributions of Blazars Observed with BeppoSAX.* In P. Giommi, E. Massaro and G. Palumbo, editors, *Blazar Astrophysics with BeppoSAX and Other Observatories*, 63.

Giovannini G., Cotton W.D., Feretti L. et al. (2001). *VLBI Observations of a Complete Sample of Radio Galaxies: 10 Years Later.* ApJ **552** 508–526. arXiv:astro-ph/0101096.

Goebel F., Bartko H., Carmona E. et al. (2008). *Upgrade of the MAGIC Telescope with a Multiplexed Fiber-Optic 2GSamples/s FADC Data Acquisition System system.* In *International Cosmic Ray Conference*, vol. 3 of *International Cosmic Ray Conference*, 1481–1484.

Gorjian V., Wright E.L. and Chary R.R. (2000). *Tentative Detection of the Cosmic Infrared Background at 2.2 and 3.5 Microns Using Ground-based and Space-based Observations.* ApJ **536** 550–560. arXiv:astro-ph/0103101.

Gould R.J. and Schréder G.P. (1967). *Pair Production in Photon-Photon Collisions.* Physical Review **155** 1404–1407.

Greisen K. (1966). *End to the Cosmic-Ray Spectrum?* Physical Review Letters **16** 748–750.

Hartman R.C., Bertsch D.L., Bloom S.D. et al. (1999). *The Third EGRET Catalog of High-Energy Gamma-Ray Sources.* ApJS **123** 79–202.

Hartman R.C., Böttcher M., Aldering G. et al. (2001). *Multiepoch Multiwavelength Spectra and Models for Blazar 3C 279.* ApJ **553** 683–694. arXiv:astro-ph/0102127.

Hartman R.C., Webb J.R., Marscher A.P. et al. (1996). *Simultaneous Multiwavelength Spectrum and Variability of 3C 279 from 10 9 to 10 24 Hz.* ApJ **461** 698–+.

Hauser M.G., Arendt R.G., Kelsall T. et al. (1998). *The COBE Diffuse Infrared Background Experiment Search for the Cosmic Infrared Background. I. Limits and Detections.* ApJ **508** 25–43. arXiv:astro-ph/9806167.

Hauser M.G. and Dwek E. (2001). *The Cosmic Infrared Background: Measurements and Implications.* ARA&A **39** 249–307. arXiv:astro-ph/0105539.

Heck D., Knapp J., Capdevielle J.N. et al. (1998). *CORSIKA: a Monte Carlo code to simulate extensive air showers.*

Hess V.F. (1912). *Über Beobachtungen der durchdringenden Strahlung bei sieben Freiballonfahrten.* Physikalische Zeitschrift **13** 1084–1091.

Hillas A.M. (1982). *Angular and energy distributions of charged particles in electron-photon cascades in air.* Journal of Physics G Nuclear Physics **8** 1461–1473.

Hillas A.M. (1985). *Cerenkov light images of EAS produced by primary gamma.* In F.C. Jones, editor, *International Cosmic Ray Conference*, vol. 3 of *International Cosmic Ray Conference*, 445–448.

Hinton J.A., Skilton J.L., Funk S. et al. (2009). *HESS J0632+057: A New Gamma-Ray Binary?* ApJ **690** L101–L104. 0809.0584.

Horan D., Badran H.M., Bond I.H. et al. (2004). *Constraints on the Very High Energy Emission from BL Lacertae Objects.* ApJ **603** 51–61. arXiv:astro-ph/0311397.

Horan D. and Wakely S. (2008). *TeVCat: An online catalog for Very High Energy Gamma-Ray Astronomy.* In *American Astronomical Society Meeting Abstracts*, vol. 211 of *American Astronomical Society Meeting Abstracts*, 160.03. URL http://tevcat.uchicago.edu.

Impey C.D., Lawrence C.R. and Tapia S. (1991). *Optical polarization of a complete sample of radio sources.* ApJ **375** 46–68.

Joshi M. and Böttcher M. (2007). *Modeling the Spectral Energy Distribution and Variability of 3C 66A during the WEBT Campaign of 2003-2004.* ApJ **662** 884–891. 0704.0269.

Kaaret P. (1999). *Pulsar radiation and quantum gravity.* A&A **345** L32–L34. arXiv:astro-ph/9903464.

Kashlinsky A. (2008). *Cosmic Infrared Background from Early Epochs: Searching for Signatures of the First Stars.* In B.W. O'Shea and A. Heger, editors, *First Stars III*, vol. 990 of *American Institute of Physics Conference Series*, 127–131.

Kashlinsky A., Arendt R.G., Mather J. et al. (2005). *Tracing the first stars with fluctuations of the cosmic infrared background.* Nature **438** 45–50. arXiv:astro-ph/0511105.

Kashlinsky A. and Odenwald S. (2000). *Clustering of the Diffuse Infrared Light from the COBE DIRBE Maps. III. Power Spectrum Analysis and Excess Isotropic Component of Fluctuations.* ApJ **528** 74–95. arXiv:astro-ph/9908304.

Kataoka J., Mattox J.R., Quinn J. et al. (1999). *High-Energy Emission from the TEV Blazar Markarian 501 during Multiwavelength Observations in 1996.* ApJ **514** 138–147. arXiv:astro-ph/9811014.

Katarzyński K., Ghisellini G., Tavecchio F. et al. (2006). *Hard TeV spectra of blazars and the constraints to the infrared intergalactic background.* MNRAS **368** L52–L56. arXiv:astro-ph/0603030.

Kerrick A., Akerlof C.W. and et al. (1993). *Search for TeV Gamma-Ray Emission from AGN's.* In *International Cosmic Ray Conference*, vol. 1 of *International Cosmic Ray Conference*, 405–+.

Kinney A.L., Bohlin R.C., Blades J.C. et al. (1991). *An ultraviolet atlas of quasar and blazar spectra.* ApJS **75** 645–717.

Kino M., Takahara F. and Kusunose M. (2002). *Energetics of TeV Blazars and Physical Constraints on Their Emission Regions.* ApJ **564** 97–107. arXiv:astro-ph/0107436.

Kirk J.G. (1994). *Particle Acceleration (With 26 figures).* In A.O. Benz and T.J.L. Courvoisier, editors, *Saas-Fee Advanced Course 24: Plasma Astrophysics*, 225–+.

Kirk J.G. and Duffy P. (1999). *TOPICAL REVIEW: Particle acceleration and relativistic shocks.* Journal of Physics G Nuclear Physics **25** 163–+.

Kneiske T.M., Bretz T., Mannheim K. et al. (2004). *Implications of cosmological gamma-ray absorption. II. Modification of gamma-ray spectra.* A&A **413** 807–815. arXiv:astro-ph/0309141.

Kneiske T.M., Mannheim K. and Hartmann D.H. (2002). *Implications of cosmological gamma-ray absorption. I. Evolution of the metagalactic radiation field.* A&A **386** 1–11. arXiv:astro-ph/0202104.

Kniffen D.A., Bertsch D.L., Fichtel C.E. et al. (1993). *Time variability in the gamma-ray emission of 3C 279.* ApJ **411** 133–136.

Krawczynski H., Hughes S.B., Horan D. et al. (2004). *Multiwavelength Observations of Strong Flares from the TeV Blazar 1ES 1959+650.* ApJ **601** 151–164. arXiv:astro-ph/0310158.

Kuiper L., Hermsen W., Verbunt F. et al. (2000). *The likely detection of pulsed high-energy gamma -ray emission from millisecond pulsar PSR J0218+4232.* A&A **359** 615–626. arXiv:astro-ph/0005338.

Lagache G. and Puget J.L. (2000). *Detection of the extra-Galactic background fluctuations at 170 mu m.* A&A **355** 17–22. arXiv:astro-ph/9910255.

Lainela M., Takalo L.O., Sillanpää A. et al. (1999). *The 65 Day Period in 3C 66A during Bright State.* ApJ **521** 561–564.

Larionov V.M., Villata M., Raiteri C.M. et al. (2008). *Optical and near-IR brightening of the blazar 3C 66A detected by the GASP.* The Astronomer's Telegram **1755** 1–+.

Lessard R.W., Buckley J.H., Connaughton V. et al. (2001). *A new analysis method for reconstructing the arrival direction of TeV gamma rays using a single imaging atmospheric Cherenkov telescope.* Astroparticle Physics **15** 1–18. arXiv:astro-ph/0005468.

Levenson L.R. and Wright E.L. (2008). *Probing the 3.6 μm CIRB with Spitzer in Three DIRBE Dark Spots.* ApJ **683** 585–596. 0802.1239.

Levenson L.R., Wright E.L. and Johnson B.D. (2007). *DIRBE Minus 2MASS: Confirming the CIRB in 40 New Regions at 2.2 and 3.5 μm.* ApJ **666** 34–44. 0704.1498.

Li T.P. and Ma Y.Q. (1983). *Analysis methods for results in gamma-ray astronomy.* ApJ **272** 317–324.

Lindfors E., Reinthal R., Mazin D. et al. (2009). *The connection between optical and VHE γ-ray high states in blazar jets.* In *31st International Cosmic Ray Conference.*

Liu H.T., Bai J.M. and Ma L. (2008). *Absorption of 10 GeV-1 TeV Gamma Rays by Radiation from the Broad-Line Region in 3C 279*. ApJ **688** 148–158. 0807.3133.

Longair M.S. (1992). *High energy astrophysics. Vol.1: Particles, photons and their detection*.

Maccagni D., Garilli B., Schild R. et al. (1987). *X-ray/optical brightness trends in 3C 66A*. A&A **178** 21–24.

MacDonald G.H., Kenderdine S. and Neville A.C. (1968). *Observations of the structure of radio sources in the 3C catalogue-I*. MNRAS **138** 259–+.

Madau P. and Pozzetti L. (2000). *Deep galaxy counts, extragalactic background light and the stellar baryon budget*. MNRAS **312** L9–L15. arXiv:astro-ph/9907315.

Madau P. and Silk J. (2005). *Population III and the near-infrared background excess*. MNRAS **359** L37–L41. arXiv:astro-ph/0502304.

Madejski G.M. and Sikora M. (2006). *High Energy Observations of Blazars: the Future*. In H.R. Miller, K. Marshall, J.R. Webb and M.F. Aller, editors, *Blazar Variability Workshop II: Entering the GLAST Era*, vol. 350 of *Astronomical Society of the Pacific Conference Series*, 215–+.

Majumdar P. et al. (2005). *Monte Carlo simulation for the MAGIC telescope*. In *International Cosmic Ray Conference*, vol. 5 of *International Cosmic Ray Conference*, 203–+.

Mannheim K. and Biermann P.L. (1992). *Gamma-ray flaring of 3C 279 - A proton-initiated cascade in the jet?* A&A **253** L21–L24.

Maraschi L., Ghisellini G. and Celotti A. (1992). *A jet model for the gamma-ray emitting blazar 3C 279*. ApJ **397** L5–L9.

Maraschi L., Grandi P., Urry C.M. et al. (1994). *The 1993 multiwavelength campaign on 3C 279: The radio to gamma-ray energy distribution inlow state*. ApJ **435** L91–L95.

Maraschi L. and Tavecchio F. (2003). *The Jet-Disk Connection and Blazar Unification*. ApJ **593** 667–675. arXiv:astro-ph/0205252.

Martínez M. and Errando M. (2009). *A new approach to study energy-dependent arrival delays on photons from astrophysical sources*. Astroparticle Physics **31** 226–232. 0803.2120.

Matsuhara H., Kawara K., Sato Y. et al. (2000). *ISO deep far-infrared survey in the "Lockman Hole". II. Power spectrum analysis: evidence of a strong evolution in number counts*. A&A **361** 407–414. arXiv:astro-ph/0006444.

Matsumoto T., Matsuura S., Murakami H. et al. (2005). *Infrared Telescope in Space Observations of the Near-Infrared Extragalactic Background Light*. ApJ **626** 31–43. arXiv:astro-ph/0411593.

Mazin D. (2007). *A study of very high energy gamma-ray emission from agns and constraints on the extragalactic background light*. Ph.D. thesis, Technische Universität München.

Mazin D. and Raue M. (2007). *New limits on the density of the extragalactic background light in the optical to the far infrared from the spectra of all known TeV blazars.* A&A **471** 439–452. arXiv:astro-ph/0701694.

Metcalfe L., Kneib J.P., McBreen B. et al. (2003). *An ISOCAM survey through gravitationally lensing galaxy clusters. I. Source lists and source counts for A370, A2218 and A2390.* A&A **407** 791–822. arXiv:astro-ph/0305400.

Miller J.S., French H.B. and Hawley S.A. (1978). *Optical spectra of BL Lacertae objects.* In A.M. Wolfe, editor, *BL Lac Objects*, 176–187.

Mirabel I.F. and Rodriguez L.F. (1994). *A Superluminal Source in the Galaxy.* Nature **371** 46–+.

Mirzoyan R. (1997). *On the Calibration Accuracy of Light Sensors in Atmospheric Cherenkov Fluorescence and Neutrino Experiments.* In *International Cosmic Ray Conference*, vol. 7 of *International Cosmic Ray Conference*, 265–+.

Neronov A. and Aharonian F.A. (2007). *Production of TeV Gamma Radiation in the Vicinity of the Supermassive Black Hole in the Giant Radio Galaxy M87.* ApJ **671** 85–96. 0704.3282.

Neshpor Y.I., Stepanyan A.A., Kalekin O.P. et al. (1998). *Blazar 3C 66A: Another extragalactic source of ultra-high-energy gamma-ray photons.* Astronomy Letters **24** 134–138.

Nieppola E., Tornikoski M. and Valtaoja E. (2006). *Spectral energy distributions of a large sample of BL Lacertae objects.* A&A **445** 441–450. arXiv:astro-ph/0509045.

Nieppola E., Valtaoja E., Tornikoski M. et al. (2008). *Blazar sequence - an artefact of Doppler boosting.* A&A **488** 867–872. 0803.0654.

Ostankov A., Paneque D., Lorenz E. et al. (2000). *A study of the new hemispherical 6-dynodes PMT from electron tubes.* Nuclear Instruments and Methods in Physics Research A **442** 117–123.

Padovani P. (2007). *The blazar sequence: validity and predictions.* Ap&SS **309** 63–71. arXiv:astro-ph/0610545.

Paneque D., Gebauer H.J., Lorenz E. et al. (2003). *A method to enhance the sensitivity of photomultipliers for air Cherenkov telescopes.* Nuclear Instruments and Methods in Physics Research A **504** 109–115.

Papovich C., Dole H., Egami E. et al. (2004). *The 24 Micron Source Counts in Deep Spitzer Space Telescope Surveys.* ApJS **154** 70–74. arXiv:astro-ph/0406035.

Perlman E.S., Harris D.E., Biretta J.A. et al. (2003). *Month-Timescale Optical Variability in the M87 Jet.* ApJ **599** L65–L68. arXiv:astro-ph/0311161.

Pian E., Urry C.M., Maraschi L. et al. (1999). *Ultraviolet and Multiwavelength Variability of the Blazar 3C 279: Evidence for Thermal Emission.* ApJ **521** 112–120. arXiv:astro-ph/9906326.

Primack J.R., Bullock J.S. and Somerville R.S. (2005). *Observational Gamma-ray Cosmology*. In F.A. Aharonian, H.J. Völk and D. Horns, editors, *High Energy Gamma-Ray Astronomy*, vol. 745 of *American Institute of Physics Conference Series*, 23–33.

Primack J.R., Gilmore R.C. and Somerville R.S. (2008). *Diffuse Extragalactic Background Radiation*. ArXiv e-prints 0811.3230.

Protheroe R.J. and Biermann P.L. (1997). *Photon-photon absorption above a molecular cloud torus in blazars*. Astroparticle Physics **6** 293–300. arXiv:astro-ph/9608052.

Reimer A. (2007). *The Redshift Dependence of Gamma-Ray Absorption in the Environments of Strong-Line AGNs*. ApJ **665** 1023–1029. 0705.1534.

Renault C., Barrau A., Lagache G. et al. (2001). *New constraints on the cosmic mid-infrared background using TeV gamma-ray astronomy*. A&A **371** 771–778. arXiv:astro-ph/0012094.

Riegel B. et al. (2005). *A tracking monitor for the MAGIC Telescope*. In *International Cosmic Ray Conference*, vol. 5 of *International Cosmic Ray Conference*, 219–+.

Risse M. (2004). *Properties of Extensive Air Showers*. Acta Physica Polonica B **35** 1787–+. arXiv:astro-ph/0402300.

Roach F.E. and Gordon J.L. (1973). *The light of the night sky*. Geophysics and Astrophysics Monographs **4**.

Rolke W.A., López A.M. and Conrad J. (2005). *Limits and confidence intervals in the presence of nuisance parameters*. Nuclear Instruments and Methods in Physics Research A **551** 493–503. arXiv:physics/0403059.

Rovelli C. (1998). *Loop Quantum Gravity*. Living Reviews in Relativity **1** 1–+. arXiv:gr-qc/9710008.

Salvaterra R. and Ferrara A. (2006). *Where are the sources of the near-infrared background?* MNRAS **367** L11–L15. arXiv:astro-ph/0509338.

Sarkar S. (2002). *Possible Astrophysical Probes of Quantum Gravity*. Modern Physics Letters A **17** 1025–1035. arXiv:gr-qc/0204092.

Schmidt F. (2007). *Corsika shower images*. http://www.ast.leeds.ac.uk/∼fs/showerimages.html.

Shakura N.I. and Sunyaev R.A. (1973). *Black holes in binary systems. Observational appearance*. A&A **24** 337–355.

Sikora M. and Madejski G. (2001). *Blazars*. In F.A. Aharonian and H.J. Völk, editors, *American Institute of Physics Conference Series*, vol. 558 of *American Institute of Physics Conference Series*, 275–+.

Sitarek J. and Bednarek W. (2008). *Modification of the gamma-ray spectra by internal absorption in optically violently variable blazars: the example cases of 3C 273 and 3C 279*. MNRAS **391** 624–638. 0807.4228.

Springer R.W. (2005). *Measurements of UHECR Spectrum with the HiRes detector*. In *International Cosmic Ray Conference*, vol. 7 of *International Cosmic Ray Conference*, 391–+.

Stecker F.W. (1999). *Intergalactic extinction of high energy gamma-rays.* Astroparticle Physics **11** 83–91. arXiv:astro-ph/9812286.

Stecker F.W. and de Jager O.C. (1996). *Absorption of high energy gamma-rays by low energy intergalactic photons.* Space Science Reviews **75** 401–412. arXiv:astro-ph/9501065.

Stecker F.W., Malkan M.A. and Scully S.T. (2006). *Intergalactic Photon Spectra from the Far-IR to the UV Lyman Limit for $0 < z < 6$ and the Optical Depth of the Universe to High-Energy Gamma Rays.* ApJ **648** 774–783. arXiv:astro-ph/0510449.

Stepanyan A.A., Neshpor Y.I., Andreeva N.A. et al. (2002). *Observations of the Flux of Very-High-Energy Gamma Rays from the Blazar 3C 66A.* Astronomy Reports **46** 634–638.

Stull M.A., Price K.M., Daddario L.R. et al. (1975). *Study of the brightness and polarization structure of extragalactic radio sources.* AJ **80** 559–580.

Sudou H., Iguchi S., Murata Y. et al. (2003). *Orbital Motion in the Radio Galaxy 3C 66B: Evidence for a Supermassive Black Hole Binary.* Science **300** 1263–1265. arXiv:astro-ph/0306103.

Swordy S. (2008). *Discovery of >100 GeV Gamma-ray Emission from the Blazar 3C66A by VERITAS.* The Astronomer's Telegram **1753** 1–+.

Takeda M., Hayashida N., Honda K. et al. (1998). *Extension of the Cosmic-Ray Energy Spectrum beyond the Predicted Greisen-Zatsepin-Kuz'min Cutoff.* Physical Review Letters **81** 1163–1166. arXiv:astro-ph/9807193.

Takeda M., Hayashida N., Honda K. et al. (1999). *Small-Scale Anisotropy of Cosmic Rays above 10^19 eV Observed with the Akeno Giant Air Shower Array.* ApJ **522** 225–237. arXiv:astro-ph/9902239.

Tamm I.E. and Frank I.M. (1937). *Coherent radiation of fast electrons in a medium.* Dokl. Akad. Nauk. USSR **544** 107.

Tavecchio F. and Ghisellini G. (2008). *Spine-sheath layer radiative interplay in subparsec-scale jets and the TeV emission from M87.* MNRAS **385** L98–L102. 0801.0593.

Tavecchio F. and Ghisellini G. (2009). *3C 66B as a TeV radio galaxy.* MNRAS **394** L131–L135. 0811.1883.

Tavecchio F., Maraschi L. and Ghisellini G. (1998). *Constraints on the Physical Parameters of TeV Blazars.* ApJ **509** 608–619. arXiv:astro-ph/9809051.

Tavecchio F. and Mazin D. (2009). *Intrinsic absorption in 3C 279 at GeV-TeV energies and consequences for estimates of the extragalactic background light.* MNRAS **392** L40–L44. 0809.2467.

Tescaro D., Bartko H., Galante N. et al. (2007). *Study of the performance and capability of the new ultra-fast 2 GSample/s FADC data acquisition system of the MAGIC telescope.* ArXiv e-prints 0709.1410.

Teshima M. (2008). *MAGIC discovers VHE gamma ray emission from the blazar S50716+714.* The Astronomer's Telegram **1500** 1–+.

Teshima M., Prandini E., Bock R. et al. (2008). *Discovery of Very High Energy Gamma-Rays from the Distant Flat Spectrum Radio Quasar 3C 279 with the MAGIC Telescope.* In *International Cosmic Ray Conference*, vol. 3 of *International Cosmic Ray Conference*, 1045–1048.

Tikhonov A. and Arsenin V. (1977). *Solutions of III-posed problems.* Washington : Winston.

Tosti G. (2008). *Fermi LAT detections of gamma ray activity in three blazars: 3C 66A, PKS 0208-512, PKS 0537-441.* The Astronomer's Telegram **1759** 1–+.

Unwin S.C., Cohen M.H., Hodges M.W. et al. (1989). *Superluminal motion in the quasar 3C 279.* ApJ **340** 117–128.

Urry C.M. and Padovani P. (1995). *Unified Schemes for Radio-Loud Active Galactic Nuclei.* PASP **107** 803–+. arXiv:astro-ph/9506063.

Valtaoja E., Terasranta H., Urpo S. et al. (1992). *Five Years Monitoring of Extragalactic Radio Sources - Part Four - Variability Statistics and the Unified Models for AGN / Active Galactic Nuclei.* A&A **254** 80–+.

Vassiliev V.V. (2000). *Extragalactic background light absorption signal in the TeV gamma-ray spectra of blazars.* Astroparticle Physics **12** 217–238. arXiv:astro-ph/9908088.

Weekes T.C., Cawley M.F., Fegan D.J. et al. (1989). *Observation of TeV gamma rays from the Crab nebula using the atmospheric Cerenkov imaging technique.* ApJ **342** 379–395.

Wehrle A.E., Pian E., Urry C.M. et al. (1998). *Multiwavelength Observations of a Dramatic High-Energy Flare in the Blazar 3C 279.* ApJ **497** 178–+. arXiv:astro-ph/9711243.

Weinberg S. (1995). *The quantum theory of fields. Vol.1: Foundations.*

Whitney A.R., Shapiro I.I., Rogers A.E.E. et al. (1971). *Quasars Revisited: Rapid Time Variations Observed Via Very-Long-Baseline Interferometry.* Science **173** 225–230.

Wills B.J. and Wills D. (1974). *C 66A: a Bright New Quasi-Stellar Object.* ApJ **190** L97+.

Wills B.J., Wills D., Breger M. et al. (1992). *A survey for high optical polarization in quasars with core-dominant radio structure - Is there a beamed optical continuum?* ApJ **398** 454–475.

Wright E.L. (2001). *DIRBE minus 2MASS: Confirming the Cosmic Infrared Background at 2.2 Microns.* ApJ **553** 538–544. arXiv:astro-ph/0004192.

Wright E.L. (2004). *COBE observations of the cosmic infrared background.* New Astronomy Review **48** 465–468. arXiv:astro-ph/0306058.

Wright E.L. and Reese E.D. (2000). *Detection of the Cosmic Infrared Background at 2.2 and 3.5 Microns Using DIRBE Observations.* ApJ **545** 43–55. arXiv:astro-ph/9912523.

Wurtz R., Stocke J.T. and Yee H.K.C. (1996). *The Canada-France-Hawaii Telescope Imaging Survey of BL Lacertae Objects. I. Properties of the Host Galaxies.* ApJS **103** 109–+.

Xu C.K., Donas J., Arnouts S. et al. (2005). *Number Counts of GALEX Sources in Far-Ultraviolet (1530 Å) and Near-Ultraviolet (2310 Å) Bands.* ApJ **619** L11–L14. arXiv:astro-ph/0411317.

Yao W.M. et al. (2006). *Review of Particle Physics.* Journal of Physics G Nuclear Physics **33** 1–1232.

Zatsepin G.T. and Kuzmin V.A. (1966). *Upper Limit of the Spectrum of Cosmic Rays.* Soviet Journal of Experimental and Theoretical Physics Letters **4** 78–+.